

University of Southampton Research Repository

Copyright © and Moral Rights for this thesis and, where applicable, any accompanying data are retained by the author and/or other copyright owners. A copy can be downloaded for personal non-commercial research or study, without prior permission or charge. This thesis and the accompanying data cannot be reproduced or quoted extensively from without first obtaining permission in writing from the copyright holder/s. The content of the thesis and accompanying research data (where applicable) must not be changed in any way or sold commercially in any format or medium without the formal permission of the copyright holder/s.

When referring to this thesis and any accompanying data, full bibliographic details must be given, e.g.

Thesis: Author (Year of Submission) "Full thesis title", University of Southampton, name of the University Faculty or School or Department, PhD Thesis, pagination.

Data: Author (Year) Title. URI [dataset]

University of Southampton

Faculty of Engineering and Physical Sciences

School of Electronics and Computer Science

**Vanadium dioxide for nanophotonic memory: device design
and low-temperature annealing**

by

Yuxin Du

Thesis for the degree of Doctor of Philosophy

April 2025

University of Southampton

Abstract

Faculty of Engineering and Physical Sciences

School of Electronics and Computer Science

Doctor of Philosophy

Vanadium dioxide for nanophotonic memory: device design and low-temperature annealing

By Yuxin Du

Optical memory is considered a promising solution to overcome the bottlenecks of the traditional von Neumann architecture, with its core challenge lying in the search for suitable functional materials. Vanadium dioxide (VO_2), as a solid-state phase change material, exhibits great potential in optical circuits, neuromorphic computing, and radiative cooling due to its phase transition properties near room temperature. Currently, VO_2 based memory devices typically rely on the intrinsic hysteresis characteristics of the material, posing significant challenges for large-scale production and design optimisation. Moreover, the practical application of VO_2 in optical memory remains constrained by fabrication techniques. Conventional VO_2 thin film fabrication generally requires high-temperature ($>400^\circ\text{C}$) direct deposition or the deposition of amorphous VO_2 followed by high-temperature annealing to achieve high-quality crystalline phases. However, such high-temperature processes not only limit the compatibility of VO_2 with CMOS integrated circuits, particularly post-metallisation processes, but also make it difficult to deposit VO_2 onto flexible polyimide substrates, restricting its applications in flexible substrates.

To address these challenges, this thesis explores a low-temperature VO_2 thin film fabrication method combining atomic layer deposition (ALD) and low-temperature annealing. Systematic material characterisation demonstrates, for the first time, the successful realisation of high-quality VO_2 thin films on a silicon substrate under a 300°C annealing condition, significantly reducing the thermal budget. Further investigations reveal that lowering the annealing temperature to 250°C results in insufficient VO_2 crystallisation, whereas increasing it to 400°C leads to over-oxidation, forming V_2O_5 . Additionally, this method is applied to flexible polyimide substrates and verifies that the high-quality phase change characteristics of VO_2 are preserved.

Through Raman spectroscopy and X-ray diffraction (XRD) identified that the annealing process primarily alters crystal strain, which in turn influences the phase transition temperature and refractive index. This insight provides a qualitative understanding of how high-quality VO₂ thin films can be obtained for specific applications. Furthermore, the investigation of the annealing behaviour of W-doped VO₂ found that tungsten doping affects both the annealing and oxidation processes. The results indicate that finely tuned annealing conditions are required to achieve W:VO₂ films with high optical contrast.

This thesis also proposed a device-level bistability approach that leverages the refractive index contrast between the insulating and metallic phases of VO₂. This method exhibits different bistability ranges across various device structures, offering a novel approach to VO₂-based optical memory. Unlike conventional VO₂ optical memory that relies on the material's hysteresis properties through globally change of the ambient temperature, this approach enhances the robustness of large-scale manufacturing. Furthermore, the bistability characteristics of the microring structure enable it to mimic short-term associative learning. By systematically optimising the structure through finite element simulations, I achieve an optical contrast of 0.59 (ER=8.04 dB). The volatile nature of VO₂ allows it to mimic the learning and forgetting mechanisms of biological neural systems. Additionally, within the bistability range, only a small input stimulus is required to maintain associative memory states.

This work paves the way for low-power on-chip photonic neuromorphic computing based on VO₂, expanding its potential applications in CMOS-compatible optical memory application.

Contents

Abstract	3
List of Publications.....	9
List of Abbreviations.....	11
Research Thesis: Declaration of Authorship	13
Acknowledgements	14
Chapter 1. Introduction and research background.....	15
1.1 Motivation and project aim	15
1.2 Introduction to VO ₂	17
1.2.1 VO ₂ phase change kinetics.....	18
1.2.2 VO ₂ crystal structure.....	20
1.2.3 VO ₂ band structure.....	21
1.2.4 Discussion of VO ₂ phase change mechanism	22
1.3 VO ₂ phase transition modulation	24
1.3.1 Doping	24
1.3.2 Strain engineering.....	26
1.3.3 Others.....	28
1.4 Applications of VO ₂ thin film on silicon photonics.....	29
1.4.1 Optical driven VO ₂ for optical switch.....	29
1.4.2 VO ₂ integrated photonic volatile memory	34
1.4.3 VO ₂ application based on non-volatile characteristic	37
1.4.4 Implementation of VO ₂ on neuromorphic computing.....	39
1.5 Thesis synopsis.....	44
Chapter 2. Methods	46
2.1 Vanadium dioxide thin film deposition method.....	47
2.1.1 Atomic layer deposition	47
2.1.2 Chemical vapor deposition	51

2.1.3 Sputtering	52
2.1.4 Pulsed laser deposition.....	53
2.1.5 Molecular beam epitaxy.....	55
2.1.6 Sol-Gel Method	55
2.1.7 Discussion of VO ₂ thin film synthesis method	56
2.2 Annealing treatments in atomic layer deposition	57
2.3 VO ₂ characterisation technology.....	60
2.3.1 Raman Spectroscopy.....	60
2.3.2 X-ray Photoelectron Spectroscopy	62
2.3.3 Fourier Transform Infrared Spectroscopy	63
2.3.4 Ellipsometry	63
2.4 Silicon waveguide and microring resonator	65
2.4.1 Silicon waveguide.....	65
2.4.2 Silicon microring resonator	68
2.5 Conclusion to Chapter 2	72
Chapter 3. Low-temperature vanadium dioxide for CMOS integration and flexible polyimide applications.....	74
3.1 Introduction.....	74
3.2 Experimental Procedure	75
3.2.1 VO ₂ growth through atomic layer deposition	75
3.2.2 Post-deposition anneal.....	77
3.2.3 Selection of annealing parameters	77
3.2.4 Material characterisations	78
3.2.5 Optical characterisations.....	82
3.2.6 Scanning electron microscopy measurement	85
3.3 Results and discussion	85
3.3.1 VO ₂ film morphology before annealing.....	85
3.3.2 Effect of oxygen partial pressure on VO ₂ anneal.....	85

3.3.3 Effect of annealing temperature on VO ₂ thin film	93
3.3.4 Effect of annealing duration on VO ₂ anneal	104
3.3.5 Quantification of VO ₂ thin films using Raman	109
3.3.6 Further investigation of crystal strain through Raman peak shifts.....	113
3.3.7 Discussion of tuneable refractive index via strain	116
3.3.8 Discussion of the annealing effect on the VO ₂ surface topography	118
3.4 Conclusion to Chapter 3	121
Chapter 4. Device-level bistability in VO ₂ microring resonator for optical memory.....	123
4.1 Introduction.....	123
4.2 Methodology.....	125
4.2.1 Device structures	125
4.2.2 VO ₂ refractive index modelling.....	126
4.2.3 Running COMSOL on the university supercomputer	129
4.2.4 COMSOL run file of Iridis 5	130
4.2.5 Boundary conditions and material parameters	130
4.2.6 Time-Harmonic EM Heating and two-way coupling	133
4.2.7 Study of comparison between Lumerical and COMSOL	135
4.3 Device-level bistability in a straight waveguide	146
4.4 Device-level bistability on VO ₂ -Integrated microring resonator	151
4.4.1 Analysis of VO ₂ side part effect on the device performance	156
4.4.2 Implementation of photonic associative learning in microring resonator	157
4.4.3 Optimisation strategy for optical contrast	161
4.5 Conclusion to Chapter 4	166
Chapter 5. Conclusions and future work	167
5.1 Conclusions	167
5.2 Future work	168
Appendix A. Simulations and Optimisation for VPAM	171
A1. Run code in Iridis supercomputer	171

A2. COMSOL mesh density comparison of all four condition steps	171
A3. Discovery of VO ₂ patch relative position effect on the Si microring.	172
A4. Actual measured values of mesh size in Lumerical software.....	172
A5. Comparison between device level bistability with and without applying the Looyenga mixing rule	173
A6. Raw simulation results in the main text, Fig. 4.21-Fig. 4.23.	174
A7. Optical bistability of straight waveguides that have VO ₂ patches of varying lengths on top.	176
Appendix B. Annealing optimisation for flexible polyamide.....	178
Appendix C. Datasheet contains information on the decomposition temperature of DuPont Kapton FPC 350	179
Appendix D. ‘Particle-like’ surface morphology introduced by dewetting and substrates.....	180
D1. Dewetting behaviour of Au thin film under annealing temperature of 550°C	180
D2. 460°C annealed VO ₂ film on 90 nm SiO ₂ synthesised by ALD using TEMAV and O3 precursors	180
Appendix E. Raman peak position of known vanadium oxides	182
Bibliography.....	184

List of Publications

Journal Publication:

Du, Y., Wheeler, C., de Groot, C. H., Muskens, O. L., Fang, X., & Sun, K. (2025). Low-temperature vanadium dioxide for CMOS integration and flexible polyimide applications. *Optical Materials Express*, 15(3), 465-476.

Conference attendances:

1. Authors: Yuxin Du, Kai Sun, Zihang Zheng, Cornelis H. de Groot and Xu Fang

Title: Optical Modulation in a Si Microring Resonator Inspired by Biological Classical Conditioning

Conference information: Photonics in Switching and Computing (PSC), Online. 27 - 29 Sep 2021.
1 pp.

2. Authors: Du, Yuxin, Sun, Kai, Zheng, Zihang, De Groot, Kees and Fang, Xu

Title: Low temperature annealing for vanadium dioxide in photonic integrated circuits

Conference information: The 84th JSAP Autumn Meeting 2023, Kumamoto, Japan. 19 - 23 Sep 2023. 1 pp.

3. Authors: Zheng, Zihang, Sun, Kai, Du, Yuxin, De Groot, Kees and Fang, Xu (2023)

Title: Vanadium dioxide-enabled tuneable metasurfaces

Conference information: The 84th JSAP Autumn Meeting 2023, Kumamoto, Japan. 19 - 23 Sep 2023. 1 pp.

4. Authors: Zheng, Zihang, Sun, Kai, Du, Yuxin, Muskens, Otto, De Groot, Kees and Fang, Xu (2022)

Title: Vertical growth models for analysing vanadium dioxide phase transition in thin films.

Conference information: IOP Photon 2022, East Midlands Conference Centre, Nottingham, United Kingdom. 30 Aug - 02 Sep 2022.

5. Authors: Zheng, Zihang, Sun, Kai, Du, Yuxin, Muskens, Otto, De Groot, Kees and Fang, Xu

Title: Vertical growth models outperform effective medium models in analysing VO₂ phase transition

Conference information: CLEO, San Jose, United States. 15 - 20 May 2022. 1 pp.

List of Abbreviations

ALD - Atomic layer deposition

CMOS - Complementary Metal-Oxide-Semiconductor

CVD - Chemical vapour deposition

DNN - Deep Neural Network

FDTD - Finite-difference time-domain

FTIR - Fourier transform infrared microscope

FWHM – Full width half maximum

GST - Germanium-antimony-tellurium (GeSbTe)

IMT - Insulator-to-Metal Transition

MIT - Metal–Insulator Transition

MBE - Molecular Beam Epitaxy

MSE – Mean square error

PCM - Phase Change Material

PLD - Pulsed Laser Deposition

PECVD - Plasma-enhanced chemical vapour deposition

Q factor – Quality factor

SEM - Scanning Electron Microscopy

SR-FF - Set-Reset Flip-Flop

SCCM - Standard Cubic Centimetres per Minute

SOI – Silicon on insulator

TEMAV - Tetrakis(ethylmethylamino) vanadium

VO₂ - Vanadium dioxide

WDM - Wavelength Division Multiplexing

XPS - X-ray Photoelectron Spectroscopy

XRD - X-ray Diffraction

Research Thesis: Declaration of Authorship

Print name: Yuxin Du

Title of thesis: Vanadium dioxide for nanophotonic memory: device design and low-temperature annealing

I declare that this thesis and the work presented in it are my own and has been generated by me as the result of my own original research.

I confirm that:

1. This work was done wholly or mainly while in candidature for a research degree at this University;
2. Where any part of this thesis has previously been submitted for a degree or any other qualification at this University or any other institution, this has been clearly stated;
3. Where I have consulted the published work of others, this is always clearly attributed;
4. Where I have quoted from the work of others, the source is always given. With the exception of such quotations, this thesis is entirely my own work;
5. I have acknowledged all main sources of help;
6. Where the thesis is based on work done by myself jointly with others, I have made clear exactly what was done by others and what I have contributed myself;
7. Parts of this work have been published as the journal papers and conference contributions in the list of publications.

Signature:Date:

Acknowledgements

Words cannot express my gratitude to my supervisors: Dr. Xu Fang, Professor Kees de Groot, and Dr. Kai Sun. Dr. Xu Fang has provided me with numerous invaluable opportunities and constant support. He has been a role model for me, both academically and personally. Without his support, this research and others not covered in this thesis would never have been completed. Professor Kees de Groot and Dr. Kai Sun have been sources of inspiration, offering timely suggestions, kindness, enthusiasm, and dynamism, which have enabled me to complete my thesis.

I am also grateful to my collaborators, especially my office mates, who have provided precious advice and technical support to help with my research. I would like to thank my colleagues, Jianzhi Huang and Callum Wheeler, for their assistance with the XPS and SEM measurements. Additionally, I would like to thank Professor Otto Muskens, who kindly provided an optical measurement device for measuring my fabricated sample in my final year. Without his help, I would not have been able to present the actual FTIR results in this thesis. Finally, I would like to thank Consorzio CREO (Italy) for providing the Kapton.

Chapter 1. Introduction and research background

1.1 Motivation and project aim

The volume of information stored in data centres and the computational demands of data-intensive applications, particularly deep learning and artificial intelligence, are growing exponentially. One example of this trend comes from deep learning: between 2015 and 2020, the computational power required to train state-of-the-art deep neural networks (DNNs) increased by more than 300,000 times, doubling approximately every 3.4 months [1, 2], whereas the computational efficiency of graphics processing units (GPUs) only improved by a factor of 300 over the same period [3, 4]. This explosive growth in computing demands poses a significant challenge to the traditional von Neumann architecture, necessitating the development of new paradigms in memory and computation to enhance data processing efficiency. Compared with traditional memory (e.g., RAM/ROM), optical memory has gained increasing attention as a promising storage technology due to its ultra-high-speed data transmission and high parallel computing capabilities (e.g., wavelength-division multiplexing, WDM) [5, 6].

Since the first optical memory was reported in 1965 [7], and two decades later, the emergence of the first optical set-reset flip-flop (SR-FF) with a response time of less than 1 ns [8]. Integrated optical memory leverages the speed and energy advantages of photons, providing a significant opportunity to optimise computing architectures. While silicon photonics has become the leading platform for information transmission, its intrinsically limited optical properties have led researchers to explore hybrid silicon photonic architectures, incorporating III-V compound semiconductors [9, 10], two-dimensional materials [11], and phase-change materials (PCMs) [12] to enhance optical storage and computing functionalities.

Memory devices are typically classified into volatile and non-volatile memory, with the key distinction being whether data can be retained without power consumption. Moreover, they differ significantly in terms of access speed, power consumption, and application scenarios. Volatile memory, such as DRAM, is commonly used for fast access operations, offering high-speed response and high throughput [13]. In contrast, non-volatile memory is suited for long-term data

storage, where speed requirements are relatively lower [14]. In recent years, chalcogenide-based phase-change materials (PCMs), such as germanium-antimony-tellurium (GST), have been extensively explored for non-volatile storage applications. However, these materials still exhibit certain limitations when applied to high-speed and highly durable volatile cache storage [15-17].

Vanadium dioxide (VO_2) is a promising phase-change material, capable of reversibly transitioning from a low-temperature monoclinic phase to a high-temperature rutile phase at approximately 68°C [18, 19]. It exhibits exceptional endurance, maintaining stable performance over 10^7 switching cycles without degradation [20], making it highly attractive for short-term optical memory applications [21, 22]. Compared to other phase-change materials, the relatively low phase transition temperature of VO_2 means lower energy requirements for triggering transitions, potentially leading to significantly reduced overall device power consumption, which is particularly beneficial for computational applications. For example, recent work demonstrates that state-of-the-art computing architecture is based on coupled VO_2 oscillators that can effectively solve complex optimisation problems [23]. Recent work also demonstrates the potential of using Atomic layer deposition (ALD) to fabricate VO_2 -based memristors, which is important for developing high-density, energy-efficient neuromorphic computing hardware [24].

Current VO_2 thin-film fabrication methods often require either high-temperature direct deposition or high-temperature post-annealing of amorphous VO_2 to achieve high-quality crystalline phases [25, 26]. However, these high-temperature processes limit the compatibility of VO_2 with CMOS fabrication, particularly in post-metallisation steps [27]. Although some studies have successfully achieved annealing temperatures around 400°C for ultra-thin (~ 10 nm) VO_2 films, this approach is not applicable to thicker VO_2 structures and fails to meet the requirements for large-scale production [28]. Therefore, realising VO_2 -based optical memory devices still presents several key challenges. Current research on VO_2 primarily focuses on material-specific applications, with less emphasis on its compatibility with existing CMOS technology. In these studies, the reported VO_2 growth temperature typically falls within the range of 400 to 700°C , which exceeds the thermal budget of CMOS circuits and poses a significant challenge for direct integration [29, 30]. Moreover, most research works only demonstrated functional VO_2 with phase change, but VO_2 process conditions have not been investigated to achieve desirable VO_2 in terms of high optical contrasts, desirable refractive index and tuneable phase transition temperatures. On the other hand, as research progresses, further pushing down the VO_2 formation temperature

to levels compatible with flexible substrates has a significant academic impact. Compared to conventional silicon or glass substrates, flexible substrates (e.g., polyimide) offer advantages such as lightweight, flexible, and impact resistant, making them highly attractive for applications in healthcare [31], wearable electronic textiles [32] and radiative cooling applications [33].

In terms of optical memory, previous work paid more attention to the electric drive device [34-37], with less focus on the optically driven devices [22, 38]. Besides, in the above-mentioned memory devices, VO_2 is traditionally utilised for its inherent bistability arising from the hysteresis in its phase transition during heating and cooling processes. Therefore, the phase-change VO_2 needs to be further investigated as devices to enable new functions and new capabilities.

In order to reduce the computation energy, which is an important consideration for device efficiency, doping VO_2 with tungsten/Molybdenum is a promising strategy to lower the phase transition temperature. However, this advantage comes at the cost of narrowing the hysteresis width, which is crucial for devices that depend on material hysteresis-based bistability [39, 40]. Additionally, achieving precise control over the hysteresis loop is technically demanding, potentially hindering design optimisation and large-scale production.

Therefore, the primary goal of this thesis focuses on tackling these challenges including low-temperature synthesis of high-quality VO_2 and exploring VO_2 -based photonic memories, paving the way for its integration into optical memory.

1.2 Introduction to VO_2

Vanadium oxides exhibit various crystal structures and oxidation states, with different vanadium oxides undergoing insulator-to-metal transitions (IMT) at specific temperatures. As a result, precise experimental conditions are required to synthesise the desired oxide. The most commonly synthesised vanadium oxides include V_2O_3 , VO_2 , and V_2O_5 . V_2O_3 has attracted attention due to its well-defined Mott transition properties, while V_2O_5 is the most stable compound, representing the highest oxidation state of vanadium oxides.

Apart from VO_2 , most vanadium oxides (VO_x) can be categorised into two types: Wadsley-type ($\text{V}_n\text{O}_{2n+1}$) and Magnéli-type ($\text{V}_n\text{O}_{2n-1}$). Most Magnéli-type vanadium oxides exhibit IMT, whereas only a few Wadsley-type vanadium oxides have a distinct IMT temperature (e.g., V_2O_5 , V_6O_{13}) [41]. Figure 1.1 illustrates the phase transition temperatures of most known vanadium oxides, showing that among them, only VO_2 has a transition temperature near room temperature (68°C), accompanied by significant changes in its electronic and optical properties. This unusual feature makes VO_2 highly promising for practical applications such as optical switches [42], space technology [43] and smart window coatings [44].

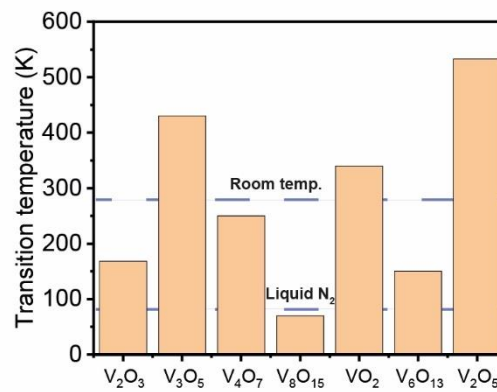


Figure 1.1 Vanadium oxides and their transition temperatures. The blue dashed lines are the room and liquid nitrogen temperature, respectively.

1.2.1 VO_2 phase change kinetics

The phase transition of VO_2 is a complex process involving both thermodynamic and kinetic factors. The stability of the system and the direction of the phase transition are governed by changes in Gibbs free energy, while the transition rate is controlled by the activation energy barrier.

According to the definition of Gibbs free energy, the free energy of VO_2 can be expressed as:

$$G = H - TS \quad (1.1)$$

where H represents the enthalpy of the system, T is the temperature, and S is the entropy, which reflects the degree of disorder of the molecules or atoms. The enthalpy (H) is the total energy of the system, determined by the internal energy (E) and the work done due to compression ($P \cdot V$), as described by:

$$H = E + PV \quad (1.2)$$

where, E includes the total bonding energy (encompassing chemical bonds and lattice energy), P is the pressure, and V is the volume.

At a given temperature and pressure, a phase can be defined as being in a stable equilibrium when the Gibbs free energy reaches its minimum value, and no external energy is added to induce a state change. This condition can be mathematically expressed as:

$$dG = 0 \quad (1.3)$$

However, satisfying this condition does not necessarily mean that the Gibbs free energy is minimised globally, as the system may be in a metastable state.

The phase transition of VO_2 can be explained through Fig. 1.2 When the change in Gibbs free energy is negative ($\Delta G < 0$), as given by Equation 1.4, the transition from state B to state A is a spontaneous process, even though the activation energy barrier must still be overcome. This indicates that the system's free energy decreases continuously during the transition from the high-temperature phase (Fig. 1.2 (b)) to the low-temperature phase (Fig. 1.2 (a)), driving the system toward a more stable state:

$$\Delta G = G_{\text{final}} - G_{\text{initial}} < 0 \quad (1.4)$$

Conversely, during heating, the Gibbs free energy of the R phase is higher than that of the M1 phase, requiring external energy input to overcome the energy barrier from M1 to R. This difference manifests as a thermal hysteresis in the phase transition of VO_2 , where the width of the hysteresis is determined by the magnitude of the activation energy.

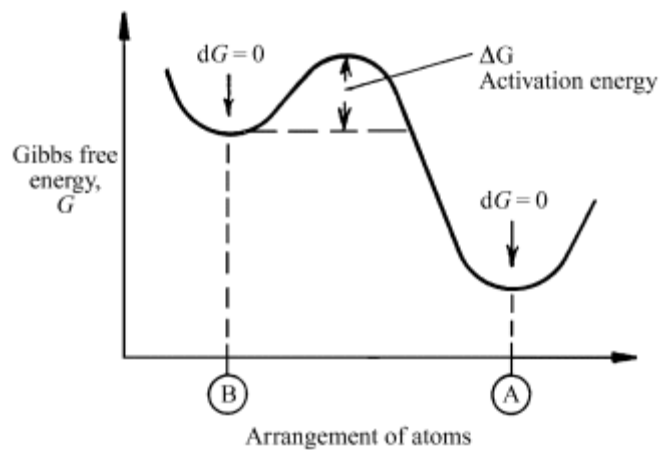


Figure 1.2. Phase Transition energy schematic. The activation energy required to overcome the metastable state potential barrier is defined as ΔG [45]. Copyright of ScienceDirect.

1.2.2 VO₂ crystal structure

VO₂ exhibits multiple crystal structures, whose formation strongly depends on the preparation method. These crystal structures include VO₂(M1), VO₂(R), and a few intermediate and metastable phases, such as VO₂(M2), VO₂(A), and VO₂(B). These distinct crystal structures differ significantly in their physical properties, including crystal structure, phase transition temperature, and density [46].

VO₂ exhibits a reversible metal-insulator transition (MIT) at its critical temperature, transitioning from a low-temperature monoclinic phase (M1) to a high-temperature rutile phase (R). Figure 1.3 illustrates schematic representations of the VO₂ crystal structure below and above the transition temperature T_c . When the temperature exceeds 68°C, VO₂ exists in the metallic rutile phase, characterised by lattice parameters $a = b = 0.455$ nm, $c = 0.288$ nm and $\beta = 180^\circ$ within the space group $P4_2/mnm$ (No. 136). The V atoms are aligned parallel to the C_r -axis, occupying the eight vertices and the centre of the unit cell. Each V atom is surrounded by an edge-sharing octahedron of oxygen atoms (VO₆).

Below the transition temperature, the structure becomes distorted, and the V-V bonds at the outermost layer tilt into a zigzag pattern. The highly symmetric tetragonal structure transitions to a low-symmetry monoclinic structure, corresponding to the insulating M1 phase within the space group $P2_1/c$ (No. 14). The lattice parameters in this phase are $a=0.575$ nm, $b=0.542$ nm, $c=0.577$ nm, and $\beta=122.6^\circ$. The dimerisation in the M1 phase results in two distinct V-V bond lengths: a shorter intradimer length of 2.65 Å and a longer interdimer length of 3.12 Å, different from the equidistant V-V bonds in the rutile phase [18, 47].

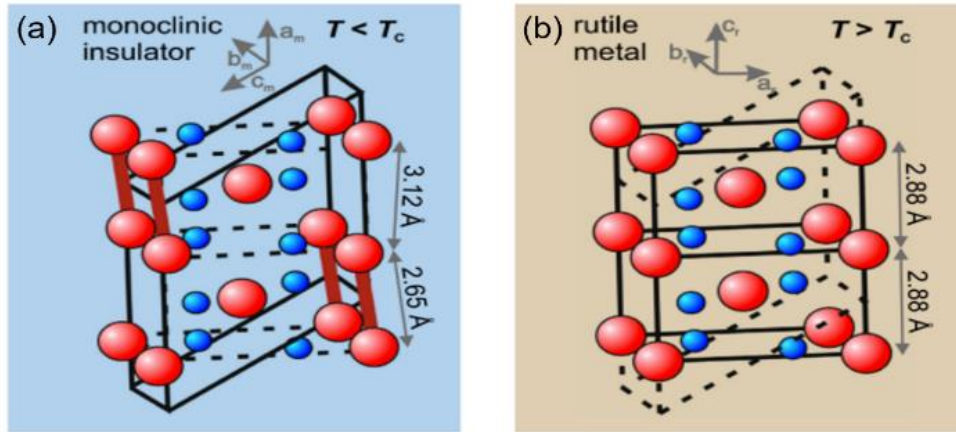


Figure 1.3. Crystal structure change of VO_2 between (a) the monoclinic insulating phase, M1 and (b) the tetragonal rutile metallic phase, R, during IMT in a three-dimensional view. The red dots are vanadium atoms, and the blue dots are the oxygen atoms [47]. Copyright of American Physical Society.

1.2.3 VO_2 band structure

During the phase transition, in addition to changes in the crystal structure, the band structure of VO_2 also undergoes significant transformations. Decades ago, Goodenough proposed a band structure model to explain the conductive properties of the rutile phase and the insulating properties of the monoclinic phase [48]. When VO_2 is in the high-temperature phase ($T > T_{\text{IMT}}$), the $d_{||}$ orbitals overlap with the π^* orbitals, and the π^* orbitals are partially filled with electrons. The Fermi level lies at the overlap of the π and $d_{||}$ bands, giving VO_2 its metallic characteristics (Fig. 1.4 (a)). In the low-temperature phase ($T < T_{\text{IMT}}$), the V atoms shift along the c-axis, which raises the antibonding π^* energy levels. Simultaneously, the strong interactions within the $d_{||}$ orbitals of the V-V pairs cause the $d_{||}$ band to split into bonding $d_{||}$ states and antibonding states. This splitting creates a bandgap of approximately 0.7 eV between the π^* and $d_{||}$ bands, resulting in the insulating phase (Fig. 1.4 (b)).

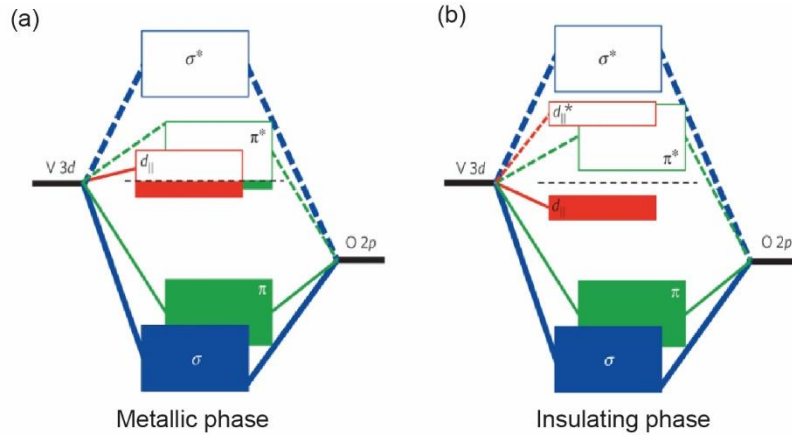


Figure 1.4. The energy-band diagram of the VO_2 between the (a) Metallic phase and (b) Insulating phase. The black dashed line in the middle represents the Fermi level [49]. Copyright of Nature Portfolio.

1.2.4 Discussion of VO_2 phase change mechanism

The mechanism of the phase transition in VO_2 has three main interpretations: 1. Peierls transition driven purely by structural changes (Purely structural). 2. Mott-Hubbard transition driven purely by strong electronic correlations (Purely electrical). And 3. A synergistic coupling of Mott-Peierls transition mechanisms.

It is widely believed that the appearance of a bandgap in the insulating state of VO_2 results from lattice distortions in the monoclinic phase, suggesting that structural changes drive the Peierls transition mechanism. This perspective has been supported by theoretical [50] and experimental studies [51]. Evidence supporting the Peierls transition includes the observation of V-V bond dimerisation in the monoclinic phase, which doubles the lattice constant along the c-axis compared to the rutile phase, thus providing a plausible explanation for the bandgap formation. Furthermore, the phase transition in VO_2 is accompanied by significant lattice transformation and latent heat, consistent with the lattice reconstruction described in Peierls transition theory [10, 11].

In contrast, the Mott transition involves the transition and rearrangement of electrons without lattice reconstruction [52]. These changes in electronic states can occur on ultrafast timescales. A direct piece of evidence supporting the Mott transition in VO_2 is the observed M2 phase, which

contains two distinct types of V-V atomic chains: one is a straight chain composed of dimerised V-V bonds, while the other is a zigzag chain with equidistant V-V bonds. In comparison, the M1 phase only features one type of dimerised V-V bond chain. This structural difference indicates that the electronic correlation effects in the M2 phase are more pronounced, with electrons localised on individual V atoms, forming localised electronic states. This electron correlation effect is a key feature of Mott insulators [53, 54].

Another characteristic supporting the Mott transition in VO_2 is the narrowing of the $d_{||}$ orbital. In the metallic state, the π^* band effectively screens the correlation effects of $d_{||}$ electrons, resulting in a broader $d_{||}$ band. However, in the insulating state, the π^* band shifts to higher energy, weakening its overlap with the $d_{||}$ band, thereby reducing the screening effect and causing the $d_{||}$ band to narrow [55].

Table 1.1 summarises the characteristics of the Peierls transition theory and the Mott-Hubbard transition theory, highlighting the difficulty of using a single theory to explain all experimental phenomena. This has led to long-standing debates about the physical mechanisms underlying the phase transition in VO_2 . For example, in recent studies, researchers employed Fourier-transform holography (FTH) and coherent diffraction imaging (CDI) to observe ultrafast structural changes in VO_2 induced by laser pulses on the picosecond and femtosecond timescales [56]. Recent simulations have also demonstrated that the two-phase transition mechanisms decouple and interact on different timescales. Using density functional theory (DFT), researchers found that the insulator-to-metal transition (IMT) driven by electronic excitation occurs almost instantaneously (<10 fs), consistent with the characteristics of a Mott transition. In contrast, the structural phase transition (SPT) takes longer, as it is triggered by V-V bond expansion and increased twisting angles, which align with the characteristics of a Peierls transition [57]. Experimental studies using broadband time-resolved pump-probe ellipsometry with 35 fs laser pulses on 25 nm VO_2 thin films captured distinct optical property changes associated with the photo-induced IMT on the picosecond timescale, differing from thermally induced transitions. This work identified different thermal and non-thermal dynamics in photo-induced IMT, offering new insights into the ultrafast dynamics of VO_2 phase transitions [58]. With continued advancements in research, there is growing consensus that the phase transition in VO_2 results from the synergistic interplay of Peierls and Mott-Hubbard mechanisms [19, 59].

Table 1.1. Key features that support different VO₂ transition mechanisms.

VO ₂ Peierls transition features	VO ₂ Mott transition features
Doubling of unit cell [60, 61]	Existence of M2 phase [53, 54]
Pairing of vanadium atoms [62, 63]	Narrowing of d band [64, 65]
latent heat induced in transition [66, 67]	Ultrafast phase transition [57, 68]

1.3 VO₂ phase transition modulation

One of the main interests of VO₂ research is the regulation of phase transition characteristics, e.g., critical temperature (T_{IMT}). Methods for manipulating phase transitions include substrate selection, element doping, etc.

1.3.1 Doping

Doping is one of the most effective methods for regulating the phase transition temperature of VO₂. Table 1.2 summarises most of the dopants studied in the past and their effects on the phase transition temperature. Generally, the fundamental mechanism by which doping influences the phase transition temperature is through altering the phase transition energy barrier. The selection of dopants that reduce the phase transition temperature typically relies on two strategies: A) Increasing the carrier concentration to accelerate the electronic transition. B) Introducing distortions in the atomic structure to facilitate the structural phase transition.

Doping elements increase the carrier concentration in VO₂. When dopants act as donors or acceptors, they inject electrons or holes into the electronic structure of VO₂, thereby increasing the carrier concentration. This higher carrier concentration reduces the energy difference between the M1 and R phases, leading to a lower phase transition temperature. One approach to increasing carrier concentration is doping with small-sized elements such as H, Li, and B, which inject electrons into VO₂. Another approach is substituting V sites with high-valence elements such as W, Nb, and Mo. Among these, W has been experimentally demonstrated to be the most effective dopant for lowering the phase transition temperature, with a rate of approximately 20 °C/at.%. He *et al.* showed that increasing the W doping concentration reduces the optical band gap from 0.65 eV to 0.54 eV [69].

Doping can also introduce structural distortions in VO_2 . Certain dopants modify the equidistant V-V bonds in $\text{VO}_2(\text{R})$, creating a configuration similar to that in $\text{VO}_2(\text{M})$. For instance, Zhang *et al.* found that the V-V chains in B-doped VO_2 exhibit a zigzag pattern resembling the insulating phase. Their first-principles calculations predicted that B doping reduces the phase transition temperature by 83 °C/at.% [70].

In fact, these two mechanisms are inherently difficult to completely separate. For example, W doping not only increases the carrier concentration in VO_2 but also induces compressive strain, causing structural distortions that jointly lower the phase transition temperature.

Compared to the extensive studies on dopants that lower the phase transition temperature, research on increasing the transition temperature through doping is relatively limited. Existing studies suggest that dopants with valences lower than vanadium, such as Ga, tend to raise the MIT temperature. When the doping level of Ga exceeds 1 %, T_{MIT} can be increased by approximately 8 °C/at.% [19, 71]. However, some studies have reported inconsistent findings [72, 73].

Fundamentally, similar to the mechanism of lowering the phase transition temperature, raising the transition temperature through doping also involves modifying the electronic structure and lattice arrangement of VO_2 to increase the energy required for the phase transition. For instance, Victor *et al.* demonstrated that Fe doping significantly raises the phase transition temperature of VO_2 , reaching up to 134°C as the Fe^{3+} doping concentration increases. This is because the introduction of Fe^{3+} ions alters the electron density in the V-V chains of VO_2 , thereby increasing the energy barrier for the phase transition [74].

Table 1.2. Effects of most existing dopants on the VO₂ thin film transition temperature.

Dopant	Doping level (%)	dt _{I_{MT}} /dx (°C/at.%)	Reference
H ⁺	3	-38	[75] *
Li ⁺	3	-43	[76] *
Na ⁺	3	-49	[76] *
K ⁺	3	-94	[76] *
Be ²⁺	3	-58	[77] *
Mg ²⁺	5	-3	[78]
B ³⁺	N/A	-83	[70] *
Cr ³⁺	20	↑	[79]
Ti ⁴⁺	2	↑	[80]
Fe ³⁺	12.6	+5.2	[74]
Ga ³⁺	1.3	+8	[81]
Nb ⁵⁺	7	-2	[82]
W ⁶⁺	2	-20	[83]
Ce ³⁺	1	-4.5	[72]
Al ³⁺	10	-2.7	[73]
Mo ⁶⁺	2	-11	[71]

* In the table represent simulation work. ↑ in the table represents the positive dopant effect but no specific data was recorded.

1.3.2 Strain engineering

Research on the effect of stress on the phase transition temperature of VO₂ dates back to half a century ago. Ladd *et al.* observed that hydrostatic pressure had a slight effect on the phase transition temperature, with a rate of 0.6 K/GPa, whereas uniaxial stress applied along the c-axis exhibited a significant impact, with a rate of -12 K/GPa [84]. Subsequent studies confirmed that the phase transition temperature of VO₂ is closely related to the c-axis length (the distance between adjacent vanadium atoms). Stress along the c-axis intensifies the overlap of d-orbitals and increases the bandwidth of the d-band, making VO₂ more stable in the rutile phase and thus

lowering the phase transition temperature [85]. Similarly, Muraoka *et al.* found that VO₂ thin films grown on TiO₂ (110) substrates exhibited an extended c-axis and an increased T_{IMT} of 369 K [86]. The phase transition temperature T_{IMT} can be tuned through uniaxial stress σ , as described by the Clausius-Clapeyron equation [78]:

$$\frac{dT_{IMT}}{d\sigma} = \frac{\epsilon_0 T_{IMT}^0}{\Delta H} \quad (2.5)$$

where T_{IMT} is the phase transition temperature, σ is the externally applied stress, ϵ_0 is the initial strain of the material, reflecting how the internal structure responds to external stress. T_{IMT}^0 the initial phase transition temperature under zero stress. ΔH is the latent heat of the phase transition, representing the heat absorbed or released during the transition.

The most direct way to apply strain to VO₂ is by depositing VO₂ thin films onto specific substrates, introducing interactions between the film and the substrate. Various substrate materials have been explored to deposit VO₂, such as silicon (Si), quartz (SiO₂), sapphire (Al₂O₃), titanium dioxide (TiO₂), and magnesium fluoride (MgF₂), to control interfacial strain and phase transition temperature [87-91].

Zhang *et al.* found that VO₂ films deposited on sapphire substrates exhibited near-single-crystal characteristics, with phase transition temperatures (T_{IMT}) close to the intrinsic phase transition temperature of VO₂ (340 K). In contrast, VO₂ films deposited on silicon (Si) and quartz substrates showed slightly reduced phase transition temperatures. They attributed this difference to the varying effects of substrate materials on the crystal structure and interfacial stress/characteristics of VO₂, which in turn influenced the phase transition temperature [92]. This perspective was supported by Choi *et al.*, who observed a 10 K variation in the phase transition temperatures of VO₂ films deposited on different alumina substrates. They concluded that the variations were due to differences in the VO₆ octahedral symmetry induced by the substrate. The more symmetric the VO₆ octahedral structure, the lower the energy barrier required for the phase transition, resulting in a lower IMT temperature [93].

1.3.3 Others

The properties of VO₂ are highly sensitive to oxygen participation, as oxygen vacancies typically act as electron donors. Consequently, the insulating phase of VO₂ becomes more conductive under oxygen-deficient conditions. The IMT temperature of VO₂ is also affected by oxygen levels. Studies have shown that the T_{IMT} decreases under oxygen-deficient conditions [94] and slightly increases under oxygen rich conditions [95].

In addition, the thickness of VO₂ thin films has been found to influence their phase transition, likely due to changes in crystal structure, surface morphology, and the stress between the film and substrate. Yang *et al.* observed that during the heating process, the phase transition speed of VO₂ decreases with decreasing thickness, which they attributed to stress between the thin film and substrate. Conversely, during cooling, the phase transition speed was found to be inversely proportional to film thickness, possibly due to poorer heat dissipation in thicker films [96]. Table 1.3 lists the findings of various studies on the relationship between VO₂ film thickness and IMT. Most studies indicate a positive correlation between the phase transition temperature and film thickness, where increasing film thickness leads to a higher phase transition temperature. This is because thinner films have stronger interfacial interactions with the substrate, resulting in greater interfacial stress. As the film thickens, the surface gradually relaxes, reducing the influence of interfacial stress and leading to an increase in the phase transition temperature. The only exception is the recent work by Geng *et al.*, who reported a negative correlation between phase transition temperature and thickness for VO₂ films grown on quartz substrates. They observed that as the film thickness increased from 10 nm to 160 nm, the phase transition temperature decreased from 76°C to 68°C.

Table 1.3. Summary of the study on the correlation between VO₂ thin film thickness and IMT temperature.

Author	Positive correlation	Negative correlation	Substrate	Deposition method	Date	Reference
Geng <i>et al.</i>		√	Quartz	Sputtering	2024	[97]
Driouach <i>et al.</i>	√		Sapphire	Sputtering	2023	[98]
Han <i>et al.</i>	√		Sapphire	PLD	2021	[99]
Shao <i>et al.</i>	√		MgF ₂	Sputtering	2020	[100]

Jian <i>et al.</i>	√	Sapphire	PLD	2017	[101]
Zhi <i>et al.</i>	√	TiO ₂	PLD	2014	[102]
Xu <i>et al.</i>	√	Sapphire	Sputtering	2005	[103]

1.4 Applications of VO₂ thin film on silicon photonics

1.4.1 Optical driven VO₂ for optical switch

Optical switches play a crucial role in photonic integrated circuits (PICs) and are typically implemented in the form of optical waveguides or microring resonators. The three main criteria for evaluating the performance of optical switches are energy consumption, optical contrast, and switching speed. The use of laser-induced phase transition in VO₂ has been extensively studied, with early experiments focusing on continuous wave (CW) and nanosecond lasers. In 1991, Egorov *et al.* were the first to demonstrate a photo-induced phase transition in VO₂ using CW light (632 nm, 2 mW or 1 mJ/cm²). Later, Chudnovskii *et al.* triggered the VO₂ phase transition using a Nd:YAG laser (neodymium-doped yttrium aluminum garnet, 1064 nm) [104, 105]. In these early works, the phase transition time for VO₂ ranged from milliseconds to microseconds.

As research progressed, scientists discovered that femtosecond lasers could significantly enhance the speed of VO₂ phase transitions. This is because, under femtosecond pulse excitation, the phase transition in VO₂ is primarily driven by the photo-excited carrier transition. The ultrafast excitation of electrons from the valence band to the conduction band occurs on the femtosecond timescale, while the contribution of the photothermal effect to the phase transition is minimal [106]. In a landmark study, Cavalleri *et al.* demonstrated a VO₂ phase transition time of less than 100 fs using high-power femtosecond laser pulses. They concluded that the phase transition was driven by the direct excitation of electronic states by photons, rather than by thermally induced lattice rearrangement [68]. This finding suggests that, under certain conditions, the ultrafast phase transition of VO₂ can be achieved via a Mott transition (primarily driven by electronic transitions), without the need for the slower Peierls transition (which requires lattice rearrangement).

The phase transition speed of VO₂ is limited by several factors, most notably the thermal effect (as seen in CW-induced transitions) and lattice rearrangement. Since the propagation of lattice

vibrations is constrained by the speed of sound in the material, thermally driven phase transitions that rely on lattice rearrangement are inherently slower, typically limited to the picosecond timescale [107]. This constraint underscores the inherent speed limitations of thermal and lattice-driven transitions in VO₂.

In practical applications, optically driven thermal effects remain the dominant mechanism for VO₂-based optical switches. In 2012, Ryckman *et al.* demonstrated the photo-thermal induced phase transition of VO₂ using a 532 nm pump laser. The optical heating induced by the laser triggered the phase transition in VO₂, and the transition from the insulating to metallic state caused a significant reduction in the refractive index of the VO₂ layer. This, in turn, resulted in a blue shift of the resonance frequency in microring resonators (Fig. 1.5). Furthermore, as the radius of the ring increased, the magnitude of the wavelength shift decreased. This effect was attributed to the reduced coverage ratio of VO₂ on the resonator. While the response time in this study was relatively slow (on the order of seconds), it was found that increasing the pump power could reduce the response time to the millisecond range or even faster. This demonstrated that pump power intensity is a critical factor in controlling the response time of thermal-driven optical switches [108].

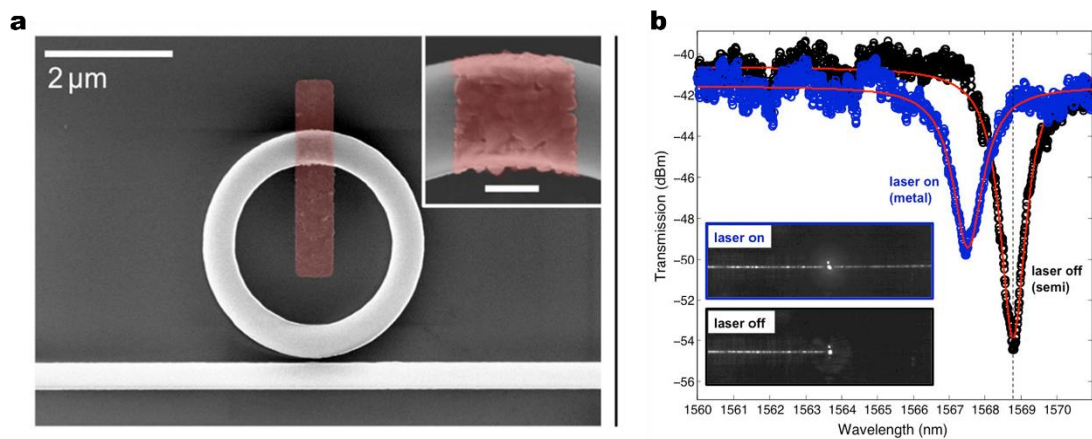


Figure 1.5. All optical hybrid VO₂/Si device [108]. (a) SEM image of a Si-VO₂ micro-ring resonator with 1.5 μm radius. (b) Optical transmission before and after VO₂ phase transition. Inset: IR camera images at a fixed probe wavelength, $\lambda = 1568.78$ nm (dashed line). Copyright of Optica Publishing Group.

In 2013, Ryckman *et al.* further investigated the timescales of such devices by exciting the insulator-metal transition (IMT) of VO₂ using nanosecond pulsed lasers. They found that by

increasing the pump flux by an order of magnitude and extending the length of the VO₂ patch from 500 nm to 1 μm, the relaxation time increased from approximately 30 ns to 3 μs. This observation suggests that the relaxation dynamics are governed by the thermal diffusion of the monoclinic phase [109].

Parra *et al.* further explored VO₂/Si hybrid photonic switches based on silicon straight waveguides. In their design, the phase transition was primarily driven by the thermal effect induced by optical absorption in the VO₂ layer. They achieved a switching speed as low as 318 ns with a single-shot switching energy of 15.8 nJ [110]. To further improve the switching speed, they proposed reducing the size of the VO₂ patch or incorporating heat-dissipation materials to accelerate cooling. Building on these concepts, Wang *et al.* investigated the cumulative thermal effects of VO₂ using a high-repetition-rate femtosecond laser. Their findings revealed that the switching speed of thermally driven mechanisms is fundamentally limited by thermal diffusion and the lattice response time [111]. This limitation highlights the challenge of achieving sub-nanosecond switching speeds using a thermally driven mechanism.

An alternative research direction focuses on Mott transition-driven ultrafast switching. In 2021, a hybrid VO₂-Si integrated device demonstrated sub-picosecond all-optical switching for the first time (Fig. 1.6). By directly exciting electron state transitions and bypassing the constraint of lattice rearrangement, they achieved an ultrafast switching speed of 0.55 ps. Moreover, they reported a maximum optical transmission contrast of 22 % at telecommunications wavelengths. These results underscore the fact that, on ultrafast timescales, the phase transition of VO₂ is primarily governed by the Mott transition rather than the Peierls transition [112].

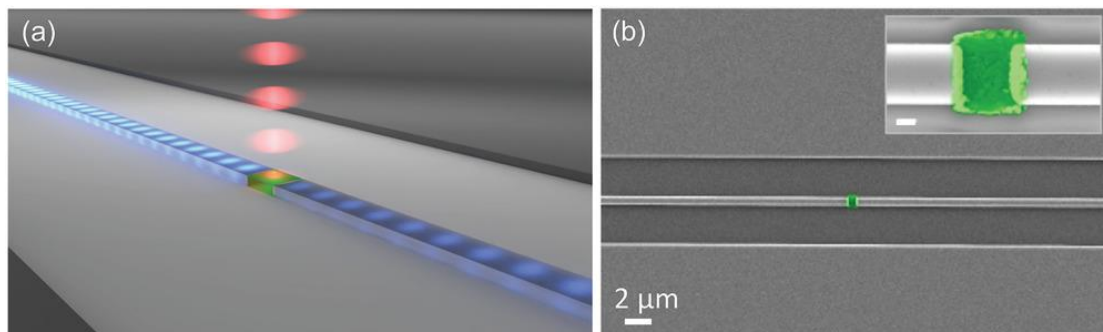


Figure 1.6. (a) Schematic of the sub-picosecond response VO₂-Si hybrid device, where an optical pulse (light blue) propagates from the left to the right (dark blue). The VO₂ patch (green section) is positioned in the center and is illuminated by a 1670

nm optical pulse (red). (b) False-color scanning electron microscope (SEM) image of the embedded VO₂-Si waveguide [112]. Copyright of Wiley.

Although some recent studies, such as those by Chen *et al.*, have revealed the presence of significant photostriction during photo-induced phase transitions in VO₂ ceramics using a 655 nm laser [85]. This phenomenon suggests that photon excitation not only induces changes in electronic states but also generates mechanical strain through strong photon-lattice coupling (Fig 1.7 (a)). By employing first-principles ab initio molecular dynamics (AIMD) simulations, they confirmed the role of photostriction in the IMT process. This indicates that, under certain conditions, non-thermal mechanisms induced by photon excitation may play a more critical role than conventional thermal effects.

Additionally, Yael *et al.*, conducted an in-depth study of the thermal and non-thermal dynamics during the VO₂ phase transition using femtosecond laser pulses. By using ellipsometry to track the time-resolved changes in the electronic states and lattice response during the IMT, they found that the photo-induced phase transition characteristics are highly dependent on the pump wavelength and laser fluence (Fig. 1.7 (b)) [86]. The experimental results showed that short-wavelength, high-power laser pulses are more effective in directly exciting electronic transitions, thereby triggering a Mott transition. In contrast, low-power or long-wavelength laser pulses primarily induce a thermally driven Peierls transition. This observation further supports the idea that the IMT in VO₂ may involve a complex coupling between the Mott and Peierls mechanisms.

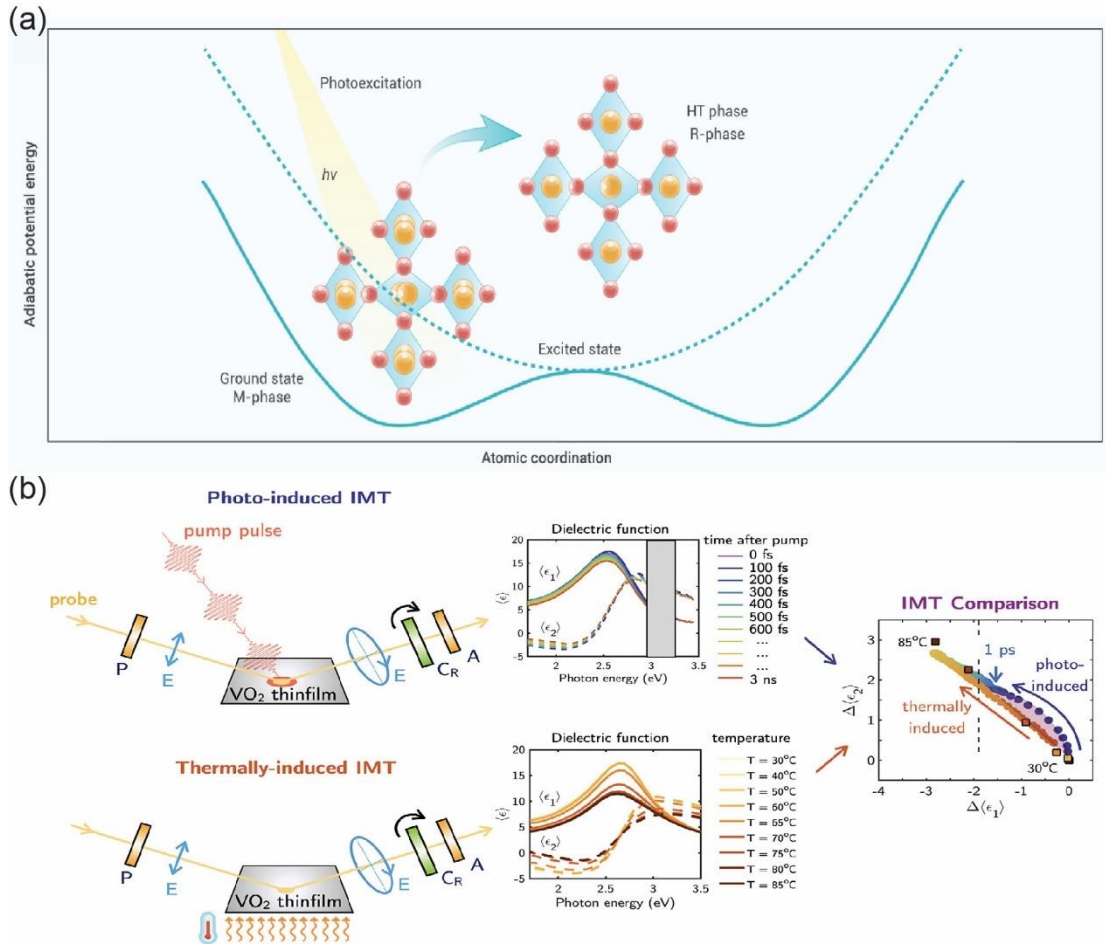


Figure 1.7. (a) Potential energy surfaces of VO₂ in the ground state (M-phase) and the excited state (R-phase) under photoexcitation. (b) Schematic illustration of ellipsometric measurements capturing the pseudo-dielectric function of VO₂ thin films during photo-induced and thermally-induced insulator-to-metal transitions (IMT) [86]. Copyright of Nature Portfolio.

Against this background, the mechanism of light-driven VO₂ optical switch devices are as complex as the phase transition mechanism of VO₂ itself. The Mott transition involves rapid transitions in electronic states, with timescales ranging from femtoseconds to picoseconds, making it suitable for explaining the ultrafast response of purely optically driven mechanisms. In contrast, the Peierls transition involves lattice rearrangement, which is constrained by thermal diffusion and the propagation speed of sound, resulting in a much slower timescale—typically on the order of nanoseconds or longer.

However, it is experimentally challenging to eliminate the thermal effect. In practical VO₂-based optical switches, the thermal effect is inherently coupled with the optical effect. This coupling

significantly influences not only the IMT but also prolongs the metal-to-insulator transition (MIT) during the relaxation process. This explains why, in most reported opto-thermal driven switch devices, the fastest switching speeds achieved are only in the range of hundreds of nanoseconds, whereas purely optically driven mechanisms have demonstrated picosecond-level ultrafast switching.

Therefore, one promising strategy for the future design of ultrafast, VO₂-based, integrated photonic switches is to precisely tune the excitation source to trigger only the electronic IMT of VO₂ while avoiding parasitic thermal effects. Additionally, optimal thermal management design to facilitate effective heat dissipation can further reduce the IMT relaxation time, minimising delays caused by the slower Peierls transition.

1.4.2 VO₂ integrated photonic volatile memory

Current optical memory devices can be classified into bit-level and packet-level configurations based on the amount of stored information (see Fig. 1.8). Bit-level optical memory can be further divided into volatile and non-volatile memory. Compared to non-volatile optical memory, volatile memory typically offers faster access speeds and higher operating speeds, making it well-suited for applications that require rapid switching.

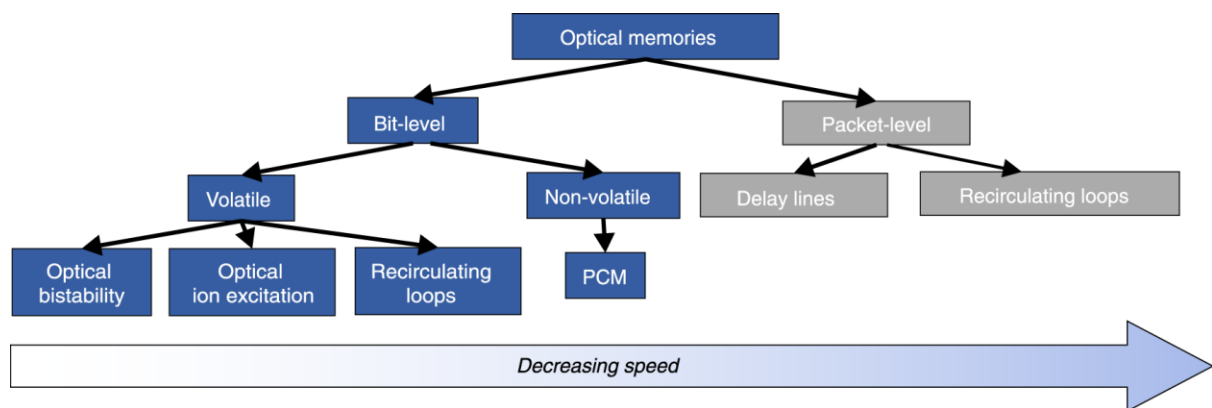


Figure 1.8. Classification of optical memory technologies [113]. Copyright of Nature Portfolio.

A key limitation of common chalcogenide-based optical memories is their relatively poor durability, with lifetimes typically ranging from 10^3 to 2×10^4 cycles [114, 115]. This makes VO₂ a promising candidate for applications that require frequent switching. Moreover, the hysteresis

response of VO_2 enables bistability, which supports the design of ultra-compact photonic memory devices, offering the potential for fast, low-power optical storage systems.

In 2022, Jung *et al.* experimentally demonstrated a hybrid optical memory device based on VO_2 (Fig. 1.9). The device operates under the combined action of a $1.5\ \mu\text{m}$ optical pulse and a bias voltage, achieving a write speed of 100 ns with an energy consumption of only 23.5 pJ. It provides an optical contrast of approximately 23%, defined as the difference in transmittance between the insulating and metallic states of VO_2 . Notably, the device can maintain its memory state for up to 200 hours under a constant bias voltage, showcasing the feasibility of using VO_2 for hybrid volatile memory applications [22].

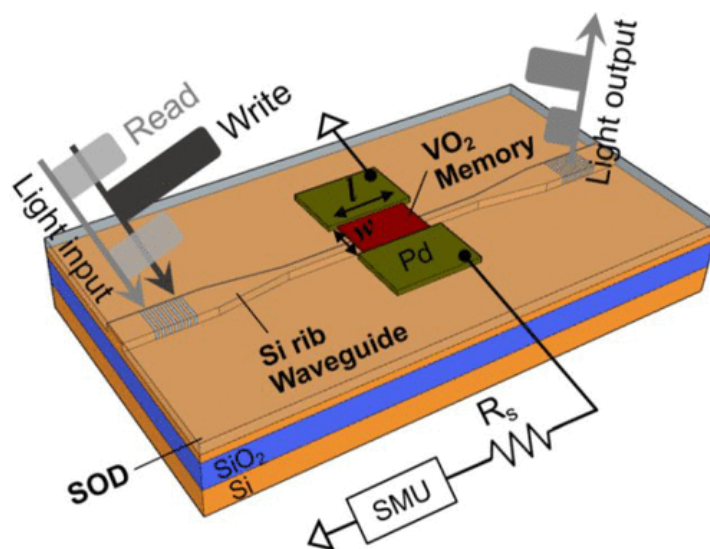


Figure 1.9. Schematic diagram of the waveguide-integrated VO_2 -Si optical memory [22].

Copyright of American Chemical Society.

Recent studies have demonstrated a high-durability, ultra-compact VO_2/Si photonic volatile memory capable of withstanding up to 10^7 write/erase cycles, with performance in terms of speed and energy consumption surpassing that of chalcogenide-based non-volatile memory. This feature makes VO_2 more suitable for short-term storage applications that require frequent read/write operations, rather than for long-term data storage [20].

When designing such memory devices, optical contrast and extinction ratio become critical parameters, as they directly determine the number of distinguishable optical states in the device.

High optical contrast and extinction ratio ensure stability and accuracy in multi-state storage. The potential for VO₂-based multi-state memory was first explored a decade ago, initially realised using VO₂/TiO₂ heterostructures [116]. More recently, a fully all-optical multi-state response was achieved on silicon waveguides for the first time (Fig. 1.10 (a)) [117]. In this hybrid VO₂/Si waveguide device, the insulator-metal transition (IMT) of VO₂ is controlled by thermal excitation, which can be achieved either by all-optical methods using optical pulses or by electrical heating, enabling multi-level memory responses (Fig. 1.10 (b)). This design allows a 2 µm VO₂/Si waveguide device to achieve up to 32 distinct storage states, with a maximum extinction ratio of 11.22 dB.

To further enhance the stability of the multi-level response, researchers have also integrated BaTiO₃ and Si₃N₄ into the platform, along with a highly efficient microheater based on indium tin oxide (ITO). This heater enables precise electrical heating to control the phase transition of VO₂, significantly improving the stability and accuracy of the multi-level memory response [118].

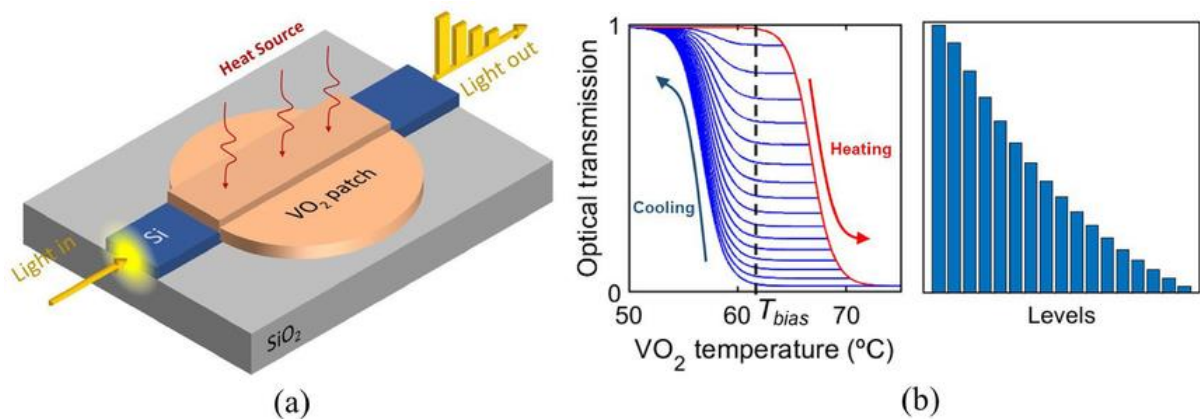


Figure 1.10. Hybrid VO₂/Si waveguide device based on a VO₂ patch deposited on top of a silicon waveguide [117]. (b) Multilevel memory response achieved by exploiting the hysteretic response of the VO₂ with temperature [117]. Copyright of Optica Publishing Group.

In previous studies, bistable responses in VO₂-based photonic devices were typically achieved by exploiting the material's intrinsic hysteresis, which was triggered through electrical or thermal control of the entire device. Such approaches generally rely on heating or cooling the VO₂ globally, or on varying the ambient temperature to traverse the hysteresis loop. In contrast, although the overall structure of the VO₂-based photonic memory device proposed in Chapter 4 is structurally similar to designs reported in earlier literature, this

work focuses on locally tuning the temperature of VO₂ through photothermal effects induced by varying the optical input power. While the same thermally driven phase transition occurs, the optical response of the device in Chapter 4 arises from the distinct absorption characteristics of VO₂ in its insulating and metallic states, which are harnessed through structural design within local regions of the waveguide or microring resonator.

1.4.3 VO₂ application based on non-volatile characteristic

In addition to its inherent volatile behaviour, VO₂ can also exhibit non-volatile behaviour under certain specific conditions (albeit less commonly). This unusual feature allows VO₂ to retain its ON/OFF states without external stimuli, offering significant potential for applications in non-volatile devices. In 2021, Jung *et al.* reported the first VO₂-based light-addressable non-volatile memory that operates at room temperature [38]. The device uses a low-power laser pulse for writing, while the insulating and metallic states are read by monitoring voltage oscillations under an applied bias current. The reset operation can be achieved by applying a small bias current. This groundbreaking work challenged the traditional notion that VO₂ only exhibits volatile properties, providing valuable insights for the future development of VO₂-based non-volatile devices.

Table 1.4 summarises most of the research on VO₂-based non-volatile devices over the past four years. These works generally achieve non-volatile behaviour by either modifying the electronic structure of VO₂ or controlling oxygen vacancies under external conditions. Despite the diversity of approaches, including heterojunction structures, multi-field co-excitation, and oxygen vacancy control, these methods still face significant limitations and challenges.

For instance, methods relying on complex fabrication processes (such as VO₂/graphene heterostructures and VO₂/BiFeO₃ heterostructures) increase the production cost and complexity; Approaches requiring high-energy external stimuli (like multi-field co-excitation and UV light irradiation) suffer from high power consumption, limiting their practicality in low-power devices; The oxygen vacancy control mechanism shows potential for achieving non-volatile phase transitions, but the non-uniform distribution of defects can lead to device performance instability, especially over long-term operation.

Given these challenges, future research on VO₂-based non-volatile devices should prioritise efforts to achieve: (a) Process simplification: Develop simple, scalable, and CMOS-compatible fabrication methods. (b) Low-power operation: Minimise the energy required for phase transitions and device switching. (c) Material stability and reproducibility: Enhance the control of oxygen vacancy distribution and develop robust, repeatable device performance. These directions will be critical for the successful development of practical VO₂-based non-volatile devices for next-generation memory and photonic applications.

Table 1.4. Summary of recent studies on VO₂ non-volatility.

Author	Method	Limitation	Mechanism of VO ₂ non-volatility	Date	Ref
Yu <i>et al.</i>	VO ₂ /graphene heterostructure	Complex manufacturing process	The electron exchange between VO ₂ and graphene stabilises the phase transition of VO ₂	2024	[119]
Xu <i>et al.</i>	Multi-external stimuli work synergistically	Large power consumption and complex thermal management	Photogenerated carriers suppress the accumulation of oxygen vacancies	2024	[120]
Basak <i>et al.</i>	Multiple ramp reversal protocol sequence	The distribution of defects could be uneven, resulting in unstable device performance	The lattice structure and electron distribution change during the IMT, accompanied by the diffusion of point defects	2023	[121]
Li <i>et al.</i>	UV light irradiation	UV-light dependence and complex oxygen vacancy control	Oxygen vacancies in VO ₂ change the electronic structure by adding electrons to the V-3d orbitals	2022	[122]

Lee et al.	VO ₂ /BiFeO ₃ heterostructure	Complex manufacturing process	The polarisation of the ferroelectric material BFO affects the electronic structure of VO ₂	2022 [123]
Jung et al.	Combining light-induced phase change and current bias control	Large power consumption; Slow VO ₂ response speed	N/A	2021 [38]

1.4.4 Implementation of VO₂ on neuromorphic computing

Neuromorphic computing is inspired by the human brain, mimicking the ultrafast and energy-efficient information processing of neural synaptic systems. It is characterised by features such as high energy efficiency, parallel processing, and dynamic adaptability. Existing neuromorphic computing architectures are still primarily realised using CMOS-based silicon circuits, which require a large number of transistors to emulate the integration, biasing, and dynamic weight modulation of neurons and synapses. Although significant progress has been made at the algorithmic level, issues related to high energy consumption and low efficiency at the hardware level remain key bottlenecks, limiting further development of this field. As a result, the search for efficient materials and architectures to replace conventional silicon circuits has become a major focus of research.

One prominent advantage of all-optical neurons is their inherent speed, which is significantly faster than optoelectronic methods. This is because the latter relies on carrier drift (the movement of electrons or holes under an electric field), which is much slower than purely photonic processes. In neuromorphic computing, neurons and synapses serve as key components, responsible for nonlinear information processing and dynamic storage, respectively. Table 1.5 summarises the core components of all-optical neural networks, highlighting the roles and functionalities of different optical elements in neuromorphic systems.

Table 1.5. Key components in photonic neural networks [124].

Components	Functions	Photonic devices
------------	-----------	------------------

Neuron	Summation and thresholding (nonlinear node)	Optical amplifier, optical bistable device, Photodetectors
Synapse	Weighting and memory (coding scheme)	MZI, Ring resonators, PCMs
Axon and dendrite	Interconnection (network)	Waveguides

Chalcogenides are currently the mainstream phase change materials used in neuromorphic computing. While the non-volatile nature of these materials offers significant advantages for long-term data storage, they exhibit certain limitations in high-frequency switching scenarios. For example, in spiking neural networks (SNNs), GST requires an external RESET signal to switch the material from a high-conductivity state (SET) back to a low-conductivity state (RESET). This additional reset process not only increases the operational complexity but also negatively impacts the energy efficiency of the device [125, 126]. Moreover, because of the need for reset pulses, these materials lack the self-regulating dynamic behaviour seen in biological neurons.

In biological neurons, after a spike event, the membrane potential naturally dissipates back to the resting state without any additional energy input. In stark contrast, GST-based devices require an extra energy driven reset operation. This difference highlights a key challenge for GST materials in applications requiring high-frequency spiking and dynamic adjustments, such as real-time computation and neural network training. The inability of GST to autonomously recover after a spike limits its energy efficiency and speed, making it less suitable for tasks that demand rapid, frequent spiking and self-regulated dynamic behaviour [127].

In contrast, VO_2 , as a volatile phase change material, naturally returns to its initial insulating state after the input signal is removed, due to thermal dissipation. This behaviour mimics the natural reset process of biological neurons, where membrane potentials passively return to a resting state without the need for external intervention. For example, Gao *et al.* utilised sub-hysteresis loops in a VO_2 memristor to achieve multi-level storage and spike-timing dynamic modulation. This approach enabled continuous operation without the need for external reset pulses, offering a significant energy efficiency advantage for the hardware implementation of large-scale neural networks [128].

In artificial neural networks (ANNs), the nonlinear dynamic behaviour of VO_2 has been used to construct nonlinear activation functions, significantly enhancing the computational efficiency of the network [129]. In spiking neural networks (SNNs), the hysteresis window of VO_2 supports synaptic weight adjustment, allowing for more efficient spike-driven processing. For instance, in a recent study, Morcillo *et al.* proposed a silicon photonics-based electro-optical spiking device built on a VO_2/Si waveguide platform integrated with an ITO (indium tin oxide) microheater. This design achieved a leaky integrate-and-fire (LIF) response with inhibitory optical spikes at input power levels in the milliwatt range (Fig. 1.11) [130]. This approach demonstrates the potential of hybrid VO_2 -silicon platforms for photonic neuromorphic computing.

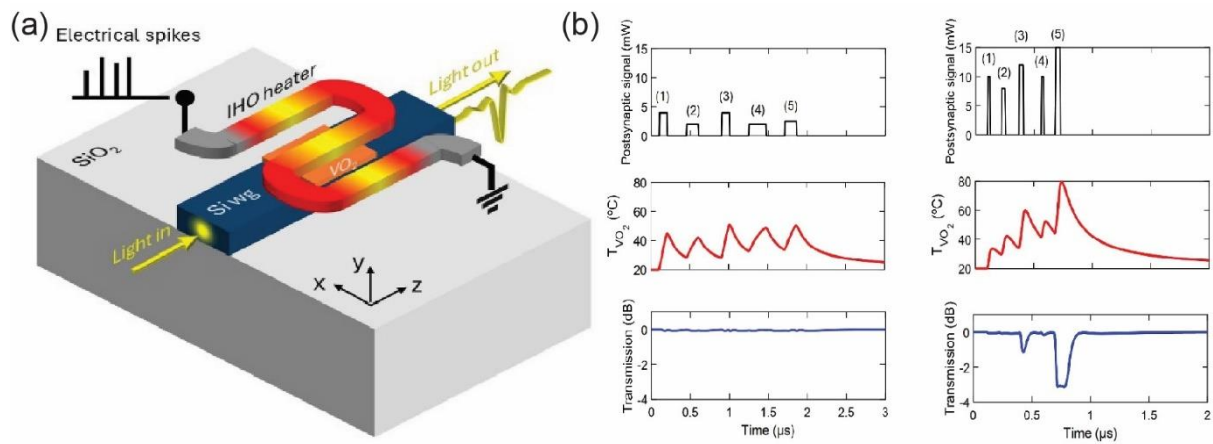


Figure 1.11. (a) Schematic diagram of the spiking device using Si waveguide with a small thin patch of VO_2 on top. (b) Comparison between a nonfiring and firing response under postsynaptic signals with different pulse amplitudes, pulse durations, and delays between consecutive pulses [130]. Copyright of Optica Publishing Group.

Similarly, Yi *et al.* utilised a VO_2 -based memristor to design a simple circuit that could successfully mimic a range of spiking behaviours observed in biological neurons. These included all-or-none responses, refractory periods, bistability, and 23 different types of spiking behaviours. Their design simplified the hardware architecture and significantly reduced energy consumption, paving the way for large-scale neuromorphic integration [131].

The inherent bistable nature of VO_2 is also being leveraged in the design of hardware synapses and neuronal elements. By controlling the hysteresis window width of VO_2 , a trade-off can be achieved between fast response and state stability. A narrow hysteresis window is well-suited for

high-speed switching applications, while a wider hysteresis window enhances the system's noise immunity, making it more effective in multi-state storage [36].

Moreover, recent research has further explored the use of VO_2 in classical conditioning, also known as Pavlovian modulation (Fig1. 12). Classical conditioning simulates the process of forming conditioned reflexes in biological neural systems, a critical function for the realisation of brain-inspired computing. For example, Wang et al. developed an artificial synapse device based on a VO_2/HfS_2 heterostructure. In this device, optical pulses were used to induce a post-synaptic current (PSC).

When a single, low-intensity optical pulse (the conditioned stimulus, CS) was applied, only a short-term memory (STM) response was observed. However, when the CS was repeatedly applied together with a high-intensity optical pulse (the unconditioned stimulus, US), the device eventually developed a relatively persistent PSC response under the action of the CS alone. This behaviour mirrors the learning process seen in biological neural systems. The mechanism behind this effect lies in the phase transition of VO_2 , which alters the band structure of the heterojunction, promoting carrier separation and carrier trapping. This process allows for the long-term retention of the learned response [132].

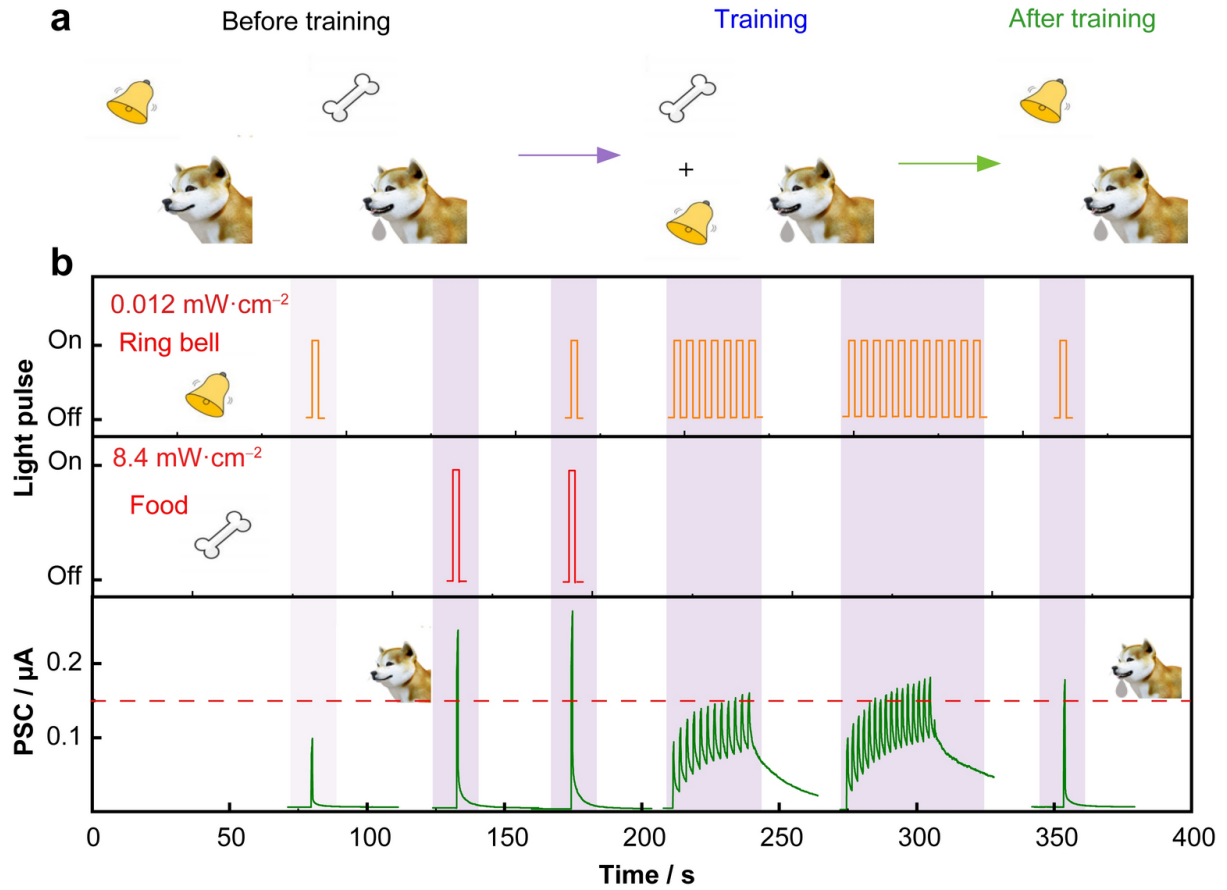


Figure 1.12. Pavlovian experiment simulation with HfS₂/VO₂ heterojunction artificial photoelectronic synapse. (a) Schematic diagram of Pavlov's dog experiment. (b) Training of HfS₂/VO₂ heterojunction under different intensities of UV light to complete associative learning simulations with $V_{ds} = 3$ V (405 nm, 0.012 and 8.4 mW·cm⁻²) [132]. Copyright of Yuke Publishing.

However, each technology has its own set of drawbacks, such as energy efficiency, speed, thermal crosstalk, and manufacturing complexity [133, 134]. Currently, most research on VO₂-based neuromorphic computing still focuses on electrical stimulation, possibly because electric fields are easier to control and enable higher integration density. In contrast, optical stimulation offers unique advantages, especially in all-optical networks, where it provides high bandwidth and low crosstalk, opening up new possibilities for future development. The use of optical signals allows for faster, parallel processing without the need for electrical-to-optical conversion, making it highly suitable for next-generation photonic neuromorphic systems.

1.5 Thesis synopsis

This thesis presents the application of the phase change material vanadium dioxide (VO_2) in all-optical memory on Si photonic chips. This work represents the first simulated demonstration of device-level bistability and photonic associative memory based on VO_2 , establishing a novel connection between emerging materials research and optical memory. Notably, a key challenge remains the high processing temperature required for VO_2 fabrication, particularly the post-deposition annealing step, which is incompatible with current CMOS technology. This challenge underscores the urgent need for low-temperature VO_2 fabrication techniques to facilitate the integration of such devices into practical applications, ensuring CMOS compatibility and expanding the potential of VO_2 for use on flexible polyimide substrates. Addressing this challenge is crucial for fully harnessing VO_2 's capabilities in next-generation electronic and photonic devices.

The structure of this thesis is organised as follows:

Chapter 1: This chapter outlines the research objectives, provides a comprehensive background and theoretical foundation for VO_2 , detailing its phase transition mechanisms and control method. Furthermore, this chapter reviews the mainstream applications of VO_2 thin films in silicon photonics, laying the groundwork for the novel photonic applications discussed in the results chapter.

Chapter 2: This chapter describes the VO_2 thin-film deposition techniques, characterisation methods, and post-deposition annealing processes employed in this study, which serve as the experimental basis for Chapter 3. This chapter also introduces the ring-resonator device architectures relevant to the project in Chapter 4.

Chapter 3: This chapter presents the experimental optimisation of low-temperature post-deposition annealing for VO_2 thin films, demonstrating its feasibility for flexible electronics and CMOS integration. The study highlights the importance of precise control over annealing parameters, including oxygen partial pressure, annealing temperature, and duration in tailoring the phase change behaviour and optical properties of VO_2 . Through comprehensive characterisation, I analyse how different annealing conditions affect the VO_2 phase transition

temperature, refractive index, and material quality, offering insights into the fabrication of high-quality VO₂ thin films. Additionally, this chapter investigates the impact of annealing on the surface morphology of VO₂ thin films and establishes a strong correlation between Raman spectroscopy and XPS data, providing a simpler and more efficient approach for VO₂ characterisation. Finally, I explore the annealing behaviour of W-doped VO₂ (W:VO₂), focusing on the influence of tungsten doping on oxidation and phase transition characteristics, which pave the way for low-power optical applications.

Chapter 4: This chapter proposes a device-level bistability approach that differs from traditional VO₂-based optical memory relying on intrinsic hysteresis. Instead, this method leverages the optical contrast between the two phases of VO₂, thereby eliminating operational complexities associated with hysteresis. Based on this mechanism, I systematically optimise VO₂-based silicon ring resonator devices, achieving a high-contrast photonic associative memory (VPAM) capable of short-term associative learning. This work establishes a novel connection between VO₂ research and all-optical neuromorphic computing.

Chapter 5: This chapter summarises the main achievement of my PhD research and proposes future work that can be derived from this thesis.

Chapter 2. Methods

In recent years, there has been growing interest in thermochromic compounds within the scientific community due to their ability to reversibly alter material properties in response to changes in temperature. Vanadium dioxide (VO_2) is one such compound and serves as the key focus of this study. In the literature, VO_2 is often referred to interchangeably as a phase transition material or a phase change material [135-137]. However, strictly speaking, phase change involves change between phases, e.g., amorphous between crystalline, whereas phase transition mostly refers to the transition between different crystalline structures, which are all subject to the crystalline phase. To avoid confusion and inconsistency, VO_2 is referred to as phase change material in this thesis.

At room temperature, VO_2 exists in its insulating (or dielectric) phase. When heated above its critical transition temperature (T_{IMT} or T_c , typically around 68°C), VO_2 undergoes a phase transition to its metallic state. During this transformation, both the electrical resistance and optical reflectance of the material change significantly [138, 139]. This temperature-dependent switching behaviour makes VO_2 a highly promising material for a variety of applications, including smart windows [140], sensors [122], and actuators [141].

Over the years, there has been significant interest in tuning the phase transition temperature of VO_2 to meet the needs of different application scenarios. Techniques such as elemental doping and strain engineering have been widely used to achieve this goal. By controlling these parameters, researchers can modulate the phase transition temperature to fit specific device requirements.

This chapter provides an in-depth exploration and comparison of the various deposition techniques available for producing VO_2 thin films, such as atomic layer deposition (ALD). Additionally, it presents a detailed review of the main materials and optical characterisation techniques employed in this work, providing a foundation for the experimental and analytical approaches used in subsequent chapters.

2.1 Vanadium dioxide thin film deposition method

There are various methods for the synthesis of VO_2 , with different methods suited for different application areas. The common methods for VO_2 synthesis can be broadly classified into three categories based on the reaction type: 1. gas-phase reactions, such as atomic layer deposition (ALD), chemical vapour deposition (CVD), pulsed laser deposition (PLD), and sputtering. 2. liquid-phase reactions, such as the sol-gel method and the hydrothermal method. 3. solid-phase reactions, such as thermal reduction.

In solid phase reactions, vanadium source materials (such as metallic vanadium or low-valence vanadium oxides) are annealed with an oxygen source at high temperatures, leading to the formation of VO_2 through a solid-state reaction. This method is typically used for the synthesis of VO_2 powders rather than VO_2 thin films [142, 143]. Liquid phase methods, such as the hydrothermal method, often require precise control of temperature and atmosphere, making large-scale production challenging [144, 145]. Most gas-phase methods, as well as some liquid phase methods, are widely used for the deposition of VO_2 thin films. This section will provide a detailed discussion of these methods, highlighting their respective advantages and disadvantages.

2.1.1 Atomic layer deposition

Atomic Layer Deposition (ALD) is an advanced thin-film deposition technique. It is commonly applied in depositing alumina (Al_2O_3) for CMOS and has also gained attention in the synthesis of VO_2 films. Common precursors for vanadium include Tetrakis ethylmethyl amino vanadium (TEMAV) and Vanadium oxy-tri-isopropoxide (VTOP), with typical oxidising agents being H_2O and O_3 [146-148]. Unlike chemical vapour deposition (introduced later), as a self-limiting growth technique, ALD technique only introduces one precursor at a time [149] and thus is also referred as surface reaction with precursor only reacting with the surface groups. Figure 2.1 shows a schematic diagram of the ALD process using TEMAV as the vanadium precursor. This process starts with the TEMAV dosing, proceeds with the purging step, followed by the introduction of oxidising agents (ozone and deionised water), and a final purge step to remove any residual byproducts.

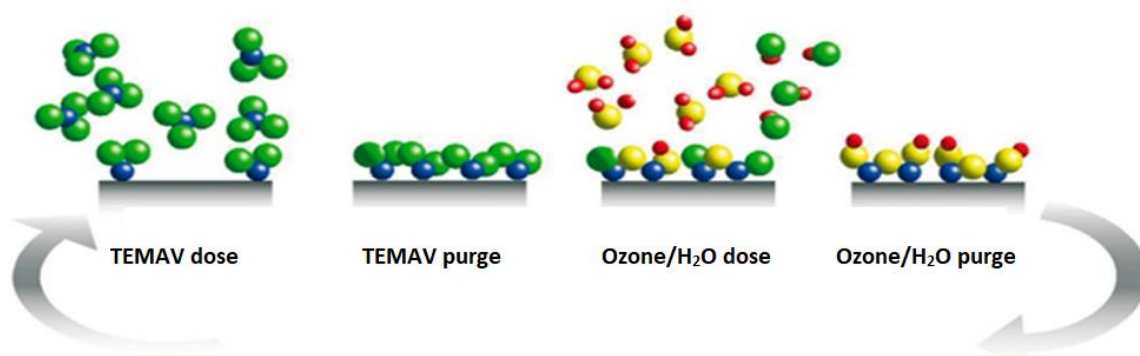


Figure 2.1. Schematic diagram of the atomic layer deposition (ALD) process cycles for VO_2 film growth.

The ALD procedure for VO_2 typically consists of sequentially exposing the substrate to vanadium precursors and oxidising agents. This method ensures a controlled and uniform growth of VO_2 films. The benefit of ALD lies in its capacity to generate extremely thin films, which is significant for applications where precise control over thickness is necessary for the material's phase transition features [150]. Another key advantage of ALD in VO_2 film fabrication is the uniformity of the film across a large substrate area, which is often a challenge with other deposition techniques [151, 152]. This uniformity is critical in applications requiring consistent phase transition behaviour across the entire thin film. However, one of the challenges in ALD of VO_2 is the long formation time.

In the ALD process, doping is achieved by alternating the introduction of a precursor and a doping agent within the deposition cycles. ALD offers significant flexibility in doping, which is a crucial aspect in modifying the intrinsic properties of VO_2 . Doping involves the specific elements in the VO_2 structure, which allow for precise control and alter its phase transition characteristics. By precisely introducing dopants at certain concentrations during the atomic layer deposition (ALD) process, it is possible to adjust the electrical, optical, and thermal characteristics of VO_2 to meet different application requirements [153].

One important instance is doping tungsten atoms into the VO_2 lattice (W:VO_2). This doping has been found to effectively reduce the phase transition temperature of VO_2 closer to room temperature, which is particularly beneficial for applications in environments where temperature control is critical. This doping enhances the functionality of VO_2 , especially in memory

applications, which is important in minimising energy consumption [154]. The lower transition temperature can lead to lower operating temperatures, reducing the energy required for thermal management of the computing devices.

In addition to altering the transition temperature, doping can also be used to control the hysteresis width of the VO_2 phase transition. For example, the W-doped VO_2 is reported to shrink the hysteresis, and the Al-doped VO_2 is reported to broaden the hysteresis width [154, 155]. This is an important aspect in applications where varying responses to temperature changes are required, such as in smart energy-saving devices or ultrafast sensors [156, 157]. By adjusting the doping level, it is possible to deposit VO_2 films with tailored hysteresis properties, optimising them for specific applications.

The working principle of the ALD process is shown in Fig. 2.2. It involves the alternate exposure of the substrate to a vanadium precursor and oxidising agent, followed by respective purge steps. The thickness of the ALD films can be precisely controlled by changing the number of ALD cycles. Precise control of deposition parameters, such as temperature, precursor pulse time, and purge time, is essential to ensure the desired phase and properties of VO_2 .

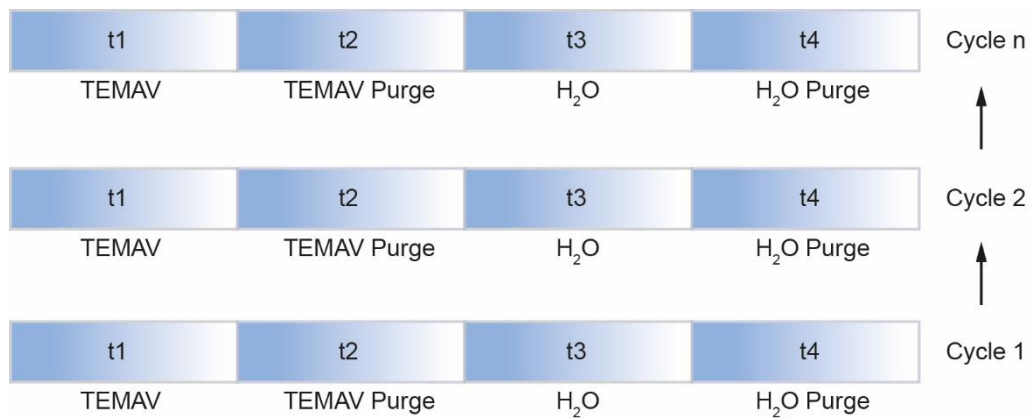


Figure 2.2. Schematic diagram of VO_2 thin film formation using atomic layer deposition (ALD). The vanadium and oxidising precursors are TEMAV and H_2O , respectively. The ALD process consists of four steps in a single cycle, from t1 to t4, where t1 is the TEMAV pulse stage, followed by the corresponding TEMAV purge step, t2. The H_2O pulse stage is represented as t3, followed by the H_2O purge stage (t4). From cycle 1 to cycle n, the VO_2 thin film grows in cycles, starting from the bottom to the top.

Figure 2.3 shows the common trend of the ALD process with different step process durations, which also stands for precursor dosing and precursor purging. As a self-limiting process, the growth rate increases with precursor dosing time (t_1) (e.g., TEMAV) and achieves saturation when sufficient precursor is applied to fully cover the surface (Fig. 2.3a). At the precursor purge step (Fig. 2.3b), the inertia gas is applied to remove extra precursor from the surface. With insufficient purging (t_2), the growth rate is high as the extra precursor on the film would react with the other precursor, referred to as a CVD growth. With sufficient purging (t_2), the growth rate decreases and reaches a stable rate. Similar independences are also on the other precursor (e.g., H_2O) dosing (t_3) (Fig. 2.3c) and purging (t_4) (Fig. 2.3d). The saturation and stabilisation time are referred to as ‘threshold’. Here, it is worth mentioning that the four steps have cross-interactions. For example, the deficiency of one precursor dosing can affect the sufficiency of purging and in turn affect the saturation point of the dosage of another precursor.

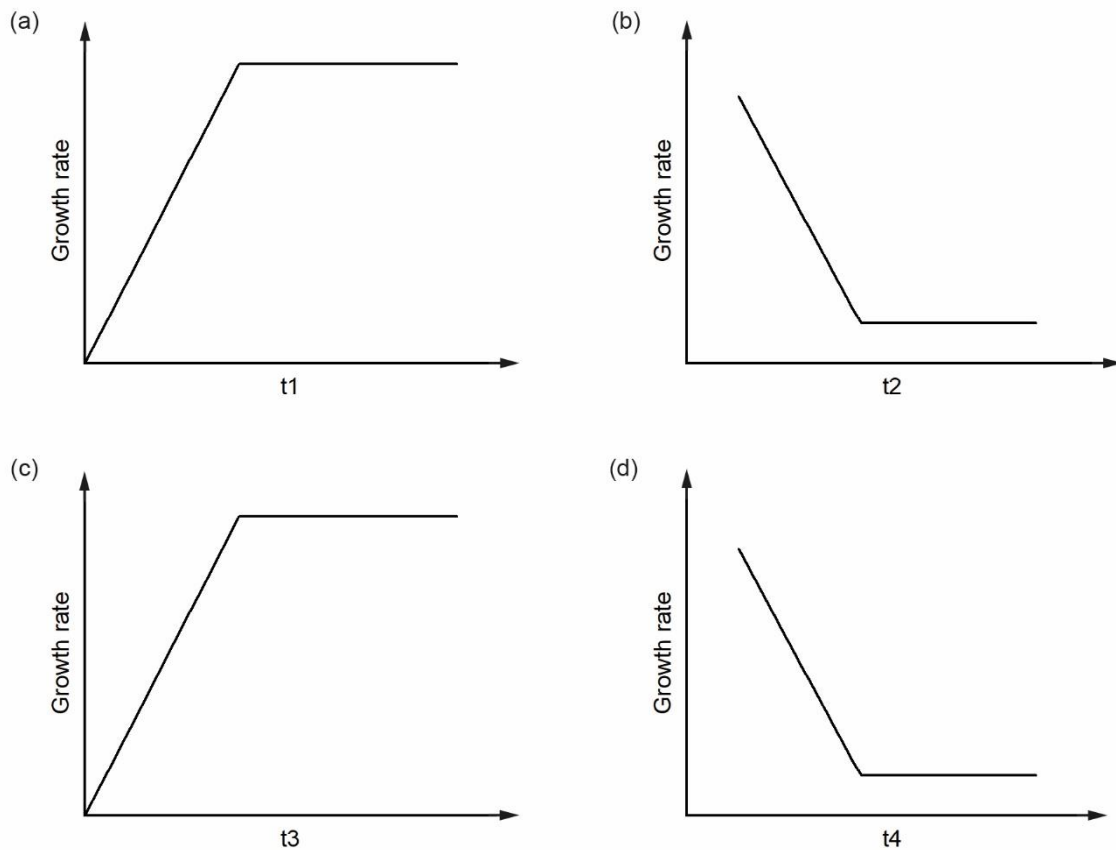


Figure 2.3. Schematic diagram of VO_2 growth rate against (a) Pulse of vanadium precursor. (b) Purge of vanadium precursor. (c) Pulse of oxidising precursor. And (d) Purge of oxidising precursor in a single ALD cycle. Note that all lines are indicative of trends only.

Understanding the principle of these trends is important in developing and optimising the ALD process. The objective is to determine the ‘threshold’ point for each stage. For instance, continuously feeding the vanadium precursor beyond its growth rate limit not only increases the deposition time but also leads to waste of precursor. This principle holds true for other steps in the process as well.

2.1.2 Chemical vapor deposition

Chemical Vapor Deposition (CVD) is another widely used technique to fabricate thin film, including VO₂ thin film. Unlike ALD with its self-limiting and sequential reaction steps, CVD is a continuous process that generally results in thicker films and is widely utilised for its operational simplicity and scalability.

During the CVD process, the substrate is exposed to one or more volatile precursors, which react on the substrate surface and produce the desired thin film. For the deposition of VO₂ films, precursors such as vanadyl (V) triisopropoxide (VO(OC₃H₇)₃) and Vanadyl acetylacetonate (VO(acac)₂) can be used [158, 159]. The reaction is often excited by applying heat, which led the decomposition of precursors and the subsequent formation of the VO₂ layer.

The growth rate of films in a CVD process is influenced by a number of factors, including the concentration of precursors [160], reaction temperature [158], and the flow rate of gases in the reaction chamber [161]. The schematic diagram of CVD process for VO₂ growth is shown in Fig. 2.4. Unlike ALD, where the film formation is per cycle and in atomic-scale which can be precisely controlled, CVD growth is continuous and often requires real-time monitoring and adjustment to maintain the desired film characteristics.

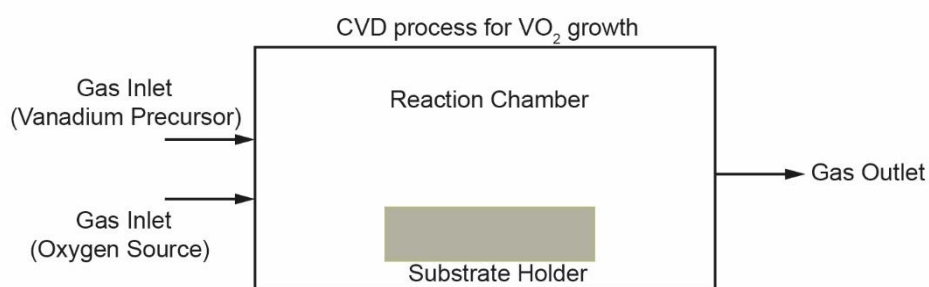


Figure 2.4. Schematic diagram illustrating the Chemical Vapor Deposition (CVD) process for the growth of VO_2 . The setup includes gas inlets for the vanadium precursor and oxygen source, a reaction chamber with a substrate holder, and a gas outlet for evacuating byproducts.

One advantage of CVD is that it is a non-line-of-sight process with good throwing power, which makes it able to coat films on large substrates with complex shapes. The low toxicity, explosivity and inflammability also make it suitable for industrial-scale fabrication [162]. Nevertheless, the challenge of achieving ultra-thin film is a notable problem in CVD, particularly when compared to ALD. Furthermore, CVD often requires higher temperatures, which can influence the crystallinity of the VO_2 films. Precisely controlling these conditions is important for ensuring the functional properties of the VO_2 , especially its phase transition behaviour.

2.1.3 Sputtering

Sputtering is a physical vapour deposition (PVD) method, it involves the erosion of a target material, which is then deposited onto a substrate to form a thin film. This process is driven by the bombardment of the target with high-energy particles, typically ions of an inert gas like argon [163]. The schematic diagram of a reactive magnetron sputtering system is shown in Fig. 2.5 [164].

In the deposition of VO_2 films through the sputtering process, the target material and chamber atmosphere are important. One instance is employing a V_2O_5 target, without the use of plasma. The inert gas in the vacuum chamber is ionised and accelerated towards the V_2O_5 target. Upon impact, the energy transfer causes atoms from the target to be ejected and subsequently deposited on the substrate, forming the VO_2 film [165]. The growth rate of the film during sputtering is influenced by the power applied to the target [166], the pressure of the chamber [167], and the distance between the target and the substrate [168].

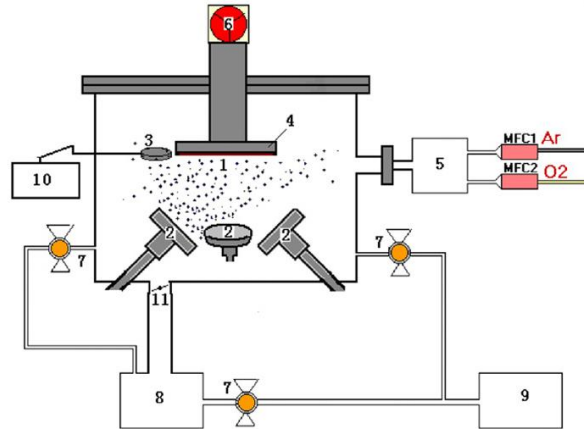


Figure 2.5. Schematic diagram of the reactive magnetron sputtering system, illustrating the key components [164]: (1) Substrate, where the thin film is deposited. (2) Magnetron Sources, responsible for the sputtering of target material. (3) Quartz Microbalance, for measuring thin film thickness in real time. (4) Resistive Heater, to control the substrate temperature. (5) Gas Supply, for introducing reactive gases into the chamber. (6) Rotating Controller, to adjust the substrate position. (7) Small Angle Valves, for precise control of gas flow. (8) Turbo Pump, for achieving high vacuum levels. (9) Rotary Pump, for initial chamber evacuation; (10) Frequency Meter, to monitor the oscillation frequency of the quartz microbalance. (11) Slide Valve, for isolating the vacuum pumps. Copyright of IOP Publishing.

Sputtering offers several advantages. It can generate a high-energy flow that exhibits high surface mobility, allowing the formation of smooth, dense, and continuous films with more ease. Additionally, sputtering allows for the deposition of films at lower temperatures compared to CVD, which is beneficial for substrates that are sensitive to high temperatures. The uniformity of the VO_2 film is another significant consideration. Sputtering is known for providing excellent uniformity across the substrate, which is crucial for applications requiring consistent performance, such as energy-efficient window fabrication [169]. However, sputtering cannot offer exceptional control over film thickness especially for the very thin films, which may not be suitable for applications that rely on the film thickness.

2.1.4 Pulsed laser deposition

Pulsed Laser Deposition (PLD) is a physical vapour deposition (PVD) process characterised by its fast deposition rate, contamination-free environment, high crystalline quality, and smooth film surfaces. Compared to other thin-film deposition techniques, PLD offers several advantages,

such as flexibility in target size and composition (which can be either solid or liquid), making it a versatile method for synthesising VO_2 thin films. A schematic diagram of a typical PLD system is shown in Fig. 2.6 [170].

During deposition, a pulsed laser emits a high-energy beam onto the target material, causing the target to evaporate in a vacuum chamber filled with an inert (argon) or reactive (oxygen) atmosphere. The evaporated species then deposit on the substrate, forming the desired thin film. The target material is typically vanadium (V), VO_2 , or V_2O_5 , and by adjusting the oxygen partial pressure, vanadium oxide films with different oxygen contents can be deposited [171].

Since the laser energy is directly focused on the target surface, PLD enables precise control over the growth orientation and chemical composition of the thin film. This feature is especially useful for synthesising thin films with complex compositions. Because the laser-induced evaporation occurs within a nanosecond to femtosecond range, PLD effectively avoids decomposition or compositional deviation that may occur during prolonged heating, allowing the stoichiometry of the target material to be well preserved in the film [172].

However, PLD also has notable limitations. Due to the localised nature of the laser beam, compositional uniformity can only be maintained within a small area, making it challenging to achieve large-area uniform deposition. As a result, PLD is primarily suitable for the preparation of small-area samples rather than large-scale production.

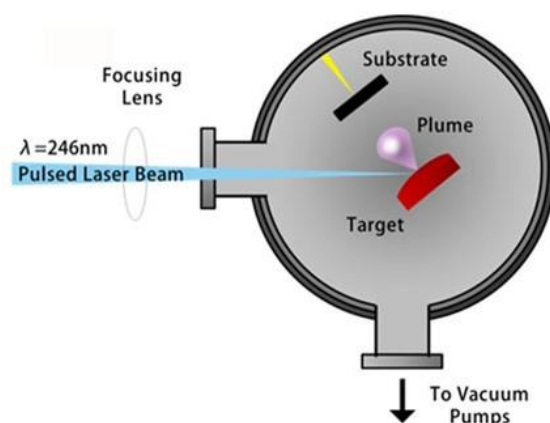


Figure 2.6. Schematic diagram of a classic pulse laser deposition system.

2.1.5 Molecular beam epitaxy

Molecular Beam Epitaxy (MBE) is one of the most suitable techniques for growing ultra-thin VO_2 films, as it allows for atomic-level control of film thickness and composition with high reproducibility. Recently, Alyson *et al.* deposited a 12 nm ultra-thin VO_2 film on TiO_2 and Al_2O_3 substrates using MBE and observed a two-orders-of-magnitude resistivity transition [173].

To overcome the inherent limitations of high deposition temperatures associated with MBE, Liu *et al.* utilised reactive magnetron sputtering to reduce the growth temperature to 450°C , successfully producing stoichiometric epitaxial VO_2 thin films. This approach achieved a three-orders-of-magnitude resistivity change, significantly lowering the cost associated with the MBE method for VO_2 thin-film synthesis [174].

However, due to its extremely low deposition rate, MBE is generally only suitable for small-scale experimental growth rather than large-scale production. While some studies have reported low-temperature growth of VO_2 films at around 400°C , these efforts mostly involve the fabrication of ultra-thin films (~ 10 nm) [28]. For thicker films, most MBE based VO_2 growth still requires high-temperature conditions to ensure precise atomic deposition [175]. These challenges make it difficult for MBE to be compatible with modern CMOS manufacturing processes.

2.1.6 Sol-Gel Method

The sol-gel method is one of the earliest chemical wet-chemical techniques proposed for the synthesis of VO_2 thin films [176]. The main advantage of the sol-gel method lies in its low cost and suitability for large-area thin-film fabrication. By adjusting parameters such as precursor concentration, annealing temperature, and annealing time, the phase composition and thickness of VO_2 films can be effectively controlled. The sol-gel process typically involves three stages: sol preparation, gel formation, and post-annealing to achieve the crystallisation of VO_2 .

During the sol preparation stage, a vanadium-containing precursor (most commonly tetravalent vanadium alkoxide) is dissolved in a solvent [177]. By controlling the concentration of the precursor solution and the chemical reaction conditions, a stable VO₂ sol is formed. The sol is then uniformly coated onto the substrate surface, and after drying to remove the solvent, it transitions to a gel state. Following gel formation, the film is subjected to high-temperature annealing in an inert gas environment to form a crystalline VO₂ thin film.

Traditional sol-gel preparation of VO₂ thin films typically relies on high-temperature post-treatment (~600°C) [178, 179]. To address this limitation, Basso *et al.* recently introduced laser annealing, significantly reducing the thermal impact on the substrate compared to conventional high-temperature annealing. However, laser annealing presents certain unavoidable challenges, such as limited treatment area and poor film uniformity [180].

2.1.7 Discussion of VO₂ thin film synthesis method

The fabrication methods for VO₂ thin films have their respective advantages and limitations, making them suitable for different application needs. Table 2.1 summarises the constraints of various fabrication methods in terms of key parameters such as deposition temperature, conformality, and uniformity.

For high-temperature gas-phase deposition processes, CVD and sputtering offer high deposition uniformity but only moderate conformality. Additionally, CVD faces certain challenges in controlling the thickness of the thin film. PLD operates at moderate temperatures and allows for precise stoichiometric control, but its film uniformity and conformality are relatively poor, making it more suitable for experimental studies of small-area, high-purity films. MBE provides high uniformity but low conformality and slow deposition rates. Moreover, due to crystal matching requirements, MBE is limited to deposition on crystalline substrates and cannot be used on amorphous substrates. This makes MBE great for producing ultra-thin, high-quality films, but its slow growth rate and substrate restrictions hinder its use in large-scale production.

The sol-gel method, a liquid-phase synthesis technique, is widely adopted due to its low cost and suitability for large-area thin-film fabrication. However, the uniformity of sol-gel-derived films is

relatively poor, and shrinkage during the drying process often affects the film's reliability and durability.

Among these methods, ALD stands out as a low-temperature gas-phase deposition process (150–200°C) that is compatible with modern CMOS processes. It is especially advantageous for thermally sensitive substrates, offering high film uniformity and excellent conformality. ALD is particularly suitable for applications requiring the deposition of uniform, conformal thin films (e.g., uniform conformal deposition on waveguides in Chapter 4) as well as for the deposition of thin films on low thermal budget flexible substrates presented in Chapter 3.

Table 2.1. Summary of the preparation methods of VO₂ thin films.

Reaction environment	Method	Temperature (°C)	Uniformity	Conformality	Other Cons
Gas phase synthesis	ALD	~ 175	High	High	Relative low deposition speed
	CVD	~ 700	High	Moderate	Difficult to achieve thin film
	Sputtering	~ 700	High	Low	Thickness control
	PLD	~ 500	Low	Low	Small scale deposition
	MBE	> 500	High	Low	Low speed, critical requirement in the underneath layer
Solution phase synthesis	Sol-gel	~ 600	Low	High	Shrinkage upon drying

2.2 Annealing treatments in atomic layer deposition

Among the various ALD precursors that have been developed for VO₂, tetrakis(ethylmethylamino) vanadium (TEMAV) has been increasingly used since it is a liquid precursor and the synthesised films mainly consist of +4 valency, leading to the growth of pure phase VO₂. Using this precursor,

the maximum deposition temperatures for VO₂ have been reported to be up to 200°C without triggering precursor decomposition [30, 154].

Given that VO₂ films deposited at temperatures below 200°C remain amorphous and consequently do not exhibit insulator-to-metal transition (IMT) behaviour, the introduction of a post-annealing process becomes essential [181-183]. The post annealing process serves two main purposes: Transformation from amorphous to crystalline VO₂; Formation of correct stoichiometry as VO₂. Figure 2.7 illustrates the schematic representation of the initial amorphous state before annealing and the crystalline state achieved post-annealing. This schematic clarifies the structural transformation that VO₂ undergoes during the post-annealing process.

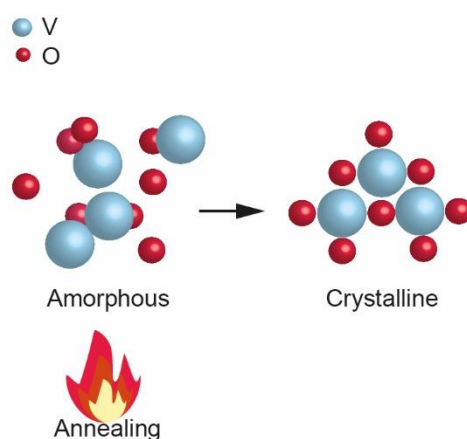


Figure 2.7. Schematic diagram of the VO₂ thin film in its amorphous state (before annealing) and its crystalline state (after the annealing process), where the blue and red bubbles represent vanadium and oxygen atoms, respectively.

Previous works have reported that the precise formation of the desired VO₂ phase during the annealing was dependent on the synergistic impact between the oxygen partial pressure, anneal temperature, and annealing duration in the annealing furnace [184-189]. Table 2.2 presents a summary of annealing conditions that have been designed for the ALD process in recent years. From Table 2.2, there is a trend where higher annealing temperatures are often paired with lower oxygen partial pressures. For instance, Marko *et al.* and Prasad *et al.* used relatively high temperatures (660-670°C and 550-700°C, respectively) with low oxygen partial pressures (10⁻⁵ to 10⁻⁴ Torr and 8 × 10⁻⁶ Torr, respectively). This indicates that at higher temperatures, the formation of VO₂ phase requires less oxygen due to increased reaction rates or more efficient oxygen incorporation into the film. For higher oxygen partial pressure and longer duration, such as

studies by Sun *et al.* and Bai *et al.*, requires lower annealing temperature. The higher oxygen partial pressure and longer duration could be attributed to compensate for the reduced reaction at lower temperatures. The insight of the annealing processes described here are applied in Chapter 3 to get the high quality and low temperature VO₂.

Table 2.2. Summary of annealing conditions in recent research works.

Author	precursor	Anneal Temperature (°C)	Oxygen partial pressure (Torr)	Anneal duration (hour)	Year	Ref
Kozen <i>et al.</i>	TEMAV+O ₃	585	1×10^{-5}	2	2017	[190]
Park <i>et al.</i>	TEMAV+H ₂ O	480	~0.008	1	2017	[191]
Lv <i>et al.</i>	TDMAV+H ₂ O	475	N/A	1.5	2017	[192]
Tadjer <i>et al.</i>	TEMAV+O ₃	660 and 670	10^{-5} to 10^{-4}	1 and 2	2017	[193]
Currie <i>et al.</i>	TEMAV+O ₃	560	8×10^{-7} to 5×10^{-6}	2	2018	[187]
Prasadam <i>et al.</i>	VTOP+H ₂ O	550 and 700	8×10^{-6}	4	2019	[146]
Bai <i>et al.</i>	TEMAV+H ₂ O	450 and 500	0.06 to 1.13	2 and 0.5	2020	[194]
Li <i>et al.</i>	VO(OC ₃ H ₇) ₃ +H ₂ O	500	113	2	2020	[195]
Ganesan <i>et al.</i>	VCl ₄ +H ₂ O	550	~0.01	1	2021	[29]
Muller <i>et al.</i>	TEMAV+H ₂ O	450	0.1	0.5	2021	[156]
Sun <i>et al.</i>	TEMAV+H ₂ O	375	1	2	2022	[154]
Boyce <i>et al.</i>	TEMAV+O ₃	400	3×10^{-5}	1	2022	[196]
Baji <i>et al.</i>	TEMAV+H ₂ O	500	~210	3 to 6	2023	[30]

Meanwhile, most annealing temperatures typically require temperatures above 400°C to optimise the VO₂ crystal quality and to obtain its phase transition characteristics effectively. However, such high temperatures make it incompatible with integration with CMOS devices, which restricts the thermal budget after the first aluminium alloy metal layer deposition. Furthermore, the use of VO₂ on flexible substrates such as DuPont Kapton, which is popular in wearable electronics due to its durability and mechanical flexibility, requires an even more conservative annealing temperature [197, 198]. Exceeding the thermal tolerance could compromise their structural integrity and limit their functional performance which presents a critical limitation to their application. The thermal budgets of various substrates, including silicon, neuromorphic chips, and flexible polyimide are schematically shown in Fig. 2.8, highlighting the substantial limitations that must be considered when integrating VO₂ with other fabrication

processes. Therefore, addressing this challenge will be critical in fully exploiting the properties of VO₂ in the next generation of electronic devices.

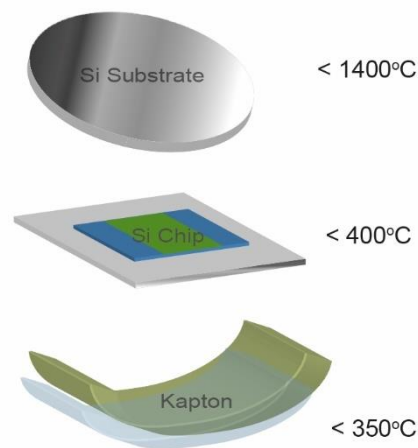


Figure 2.8. Schematic diagram of the temperature tolerance of different materials: (a) Si substrate (1400°C), (b) Si-based neuromorphic chip (400°C) and (c) flexible polyimide (Kapton, 350°C) film are compared here.

2.3 VO₂ characterisation technology

In this subsection, common characterisation techniques are introduced for VO₂ investigation, including Raman spectroscopy, X-ray photoelectron spectroscopy (XPS), ellipsometer and Fourier transformation infrared spectroscopy (FTIR). All these described techniques are used in the next chapter for VO₂ material and optical characterisation.

2.3.1 Raman Spectroscopy

Raman spectroscopy is a common tool used in material science to investigate vibrational information about the symmetry of molecules. When monochromatic light, typically a laser beam denoted by ν_0 , interacts with the electron cloud of a sample, it induces scattering processes. These processes, as illustrated in Fig. 2.9, can be categorised into three cases based on the frequency of the emitted light. If the emitted light retains the same frequency as the incident light, the process is termed elastic scattering, or a Rayleigh process, which is the most probable scenario [199]. Conversely, when the emitted light frequency is lower ($\nu_0 > \nu$), the process is identified as inelastic scattering, known as Stokes-Raman scattering. If the emitted light frequency is higher ($\nu_0 < \nu$), it represents another form of inelastic scattering, referred to as anti-

Stokes Raman scattering. The frequency shift of the emitted light, or the Raman shift, is quantified in wavenumbers (cm^{-1}), a unit of inverse length. The Raman spectrum is constructed by plotting the intensity of light measured against the Raman shift.

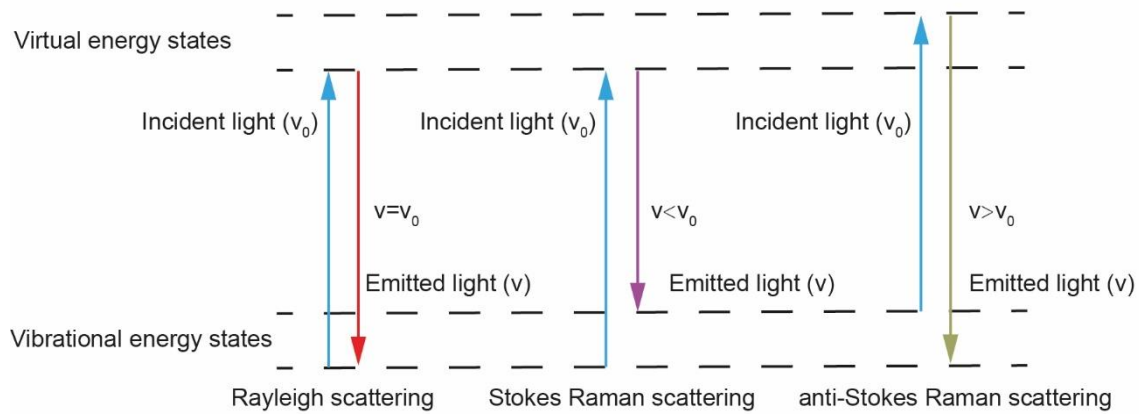


Figure 2.9. Schematic diagram of various scattering mechanisms triggered by the interaction of incident light with a sample.

The peaks of Raman spectra are highly sensitive to the structure and stress of the crystal, which makes Raman spectroscopy one of the most utilised tools for characterising VO_2 films. At room temperature, VO_2 exhibits distinct Raman spectral lines in the range of $100\text{-}1000\text{ cm}^{-1}$. The reference Raman spectrum of commonly produced monoclinic VO_2 (M1) is shown in Fig. 2.10, it is associated with 18 Raman-active vibrations, including 9 A_g (symmetric) and 9 B_g (asymmetric) modes, the A_g mode means symmetric vibrations of atoms along the symmetry axis of the crystal, whereas the B_g mode involves antisymmetric vibrations [200, 201]. Recent polarised Raman measurements on epitaxial VO_2 (M1) films have determined the symmetry of all experimentally observed Raman modes [202]. A_g phonons have been identified at $137, 194, 224, 310, 340, 393, 499, 612,$ and 663 cm^{-1} , while B_g phonons are located at $143, 224, 262, 393, 442, 484, 582,$ and 820 cm^{-1} . Notably, the red dash lines located at $194\text{ cm}^{-1}, 224\text{ cm}^{-1}$ and 612 cm^{-1} represent the highest intensity of VO_2 (M1) Raman scattering peaks [154]. This detailed understanding of Raman spectra in VO_2 greatly enhances the knowledge about its structural properties and phase transition behaviour.

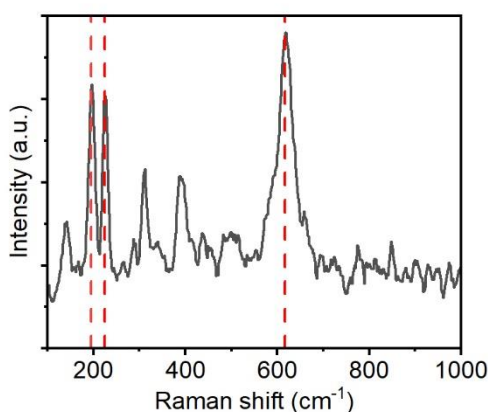


Figure 2.10. Raman spectra of VO_2 reference was measured at the room, utilising a 532 nm laser with 1 mW output power. The highest intensity of VO_2 (M1) Raman scattering peaks, marked by red dash lines, are located at 194 cm^{-1} , 224 cm^{-1} , and 612 cm^{-1} . These well-defined peaks include the characteristic Ag peaks of the V-V vibrations at 194 cm^{-1} and 224 cm^{-1} , as well as the V-O Ag vibrational peak at 612 cm^{-1} , highlighting key aspects of VO_2 molecular structure.

A lot of information on the properties of a VO_2 thin film can be obtained from its Raman spectrum. By comparing its Raman spectrum against the standard spectrum, we can identify the phase composition of VO_2 .

2.3.2 X-ray Photoelectron Spectroscopy

XPS uses X-ray beams to excite photoelectrons on the solid surface and measure the energy and number of electrons that escape from the top 10 nm of the material surface [203]. It measures the kinetic energy of the photoelectrons to ascertain their binding energies, which in turn generate distinctive spectral lines. The spectra produced offer peaks that correspond to specific elements and enable the distinction among various oxidation states or chemical bonds, thereby providing an understanding of surface chemistry.

As shown in Fig. 2.11, there are a variety of stable vanadium oxides with non +4 valence in the area close to VO_2 in the V-O phase diagram. Therefore, it is of great significance to detect the valence state of V when researching growing high quality VO_2 films. Among various valence state

detection methods, X-ray Photoelectron Spectroscopy is an easy to obtain and reliable method for thin film samples.

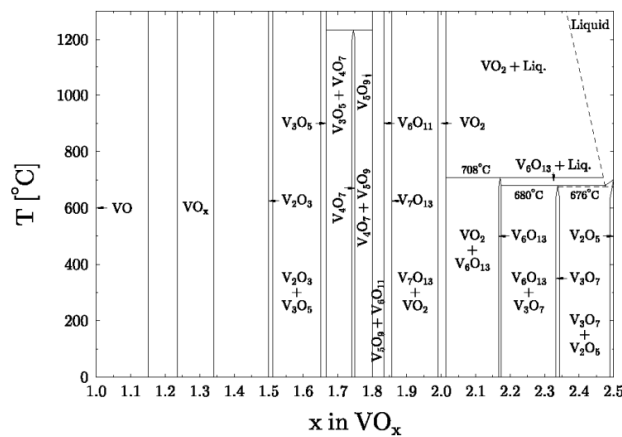


Figure 2.11. Phase diagram of vanadium oxide (VO_x) for x ranging from 1 to 2.5, across various deposition temperatures [204]. Copyright of American Physical Society.

2.3.3 Fourier Transform Infrared Spectroscopy

Fourier Transform Infrared Spectroscopy (FTIR) is a commonly used non-destructive technique for identifying the chemical composition of solid, liquid, or gas from their chemical bonding by the spectrum of absorption. Unlike other techniques, scanning wavelength one by one using monochromatic light, FTIR offers wavelength spectra converted from a broad frequency source and duration measurement. Here, FTIR is an effective tool to get transmission or reflection spectra of a sample in the near-infrared and infrared. This technique is especially effective for studying VO₂, as it exhibits significant optical contrasts between insulating and metallic phases in the NIR and IR ranges [205, 206]. In the FTIR setup, the beam splitter is essential as any material has a limited range of optical transmittance. Thus, several beam splitters may be used interchangeably to cover a wide spectral range. Here, KBr beam splitters are highly effective across a wide spectral range, especially suitable for the mid-IR range, making them a popular choice for general applications [207]. On the other hand, CaF₂ beam splitters offer excellent transmission in the NIR but the transmission cuts off at about 8 μm [208].

2.3.4 Ellipsometry

Ellipsometry is a technique based on the analysis of changes in the polarisation of light, used to characterise the optical properties and thickness of materials. By measuring the amplitude ratio

(Ψ) and phase difference (Δ) of the reflected light's p-polarised and s-polarised components and combining this with Fresnel reflection coefficients, the complex refractive index ($n+ik$) and the thin-film thickness can be extracted [209]. The relationship between Ψ and the reflection coefficients is defined as:

$$\tan \Psi = \frac{|R_p|}{|R_s|} \quad (2.1)$$

where $|R_p|$ and $|R_s|$ represent the amplitude of the reflected p-polarised and s-polarised light, respectively. This formula only involves relative changes in the reflected light, making the measurement robust against variations in the light source intensity.

To extract the optical constants (n,k) and thickness (d) of VO_2 films from ellipsometry data, experimental results are typically fitted to physical models. Commonly used optical models include the Tauc-Lorentz model, the Drude-Lorentz model, and the Effective Medium Approximation (EMA). The choice of the model depends on the phase and transition state of VO_2 .

In the monoclinic phase (insulating state) of VO_2 , the Tauc-Lorentz model is typically employed [210]. This model combines the Tauc bandgap model and the Lorentz oscillator model to describe the optical response of semiconductors and dielectric materials with bandgaps. The Tauc component characterises the absorption edge, while the Lorentz oscillators describe the optical absorption and resonances in the higher energy regions. This approach effectively captures the optical absorption edge, valence-to-conduction band transitions, and the dispersion of optical constants in the insulating phase. In the rutile phase (metallic state), VO_2 exhibits behaviour characteristic of metals. The Drude-Lorentz model is commonly applied to describe its optical response in this state [91]. The Drude model accounts for free carrier behaviour, which dominates the low-frequency response and is responsible for the high reflectivity observed in the infrared region. The Lorentz oscillators, on the other hand, describe high-frequency optical excitations, particularly in the visible and ultraviolet regions. The combination of these models provides a comprehensive description of the optical properties of VO_2 in its metallic state, including both low-frequency free carrier effects and high-frequency interband transitions.

During the metal-insulator transition (MIT), VO₂ films may exhibit a coexistence of metallic and insulating phases. In such cases, the Effective Medium Approximation (EMA) model is used to characterise the optical properties of VO₂ [211]. The EMA model treats the VO₂ film as a composite material, consisting of metallic and insulating phases. The relative volume fraction of the metallic phase, known as the "filling factor," is adjusted to fit the experimental data. The filling factor represents the fraction of the metallic phase, and the overall optical response is modelled as a weighted average of the optical constants of the two phases. This model is particularly effective in describing the optical behaviour of VO₂ during its phase transition, capturing the mixed-state characteristics.

For data analysis, the CompleteEASE software is employed to process the ellipsometry measurements. This software includes a comprehensive library of optical constants for various materials, including metals, dielectrics, and semiconductors. Users can customise models by incorporating Tauc-Lorentz oscillators, Drude-Lorentz components, and EMA approximations, allowing flexible and accurate fitting of VO₂'s optical data .

In this work, the primary focus was on evaluating the effects of annealing on the optical properties of VO₂. As such, the analysis prioritised the relative changes in n and k rather than their absolute values, providing insights into how annealing conditions influence VO₂'s optical characteristics.

2.4 Silicon waveguide and microring resonator

2.4.1 Silicon waveguide

Silicon is a versatile semiconductor material that can act as both a conductor and an insulator by controlling the activation and concentration of carriers during the doping process. This property makes silicon a great material for constructing memory chips and other electronic devices. Furthermore, as the second most abundant element in the Earth's crust, silicon is cost-effective and suitable for large-scale production.

From an optical perspective, silicon exhibits a high refractive index of 3.47 at 1550 nm [212], and it is transparent to light in the 1.1 μm to 8 μm wavelength range, covering both the SWIR and parts

of the MWIR spectrum, which covered the main target wavelengths in this study [213]. Additionally, for an input wavelength of 1.55 μm , silicon rib waveguides exhibit an average propagation loss of approximately 3.34 dB/cm for the commonly used TE mode. For the small-scale devices used in this study (on the order of tens of micrometres), this loss is negligible [214].

(a) Waveguide structure and mode analysis

A waveguide is a structure designed to guide optical waves along a specific path while minimising loss. At the 1550 nm wavelength, common waveguide structures include strip waveguides and rib waveguides. In this study, the rib waveguide was selected due to its superior properties, particularly for use in microring resonators. The rib waveguide features a flat slab at the base of the waveguide, in contrast to the fully etched structure of strip waveguides. By selecting a smaller slab thickness, the cutoff width for higher-order modes (e.g., TE_1 , TM_1) is significantly reduced, ensuring that the waveguide supports only the fundamental mode over the designed size range [215].

Depending on the polarisation direction of the propagating light, the modes in a waveguide can be classified as: a) Transverse Electric (TE) Mode: The electric field vector (E) is perpendicular to the direction of propagation, while the magnetic field (H) has both longitudinal and transverse components. b) Transverse Magnetic (TM) Mode: The magnetic field vector (H) is perpendicular to the propagation direction, while the electric field (E) has both longitudinal and transverse components. c) Transverse Electromagnetic (TEM) Mode: Both the electric (E) and magnetic (H) vectors are perpendicular to the propagation direction, but this mode requires a closed-loop path for the magnetic field lines.

In rectangular or rib waveguides, the magnetic field lines cannot form a closed loop, making it impossible for the TEM mode to propagate in these waveguide structures. Therefore, in this work, only the TE and TM modes are considered. For practical applications, the TE mode is most commonly used in photonic devices, as it can be more easily confined in the waveguide and supports a more stable mode profile.

(b) Effect of waveguide dimensions on the mode

The dimensions of a waveguide determine the types of modes it supports. Most waveguides support two independent polarisation modes: quasi-TM mode, where the primary magnetic field

component is along the transverse (horizontal) direction, and quasi-TE mode, where the primary electric field component is along the transverse direction. To avoid mode interference or the instability caused by higher-order modes, such as unpredictable free spectral range (FSR) shifts in microring resonators, it is generally preferred to operate the waveguide in a single-mode regime for each polarisation. This is achieved by modulating the waveguide dimensions to ensure that all higher-order modes become radiation modes, meaning they cannot propagate inside the waveguide.

The effective refractive index (N_{eff}) represents the equivalent refractive index of an optical mode within a waveguide. A higher N_{eff} typically indicates stronger confinement of the optical field, which reduces boundary leakage loss. Figure 2.12 illustrates the relationship between the rib waveguide width and the N_{eff} for a waveguide with a height of 220 nm, which is a standard thickness for silicon-on-insulator (SOI) wafers. It can be observed that when the waveguide width is 500 nm, only the fundamental TE mode is supported, while higher-order modes are cut off.

This design choice serves two key purposes. First, it achieves a higher effective refractive index, which enhances optical confinement and reduces propagation loss by limiting boundary leakage. Second, it ensures single-mode propagation, avoiding the interference and unpredictability caused by the presence of multiple modes. This is particularly important in photonic integrated circuits (PICs), where stable and predictable optical paths are essential for reliable operation.

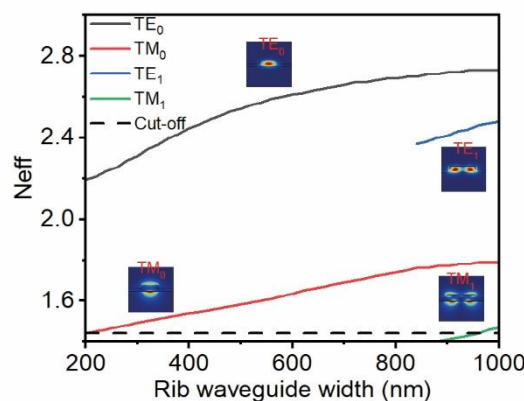


Figure 2.12. Effective refractive index (N_{eff}) as a function of rib waveguide width for a silicon-on-insulator (SOI) rib waveguide with a height of 220 nm. The plot shows the fundamental TE₀ and TM₀ modes, as well as higher-order modes (TE₁, TM₁). The dashed line indicates the cutoff width for higher-order modes, ensuring single-mode

propagation. Insets illustrate the electric field distributions of the corresponding modes. At a waveguide width of 500 nm, the waveguide supports only the fundamental TE mode, making it suitable for applications requiring low loss and high mode confinement.

2.4.2 Silicon microring resonator

The primary device discussed in later section 4.4 is the add-drop microring resonator (MRR), which consists of two straight waveguides and a circular ring-shaped waveguide. The schematic diagram of this structure is shown in Fig. 2.13.

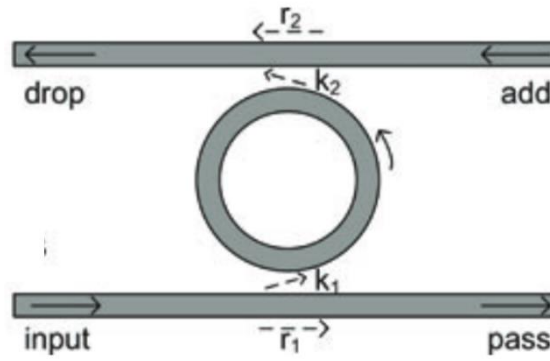


Figure 2.13. Schematic of an Add-Drop optical ring resonator configuration [216]. Copyright of Wiley.

In this structure, r represents the self-coupling coefficient, which indicates the proportion of light that remains in the same path, while k represents the cross-coupling coefficient, which indicates the proportion of light transferred to the other path. The coupling coefficients are influenced by the coupling gap between the ring and the straight waveguide. A larger coupling gap increases r and decreases k , while a smaller coupling gap increases k and decreases r . Under the assumption of lossless coupling, the relationship between the two coefficients is governed by the following equation:

$$r^2 + k^2 = 1 \quad (2.2)$$

When the following resonance condition is satisfied, a portion of the light from the input port is coupled into the ring waveguide, where it undergoes interference [216]:

$$2\pi R N_{eff} = m \lambda_{res} \quad (2.3)$$

Here, n_{eff} is the effective refractive index of the propagating mode, λ_{res} is the resonant wavelength, and m is the mode number of the resonance. From Equation 2.8, it is clear that a change in n_{eff} will directly influence λ_{res} .

Figure 2.14 illustrates some of the key parameters used to evaluate the output spectrum of an MRR. One critical parameter is the full width at half maximum (FWHM), which represents the width of the resonance peak at half of its maximum intensity. FWHM is inversely proportional to the quality factor (Q) of the resonator (Equation 2.7). A narrower FWHM corresponds to a higher Q-factor, indicating sharper resonance and higher selectivity for specific wavelengths.

The pass band refers to the portion of light that couples into the MRR output port under non-resonant conditions. Since the MRR cannot completely suppress wavelengths outside of the resonance conditions, some of the non-resonant light can bypass the ring and enter the output port. Another essential performance metric is the insertion loss (IL), which represents the total power loss experienced by the light as it passes through the MRR. The loss is caused by a combination of round-trip loss, bending loss, and coupling efficiency. The insertion loss is calculated as:

$$IL(dB) = -10 \log_{10} \left(\frac{P_{\text{out}}}{P_{\text{in}}} \right) \quad (2.4)$$

where P_{out} is the output power and P_{in} is the input power.

Table 2.3 summarises the key characteristics of round-trip loss and bending loss, as well as their influence on the overall performance of the MRR. Reducing bending loss is particularly important in compact devices, as the tighter bending radius increases the likelihood of radiation loss. Similarly, waveguide roughness and fabrication imperfections contribute to the additional loss, which affects the overall insertion loss of the system.

Table 2.3. Comparison of characteristics between round-trip loss and bending loss in a microring resonator.

Characteristic	Round-Trip Loss	Bending Loss
----------------	-----------------	--------------

Mechanism of Influence	Total loss during each round trip	Mode leakage caused by waveguide bending
Effect on Spectrum	Reduced resonance peak intensity	Reduced resonance peak intensity
Relation to Size	Proportional to ring diameter	Inversely proportional to ring diameter
Extreme Case Result	Weak resonance traces may still be seen in the remaining spectrum	The spectrum becomes flat and the resonance characteristics are completely lost

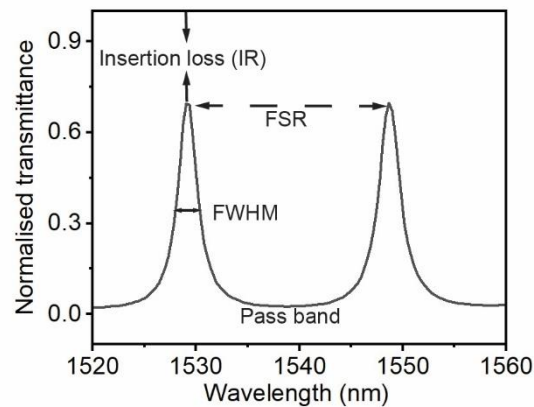


Figure 2.14. Depiction of MRR key parameters.

The Free Spectral Range (FSR) describes the spacing between adjacent resonance frequencies in a MRR. The FSR is a critical parameter that determines the number of channels that can be accommodated within a specific wavelength range. The mathematical expression for FSR is given as [216]:

$$\text{FSR} = \frac{\lambda^2}{n_g L} \quad (2.5)$$

Where λ is the wavelength of the propagating light. L is the optical path length, which is typically related to the circumference of the ring, n_g is the group index, which is related to the effective refractive index (n_{eff}) and its variation with respect to wavelength, as given by:

$$n_g = n_{\text{eff}} - \lambda_0 \frac{dn_{\text{eff}}}{d\lambda} \quad (2.6)$$

From the above equation, it is clear that FSR is primarily affected by n_{eff} and the ring radius. If N_{eff} remains constant, a larger ring radius (which increases the optical path L) leads to a smaller FSR, allowing more optical channels to be accommodated within a given wavelength range.

The Quality Factor (Q-Factor) is another crucial parameter used to evaluate the performance of an optical resonator. It indicates the amount of energy loss per cycle of oscillation. A higher Q-factor signifies lower energy loss and thus a more efficient resonator. For an add-drop microring resonator, the Q-factor is calculated as [216]:

$$\text{Q-factor} = \frac{\pi n_g L \sqrt{r_1 r_2} a}{\lambda_{\text{res}} (1 - r_1 r_2 a)} = \frac{\lambda_{\text{res}}}{FWHM} \quad (2.7)$$

where a is the single-pass amplitude transmission coefficient, which accounts for propagation loss in the ring and coupling losses. r_1 and r_2 are the self-coupling coefficients of the two bus waveguides connected to the ring. L is the optical path length.

From the Q-factor formula, it is clear that a larger ring radius results in a higher Q-factor. This is because a larger radius increases the optical path length L , which allows the light to circulate longer before being coupled out, reducing the energy loss per cycle. Additionally, higher values of r_1 , r_2 also lead to a higher Q-factor. As a result, the Q-factor can be controlled by optimising the design of the ring radius and the coupling coefficients within the ring.

In a microring resonator, there are three primary coupling regimes used to describe the coupling efficiency between the input waveguide and the ring waveguide: overcoupling, critical coupling, and undercoupling, as shown in Fig. 2.15. These regimes are determined by the gap distance (d) between the input waveguide and the ring waveguide, which controls the fraction of light coupled into the ring. For a given ring waveguide structure, there exists a critical gap d_{crit} at which the transmission at the resonance wavelength approaches zero. This means that at resonance, most

of the input light is coupled into the ring, while at non-resonant wavelengths, most of the input light remains in the through port, resulting in a transmission close to 1.

In the case of over-coupling and under-coupling, the intensity of the resonance trough is not as deep as the critical coupling point. When the coupling gap is smaller than the critical gap, the ring resonator is in an over-coupling state, the passband is wide, and at the non-resonant wavelength, a portion of the light is still coupled into the micro-ring, resulting in a transmission value of the output port at the non-resonant wavelength less than 1. On the contrary, when the coupling gap is larger than the critical gap, the ring resonator is in an under-coupling state. At this time, the passband is narrow, but the light at the resonant wavelength is not fully coupled into the ring resonator, resulting in a decrease in the power intensity of the circulating light in the ring.

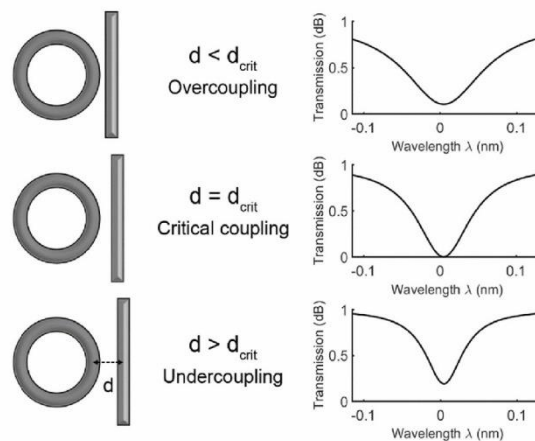


Figure 2.15. Three different coupling regimes and respective spectrum behaviour around the resonance wavelength [217]. Copyright of Optica Publishing Group.

2.5 Conclusion to Chapter 2

Vanadium dioxide exhibits a first-order solid-solid insulator-to-metal transition (IMT) near 68°C. This transition is governed by the Gibbs free energy landscape of the system, requiring either external energy input or an energetically favourable transformation where the final state possesses lower free energy. The sharp, reversible changes in electrical and optical properties accompanying this transition make VO_2 highly attractive for optical memory application.

However, the practical realisation of high-quality VO₂(M1) is complicated by vanadium's ability to exist in multiple stable oxidation states, with a natural tendency to form V₂O₅ under ambient conditions. This makes precise control over both stoichiometry and crystalline phase formation critical, especially when targeting the monoclinic VO₂ phase. To meet these stringent requirements, a fabrication method with nanometre-level precision and excellent uniformity is imperative. Among the reviewed techniques, atomic layer deposition (ALD) emerges as the suitable for large-scale and CMOS-compatible VO₂ film fabrication, owing to its layer-by-layer growth, high conformality, and low temperature deposition. Despite its advantages, ALD-deposited VO₂ typically requires post-deposition annealing to achieve the desired crystalline phase and stoichiometry. Finally, this chapter reviewed key characterisation methods such as X-ray photoelectron spectroscopy (XPS), Raman spectroscopy, ellipsometry, and FTIR, all of which are essential for accurately assessing phase purity, oxidation states, optical constants. These techniques will be used throughout the experimental sections of this thesis (especially in Chapter 3) to evaluate and optimise material properties.

The next chapter builds upon these foundations by experimentally exploring how post-deposition annealing conditions including temperature, oxygen partial pressure, and duration affect the crystallinity, optical response, and phase transition properties of VO₂ thin films deposited via ALD. These findings are critical to developing CMOS-compatible optical memory elements.

Chapter 3. Low-temperature vanadium dioxide for CMOS integration and flexible polyimide applications

3.1 Introduction

Vanadium dioxide (VO_2) is a phase-change material that has attracted interest for its broad applications in various areas including smart windows [44, 218], thermal management coatings for spacecraft and terrestrial applications [148, 219-221], optical switching [112, 222], novel memories [22, 121], neuromorphic computing, and infrared camouflage [223, 224]. The research interest in VO_2 originates from its thermochromic response, which involves a structural transition from an insulating/dielectric monoclinic structure ($\text{VO}_2(\text{M1})$) at low temperatures to a semiconducting/metallic rutile structure ($\text{VO}_2(\text{R})$) at high temperatures. The transition temperature is usually around 68°C [64, 225], but it can be lowered to room temperature by introducing dopants, e.g. W [226, 227].

To synthesise high-quality VO_2 thin films, several deposition techniques have been explored, including reactive sputtering [92, 228], sputtering and oxidation [229], Pulsed Laser Deposition (PLD) [206, 230], Chemical Vapor Deposition (CVD) [158, 161], Atomic Layer Deposition (ALD) [29, 30], and sol-gel processing [231, 232]. Among these techniques, sputtering and ALD are considered the two most compatible routes for scale-up manufacture, the latter of which is the topic of this work.

To possess the phase transition capability, a VO_2 thin film has to be crystalline in the monoclinic phase ($\text{VO}_2(\text{M1})$), and this requirement represents a significant challenge in VO_2 formation. In terms of sputtering, a vanadium film is normally formed and then oxidised into $\text{VO}_2(\text{VO}_2(\text{M1}))$ through an oxidation process at 400°C or above [174]. This temperature is high for integration with CMOS devices and polyimide substrates. ALD deposition can be at a low temperature of 150°C , but the as-deposited film is amorphous and lacks the phase transition capability. A post-deposition anneal is therefore required to crystallise amorphous VO_2 into $\text{VO}_2(\text{M1})$ [187, 194].

This anneal also ensures the correct stoichiometry of VO₂ from various vanadium oxides. However, the post-deposition annealing temperature has not been well studied, with anneal temperatures varying between 400 and 700°C [29, 30, 146, 154, 187, 190-196, 233]. Like sputtering, this temperature is incompatible with the integration with CMOS devices [27] and flexible polyimide substrates (e.g. Kapton 350°C) [220]. To fully unlock the potential of VO₂ in photonic, electronic, and optoelectronic applications, a low-temperature VO₂ formation approach is therefore highly desirable. Recently, we have demonstrated W-doped VO₂ formation through a novel ALD process and a post-deposition anneal at a temperature of 400°C and the oxygen pressure of 1 Torr [154], but this anneal condition is still above those required for polyimide substrates and CMOS integration. In this work, we have investigated VO₂ post-deposition anneals at an increased oxygen partial pressure. Through annealing optimisation, we demonstrate that VO₂ can be formed with an excellent optical contrast at the thermal budget of 300°C. We have also identified that a lower anneal at 250°C results in no crystalline structure, indicating the existence of the lowest anneal condition to ensure VO₂ crystallisation. We further demonstrate the fabrication of VO₂ films on polyimide substrates that possess a high infrared emissivity contrast of 0.30.

3.2 Experimental Procedure

3.2.1 VO₂ growth through atomic layer deposition

A series of VO₂ thin films were grown on silicon substrates and polyimide (DuPont Kapton FPC). For the Si substrates, an SiO₂/Al initial stack was formed in a Bühler Helios reactive sputtering system before VO₂ deposition. For the polyimide substrates, a similar initial stack was provided by Consorzio CREO (Italy), including a 100 nm Al layer and then a 900 nm SiO₂ layer. Compared with other underlying layers, e.g. sapphire, SiO₂ was chosen for its more representative nature in CMOS integration and radiative cooling applications, as sapphire has a high cost and high-temperature budget for formation [92]. The VO₂/SiO₂/Al stack layer formed a Salisbury screen with a high and broad reflection contrast between VO₂ at high and low-temperature states. In addition, this reflective nature allows for easy optical characterisation without the need for transmission and can also be compared with VO₂ works in radiative cooling.

Figure 3.1 (a) shows the designed VO₂ thin film as a stack on a Si substrate. The stack is formed from top to bottom, a 60 nm VO₂, 1000 nm SiO₂, and 100 nm Al. Figure 3.1 (b) shows a cross-sectional SEM of an ALD-fabricated VO₂ film before any anneal. The thicknesses of the stack are measured to be 63, 996 and 108 nm for the VO₂, SiO₂ and Al layers, respectively, which are consistent with the design. Only the top three layers (i.e., VO₂, SiO₂ and Al) are optically functional in this work, as the incident light cannot penetrate the 100 nm thick Al layer.

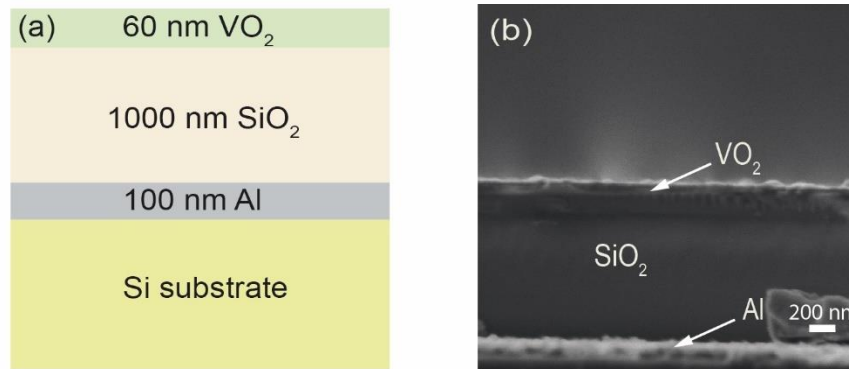


Figure 3.1. Stack diagram and SEM image of VO₂-Si thin film deposited using atomic layer deposition (ALD) (a) Stack of VO₂-Si thin film, the 60 nm VO₂ growth on the 1000 nm SiO₂ with 100 nm Aluminium underneath as an optical back-reflector. (b) cross-sectional SEM image of as-deposited VO₂ thin film in a stack of VO₂/SiO₂/Al.

For the VO₂ film growth, Tetrakis(ethylmethylamino)vanadium (IV) (TEMAV) was used as a vanadium precursor with a purity of 98 % from Strem Chemicals, alongside deionised (DI) water as the oxidiser. The ALD process was carried out in a Veeco Savannah S200 ALD system, with the reaction chamber stabilised at 200°C. The TEMAV precursor was heated to 85°C to ensure sufficient vapour pressure, and the carrier/purge nitrogen gas flow was set at 20 sccm. The ALD growth cycle consists of the four steps of TEMAV dose, TEMAV purge, water dose, and water purge, and the duration of each step is listed in Table 3.1. The VO₂ ALD process was developed and reported in our previous work [154]. The growth rate was measured to be 0.05 nm/cycle, and 1200 cycles were used for a VO₂ film thickness of about 60 nm.

Table 3.1. ALD Cycle Parameters for VO₂ Deposition.

Step Sequence	Duration (Sec)
---------------	----------------

TEMAV Dose	0.4
TEMAV Purge	9
H ₂ O Dose	0.03
H ₂ O Purge	12

3.2.2 Post-deposition anneal

In this work, the annealing process was conducted in an Oxford Instruments Agile NanoFab CVD system. This advanced system is equipped with oxygen flow, pressure control (up to 5 Torr), and lifted temperatures (up to 800°C), making it great for the investigation of various annealing conditions.

A total of 11 anneal conditions were set by varying oxygen partial pressure, annealing duration, and annealing temperature. The oxygen partial pressure was varied within a range of 1 to 2.5 Torr, which is the maximum pressure that the maximal 100 sccm O₂ can provide in this system. The anneal duration was set between 1 to 4 hours, increasing in increments of 1 hour. Lastly, the annealing temperature was set over a range from 250°C to 400°C, with adjustments made in 50°C steps.

3.2.3 Selection of annealing parameters

According to Section 2.2, oxygen partial pressure, annealing duration, and annealing temperature have been identified as the three primary factors influencing the annealing process. Theoretically, if each factor has four sub-conditions, a full factorial design ($4 \times 4 \times 4 = 64$) would be the ideal approach for systematically investigating the effects of annealing. However, due to constraints of research resources, conducting a comprehensive and systematic study presents challenges. Therefore, in this work, 12 representative conditions were selected from the three parameters. By fixing two factors and varying the third in the following three sections, we aim to isolate and analyse the impact of each variable on the annealing process.

As shown in Fig. 3.2, previous studies on VO₂ annealing based on ALD fabrication have already demonstrated a clear trend: lowering the annealing temperature inevitably requires an increased oxygen partial pressure to compensate. To date, the lowest annealing temperature reported for

ALD-based VO₂ is 400°C, with the highest oxygen partial pressure used being 1 Torr. Since further lowering the VO₂ fabrication temperature would necessitate a higher oxygen pressure, this work sets the starting oxygen partial pressure at 1 Torr, with a maximum of 2.5 Torr. This upper limit is determined by the mass flow controller (MFC) of the used annealing system's oxygen gas line, which is restricted to 100 sccm. With this 100 sccm O₂ flow rate, achieving a chamber pressure higher than 2.5 Torr would be challenging. Although additional gas flow (e.g., Ar) could increase the chamber pressure to 5 Torr, this would dilute the oxygen concentration. Since the oxygen partial pressure directly determines VO₂ oxidation and annealing, the actual oxygen partial pressure would still not exceed 2.5 Torr.

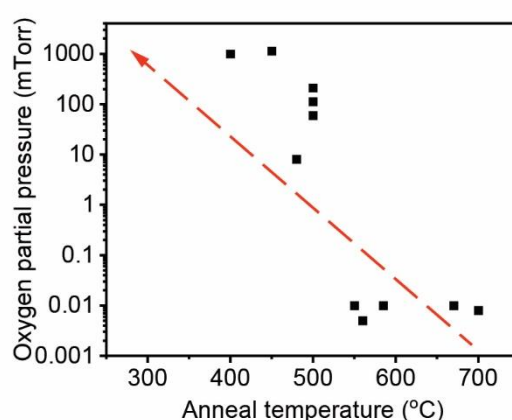


Figure 3.2. Potential trend between annealing temperature and oxygen partial pressure based on previous work. The red dashed arrow is intended to show the trend only.

3.2.4 Material characterisations

(a) Raman microscopy measurement

Raman spectroscopy measurements were conducted using the Renishaw inVia Laser Raman Spectrometer equipped with a 532 nm laser. A critical aspect of these measurements was the exposure power of the laser, which was set at 1 mW. This low-power setting was chosen to prevent the heating from triggering the VO₂ transition during the measurement, thereby avoiding any potential alteration in the film properties due to thermal effects. All samples were placed on the stage of the spectrometer and exposed to the air at room temperature. This setup ensured that the samples were in a stable environment, providing consistent and reliable measurement

conditions. A detailed discussion of the Raman scattering mechanisms and the characteristic Raman peaks of monoclinic VO₂ (M1) can be found in Section 2.3.1.

(b) X-ray photoelectron spectroscopy (XPS)

The VO₂ compositional data was collected using a Thermo Scientific Theta Probe X-ray photoelectron spectroscopy (XPS) system in vacuum, with a base pressure approximately equal to 5.0×10^{-8} Pa. Notably, no argon ion etch was performed on the samples immediately before measurements. This precaution was taken because such sputter can preferentially remove oxygen atoms from the target, which would subsequently affect the material's stoichiometry [234]. To mitigate surface charging effects caused by photoelectron emission, a flood gun was employed, with an incident X-ray spot size of about 400 μm when focused onto the sample's surface. The XPS measurement and subsequent data analysis were helped by my colleague Callum Wheeler. A general introduction to the principles of XPS and the relevance of vanadium oxidation states in VO_x systems can be found in Section 2.3.2, along with the VO_x phase diagram shown in Fig. 2.11.

Fitting procedure

All XPS data was analysed using Thermo Advantage (v5.9931) software. An extended binding energy spectral range (510 – 547 eV) was collected covering the O1s and V2p peaks simultaneously to ease analysis, as well as a survey for each sample to identify any unexpected materials if any were present. A ‘smart’ background was applied to all spectra and charge corrected to the dominant O1s peak at 530.0 eV, as a common practice for accurate fitting of the V2p peaks. All V2p spectra were fitted using the same constraints to provide consistency for compositional analysis.

The fitting of vanadium oxides from XPS spectra is a complex task as many stable VO_x compounds can coexist based on deposition and annealing conditions. Depending on the material stoichiometry, the spectra could be a convolution of many V2p ionisation energies, including V2p (5+, 4+...0). An example of the devolved XPS spectra for one typical sample is shown in Fig. 3.3. The spectra consist of two O1s peaks, the main peak at 530.0 eV for charge correction in addition to a secondary O1s shoulder centred around 530.8 (± 0.1) eV, assigned to hydroxyl (OH) bonds present on the sample due to surface contamination commonly seen in un-etched samples. The lower energy peaks can be fully described by devolving into two V2p doublets, V2p (5+) and V2p (4+), characteristic of V₂O₅ and VO₂, respectively. Certain mathematical relations must be

adhered to ensure the fitting remains physical. These include a peak separation of ≈ 7.20 eV and area ratio of 2:1 between the 3/2 and 1/2 angular momentum states. The Lorentz/Gaussian mix product was freely fitted for all peaks.

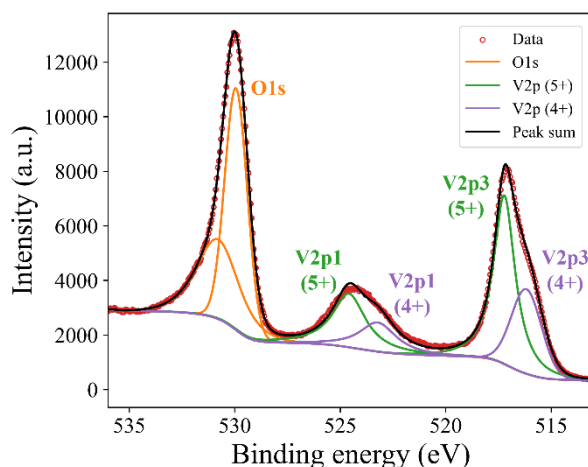


Figure 3.3. X-ray photoelectron spectroscopy (XPS) spectrum showing the intensity of emitted electrons as a function of binding energy (in eV). Data points (red circles) are fitted with peak curves corresponding to oxygen O1s and vanadium V2p states, with separate components for V2p in different oxidation states (V2p3 and V2p1 for 5+ and 4+ respectively). The sum of the fitted peaks is represented by the black line, demonstrating the deconvolution of spectral features attributed to different chemical states of the elements present

(c) Spectroscopic ellipsometry (SE) characterisation

The refractive index (n) and extinction coefficient (k) of the VO_2 samples were extracted through measurements using a Woollam M2000 spectroscopic ellipsometer over a wavelength range of 0.35 to 1.7 μm , with the measurement focused on the central region of the sample. The measurement setup was configured as described in Section 2.3.4. A detailed explanation of the oscillator models used to extract optical constants such as the Tauc–Lorentz, Drude, Lorentz, and Gaussian oscillators can also be found there. The incident angle was set to 65° . To determine the optical constants of the high-temperature phase, the sample was placed on a custom-built heating stage and heated to 90°C . A thermocouple was used to monitor the temperature, ensuring uniform heating across the sample. The sample was then held at this temperature for three minutes to reach thermal equilibrium before measurement.

The raw ellipsometry data (Ψ and Δ) were analysed using a three-layer model (Al, SiO₂, and VO₂). The dielectric function of VO₂ was extracted by fitting the measured spectroscopic ellipsometry (SE) data using the GenOsc framework in CompleteEASE software. This framework enables the simultaneous fitting of multiple oscillator models, including Drude, Lorentz, Gaussian, and Tauc-Lorentz oscillators, to accurately capture the optical response. The fitting process involved optimising oscillator parameters across multiple initial values to ensure the identification of a global minimum, thereby achieving the most accurate results.

In line with previous studies on similar multilayer stacks, different oscillator models were selected to characterise VO₂ in both insulating and metallic phases [91, 210, 235]: In the insulating phase, VO₂ behaves as a bandgap semiconductor, requiring the Tauc-Lorentz oscillator to describe interband electronic transitions. This model includes a bandgap energy parameter (E_g), which represents the minimum energy required for electron excitation from the valence band to the conduction band. In the metallic phase, due to the presence of free carriers, the Drude oscillator was introduced to model low-frequency optical absorption, which is characteristic of metals. The Lorentz oscillator was applied in both phases within the mid-to-high frequency range to capture bound electron resonance. The Gaussian oscillator was used in the insulating phase to describe localised absorption features or broad absorption peaks, while in the metallic phase, it primarily accounted for high-frequency localised absorption.

During the fitting process, key oscillator parameters included: 1. Amplitude (Amp): Represents oscillator strength, related to absorption intensity. 2. Broadening (B_i): Defines the full width at half maximum (FWHM), describing the spectral width of the absorption peak. 3. Center energy (E_n): Corresponds to the resonance energy, determining the peak absorption position. 4. Bandgap energy (E_g): Specific to the Tauc-Lorentz model, representing the minimum energy required for interband transitions.

Figure 3.4 presents the experimental refractive index (n) (Fig. 3.4(a)) and extinction coefficient (k) (Fig. 3.4(b)) of a 60 nm-thick VO₂ film in both insulating and metallic states. The results are compared with previously reported typical values for VO₂ films of similar thickness [236, 237]. The overall agreement between the ALD-deposited VO₂ in this study and prior representative works demonstrates a high consistency in refractive index behaviour.

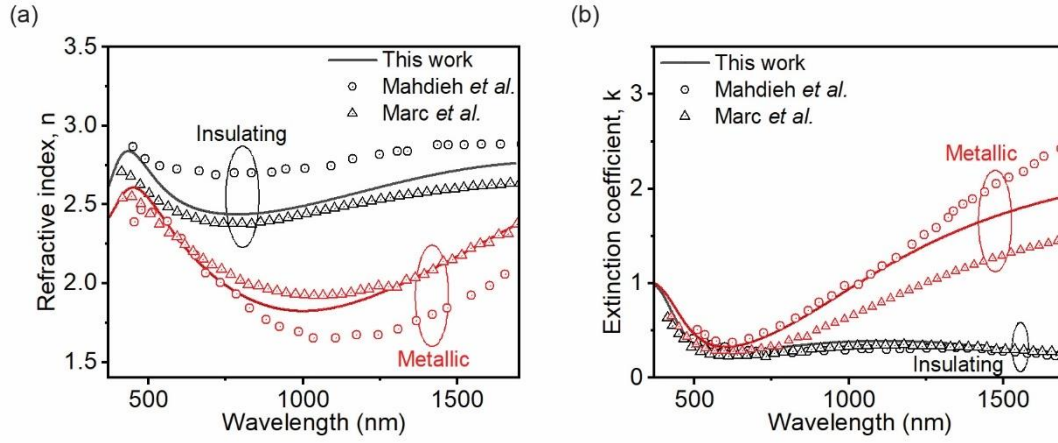


Figure 3.4. (a) Real and (b) imaginary parts of VO₂ refractive index in insulating and metallic phases compared with the literature value. The red and black solid lines represent the experimental measurements in this thesis.

(d) X-ray diffraction (XRD)

X-ray diffraction measurements were conducted at room temperature under grazing-incidence geometry using a Rigaku SmartLab thin-film diffractometer. The length-limiting slit was set to 2 mm. Data were collected over a 2θ range from 10° to 90° with a step size of 0.01° and a scanning speed of 5.0. Due to the budget limitation, only two samples can be measured among the fabricated samples. All measurements and subsequent data analysis were performed by my colleague, Bohao Ding.

3.2.5 Optical characterisations

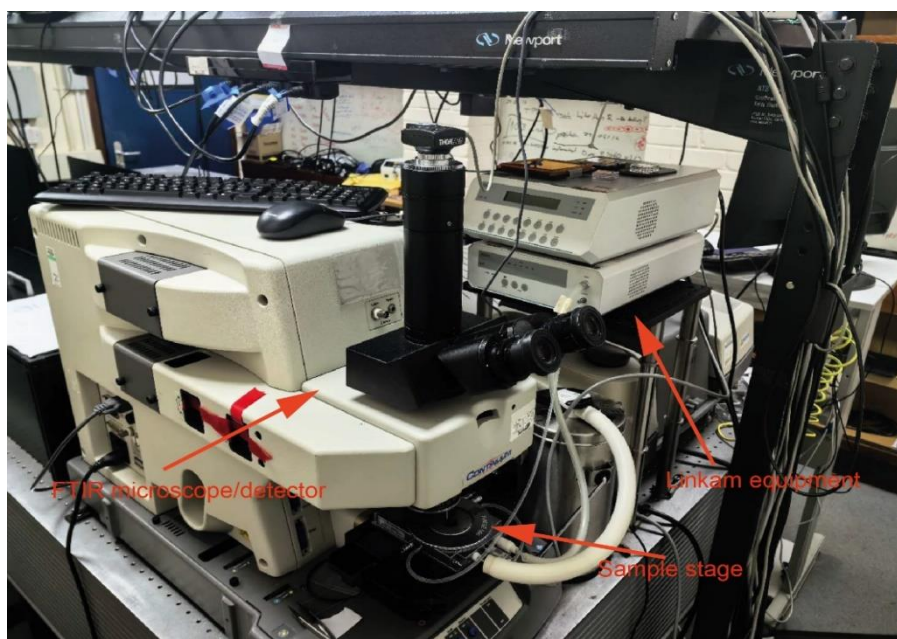


Figure 3.5. Picture of the Thermo-Nicolet Nexus 670 FTIR system with a Linkam THMS 600 heating/cooling stage.

The annealed VO₂ films were optically characterised using a Fourier transform infrared microscopy (FTIR) system (Thermo-Nicolet Nexus 670 with a continuum microscope) as shown in Fig. 3.5. To accurately measure the infrared spectrum, noise from surrounding sources of blackbody radiation must be eliminated. To reduce these, liquid nitrogen with a temperature of ≈ 63 K is used to stabilise the detector. A general introduction to FTIR spectroscopy, its measurement principles, the selection of the beam splitter can be found in Section 2.3.3. The measurements were taken using a $\times 15$ optical objective and an MCT-A detector, and with a measurement area of $100 \times 100 \mu\text{m}^2$. The experiment used a KBr beam splitter and an IR source. The reflection was normalised using a gold mirror as a reference. The VO₂ sample temperature was regulated by placing the sample on a Linkam THMS 600 stage equipped with a cap with a ZnSe window. Due to the ZnSe infrared transmission windows, the setup has a reflection measurement range from 1.6 to 18 μm . The temperature sweep was conducted by first heating up and then cooling down. The measurement was performed 1 minute after the temperature stabilisation for each set temperature.

Infrared emissivity has been chosen as the parameter for evaluating the infrared optical contrast of the VO₂ films. This choice follows our recent work [154], where we have shown

that this parameter is an effective benchmark in assessing the film quality for thermal management. Based on Kirchhoff's law, the spectral emissivity is equal to its spectral absorptance when at thermal equilibrium conditions. For an IR opaque reflector without transmission, the emissivity, $\varepsilon(\lambda)$, can be described using the relation: $\varepsilon(\lambda) = 1 - R(\lambda)$, where $R(\lambda)$ is the reflectivity at wavelength λ . The infrared emissivity (shortened as emissivity in the following discussions) is calculated by integrating absorption over a range of wavelengths, weighted by the theoretical blackbody spectrum at a given operating temperature (T) in Kelvin. This is mathematically represented as [238]:

$$\varepsilon = \frac{\int (1 - R(\lambda))B(\lambda, T)d\lambda}{\int B(\lambda, T)d\lambda} \quad (5.1)$$

where $B(\lambda, T)$ denotes the blackbody spectral distribution at the absolute temperature T . The integration range is defined by the measurable range of the FTIR system, which spans from 1.6 to 18 μm . The emissivity contrast ($\Delta\varepsilon$) is defined as the difference between the emissivity of VO_2 in its high-temperature state and its low-temperature state.

Figure 3.6 (a) shows the temperature-dependent IR emissivity as a function of temperature for a VO_2 sample at heating and cooling, noted in red and black, respectively. The emissivity increases sharply at the temperature of around 70°C for heating and decreases temperature at around 60°C for cooling, leaving a hysteresis. The temperatures are referred to as transition temperatures. To accurately extract these transition temperatures, emissivity from Fig. 3.6(a) is derived against T and then given a Lorentz-fitting as shown in Fig. 3.6(b). The peaks are defined as the phase transition temperature during heating (T_h) and cooling (T_c) and the hysteresis width is defined by the temperature distance between these two peaks.

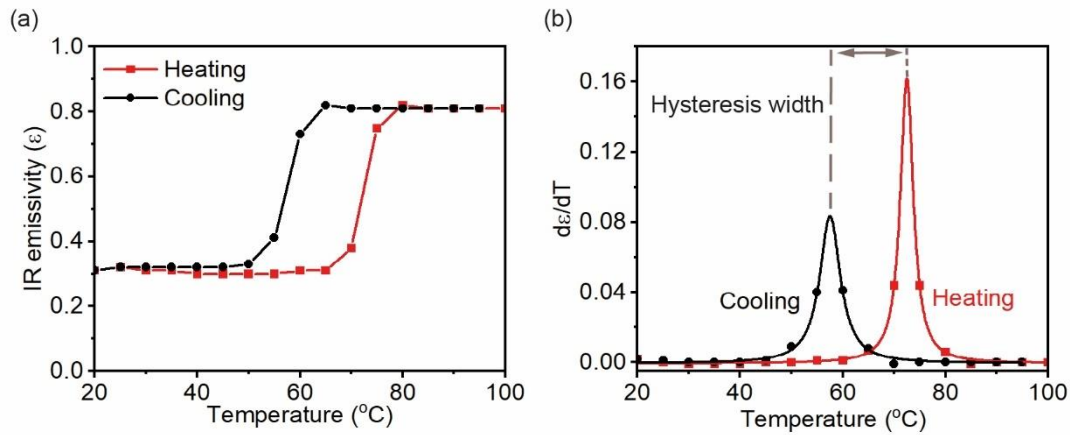


Figure 3.6. Hysteresis in the VO₂ Phase Transition. (a) Infrared (IR) emissivity (ϵ) as a function of temperature, during heating (red line) and cooling (black line). (b) The differential of emissivity (ϵ) as a function of $T (d\epsilon/dT)$ with the hysteresis width plotted by dashed lines.

3.2.6 Scanning electron microscopy measurement

The scanning electron microscopy (SEM) measurements were conducted with the assistance of my colleague, Jianzhi Huang. The measurements were performed utilising the NVision 40 FIB as an SEM with an electron acceleration voltage of 2 kV. To avoid electron charging and thus obtain optimal imaging clarity, all samples were coated with E-spacer.

3.3 Results and discussion

3.3.1 VO₂ film morphology before annealing

Figure 3.7 (a) shows a top view of an unannealed as deposited VO₂ film. No clear crystalline grain can be identified but large defects are present. It is worth noting that no defect was found on VO₂ directly grown on SiO₂-coated Si substrate as shown in Fig. 3.7 (b). The absence of visible defects in Fig. 3.7 (b) refers specifically to the lack of observable ‘black dots’. We might attribute these defects to the non-smooth surface due to the Al underlying layer.

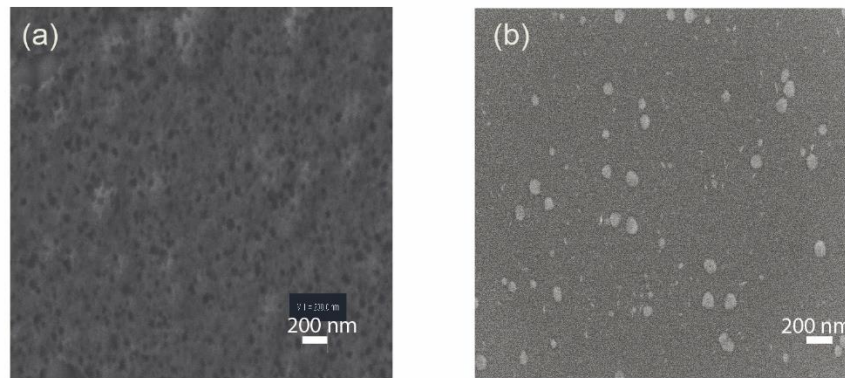


Figure 3.7. Top-view SEM images of ALD deposited unannealed VO₂-Si films on (a) Al and (b) directly on SiO₂. The scale bar is 200 nm.

3.3.2 Effect of oxygen partial pressure on VO₂ anneal

Figure 3.8 presents the FTIR reflection spectra (measured from 20°C to 100°C) of VO₂ samples annealed at 400°C for 2 hours under different oxygen partial pressures. The measurement

temperatures of 20°C and 100°C were chosen to ensure that VO₂ can fully cover both the dielectric phase and metallic phase, as these temperatures lie sufficiently below and above its known phase transition temperature (~68°C).

By calculating the mean difference in reflectance across the full measurement wavelength range (1.6 to 18 µm) at 20°C and 100°C, it is found that at an oxygen partial pressure of 1 Torr (Fig. 3.8(a)), the average reflectance difference is 39.8 %, accompanied by a redshift of the reflectance valley from 10.2 µm to 10.7 µm. This infrared reflectance contrast is attributed to the phase transition of VO₂ between its dielectric and metallic states. When O₂ pressure increases to 1.5 Torr, the average reflectance difference rises from 39.8 % to 47.7 %, indicating a more pronounced IR contrast; the reflectance minimum still shifts from 10.2 µm to 10.7 µm (Fig. 3.8 (b)). Further increasing oxygen pressure to 2 Torr slightly reduces the average reflectance contrast to 46.8 %, while the same redshift of the reflectance minimum persists (Fig. 3.8 (c)). Compared to the $\Delta R = 47.7$ % observed at 1.5 Torr, the decrease in ΔR at 2 Torr suggests that the oxygen partial pressure may approach a saturation point. When oxygen pressure is further increased to 2.5 Torr, the average reflectance difference sharply drops to 0.2 %, and no additional redshift of the reflectance minimum near 10.5 µm is observed (Fig. 3.8 (d)). This behaviour likely arises from excessive oxidation at higher oxygen partial pressure, leading to the formation of V₂O₅, which will be investigated in more detail using Raman spectroscopy.

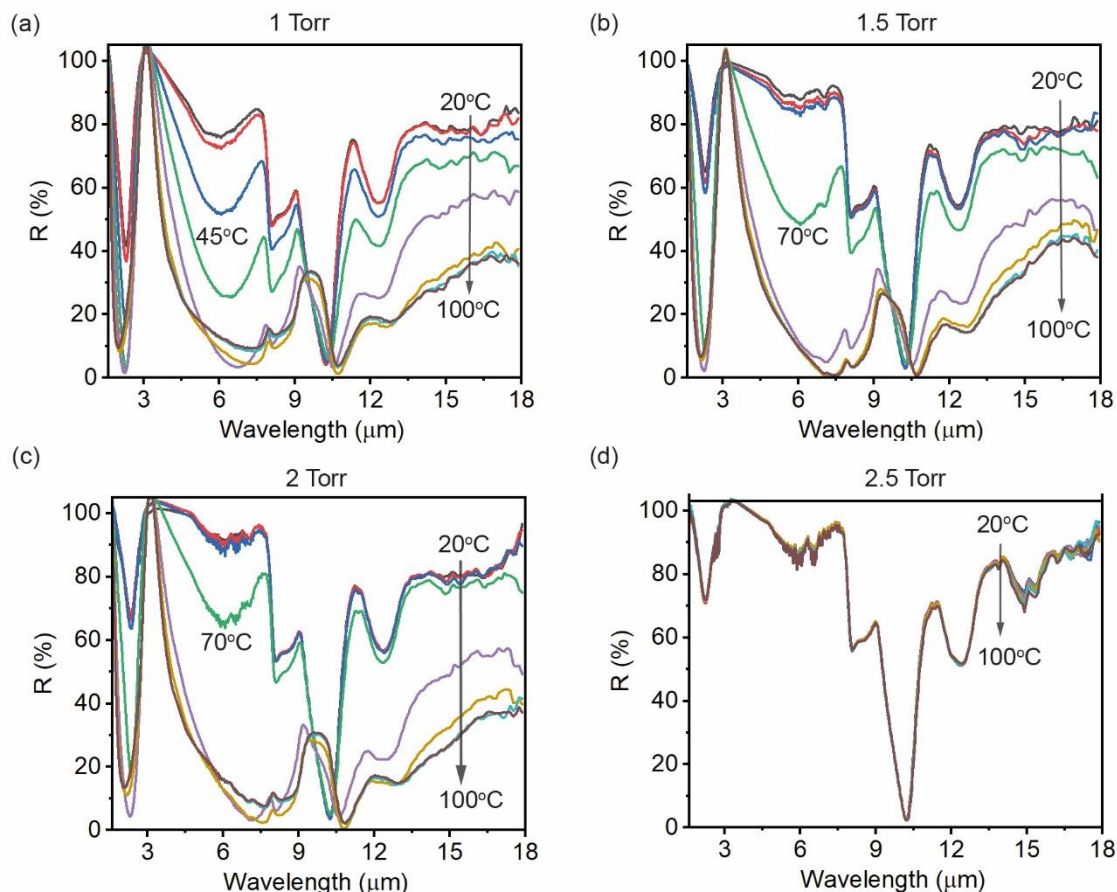


Figure 3.8. FTIR reflection spectra of the VO₂ thin films between the insulating phase (20°C) and the metallic phase (100°C) after annealing at the oxygen partial pressure of (a) 1 Torr, (b) 1.5 Torr, (c) 2 Torr and (d) 2.5 Torr.

By analysing the temperature-dependent infrared spectra, the emissivity can be determined. Specifically, the emissivity is calculated by averaging the absorption weighted by the theoretical blackbody spectrum at a given temperature. Details on the emissivity calculation method are provided in Section 3.2.4. Figure 3.7 presents the infrared emissivity hysteresis curves obtained under different annealing oxygen partial pressures. In these measurements, the sample temperature was first raised from 20°C to 100°C, then lowered back to 20°C in steps of 5°C (excluding the very end at low temperature).

Under an oxygen partial pressure of 1 Torr (Fig. 3.7 (a)), the transition temperatures during heating and cooling are 45°C (T_h) and 35°C (T_c), respectively. This yields an emissivity contrast ($\Delta\epsilon$) of 0.44 and a hysteresis width of 10 °C. At higher oxygen partial pressure (Fig. 3.7 (b)), the heating and cooling transition temperatures increase to 72°C (T_h) and 54°C (T_c), respectively, raising the

emissivity contrast ($\Delta\epsilon$) to 0.48 and widening the hysteresis to 18°C. When the oxygen partial pressure is further increased to 2 Torr (Fig. 3.7 (c)), the transition temperatures rise to 73°C (heating) and 58°C (cooling), with an emissivity contrast ($\Delta\epsilon$) of 0.50. However, the hysteresis width narrows to 15°C. Under 2.5 Torr of oxygen (Fig. 3.7 (d)), no apparent hysteresis is observed. Thus, before the contrast fully disappears, increasing the oxygen partial pressure leads to higher transition temperatures and increased emissivity. The behaviour at 1.5 and 2 Torr suggests a similar trend, implying that 1 Torr is insufficient for proper annealing, whereas 2.5 Torr results in over-oxidation. Meanwhile, no obvious trend is observed in the hysteresis width. It is worth noting that even though “68°C” is commonly cited as the transition temperature of VO₂, in practice, this transition temperature depends strongly on annealing conditions.

Furthermore, at an annealing temperature of 400°C, the slight increase in emissivity contrast when raising the oxygen partial pressure from 1.5 Torr to 2 Torr, followed by a decrease when going from 2 Torr to 2.5 Torr, indicates that at least 2 Torr is required to maximise the emissivity contrast under these conditions. From Fig. 3.5, we also see that lowering the annealing temperature demands a higher oxygen partial pressure. Consequently, using an annealing temperature below 400°C likely requires exceeding 2 Torr of oxygen partial pressure. This finding provides important guidance for the work described in the subsequent section.

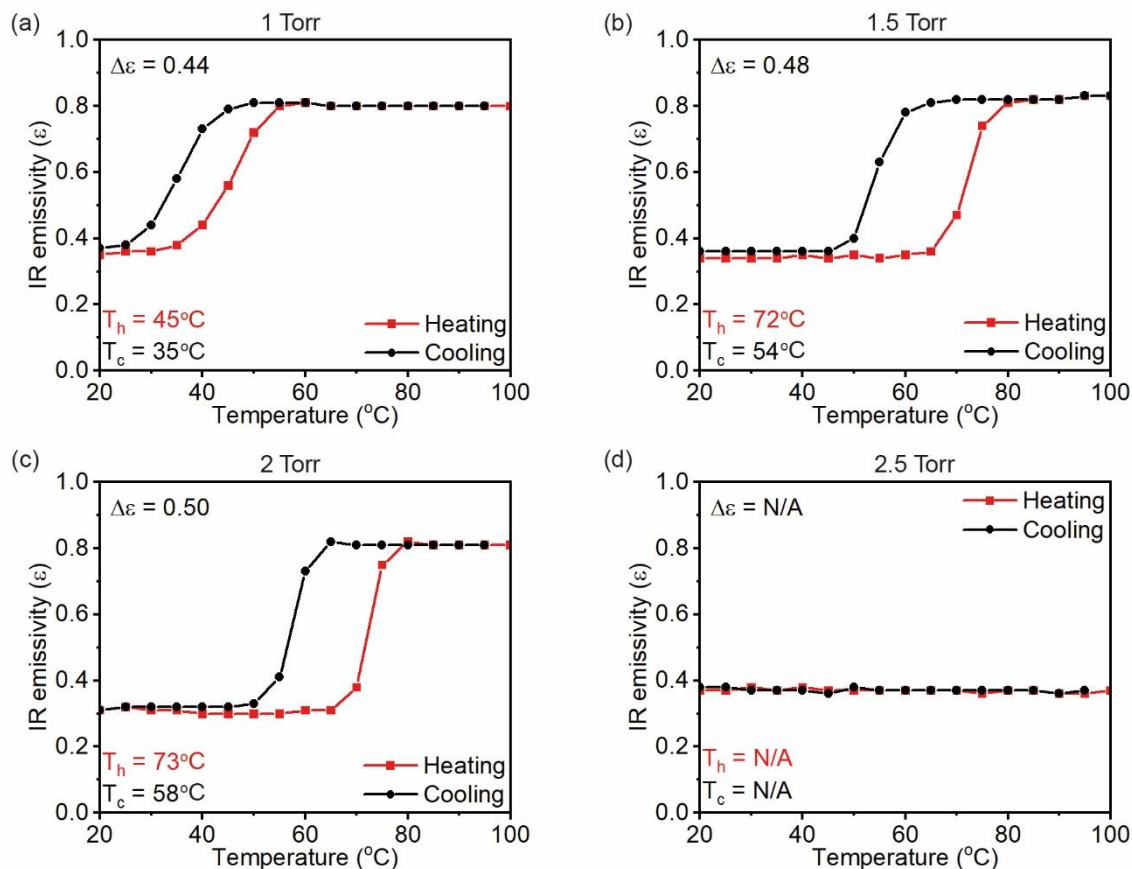


Figure 3.7. Full IR emissivity hysteresis curves (5°C step temperature for both heating and cooling) after the 1 Torr (a), 1.5 Torr (b), 2 Torr (c) and 2.5 Torr (d) oxygen pressure.

The room-temperature Raman spectroscopy was performed to investigate the sample composition and the quality of the films, as shown in Fig. 3.8. All of the peaks observed in Fig. 3.8 for each sample can be matched to the reference data reported in Table 3.2, and a comprehensive VO_x Raman table is provided in Appendix H. It is worth noting that although there are many known VO_x phases besides VO_2 and V_2O_5 , no peaks corresponding to other VO_x phases were observed in the samples prepared under these four annealing conditions.

It is clear to see that Raman spectra for 1, 1.5 and 2 Torr are consistent with known VO_2 showing peaks at 194 cm^{-1} , 224 cm^{-1} and 614 cm^{-1} . Here, 194 cm^{-1} and 224 cm^{-1} correspond to Ag peaks of the V-V vibrations and 614 cm^{-1} corresponds to the V-O Ag vibrational peak. These peaks are accompanied by other minor features consistent with the insulating monoclinic phase of VO_2 . Contrastingly, when the sample is annealed at 2.5 Torr oxygen partial pressure, the main VO_2 peaks become less pronounced and shift to 146 cm^{-1} , 285 cm^{-1} , and 996 cm^{-1} , indicating a

transition towards the pentoxide form, V_2O_5 . Therefore, Raman spectra confirm that VO_2 (M1) is formed with oxygen partial pressures 1, 1.5 and 2 Torr and further oxygen pressure leads to the formation of V_2O_5 and thus the loss of phase transition around 70°C.

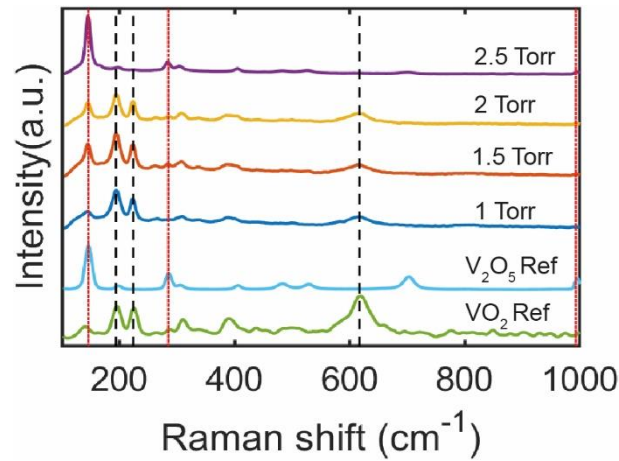


Figure. 3.8. Room temperature measured Raman spectra of VO_2 on Si substrate with 1 mW output power under different oxygen partial pressure, the black dash lines located at 194 cm^{-1} , 224 cm^{-1} and 612 cm^{-1} represent the highest intensity of VO_2 (M1) Raman scattering peak, the red dot lines located at 146 cm^{-1} , 285 cm^{-1} and 996 cm^{-1} represent the highest intensity of V_2O_5 Raman scattering peak.

Table 3.2. Comparison of the Raman peak positions identified in this work with the literature.

Material	Raman shift in this work (cm^{-1})	Raman shift from literature (cm^{-1})	Reference
$\alpha\text{-}V_2O_5$	145	143–147	[239, 240]
VO_2 (M1)	194	194–195	[239, 241]
VO_2 (M1)	224	223–224	[239, 241]
VO_2 (M1)	260	261	[241]
$\alpha\text{-}V_2O_5$	285	284–285	[239, 240]
$\alpha\text{-}V_2O_5$	304	305	[239, 240]
VO_2 (M1)	390	391	[241]
$\alpha\text{-}V_2O_5$	404	404–406	[239, 240]
$\alpha\text{-}V_2O_5$	530	528–531	[240]
VO_2 (M1)	612	612–613	[239, 241, 242]
$\alpha\text{-}V_2O_5$	992	992	[239]

The full XPS binding energy spectra for these samples are presented in Fig. 3.9. All spectra were fitted using the same procedure to ensure compositional analysis is comparable between samples, with all samples charge corrected to the well-defined O1s peak at 530.0 eV [243]. For 1 Torr oxygen anneal (Fig. 3.9(a)), clear V^{4+} doublet peaks can be identified at 516.0 eV and 523.0 eV. The V^{5+} peaks are also identified at 517.4 eV and 524.5 eV. For 1.5 Torr oxygen anneal (Fig. 3.9(b)), similar spectra are seen for V^{4+} and V^{5+} existence, but the V^{5+} peak is larger. A similar trend is also seen for 2 Torr oxygen anneal in Fig. 3.9(c). With further oxygen increase, V^{5+} becomes more dominant, indicating a larger formation of V_2O_5 .

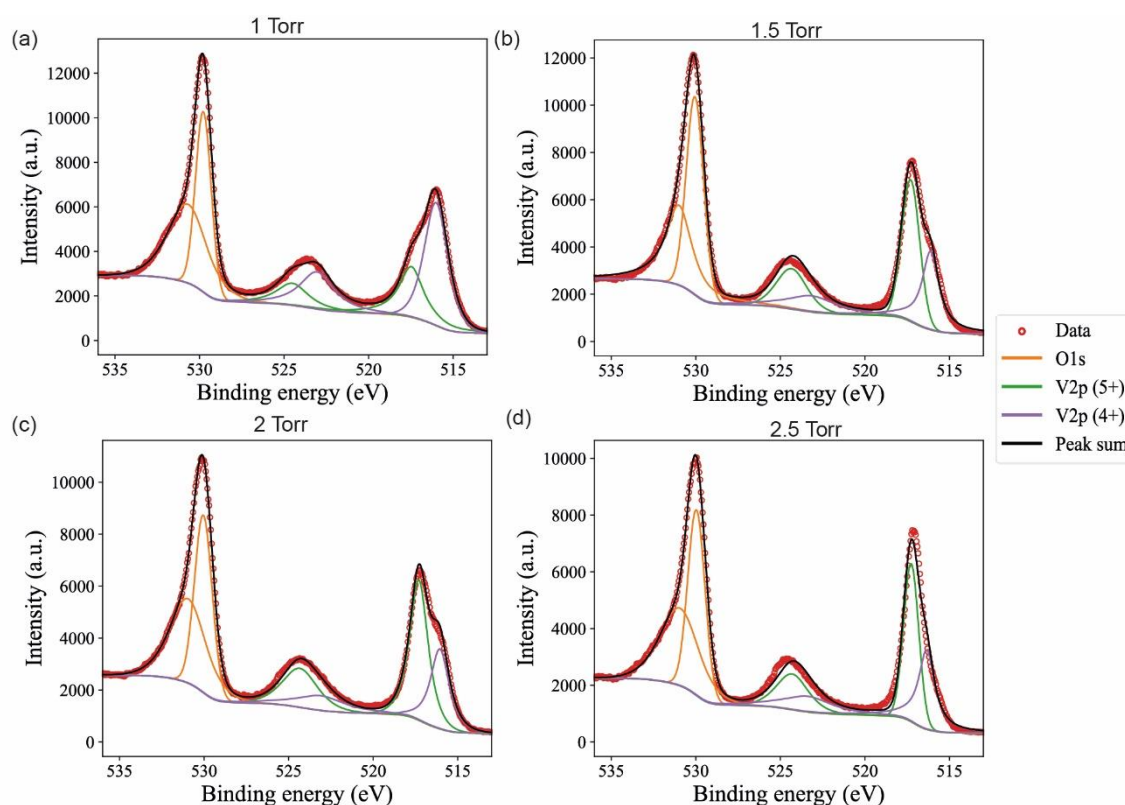


Figure 3.9. The XPS binding energy spectra covering the O1s and V2p energy ranges for samples annealed at 400°C for 2 hours at varying chamber pressures: (a) 1 Torr, (b) 1.5 Torr, (c) 2 Torr and (d) 2.5 Torr.

Since no other vanadium state had been identified in Fig. 3.9 (e.g., V^{3+}), it is possible to calculate the composition at. % of V^{4+} to V^{5+} and presented in Table 3.3. Since no other VO_x components have been read in the Raman spectrum in Fig. 3.8, the 5+ here is likely to come from V_2O_5 , while the 4+ vanadium is likely to come from VO_2 . By increasing the chamber pressure during annealing, the relative V_2O_5 composition also increases. This indicates that the samples are over-oxidising from the desired VO_2 into higher oxidation VO_x compounds with increasing pressure.

Table 3.3. Variations in atomic percentages of V^{4+} over $(V^{4+} + V^{5+})$ under different annealing pressures.

Vanadium state	Atomic percentage (%)			
	1 Torr	1.5 Torr	2 Torr	2.5 Torr
V^{4+}	64.5	43.6	46.0	39.6
V^{5+}	35.5	56.4	54.0	60.4

The complex refractive index of VO_2 thin films grown on Si substrates was measured using a spectroscopic ellipsometer at both room temperature (solid lines) and 90°C (dashed lines), as shown in Fig. 3.10. The results indicate that for samples annealed at 1 Torr (black), 1.5 Torr (red) and 2 Torr (blue), a clear phase transition was observed before and after heating. Furthermore, these three annealing conditions exhibited highly similar optical properties, suggesting that within the VO_2 formation temperature window, slight increases or decreases in annealing oxygen pressure do not significantly affect the refractive index of the samples.

Upon heating, at lower frequency, the increase in free electrons results in a reduction in the real part of the refractive index (n). Regarding the extinction coefficient (k), in the insulating phase, k approaches zero in the near-infrared (NIR) region. However, in the high-temperature metallic phase, the contribution of free carriers to the dielectric function primarily affects the infrared optical response, causing k to increase significantly with wavelength. This behaviour is typically modelled using the Drude term, which accounts for free electron absorption.

Previous studies on bulk and thin-film VO_2 have reported that Drude effects become noticeable at wavelengths starting around 800–900 nm [244, 245]. As the wavelength increases further into the infrared region, this contribution becomes more pronounced. Specifically, at the telecommunication wavelength of 1550 nm, the change in k before and after the phase transition was 1.54 for the 1 Torr annealed sample and decreased to 1.44 for the 1.5 Torr sample and 1.36 for the 2 Torr sample. Further increasing the O_2 pressure to 2.5 Torr can barely see the change

(0.08). This observation is self-consistent with the other characterisation results performed previously.

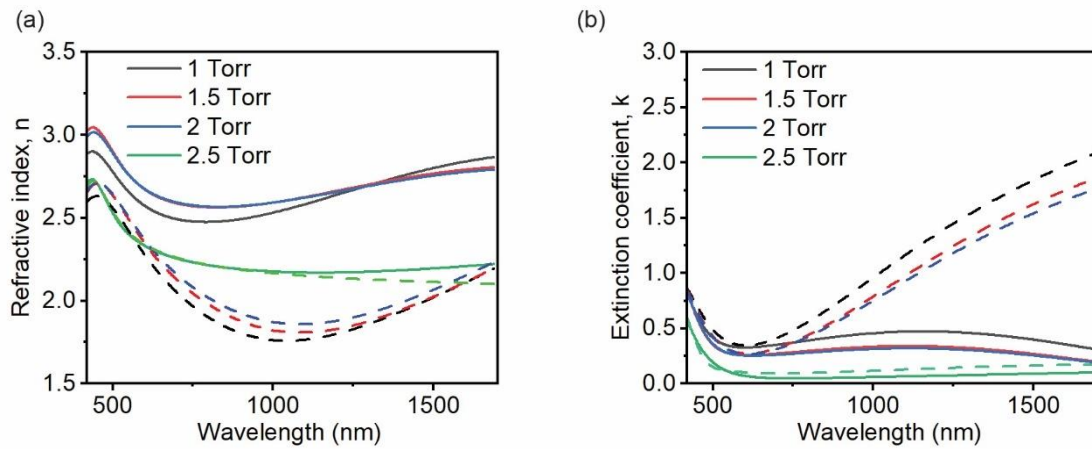


Figure 3.10. (a) Refractive index and (b) extinction coefficient at different oxygen pressures. The dotted line is measured at 90°C, and the solid line is measured at room temperature.

3.3.3 Effect of annealing temperature on VO₂ thin film

Following the investigation of the effects of oxygen partial pressures on the phase transition behaviour and optical properties of VO₂ films in the previous section, this section shifts toward the impact of annealing temperatures, which is also our main focus in this chapter. This section explores how annealing temperature influences the material characteristics of VO₂ thin films under a constant oxygen pressure of 2.5 Torr for 3 hours.

Figure 3.11 shows infrared reflection spectra of the annealed samples measured at temperatures from 20°C to 100°C. For the sample annealed at 250°C, no reflection change can be identified with the temperature change (Fig. 3.11(a)). The reflection is consistently above 90 % with several dips between 7 and 14 μm , which are attributed to SiO₂ absorption as seen in our previous work [246]. The lack of temperature response is consistent with the absence of VO₂ Raman peaks (Fig. 3.13, shown later), indicating that the 250°C anneal is insufficient for film crystallisation. At a higher annealing temperature of 300°C (Fig. 3.11(b)), the reflection decreases considerably with increasing temperature, showing the film transitioning from dielectric to metallic. This significant reflection change is consistent with the VO₂ composition verified by Raman and XPS, which will be presented later. It is also worth pointing out that the reflection dips at 10 μm redshifts at a

higher temperature, indicating its correlation with metallic VO₂ [247]. We can therefore confirm that the VO₂ film with phase transition capability is achieved through the 300°C anneal. At 350°C anneal (Fig. 3.11(c)), a similar trend is seen that the reflection decreases significantly over a broad spectrum as the temperature increases, confirming that a high-quality VO₂ film is formed. For the 400°C anneal, some reflectance reductions are seen with the temperature increase at approximately 2 μm and around 6 μm, indicating that minimum phase-transition (Fig. 3.11(d)) typical of V₂O₅, which has no phase transition at this temperature range.

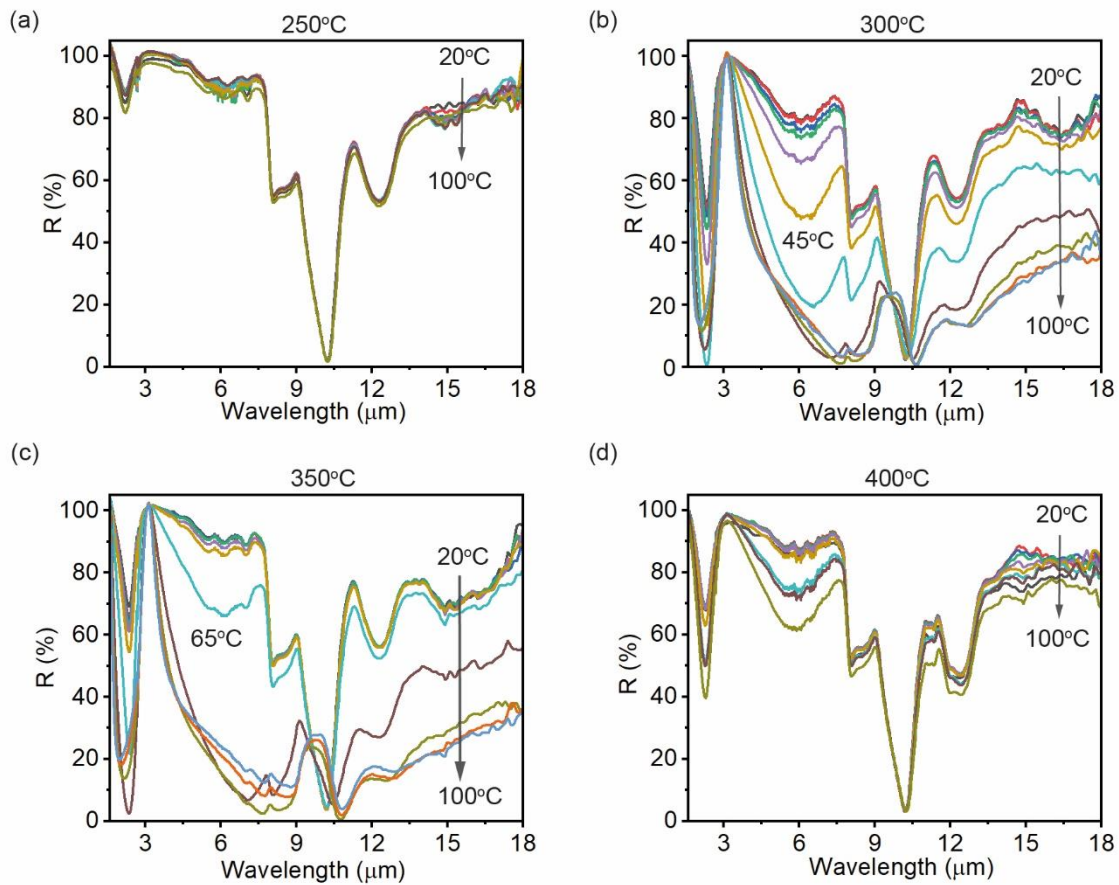


Figure 3.11. Reflection spectra of the VO₂ stacks annealed at (a) 250°C, (b) 300°C, (c) 350°C and (d) 400°C.

To further visualise the phase transition of the two anneals at 300°C and 350°C, IR emissivity hysteresis is calculated and presented against the measurement temperature in Fig. 3.12. At a relatively low annealing temperature of 250°C, the hysteresis appears indistinct, likely due to the absence of crystallinity in the sample (Fig. 3.12 (a)). For the 300°C VO₂ sample, the transition temperatures (T_h and T_c) are extracted to be 50°C and 38°C, respectively, and an IR emissivity contrast of 0.47. The 350°C VO₂ sample has transition temperatures (T_h and T_c) of 68°C and 53°C

for the heating and cooling cycles, respectively, and an IR emissivity contrast of 0.46. Here, we can see both anneals provide high-quality VO₂ with a consistent and excellent emissivity contrast, well agreeing with VO₂ films from higher thermal budgets in our previous works. Here, we also identify some variations in phase transition temperatures and this variation is also found for VO₂ reported in the literature. One possible cause could be the strain induced by the composition of different VO_x phases, which in turn affects the crystalline transition between VO₂(M1) and VO₂(R). Further XRD investigations will be performed later. Upon further increasing the annealing temperature to 400°C, the sample becomes over-oxidized, and as a result, the hysteresis behavior is nearly extinguished (Fig. 3.12 (d)).

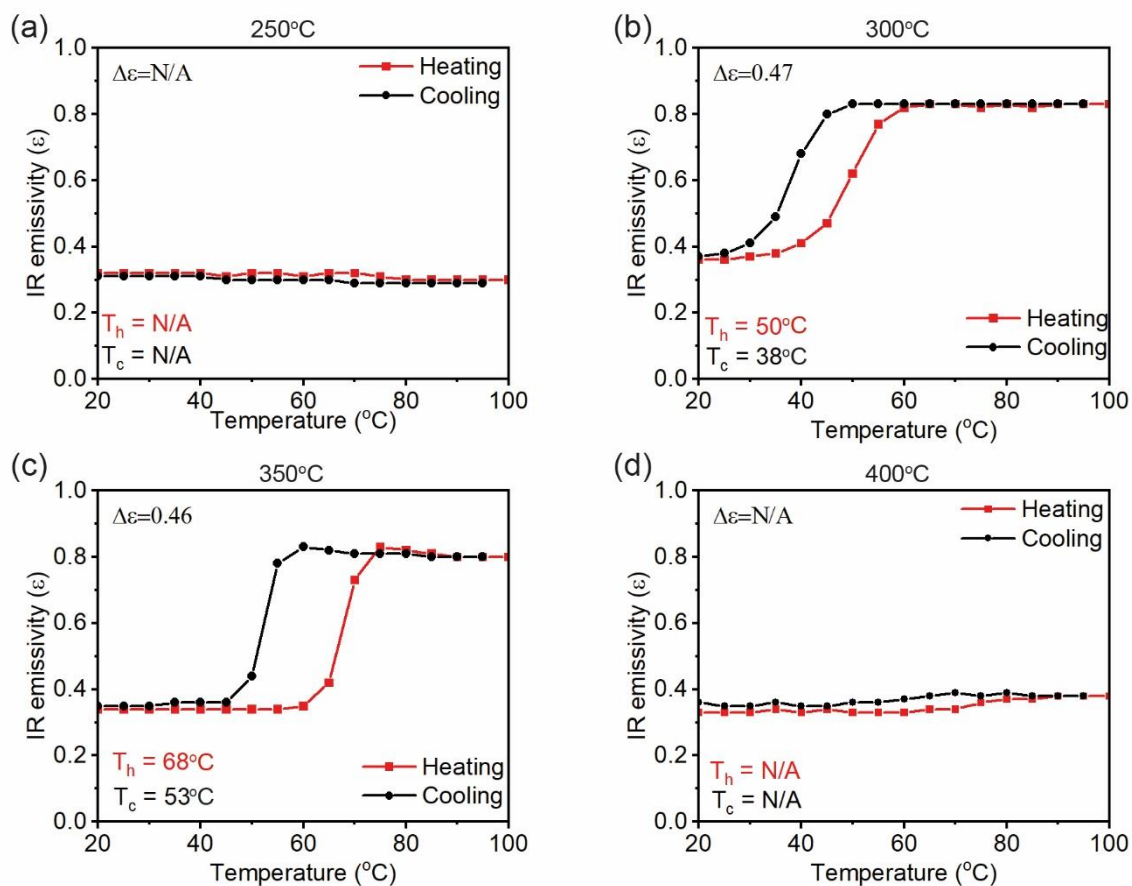


Figure 3.12. Full IR emissivity hysteresis curves (5 $^{\circ}\text{C}$ step temperature for both heating and cooling) after the 250 $^{\circ}\text{C}$ (a), 300 $^{\circ}\text{C}$ (b), 350 $^{\circ}\text{C}$ (c) and 400 $^{\circ}\text{C}$ (d) annealing temperatures treatment.

To further investigate the crystallinity of the annealed samples, Raman spectroscopy was performed at room temperature and the spectra are presented in Fig. 3.13 for VO₂ films annealed at different temperatures, together with an unannealed VO₂ film. Two spectra of VO₂ from previous work [148] and V₂O₅ from a sputter target are also presented as references. For the

unannealed VO₂ film, no Raman peak can be identified which indicates, consistent with the literature, that the film is amorphous. For the anneal at 250°C (the purple line), is similar to the unannealed film in that no Raman peak can be identified except for that around 490 cm⁻¹ (SiO₂) [248], indicating that the film remains amorphous and 250°C is not sufficient for the film crystallisation. At a higher annealing temperature of 300°C (the yellow line), several peaks can be clearly identified, including the characteristic A_g peaks of the V–V vibrations at 194 cm⁻¹ and 224 cm⁻¹, along with the V–O A_g vibrational peak at 614 cm⁻¹. These peaks reveal the monoclinic phase of VO₂, indicating that the anneal condition forms VO₂ (M1). At 350°C, Raman peaks are similar to those at 300°C, indicating that a similar VO₂ (M1) film is formed at this temperature. For the sample annealed at 400°C, the main peaks are at 146 cm⁻¹, 285 cm⁻¹, and 996 cm⁻¹, which correspond to the V₂O₅ reference. There are also minor peaks at 194 cm⁻¹ and 224 cm⁻¹. These indicate the 400°C anneal predominantly forms crystalline V₂O₅ through an overoxidation from the amorphous VO₂, with little presence of VO₂. The smaller peak at 166 cm⁻¹ and another three peaks at 840 cm⁻¹, 880 cm⁻¹ and 930 cm⁻¹ are attributed to the characteristic peak of V⁴⁺/V⁵⁺ mixed valence states [249], and V₃O₇, respectively. Therefore, Raman spectra clearly show that annealing at 350°C and 300°C results in the phase-change material VO₂ (M1). An anneal of 400°C is too high and results in V₂O₅, and an annealing temperature of 250°C is too low for crystallisation.

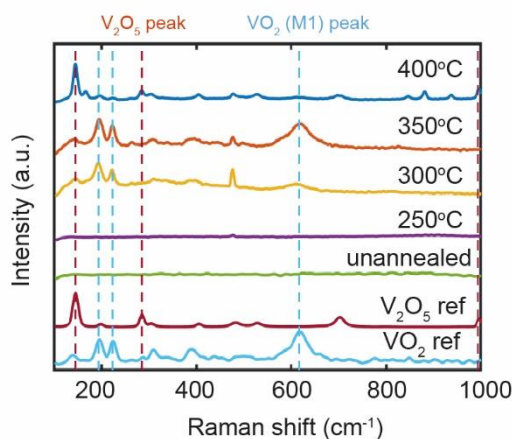


Figure 3.13. Raman spectra of VO₂ thin films formed on Si substrates after anneals at different temperatures as well as one as-deposited (unannealed).

The quality of the films was further characterised using X-ray photoelectron spectroscopy (XPS). Figure 3.14 shows XPS spectra of (a) unannealed sample and samples annealed at (b) 250°C, (c) 300°C, (d) 350°C, and (e) 400°C. The spectra feature prominent peaks corresponding to oxygen O1s and vanadium V2p orbitals. For each temperature, the spectra are deconvoluted into component peaks representing different oxidation states of vanadium (green and purple lines for

5+ and 4+ states, respectively). The black line in each plot represents the sum of fitted peaks, indicating the combined contribution of each state to the overall spectrum. For all annealing temperatures, both V^{4+} and V^{5+} appear as two sets of doublet peaks at approximately 516.0 eV, 523.0 eV and 517.0 eV, 524.3 eV, respectively [250]. For the unannealed film, it shows the presence of both V^{4+} and V^{5+} peaks with similar area contributions of both peaks. The 250°C annealed film shows an increased peak height of V^{5+} over V^{4+} in peak, indicating oxidation at the surface of the film from the anneal. At a higher annealing temperature of 300°C both V^{4+} and V^{5+} peaks present with roughly equal area size, indicating an increase of VO_2 composition. Compared with the VO_2 dominance seen in the Raman spectra, XPS shows the film as a mixture of VO_2 and V_2O_5 and this could be attributed to the shallow XPS measurement depth giving a count of the film top surface, which is potentially overoxidized as V_2O_5 . For the 350°C sample, the XPS spectra is similar to that of the 300°C sample, with a presence of V^{4+} peak together with V^{5+} peak. For the higher anneal at 400°C, V^{5+} peak becomes dominant over V^{4+} peak, indicating the film is mainly V_2O_5 . This is consistent with the V_2O_5 identification in the Raman spectra. Therefore, XPS analysis confirms that 300°C and 350°C result in presence of VO_2 and the higher 400°C leads to predominantly V_2O_5 . Regarding the increased V_2O_5 presence in 250°C annealed sample, we attribute this to the potential influence of temperature on oxygen migration deeper into the film. From XPS results (Figs. 3.14(b) and (e)), 250°C and 400°C have a high presence of V_2O_5 . However, the corresponding FTIR spectra (Figs. 3.11 (a) and (d)) indicate that the V_2O_5 behaves as dielectric with little absorption and thus small V_2O_5 presence is expected little impact on IR emissivity.

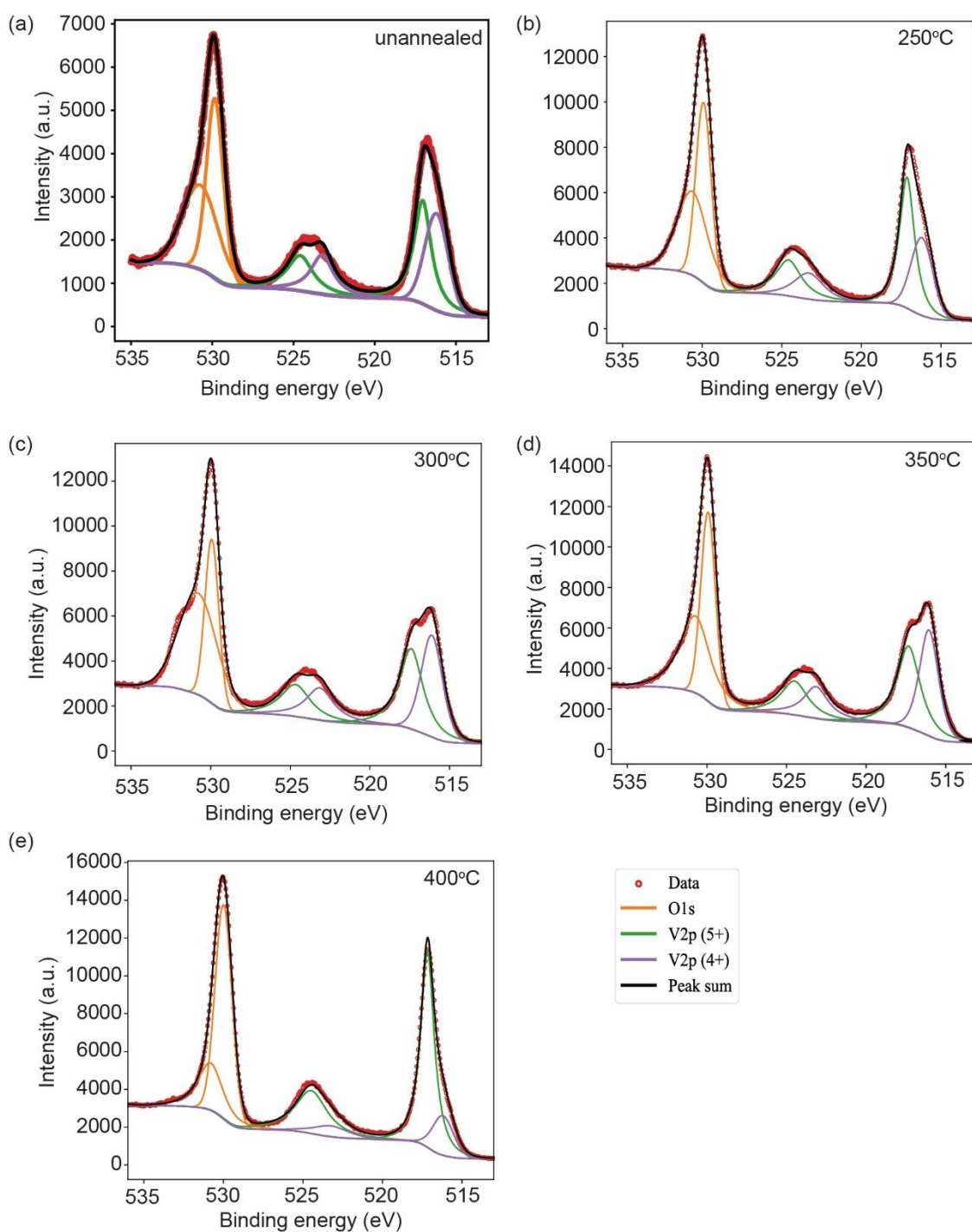


Figure 3.14 XPS Spectra of VO₂ thin films with (a) no anneal, and anneals at (b) 250°C, (c) 300°C, (d) 350°C, and (e) 400°C.

Figure 3.15 presents the XRD results for two VO₂ thin films annealed at 300°C and 350°C. As seen from the figure, both samples exhibit strong diffraction peaks at approximately 27.8°, 37.1°, 42.4°, 44.6°, and 55.6°, which aligns well with previous reports for VO₂(M1) [251-253]. Furthermore, the diffraction peaks of both films match closely with the standard JCPDS No. 43-1051 for VO₂(M), confirming that the prepared samples are indeed VO₂(M1). Other peaks correspond to the Si

substrate (including a grazing incidence reflection on the shoulder of the Si (311) plane) and the Al layer in the stack.

No additional vanadium oxide phases (such as V_2O_5) are observed in Fig. 3.15, indicating that the obtained VO_2 (M1) films possess high purity. This finding is also consistent with the Raman characterisation results. Notably, in the film annealed at 300°C, a relatively weak VO_2 (M2)(201) spike appears at around 47° [252, 254], accompanied by a shift in the Raman peaks and a decrease in the phase transition temperature (later section 3.3.7). Previous representative studies have reported that applying compressive strain at room temperature can induce the formation of the M2 phase [255, 256], and such strain can lower the required annealing temperature. Therefore, in this work, we attribute the slight compressive strain introduced by annealing as the primary reason for the reduced phase transition temperature.

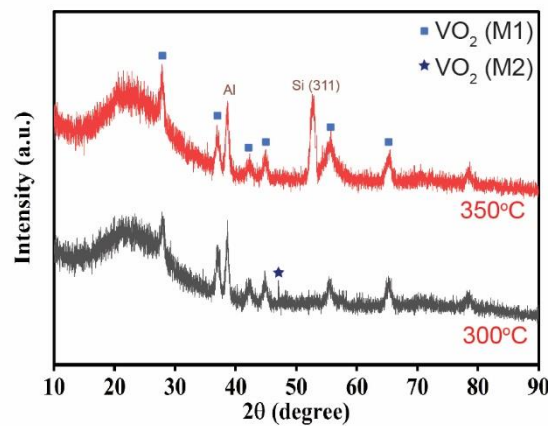


Figure 3.15. Grazing incidence X-ray diffraction of VO_2 film annealed under 300°C and 350°C.

The complex refractive index of VO_2 thin films grown on Si substrates was measured using a spectroscopic ellipsometer at both room temperature (solid lines) and 90°C (dashed lines), as shown in Fig. 3.16. The results indicate that for samples annealed at 300°C (red) and 350°C (blue), a clear phase transition was observed before and after heating. Furthermore, these two annealing conditions exhibited highly similar optical properties, suggesting that within the VO_2 formation temperature window, slight increases or decreases in annealing temperature do not significantly affect the refractive index of the samples.

Specifically, at the telecommunication wavelength of 1550 nm, the change in k before and after the phase transition was 1.50 for the 300°C annealed sample and 1.45 for the 350°C annealed sample [257]. In contrast, for samples annealed at 250°C (black) and 400°C (green), the measurements exhibit trends similar to those reported in previous studies. As with other characterisation methods presented previously, no significant phase transition was observed for these samples [258]. This indicates that annealing at temperatures too low (250°C) or too high (400°C) prevents the crystallisation and formation of stoichiometric, respectively, thereby suppressing its phase transition capability.

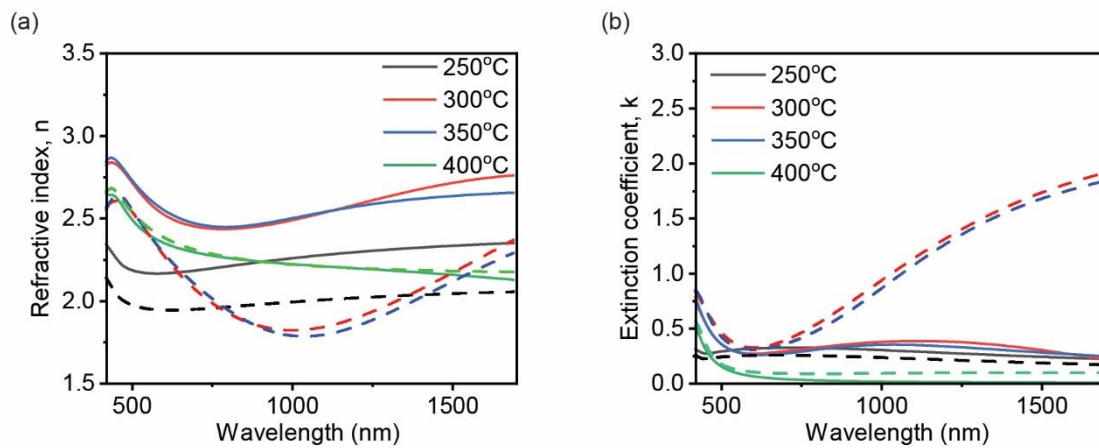


Figure 3.16. (a) Refractive index and (b) extinction coefficient at different annealing temperatures. The dashed line is the measured value at 90 degrees Celsius, and the solid line is the measured value at room temperature.

To demonstrate the developed low-temperature VO_2 thin film, a VO_2 film was also formed on flexible polyimide substrates. In this demonstration, the post-deposition annealing temperature was 300°C. Figure 3.17(a) presents a photo of a Kapton strip coated by a stack of $\text{VO}_2/\text{SiO}_2/\text{Al}$ ordered from the top down. Figure 3.17(b) presents the room temperature Raman spectrum with two references of the VO_2 and V_2O_5 . The Raman spectrum shows pronounced VO_2 peaks and therefore confirms the dominant presence of the $\text{VO}_2(\text{M1})$ phase. The infrared response of the sample is presented in Fig. 3.17(c) in the form of FTIR reflection spectra measured at various temperatures. A similar reflection contrast is seen to those on Si substrates. The IR emissivity hysteresis is presented in Fig. 3.17(d) and the VO_2 stack gives transition temperatures of 70°C and 50°C for heating and cooling, respectively. The IR emissivity contrast ($\Delta\varepsilon$) is extracted to be 0.30, lower than that of 0.47 on Si substrate under the same 300°C annealing temperature.

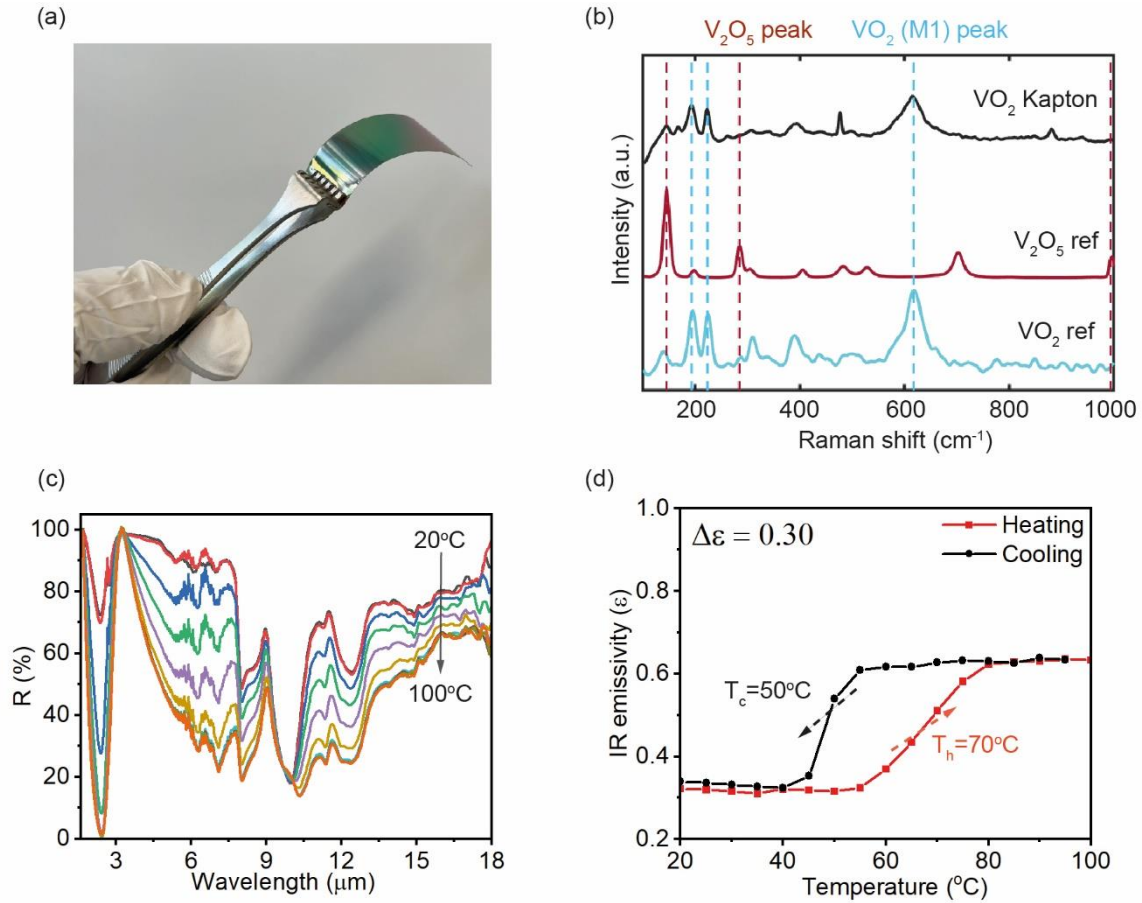


Figure 3.17. VO₂ thin film deposited, and post-deposition annealed on a flexible polyimide substrate by ALD. (a) Photograph of VO₂ grown on a polyimide. (b) Raman spectra of VO₂ grown on the polyimide (black line), with references of VO₂ (blue line) and V₂O₅ (red). (c) FTIR reflectance spectra of the VO₂ thin film on polyimide measured at from 20°C to 100°C, and (d) IR emissivity hysteresis of the VO₂ on polyimide under heating (red line) and cooling (black line).

The SiO₂ thickness impact on the spectra is presented in Fig. 3.18. The simulation was conducted using the finite element method-based numerical simulation tool COMSOL Multiphysics, which was employed to investigate SiO₂ thickness influence. This simulation used the 2D Electromagnetic Waves, Frequency Domain module, with periodic boundary conditions applied along the lateral boundaries to simulate an infinite structure and scattering boundary conditions at the outer boundaries to prevent unphysical reflections. Incident light was introduced via a periodic port, set to enter perpendicularly to the VO₂ thin film from above, with a wavelength range from 1.6 μm to 18 μm. The computational domain was meshed with an extremely fine setting to accurately resolve field variations within this spectral range. The refractive index for SiO₂ was experimentally extracted by an IR ellipsometer, from a sputtered SiO₂ film grown by a Buhler

Helios reactive sputtering system using a Si target and O₂ plasma. The refractive index of VO₂ at both low and high temperatures is from our previous work and is the same as the next chapter.

The simulated spectra closely match the experimental spectra (Figs. 3.11(b) and 3.11(c)) on Si substrates, but show less agreement with those on the polyimide substrate. Therefore, the reduction in emissivity contrast is unlikely to be caused by the SiO₂ thickness variation, suggesting that the substrate plays a significant role in the film quality. For example, the thermal transfer to rigid Si substrate is expected to be different from that to flexible polyimide, Thus, a further optimisation of the anneal conditions is necessary to achieve the highest film quality. Despite these challenges, our works clearly demonstrate the successful VO₂ formation on polyimide substrate with a remarkable phase transition capability.

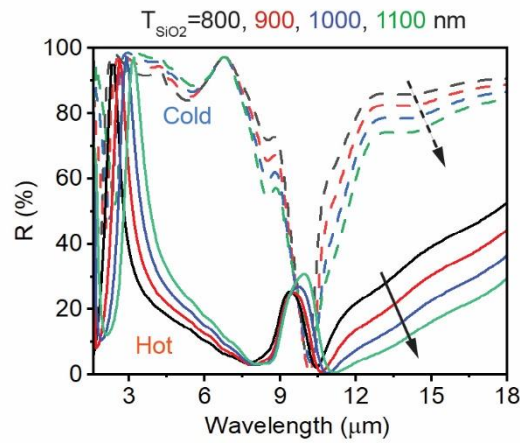


Figure 3.18. Reflection spectra as a function of wavelength for SiO₂ thicknesses of 800, 900, 1000, and 1100 nm. Solid lines represent the metallic state of VO₂, and dashed lines represent the insulating state. Arrows indicate the direction of increasing SiO₂ thickness.

Table 3.4 lists the process information of ALD VO₂ films in the literature. Most ALD VO₂ films based on TEMAV precursors were grown at temperatures of 150°C whilst those by VCl₃ require high growth temperatures at 275°C and 300°C. In all cases, the post annealing temperatures are higher than the film deposition temperatures, ranging from 400-700°C. Thus, the thermal budget for the VO₂ formation is limited by the anneal condition. Compared with ALD VO₂ films reported in the literature (Table 3.4), the VO₂ formation (including post-deposition anneal) in this work demonstrates a significantly lower thermal budget of 300°C, which makes the VO₂ formation fully compatible with integration on CMOS devices and polyimide substrates.

By correlating the annealing temperature with the oxygen partial pressure, there is a clear trend that high partial oxygen pressure corresponds to a low annealing temperature. This trend is attributed to the thermodynamic chemical equilibrium condition of the correct VO₂ stoichiometry. Two previous works [259] and [189] provided some insightful phase formation diagrams between temperature and oxygen partial pressure through *in situ* XRD measurements. Unfortunately, these *in situ* XRD measurements were not done at the film equilibrium state. Thus, a further increase in oxygen partial pressure is expected to achieve correct VO₂ stoichiometry at a lower temperature. However, on the other hand, this work has identified that no crystalline structure is formed from Raman spectra after 250°C anneal. For VO₂ crystallisation, the process typically starts with nucleation during annealing, followed by the formation of grain structures. There is limited research on VO₂ nucleation, and we therefore draw insights from the extensively studied silicon crystallisation. The nucleation rate for silicon follows an Arrhenius relationship, significantly decreasing with annealing temperature [260]. Similarly, VO₂ nucleation at 250°C is expected to take considerably longer. The trend seen in this work suggests that the lowest achievable temperature for VO₂ formation could be limited by the VO₂ crystallisation process even if the desired stoichiometry is obtained.

Table 3.4. Summary of ALD VO₂ annealing conditions in recent research works.

Ref	Anneal temp. (°C)	O ₂ partial pressure (mTorr)	Anneal duration (hour)	Growth temp. (°C)	Precursor
[146]	550 and 700	0.008	4	80	VTOP+H ₂ O
[193]	660 and 670	0.01 - 0.1	1 and 2	150	TEMAV+O ₃
[190]	585	0.01	2	150	TEMAV+O ₃
[187]	560	0.0008 - 0.005	2	150	TEMAV+O ₃
[29]	550	~0.01	1	350	VCl ₄ +H ₂ O
[30]	500	~210	3 - 6	150 - 250	TEMAV+H ₂ O
[195]	500	113	2	150	VO(OC ₃ H ₇) ₃ +H ₂ O
[191]	480	~8	1	150	TEMAV+H ₂ O
[192]	475	N/A	1.5	150 - 200	TDMAV+H ₂ O
[194]	450 and 500	60 - 1130	2 and 0.5	150	TEMAV+H ₂ O
[233]	450	13100	0.08	275 - 300	VCl ₄ +H ₂ O
[154]	400	1000	2	200	TEMAV+H ₂ O

3.3.4 Effect of annealing duration on VO₂ anneal

Since the previous section successfully demonstrated the phase transition behaviour of ALD-fabricated VO₂ thin films under low-temperature annealing conditions (300°C, 2.5 Torr) and on flexible substrates, this section will build upon that foundation by further investigating the impact of different annealing durations on the film's performance. In this study, the annealing time is varied between 1 and 4 hours.

Figure 3.19 presents the FTIR reflectance spectra of VO₂ films annealed for different durations. For a 1-hour annealing duration (Fig.3.19 (a)), the average reflectance difference between room temperature (20°C) and high temperature (100°C) across the full wavelength range is 14.7 %. Notably, compared to previously studied VO₂ samples that exhibited distinct phase transition characteristics, the reflectance dip at 10.5 µm in the 1-hour sample remains nearly unchanged. Since the 10.5 µm wavelength is attributed to SiO₂ absorption, this lack of variation suggests that the metallic like reflectance of VO₂ is relatively weak under this annealing condition. This implies that a 1 hour annealing duration may not be sufficient to fully induce the characteristic phase transition of VO₂.

Extending the annealing time to 2 hours results in an increased average reflectance difference of 22.21 %, as shown in Fig. 3.19 (b). Although the reflectance contrast between high and low temperatures becomes more pronounced, the reflectance dip at 10.5 µm remains unchanged, indicating that a 2 hour annealing duration may still be insufficient for a complete phase transition.

Further increasing the annealing duration to 3 hours leads to a significant rise in the average reflectance difference, reaching 43.2 %, accompanied by a noticeable shift in the reflectance dip from 10.2 µm to 10.7 µm, as illustrated in Fig. 3.19 (c). This observation suggests a more distinct phase transition, evidenced by both the enhanced infrared contrast and the shift in the reflectance dip.

However, when the annealing time is further extended to 4 hours (Fig. 3.19 (d)), the reflectance variation becomes minimal (only 4.13 %), and the reflectance dip at 10.5 μm remains unchanged. This indicates that excessive annealing leads to overoxidation, which may hinder the optimal phase transition of VO_2 . Additionally, a minor reflectance dip is observed around 11.5 μm , which will be further examined in the subsequent Raman analysis.

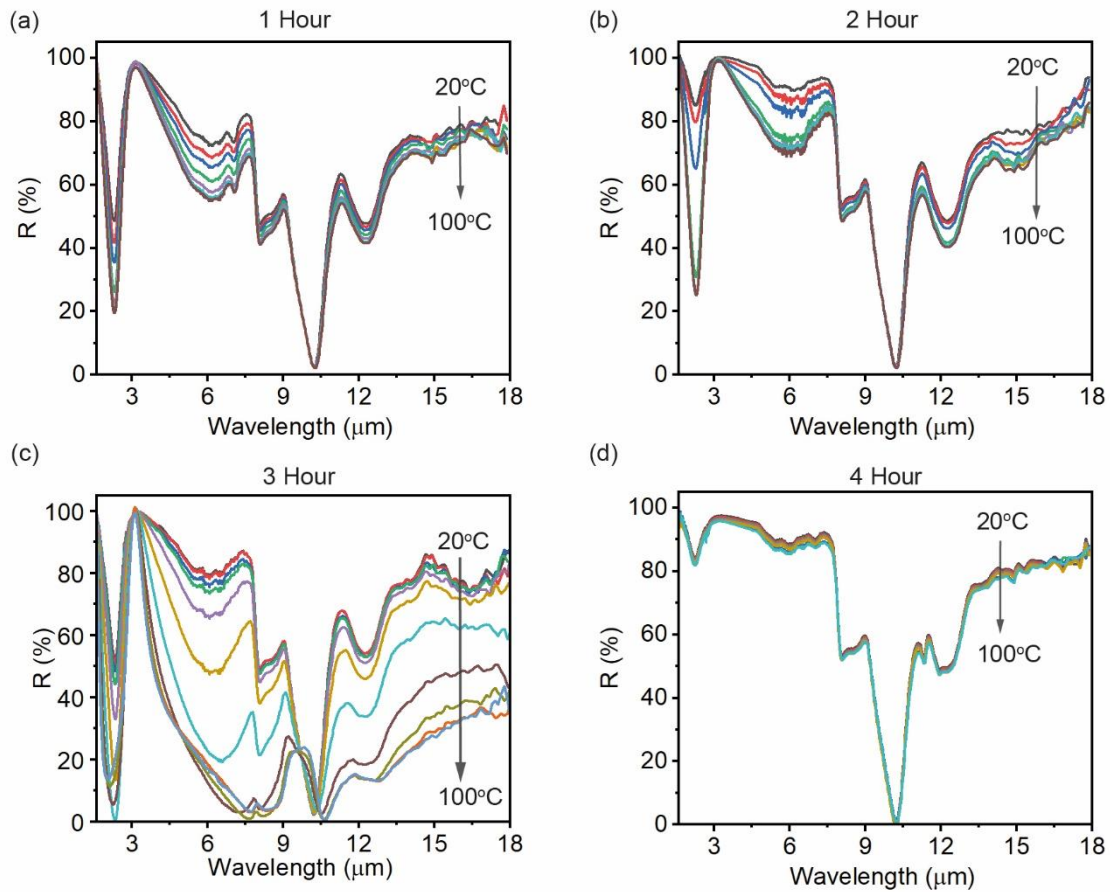


Figure 3.19. Reflection spectra of the VO_2 stacks annealed at (a) 1 hour, (b) 2 hour, (c) 3 hour and (d) 4 hour.

Figure 3.20 shows the hysteresis curves under various annealing durations. For 1 hour anneal, the hysteresis can hardly be identified from Fig. 3.20 (a). Increasing the annealing duration to 2 hours results in a slight enhancement of the transition behaviour (Fig. 3.20 (b)), but the emissivity contrast ($\Delta\varepsilon$) remains relatively low. However, the sample annealed for 3 hours clearly demonstrates a well-defined transition (Fig. 3.20 (c)). During the heating cycle, the transition temperature (T_h) is observed at 50°C, while the cooling cycle reveals a transition temperature (T_c) of 40°C. This is accompanied by a dramatic increase in emissivity contrast, with $\Delta\varepsilon$ rising from

0.04 to 0.47. Here, it is worth pointing out that the transition temperature for this undoped VO_2 is about 18°C below the known VO_2 transition temperature at 68°C , indicating a certain factor affects the phase transition. The cause of this phase transition temperature reduction will be further discussed in the later discussion section. However, further increasing the annealing duration to 4 hours leads to over-oxidation of the sample, as shown in Fig. 3.20 (d). This over-oxidation results in the near disappearance of the hysteresis behaviour. Therefore, the VO_2 with great infrared optical contrast can be achieved with an optimisation anneal time at 3 hours at 300°C (2.5 Torr O_2 pressure).

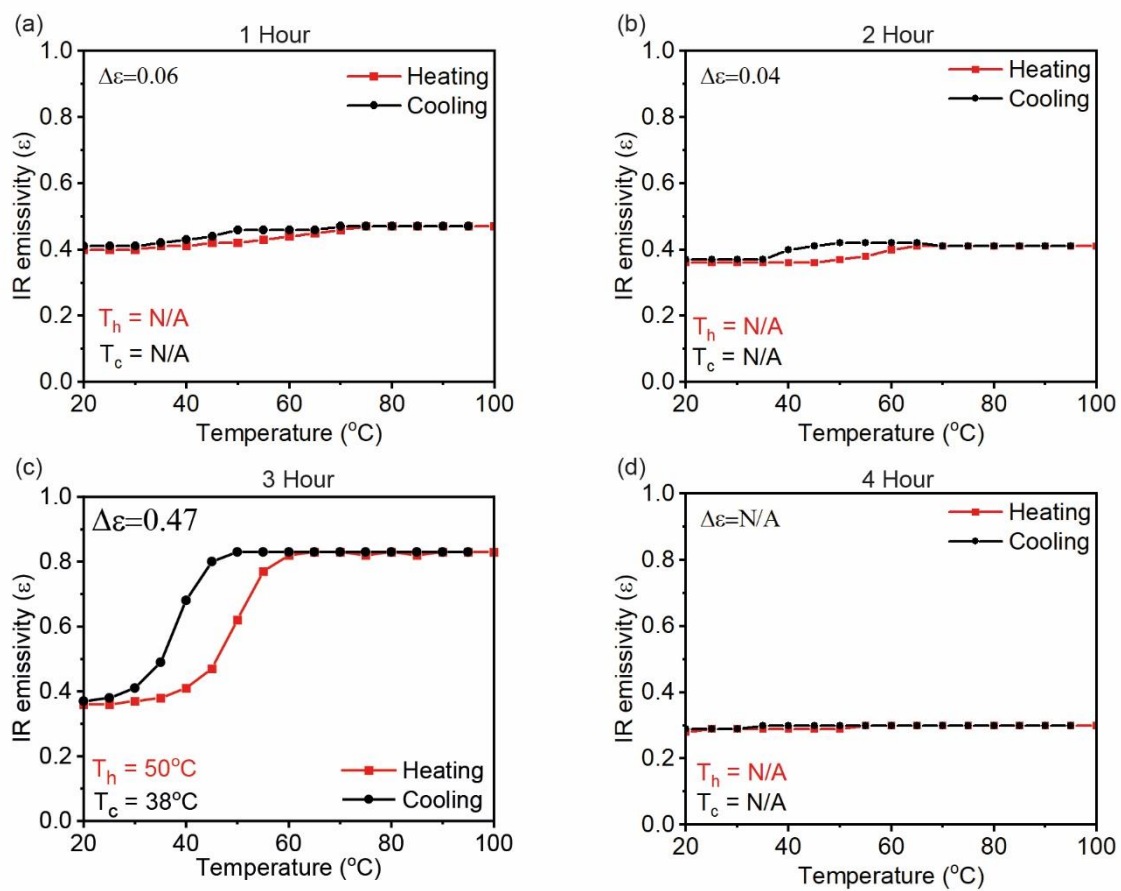


Figure 3.20. Full IR emissivity hysteresis after anneal durations of (a) 1 hour, (b) 2 hours, (c) 3 hours and (d) 4 hours.

Figure 3.21 shows the Raman spectra of VO_2 samples with varying annealing durations. For samples annealed for 1 hour and 2 hours, represented by dark blue and red lines, respectively, the main VO_2 peaks at 194 cm^{-1} , 224 cm^{-1} , and 614 cm^{-1} are tiny, indicating inadequate crystallisation of VO_2 film. This observation is consistent with the results presented in Figs. 3.20 (a) and 3.20 (b). However, an increase in annealing duration to 3 hours, as indicated by the yellow

line, reveals well-defined VO₂ Raman peaks. The Raman spectra suggest a significant improvement in the crystalline quality of the VO₂ film under 3 hours of annealing duration. In contrast, the sample annealed for 4 hours, as shown by the purple line, exhibits a noticeable disappearance in the primary VO₂ peaks. This spectral shift is indicative of over-oxidation, resulting in the formation of V₂O₅ at 146 cm⁻¹, 285 cm⁻¹ and V₃O₇ at 840 cm⁻¹, 880 cm⁻¹, and 930 cm⁻¹. The formation of V₃O₇ under 4 hours of anneal duration also corresponds to the small valley at about 11.5 μm in Fig. 3.19 (d).

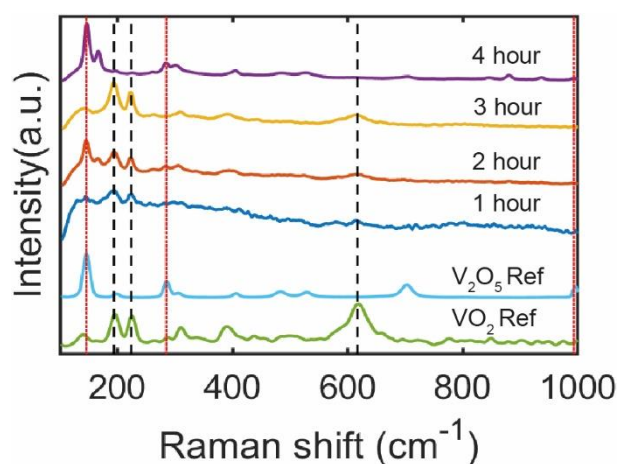


Figure 3.21. Room temperature measured Raman spectra of VO₂ on Si substrate with 1 mW output power under different annealing duration, the black dash lines located at 194 cm⁻¹, 224 cm⁻¹ and 612 cm⁻¹ represent the highest intensity of VO₂ (M1) Raman scattering peak, the red dot lines located at 146 cm⁻¹, 285 cm⁻¹ and 996 cm⁻¹ represent the highest intensity of V₂O₅ Raman scattering peak.

Figure 3.22 shows a series of X-ray photoelectron spectroscopy (XPS) spectra illustrating the effect of annealing duration on the composition of samples, with panels (a) 1 hour, (b) 2 hours, (c) 3 hours, and (d) 4 hours. Each panel shows the intensity of photoemitted electrons as a function of binding energy (eV). The spectra feature prominent peaks corresponding to oxygen O1s and vanadium V2p states. For each temperature, the spectra are deconvoluted into component peaks representing different oxidation states of vanadium (green and purple lines for 5+ and 4+ states, respectively). The black line in each plot represents the sum of fitted peaks, indicating the combined contribution of each state to the overall spectrum. Through the comparison of V⁴⁺ and V⁵⁺ peaks around 517 eV, it can be concluded that a co-existence of VO₂ and V₂O₅ for anneals of 1, 2 and 3 hours, with most V⁴⁺ peak for 3 hours. For further anneal duration of 4 hours, it is clear that V⁵⁺ becomes dominant and this is highly consistent with the FTIR results and Raman spectra.

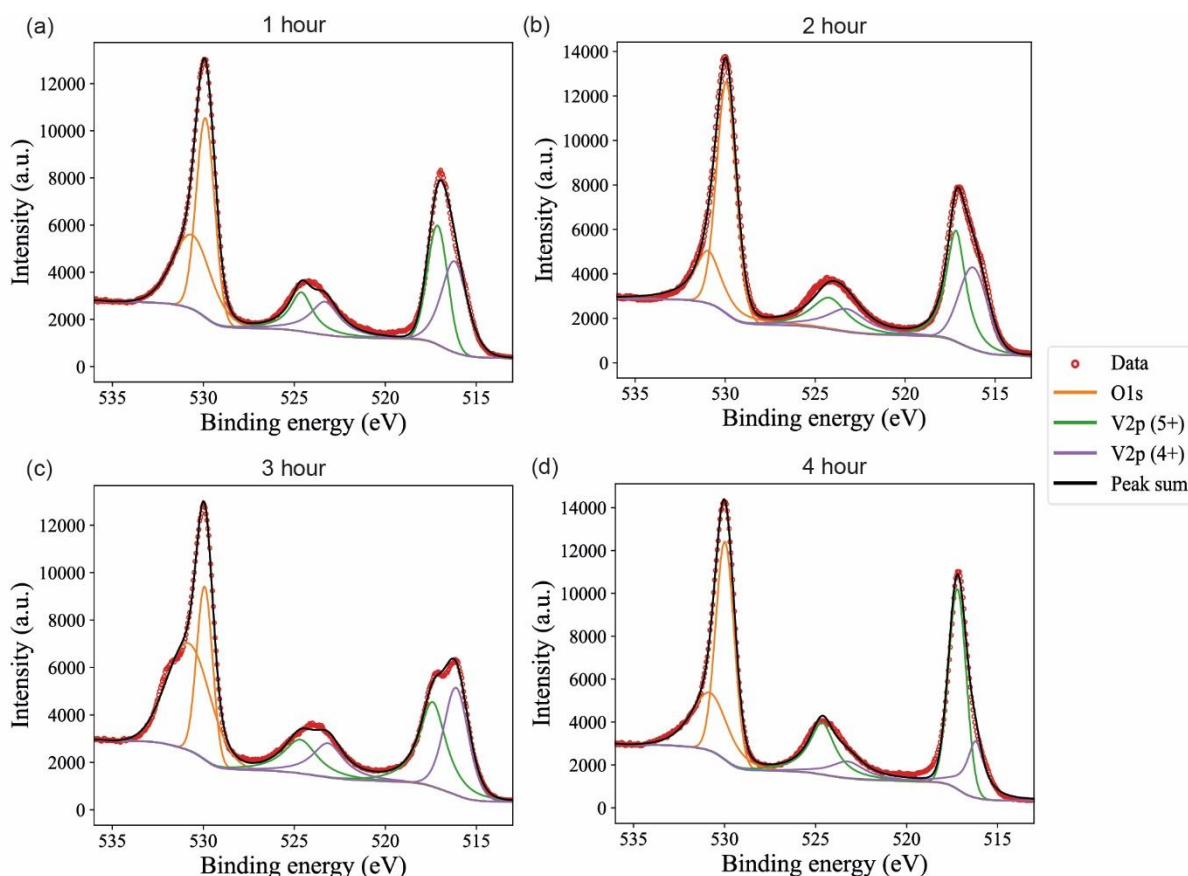


Figure 3.22. The XPS binding energy spectra covering the O1s and V2p energy ranges for samples annealed at 300°C for 2.5 Torr O₂ pressure at varying anneal duration: (a) 1 hour, (b) 2 hours, (c) 3 hours and (d) 4 hours.

Upon analysis of the XPS spectra across varying annealing temperatures, a quantitative assessment of the composition was performed by comparing the areas under the V2p peaks. After adjusting for the sensitivity factors corresponding to each state, the atomic percent (at. %) ratio of V⁴⁺ over all vanadium was determined, with detailed results presented in Table 3.5. This trend suggests that there is a propensity for the samples to undergo over-oxidation, transitioning from the desired V⁴⁺ to higher order V⁵⁺ as the duration increases.

Table 3.5. Variations in atomic percentages of V⁴⁺ over (V⁴⁺ + V⁵⁺) under different annealing durations.

Vanadium state	Atomic percentage (%)			
	1 hour	2 hours	3 hours	4 hours
V ⁴⁺	51.1	46.5	48.9	29.6
V ⁵⁺	48.9	53.6	51.1	70.4

The SE analysis of annealing duration shown in Fig. 3.23 reveals that for samples with either a too short (1h, black) or too long (4h, green) annealing time, there is no significant change in the refractive index n and extinction coefficient k before and after transition. In contrast, the 2-hour annealed sample (red) exhibits a slight phase transition capability, with the extinction coefficient k at 1550 nm increasing by 0.36 upon heating. This result is consistent with the previously observed mild phase transition in FTIR and Raman spectroscopy. When the annealing time is extended to 3 hours, the change in the extinction coefficient at 1550 nm increases significantly from 0.36 to 1.50. This suggests that under low-temperature and high-oxygen-pressure conditions, the formation of VO_2 is highly sensitive to annealing duration.

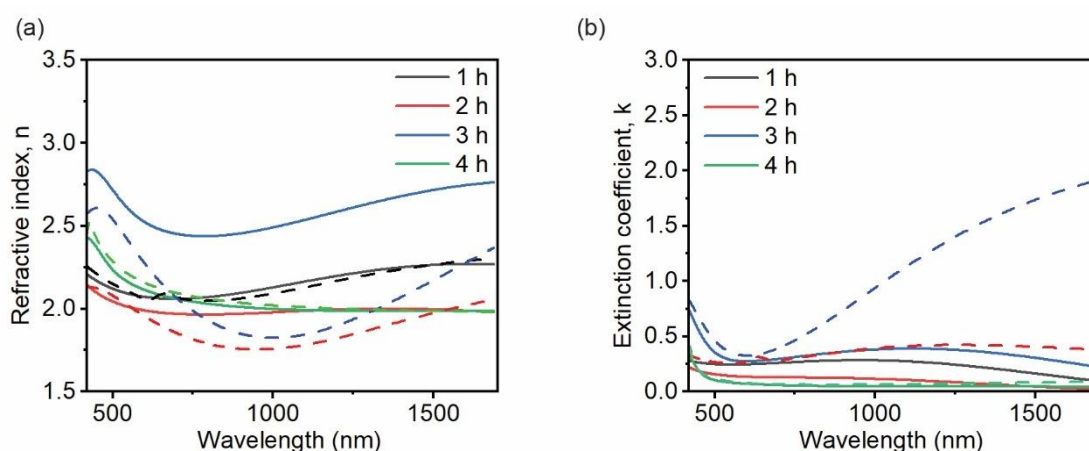


Figure 3.23. (a) Refractive index and (b) extinction coefficient at different annealing durations. The solid line is the measured value at 90°C, and the dotted line is the measured value at room temperature.

3.3.5 Quantification of VO_2 thin films using Raman

Compared with the time-consuming X-ray Photoelectron Spectroscopy process, Raman spectroscopy offers a simpler and more accessible way of characterising VO_2 . While Raman analysis typically offers qualitative information, unlike XPS, it has not been extensively used to provide quantitative information, such as the composition of vanadium oxide [239, 261]. However, there is evidence that quantitative Raman analysis has been effectively applied to other materials, like silicon crystallinity (amorphous/crystalline) [262]. The objective of this section is to develop the VO_2 quantitate Raman analysis through calibration with XPS data.

Although there are many compounds in the VO_x family, our analysis of all samples in this section found no evidence of other VO_x phases, except for a small amount of V_3O_7 detected in the Raman

spectra of a few over-oxidised samples. Among the five samples exhibiting clear phase transition behaviour, neither XRD nor Raman spectroscopy revealed any traces of other crystalline VO_x phases. Furthermore, XPS analysis of all samples in this study did not show any binding energy reference corresponding to V^{3+} at 515.7 eV. A very recent study on ALD-deposited VO_x thin films provides insight into this observation, suggesting that the final oxidation state of VO_x after annealing is directly influenced by the annealing atmosphere. Their findings indicate that amorphous VO_x annealed in an oxygen-rich environment tends to form VO_2 films, whereas samples annealed in vacuum and air are more likely to produce V_2O_3 and V_2O_5 , respectively [263]. Based on this, I infer that the detected V^{5+} in my samples most likely originates from surface oxidation leading to the formation of V_2O_5 , while the observed V^{4+} is primarily attributed to the desired VO_2 .

Figure 3.24 shows the peak-fitting approach that is applied to analyse the VO_2 and V_2O_5 fractions within the Raman spectra. This method utilises Lorentzian curve fitting to identify and quantify the contributions of VO_2 and V_2O_5 . Specifically, the 194 cm^{-1} peak is identified as the main peak for VO_2 , while the 146 cm^{-1} peak serves as the main Raman peak for V_2O_5 . The contributions of VO_2 and V_2O_5 are expressed in the areas of the fitted Lorentzian curves for these two dominant peaks, which can be defined as [264]:

$$y = y_0 + \frac{2A}{\pi} \times \frac{w}{4(x - x_c)^2 + w^2} \quad (3.2)$$

where y_0 is the offset, A is the area of the peak, w is full width at half maximum (FWHM), and x_c is the centre of the peak.

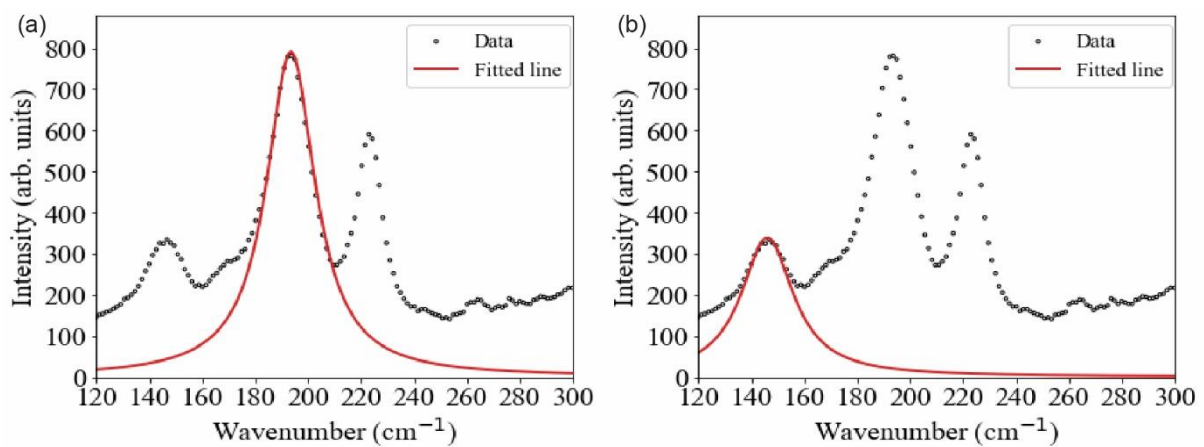


Figure 3.24. Lorentzian fitted Raman peaks of (a) VO_2 (M1) main peak at 194 cm^{-1} , and (b) V_2O_5 main peak at 146 cm^{-1} .

The film elemental composition can be quantitatively assessed from the area integration of the VO₂ (M1) main peak at 194 cm⁻¹ and V₂O₅ main peak at 146 cm⁻¹ and then compared with the XPS results. The VO₂ composition is calculated through the equation below.

$$\frac{V^{4+}}{V^{4+} + V^{5+}} = \frac{A(VO_2)}{A(VO_2) + \beta \times A(V_2O_5)} \quad (3.3)$$

where β is the factor of area contribution of V₂O₅ over VO₂.

Figure 3.25 compares V⁴⁺ composition in terms of atomic ratio extracted from Raman spectroscopy and XPS measurements for all the samples in this chapter (except the sample annealed under 250°C). In Fig. 3.25 (a), the atomic ratio of V⁴⁺ to the sum of V⁴⁺ and V⁵⁺ from XPS measurements is plotted in black dash-dot line, alongside several solid lines representing Raman spectroscopy data that have been scaled by different β factors. Here, the β factor serves as a calibration coefficient to align the Raman data with the XPS reference. Each line corresponds to a different β value, indicating the variation in Raman data alignment with the XPS background as β changes. Fig. 3.25 (b) shows the mean square error (MSE) between the calibrated Raman data and the XPS data across different β values. This plot identifies the optimal β value that minimises the error, indicating the most accurate scaling factor for Raman data to quantitatively match the XPS results. The turning point on the graph where the error reaches its minimum suggests the best β value of 2.5 for the most accurate Raman data calibration.

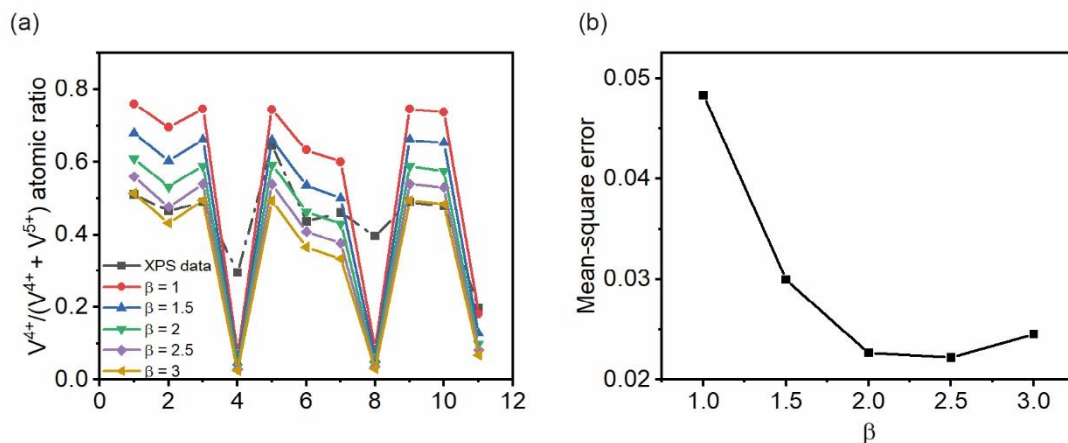


Figure 3.25. Comparison of V⁴⁺ atomic ratio from Raman Spectroscopy with XPS for quantitative analysis of vanadium oxides. (a) The atomic ratio of V⁴⁺ to the sum of V⁴⁺ and V⁵⁺ obtained from XPS data is plotted against the Raman peak area ratio for different β values in step of 0.5. (b) The mean square error between the XPS data and

the scaled Raman data is plotted as a function of β in step of 0.5, indicating the optimisation of the Raman data scaling for improved quantitative analysis. The minimum mean square error suggests the optimal β value for accurate representation of the vanadium oxide composition.

Figure 3.26 shows a calibrated analysis of 11 distinct samples utilising the previously established optimal β value. In Fig.3.26 (a), the atomic ratio of V^{4+} to the total of V^{4+} and V^{5+} is plotted against various oxygen partial pressures, XPS data and Raman fitted results are displayed as a comparison. Figure 3.26 (b) exhibits how this ratio is influenced by different annealing temperatures, and panel (c) shows the effects of various annealing times on the ratio, comparing XPS data to Raman fitted results. With optimal β value, the consistency between Raman and XPS data is less than 10 % variation for those VO_2 with good transition capability.

Conversely, samples that are over-oxidised or exhibit ambiguous phase transitions show poorer alignment between Raman and XPS measurements. Overall, Fig. 3.26 validates the quantitative Raman spectra analysis can offer a reliable insight into the vanadium oxide composition using the empirically fitted beta of 2.5.

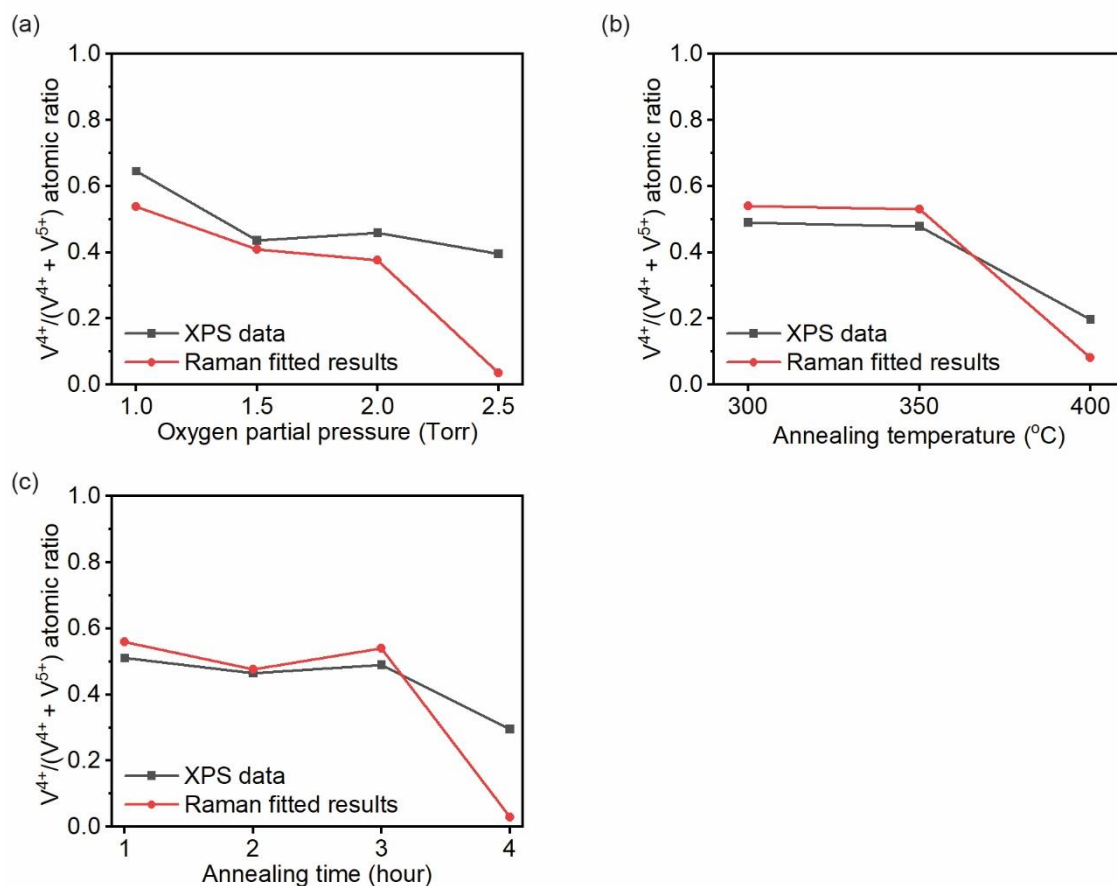


Figure 3.26. Comparative analysis of the vanadium oxide fraction using Raman fitted results and XPS data. (a) $V^{4+}/(V^{4+} + V^{5+})$ atomic ratio as the function of oxygen partial pressure. (b) The effect of annealing temperature on the $V^{4+}/(V^{4+} + V^{5+})$ atomic ratio (c) The influence of annealing time on the $V^{4+}/(V^{4+} + V^{5+})$ atomic ratio.

3.3.6 Further investigation of crystal strain through Raman peak shifts

In previous studies, VO_2 transition temperatures are found to be below the well-known value of 68°C for heating. To further investigate it, Raman peak shifts around 194 cm^{-1} are investigated to elaborate VO_2 crystallinity information, particularly strain, for the five samples with clear transition behaviours. Figure 5.27 shows how annealing pressures (1 Torr, 1.5 Torr, and 2 Torr) and temperatures (300°C and 350°C) influence Raman peak positions. In Fig. 3.27, the dots represent the original Raman data, and the solid lines are fitted curves through Lorentz fits. The fitting method is described in the previous section. Figure 3.27 (a) shows three separate Raman spectra annealed under oxygen partial pressures of 1 Torr, 1.5 Torr, and 2 Torr. The vertical black dashed

marks the central peak position of fitted 1 Torr curve (red line) at about 194 cm^{-1} as a reference. It can be seen that the central position of the peak has a tiny right shift with the increase of oxygen pressure. A similar trend is also observed in Fig. 3.27 (b), where the central peak position shifts right with increasing annealing temperature.

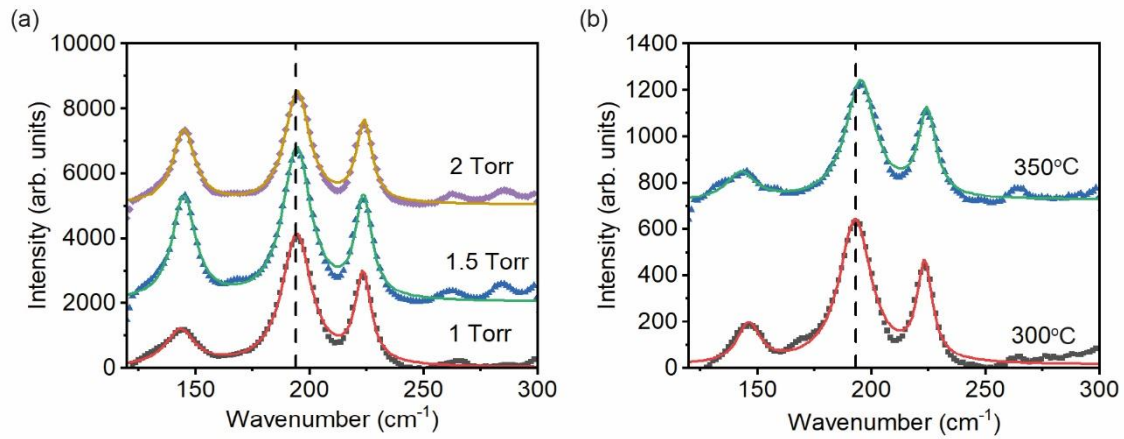


Figure 3.27. Room temperature measured Raman spectra of VO₂ after different annealing conditions. (a) spectra at various pressures: 1 Torr (red), 1.5 Torr (green), and 2 Torr (yellow). (b) spectra at different temperatures: 300°C (red) and 350°C (green). The black dashed lines indicate the central position of Lorentz fitted 1 Torr and 300°C. All the dots represent the original Raman data, all the solid lines represent the Lorentz fitted curve.

By extracting the peak position from Fig. 3.27 and correlating it to its transition temperatures, Table 3.6 provides an analysis of how annealing pressures (1 Torr, 1.5 Torr, and 2 Torr) and temperatures (300°C and 350°C) influence Raman peak positions and phase transition temperatures (T_h and T_c) of VO₂ thin films. For the pressure group samples at the same annealing temperature, the Raman peak shifts to a lower frequency as red shift with O₂ pressure decreasing from 1.5 Torr to 2 Torr, and this results in a reduced transition temperature of around 45°C for heating. For temperature studies, it shows that a lower temperature at 300°C gives the Raman peak shifting to a lower frequency, which matches the reduced transition temperature at 50°C (heating). These trends between Raman peak shifts and transition temperatures are consistent with those reported in the literature [24], induced through different substrates. The work in [24] reported that compressive strain in the VO₂ film can lead to a decrease in transition temperature. Thus, the discovery in this work provides an insight that certain fine anneal condition optimisation is required to get the desired transition temperature, even if excellent optical contrast is achieved.

Table 3.6. Correlation between Raman peak position and phase transition characteristics of VO₂ thin films under various annealing conditions.

	Group (pressure)			Group (Temperature)	
	1 Torr	1.5 Torr	2 Torr	300°C	350°C
Raman peak position (cm ⁻¹)	193.6	193.7	193.9	192.9	194.9
Transition temperature T _h (°C)	45	72	73	50	68
Transition temperature T _c (°C)	35	54	58	38	53

Figure 3.28 visually illustrates the relationship between Raman shift and phase transition temperature for the five good VO₂ samples listed in Table 3.6. Here, the phase transition temperature is defined as the average of the transition temperatures during heating and cooling, as recorded in Table 3.6. The results indicate that as increases of the anneal condition, will red shift in the Raman peak of VO₂. Furthermore, this redshift exhibits a proportional relationship with the phase transition temperature.

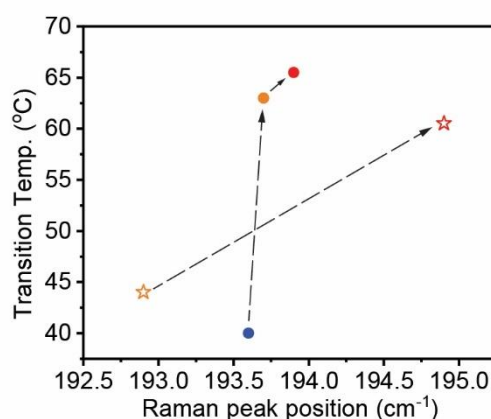


Figure 3.28. Relationship between Raman shift and average phase transition temperature of VO₂ thin film. The stars represent the temperature group and the circles represent the oxygen pressure group. The blue, yellow, and red gradients

represent the conditions between groups from small to large. The dashed arrows are only used to indicate the increase in annealing conditions between groups.

3.3.7 Discussion of tuneable refractive index via strain

Since previous sections have presented the wavelength-dependent refractive index of VO₂ thin films deposited on silicon wafers. In applications such as integrated photonics and silicon-based compatibility, the refractive index at 1550 nm is often of particular interest. Therefore, it is highlighted in Fig. 3.29 as a function of annealing conditions.

The results indicate that all three sample groups annealed at 400°C exhibit a high refractive index contrast, which may be attributed to the formation of a more densely packed crystalline phase at elevated temperatures. Notably, under the 1 Torr oxygen pressure annealing condition (blue circles), the refractive index and extinction coefficient at 1550 nm show the highest contrast, reaching 0.76 and 1.53, respectively.

Although the samples annealed at 300°C (red triangles/stars) do not exhibit the highest refractive index contrast at 1550 nm, they still achieve the second-highest extinction coefficient contrast of 1.50. This suggests that the 300°C annealing condition, while maintaining CMOS compatibility due to its lower processing temperature, also offers a competitive refractive index contrast. This finding highlights its potential for applications in VO₂ based optical switches and dynamic computing devices that rely on this property. Additionally, Fig. 3.29 reveals that the 12 samples distinctly cluster into two groups (lower-left and upper-right regions), suggesting that the effective phase transition window for VO₂ formation under different conditions is relatively narrow. Furthermore, within this phase transition window, fine-tuning the annealing conditions does not significantly alter the refractive index properties of the material.

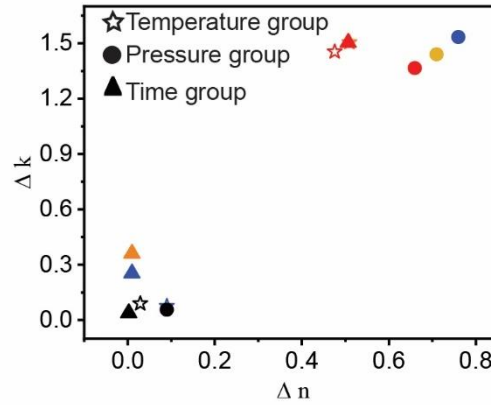


Figure 3.29. Effect of annealing conditions on the refractive index of VO₂ thin films at 1550 nm. The stars represent the temperature group, the circles represent the oxygen pressure group, and the triangles represent the time group. The progressive order of blue, yellow, red, and black represents the conditions between groups from small to large.

Figure 3.30 visually illustrates the relationship between Raman shift and refractive index for the five VO₂ samples exhibiting clear phase transition behaviour in Fig. 3.29. The results indicate that different annealing conditions influence the slopes of the relationships among n and k with oxygen pressure exhibiting the most pronounced slope. In Fig. 3.30, a clear inverse relationship between the Raman peak redshift and the refractive index contrast of VO₂ can be observed.

Although previous studies have rarely directly investigated the correlation between VO₂ refractive index and Raman shift, recent research reported a co-relation between TiO₂ strain and refractive and thus we investigate whether a similar correlation exists between refractive index and VO₂ strain. Or the strain effect on VO₂ refractive index [265]. As discussed in Section 2.2.2, compressive strain along the c -axis can lower the metal-insulator transition (MIT) temperature, whereas tensile strain can raise it. By correlating the XRD results with Raman shift, in this study, the strain induced by tuning the annealing condition is very likely to be a direct factor contributing to the increased variation in the complex refractive index of VO₂.

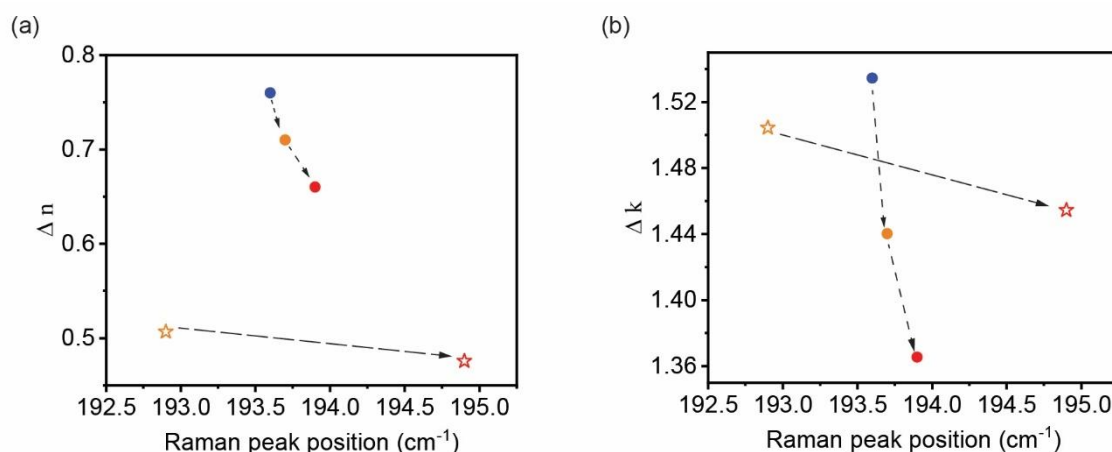


Figure 3.30. Relationship between Raman shift and (a) real part of refractive index (b) imaginary part of refractive index. The stars represent the temperature groups and the circles represent the oxygen pressure groups. The blue, yellow, and red progressive sequence represents the conditions between groups from small to large. The dotted arrows are only to indicate the increase of annealing conditions between groups.

3.3.8 Discussion of the annealing effect on the VO₂ surface topography

The VO₂ film quality was investigated through an SEM. Figure 3.31 shows top-view SEM images of VO₂ films annealed at 400°C for 2 hours under varying oxygen partial pressures. For 1 Torr oxygen partial pressure (Fig. 3.31a), numerous defects are evident on the surface and similar to an unannealed VO₂ (Fig. 3.31e). Concurrently, there is a noticeable reduction in defects at a higher oxygen pressure of 1.5 Torr and 2 Torr. At 2.5 Torr, a distinctive grain shape is seen as needle-like, corresponding to the transformation of VO₂ to V₂O₅, as previously verified by Raman spectroscopy and X-ray photoelectron spectroscopy (XPS) analyses. Therefore, defects are cured during the post-deposition anneal process and grain morphology can give an indication of VO₂ or V₂O₅ after annealing.

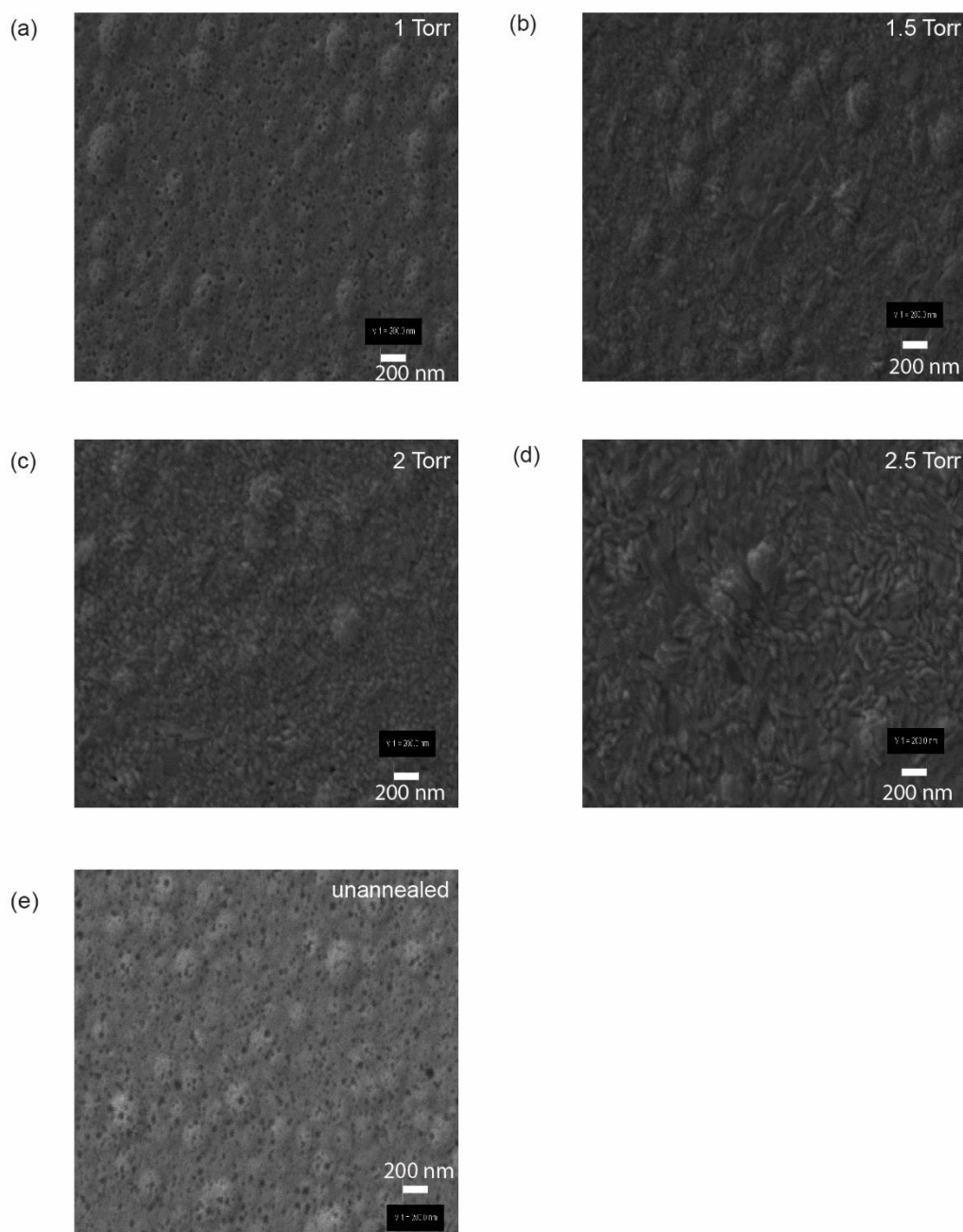


Figure 3.31. Top-view SEM images of VO₂ samples annealed at 400°C for 2 hours with different oxygen partial pressures with a 200 nm scale bar. The oxygen pressures are (a) 1 Torr, (b) 1.5 Torr, (c) 2 Torr, (d) 2.5 Torr and (e) an unannealed VO₂ sample as reference.

Figure 3.32 presents the SEM images for annealed VO₂ at various temperatures of the annealed samples. For the film annealed at 250°C (Fig. 3.32 (a)), the sample morphology is close to that of the unannealed VO₂ film, with defects clearly identified. With the annealing temperature

increased to 300°C (Fig.3.32 (b)), the film shows a pattern of small grains and the defects have disappeared. With the annealing temperature further increasing to 350°C (Fig. 3.32(c)), the film shows similar patterns to those of 300°C. For the film annealed at 400°C (Fig. 3.32(d)), a significantly different pattern is seen with large needle-like grains, indicating that the film is distinctive from the other anneals. By comparing these four films, we can conclude that the morphology of ALD-deposited VO₂ thin films can change with annealing temperature and those defects due to underlying layers can be cured under certain anneal conditions.

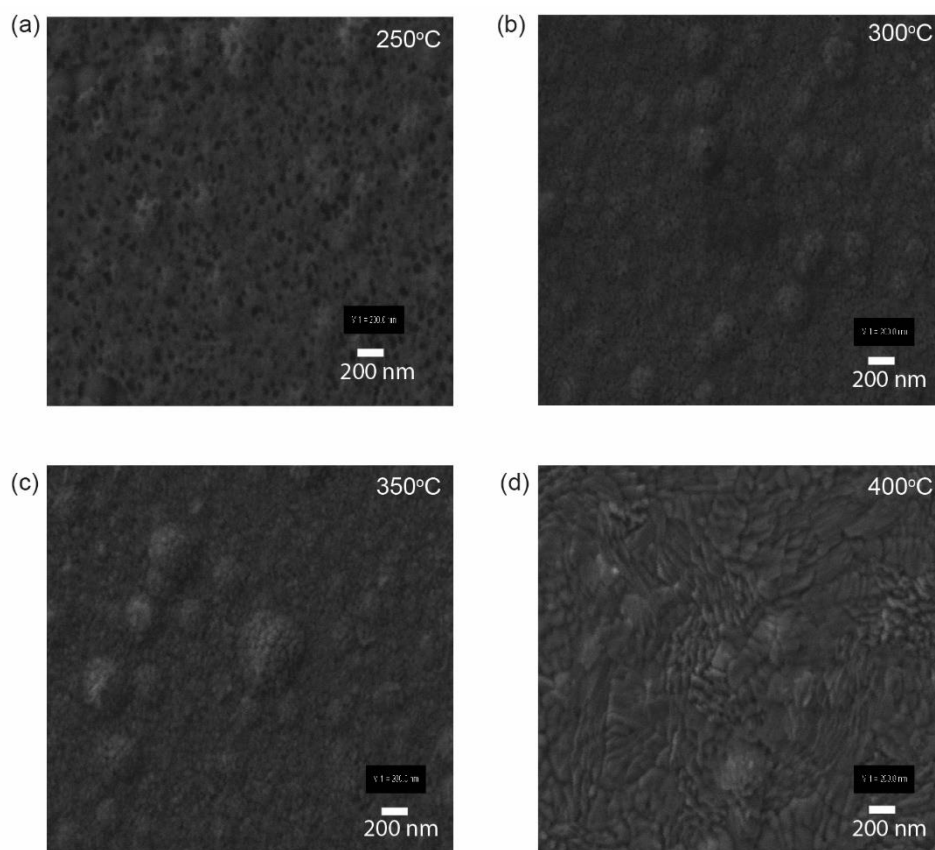


Figure 3.32. Top view SEM images of VO₂ samples annealed under 2.5 Torr oxygen partial pressure for 3 hours at different anneal temperatures with a 200 nm scale bar. The anneal temperatures are (a) 250°C, (b) 300°C, (c) 350°C, and (d) 400°C.

Now, extra focuses are given on the optimised low anneal temperature at 2.5 Torr O₂ pressure with SEM image in Fig. 3.33. For anneal durations from 1 to 3 hours, VO₂ films show similar patterns and all with no defects identified. However, 4 hours anneal shows a bit different film morphology that with little cracks in the film. This distinctive pattern indicates a different composition of the film, which well matches the little optical contrast and V₂O₅ like Raman peaks. The lack of needle-

like grains here could be attributed to its lower anneal temperature and also likely formation of V_3O_7 . In summary, VO_2 film under the optimised anneal condition has demonstrated a good film quality and free from defect, which can be very critical in electronic applications.

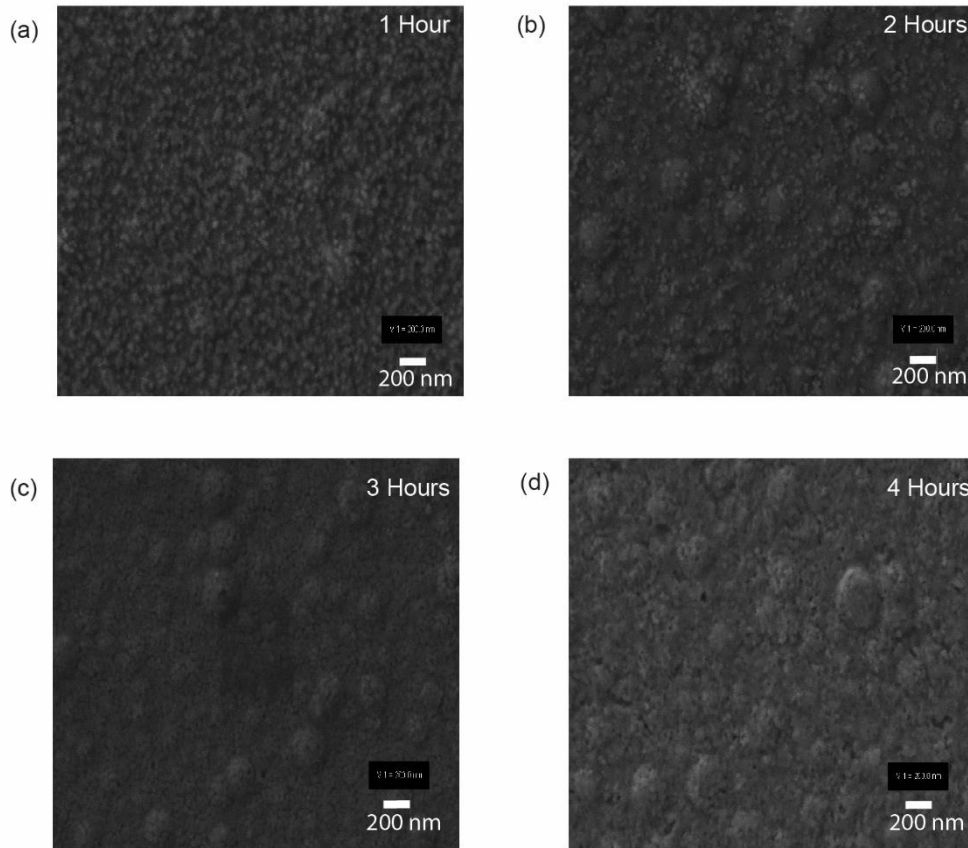


Figure 3.33. SEM top view images of VO_2 samples annealed at 300°C under 2.5 Torr oxygen partial pressure with various annealing duration with a 200 nm scale bar. The annealing duration of these samples is: (a) 1 hour, (b) 2 hour, (c) 3 hour, and (d) 4 hour.

3.4 Conclusion to Chapter 3

This chapter systematically investigates low-temperature annealing strategies for VO_2 thin films grown by atomic layer deposition, aiming to achieve high-quality phase transition properties while minimising the thermal budget. By systematically controlling the annealing temperature, oxygen partial pressure, and annealing time, a causal relationship between process parameters, material structure, and optical properties is established, providing a reliable process window for the production of VO_2 thin films compatible with CMOS processes and flexible substrates.

The study demonstrates that at a low temperature of 300°C in an oxygen atmosphere of 2.5 Torr, well-crystalline VO₂ films can be successfully induced, exhibiting a clear metal-insulator phase transition behavior and good optical constant contrast. Further reductions in the annealing temperature (e.g., 250°C) result in insufficient crystallization, while excessively high temperatures (e.g., ≥400°C) can easily induce excessive oxidation, resulting in the formation of V₂O₅, which destroys the material's reversible phase transition properties. This finding demonstrates that, with appropriate control of oxygen and annealing time, VO₂ crystallisation can be achieved even under conditions traditionally considered 'inadequate temperature', providing a viable path for subsequent integrated devices.

This chapter uses a combination of Raman spectroscopy and XPS to effectively determine the phase composition and oxidation state distribution of the thin film. The experiment also uses Raman peak shifts for the first time to analyse changes in lattice strain, further revealing the central role of strain in annealing and its regulation of the refractive index and phase transition temperature of VO₂. This provides new approaches for optically tenable design in subsequent devices. Scanning electron microscopy results show that prolonged annealing or high-temperature conditions tend to form large, coarse grains on the film surface, unlike those of VO₂. This is consistent with the overoxidation results obtained from other characterizations, suggesting that annealing time must be optimized in conjunction with temperature and oxygen partial pressure.

In summary, this chapter presents the low-temperature annealing/crystallisation process for VO₂ and demonstrates its applicability on both silicon and flexible substrates. These material optimisation results provide a critical foundation for the design of optical bistable devices and the realization of all optical short-term memory, proposed in the next chapter.

Chapter 4. Device-level bistability in VO₂ microring resonator for optical memory

4.1 Introduction

For decades, electronic logic gates and the classical von Neumann architecture have been the foundation of modern computing systems. However, with the rapid advancement of artificial intelligence and machine learning, the demand for computing power has increased exponentially, pushing the energy efficiency and processing speed of electronic systems toward their physical limits [266-268]. This challenge has spurred interest in alternative computing paradigms, among which all-optical neuromorphic computing has emerged as a promising approach [269, 270]. By replacing electronic logic gates with optical data processing and storage units and adopting bio-inspired, non-von Neumann architectures, all-optical neuromorphic computing offers the potential for ultra-fast, energy-efficient computation. A critical aspect of advancing this field is the exploration of suitable functional materials that can effectively mimic neural functionalities [271-274].

Vanadium dioxide (VO₂), a transition metal oxide, has attracted significant attention due to its unusual phase transition properties. At around 68°C, VO₂ undergoes a reversible solid-state phase transition between an insulating monoclinic phase and a metallic rutile phase, accompanied by dramatic changes in its electrical and optical properties [19]. These characteristics make VO₂ an attractive material for a variety of applications, including smart windows [275, 276], photodetectors [122, 277], space solar reflectors [219], and more recently, data processing and computing devices [38, 278, 279]. In optical memory devices, VO₂ is traditionally utilised for its inherent optical bistability arising from the hysteresis in its phase transition during heating and cooling processes [22, 36, 280, 281].

However, relying on the material's hysteresis characteristics presents several challenges. For example, doping VO_2 with tungsten is a promising strategy to lower the phase transition temperature, which in turn reduces power consumption which is an important consideration for device efficiency [39]. However, this advantage comes at the cost of narrowing the hysteresis width, which is crucial for devices that depend on hysteresis-based bistability. Consequently, despite tungsten doping being a good approach, it may have to be abandoned due to the limitations imposed by the reduced hysteresis width. Additionally, achieving precise control over the hysteresis loop is technically demanding, potentially hindering design optimisation and large-scale production.

To overcome these limitations, we propose and numerically analyse a photothermal induced that achieves bistability at the device level without relying on globally heating the device. Our design exploits the absorption contrast between the metallic and insulating phases of VO_2 to modulate the effective refractive index thereby influencing the optical properties of the device. This approach simplifies the implementation process and is conducive to future design optimisation and mass production.

Moreover, our device is capable of simulating the short-term memory and natural forgetting processes observed in biological systems. Unlike non-volatile devices, which require additional stimuli or regulatory elements to realise forgetting, our volatile memory device naturally emulates the biological forgetting mechanism, thereby avoiding information overload and system congestion. The underlying bistability of our device plays an essential role in achieving associative learning, as it provides the system with the ability to maintain different stable states

under identical input conditions, which is an essential feature for mimicking biological conditioning and memory processes. This bistable characteristic is particularly crucial in optical and neuromorphic computing, as it allows the device to reliably store and switch between the states necessary for associative learning, ensuring effective memory formation and response. In this work, we demonstrate the feasibility of the proposed device through numerical simulations, highlighting its potential for use in photonic associative learning and optical memory.

4.2 Methodology

4.2.1 Device structures

This chapter investigates the optical behaviour and bistable characteristics of VO_2 -integrated photonic structures through finite-element simulations. Two geometries are considered: a straight waveguide configuration and a microring resonator (MRR) configuration. These designs are selected to evaluate bistability in two commonly used integrated photonic elements. Before discussing the VO_2 refractive index modelling and simulation methodology, the device structures are first introduced.

Figures. 4.1(a) show schematic views of the straight waveguide device with the VO_2 patch. The silicon rib waveguide is situated on a SiO_2 substrate and has a width of 500 nm and a height of 220 nm, this dimensions is commonly used in photonic integrated circuits. A discussion of waveguide geometry can be found in Section 2.4.1. This Chapter focuses primarily on the influence of the VO_2 patch dimensions.

Figure. 4.1(b) schematically depicts the layout of the VO_2 -integrated dual waveguide microring resonator. It consists of two straight silicon waveguides and a silicon microring, with the ring partially covered by a VO_2 patch. The waveguide geometry is identical to Fig. 4.1(a). The microring is evanescently coupled to both waveguides. The waveguide cores have a cross-sectional width of 500 nm and a height of 120 nm (with a 100 nm silicon slab thickness). The ring has a bending radius of 5 μm (measured from the waveguide centre) and a coupling gap of 50 nm to the bus waveguides. It is symmetrically positioned equidistant from the two bus waveguides, and the entire device is mirror-symmetric with respect to the vertical xz-plane.

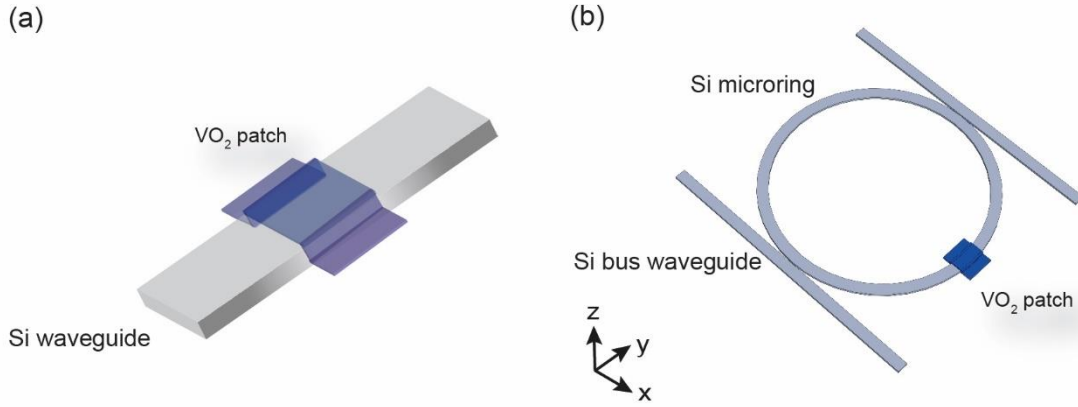


Figure 4.1. Schematic diagram of the VO₂-integrated waveguide and microring resonator. (a) Schematic diagram of VO₂ placed at the top of the waveguide. (b) Schematic diagram of VO₂ integrated microring resonator.

4.2.2 VO₂ refractive index modelling

The majority of the work does not involve calculations within the VO₂ phase transition region, except for Section 4.4. Therefore, for this portion of the study where calculations within the VO₂ phase transition region are required, the Looyenga mixing rule from effective medium theory is introduced to determine the effective refractive index of VO₂ in the transition region.

The concept of the Looyenga mixing rule is that, given the dielectric constants of VO₂ in its two stable phases, the dielectric constant of the intermediate phase, ϵ_{eff} , can be calculated. The Looyenga mixing formula is given as follows [159].

$$\epsilon_{eff}^S = [1 - f(T)] \times \epsilon(ins)^S + f(T) \times \epsilon(metal)^S \quad (4.1)$$

where $\epsilon(ins)$ and $\epsilon(metal)$ are the permittivity of VO₂ at the insulating and metallic phases, respectively. The value S varies from -1 to 1 depending on the shape of the metallic inclusions. Here, S is set as 1/3 as an empirical value for thin-film VO₂ [282].

The metallic fraction $f(T)$ can be empirically considered as a first-order equilibrium which is given by [22]:

$$f(T) = \frac{1}{1 + \exp\left(\frac{w}{K_B}\left(\frac{1}{T} - \frac{1}{T_{half}}\right)\right)} \quad (4.2)$$

where w is an energy scale for the IMT which contains information about the width of the phase change. Therefore, if two IMT regions are identical, the value of w must be the same. Here, T_{half} is the temperature at which half of the film is in the metallic phase and K_B denotes the Boltzmann constant which is $1.38 \times 10^{23} \text{ J}\cdot\text{K}^{-1}$.

The relationship between the w and $f(T)$ is analysed by setting a reference w_0 and a constant T_{half} value. Where the T_{half} value is chosen as 341.15 K (68°C) for calculation which is the typical VO₂ transition temperature. Figure 4.2 shows how the $f(T)$ curve depends on value of w_0 .

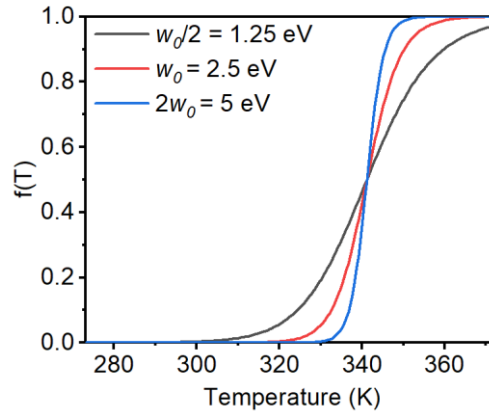


Figure 4.2. $f(T)$ curves as a function of w_0 , where w_0 value is 2.5 eV.

The w_0 value in Fig. 4.2 is 2.5 eV, $f(T)$ will dramatically change at the middle of the transition zone (T_{half}) when the w_0 value is large. The smaller w_0 will lead to a smaller gradient during IMT. If the w_0 value is infinitely small, $f(T)$ will be a constant.

The relationship between the T_{half} and $f(T)$ can be analysed by setting w_0 at 2.5 eV. Figure 4.3 provides the information on how the $f(T)$ curve depends on the value of T_{half} .

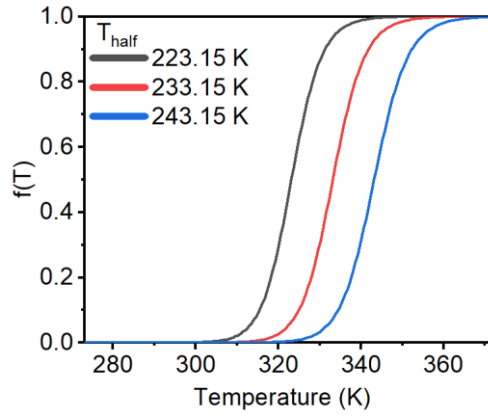


Figure 4.3. $f(T)$ curves as a function of T_{half} , where T_{half} is 223.15 K, 233.15 K and 243.15 K, respectively.

The T_{half} value in Fig. 4.2 is varies between 223.15 K to 243.15 K, it can be seen that the smaller T_{half} shifts $f(T)$ curve to lower temperature and vice versa.

Since the device-level bistability demonstrated in this work is not based on the intrinsic bistability of the material, when the temperature intervals for heating and cooling approach infinitesimally small values i.e., when the hysteresis width approaches zero, the refractive index (n) and extinction coefficient (k) of VO_2 follow the same path during both heating and cooling.

I use the heating curve of VO_2 measured by ellipsometry in previous studies as the data source [154]. At 1550 nm, the complex refractive indices of VO_2 in the low-temperature and high-temperature states are $2.47 + 0.06i$ and $1.78 + 2.47i$, respectively. The T_{half} is 71°C, and the transition temperature range (10 %-90 %) is 67–75 °C. The fitted n and k values for VO_2 during the heating process are shown in Fig. 4.4 (a, b).

In this work, the Looyenga mixing rule is used to explain the refractive index of VO_2 in the intermediate state. It has been validated that, based on the experimental data obtained, once the refractive index of VO_2 in the two stable states and T_{half} are determined, the slope of the transition region has no impact on the conclusions of this study. A comparison of simulation results without the Looyenga equation is provided in the Appendix A5.

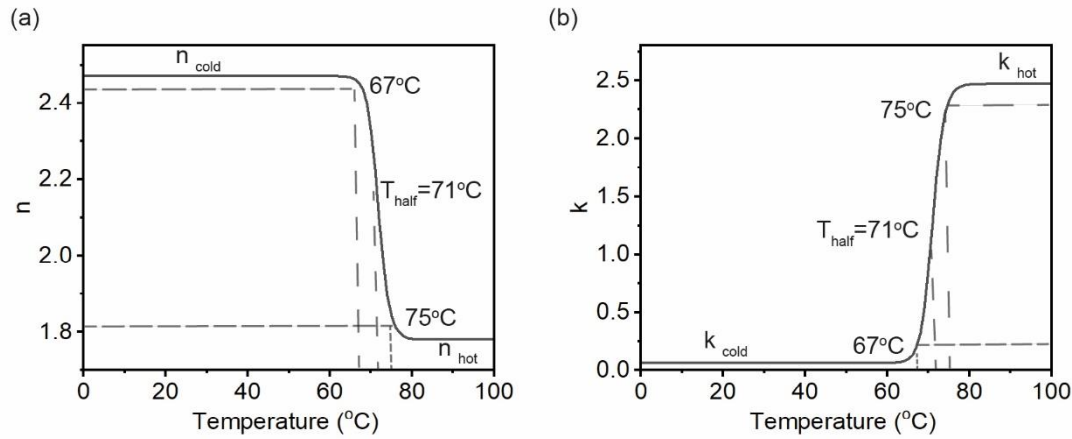


Figure 4.4. Temperature-dependent VO₂ refractive index. (a) Looyenga mixing rule calculated the real part of the refractive index. (b) Looyenga mixing rule calculated the imaginary part of the refractive index.

4.2.3 Running COMSOL on the university supercomputer

As a finite element method (FEM) simulation software, COMSOL typically demands substantial computing memory. In this work, the average memory requirement exceeds 400 GB, making local desktop computation challenging. To address this, the university's fifth-generation supercomputer, 'Iridis 5', was utilised. By accessing the high memory partition offered by the university, I was able to allocate up to approximately 750 GB of memory for the simulations. Detailed specifications and capabilities of the Iridis 5 high memory partition are outlined in Table 4.1.

Table 4.1. Information of Iridis 5 Highmem partition.

Partition name	Highmem
Maximum nodes per user	4
Usable RAM per node	About 750 GB
CPUs per node	64
Maximum wall-time	5 days

Theoretically, utilising all four nodes of the Highmem partition on Iridis 5 could provide up to 3 TB of memory (4×750 GB) and 256 CPUs (4×64). However, due to compatibility issues, the efficiency of multi-node COMSOL simulations is considerably low, often leading to exceeding the maximum

allowed wall-time on Iridis5. Therefore, it is recommended to use a single node of the Highmem partition, which offers 750 GB of memory, for high degree-of-freedom (DOF) COMSOL modelling.

In addition to the high memory requirements, computation time presents another constraint in this project. The maximum wall-time for standard HPC (High-Performance Computing) users is 60 hours, while users with higher permissions, who can access the highmem partition, are allowed up to 120 hours. If a computational job cannot be completed within 5 days, it will automatically fail.

4.2.4 COMSOL run file of Iridis 5

Running COMSOL file on Iridis 5 requires a run file. After computing, a solved file will be generated automatically. Some key run file code with notation is listed in this section. The entire run file code is provided in the Appendix A1.

#SBATCH--time=120:00:00 //wall-time setting

#SBATCH--partition=highmem //computing partition specify

#SBATCH--nodes=1//computing node number specify

#SBATCH--ntasks=64//numbers of CPUs specify

4.2.5 Boundary conditions and material parameters

Figure 4.5 shows the ring resonator structure used in the simulations. The boundary conditions are meticulously defined: 'Input F', 'Input B', and 'Output S' are designated as 'Port' boundary conditions. Surrounding the model is a 1 μm thick infinite element domain, where the outer boundaries are assigned the 'Temperature' boundary condition. For the upper surfaces of the Silicon (Si) bus waveguide, Si microring, Si thin layer, and the VO_2 patch, the boundary condition is set to 'Heat flux'. All remaining boundaries are configured with the 'Scattering boundary condition'. The waveguide structure shares the same boundary conditions. This detailed setup ensures accurate simulation of the device behaviour under various conditions.

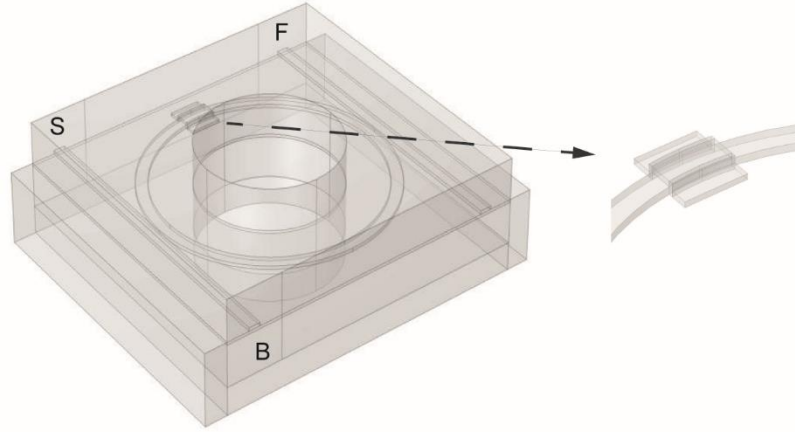


Figure 4.5. Perspective view of VO₂-Si hybrid microring resonator model in COMSOL. The 1 μm thick infinite element domain is covered around the model. The 1.5 μm thick air domain is covered at the top of the model. The SiO₂ substrate is 1.5 μm thick.

Table 4.2 lists all the material properties used in the numerical simulation. The simulation does not include any thermo-optic effect of Si, considering its small coefficient ($1.86 \times 10^{-4} / \text{K}$ [283]) and the relatively low-quality factor of the microring resonances in this device (a few hundred as described in Section 3.2.2).

Table 4.2. Material parameters used in the simulation.

Parameter	Value
VO ₂ refractive index, metallic phase	1.78+2.47i (experimental data)

VO ₂ refractive index, insulating phase	2.47+0.06i (experimental data)
Si refractive index[212]	3.47
SiO ₂ refractive index[284]	1.44
Si heat capacity [285]	705.5 J/Kg · K
Si density [285]	2330 Kg/m ³
Si thermal conductivity[285]	153 W/m · K
SiO ₂ heat capacity[285]	745 J/Kg · K
SiO ₂ density[285]	2200 Kg/m ³
SiO ₂ thermal conductivity[285]	1.38 W/m · K
VO ₂ heat capacity (J/Kg · K) [286]	690 (T < 339 K and T > 341 K) 27763.5 (339 K ≤ T ≤ 341 K)
VO ₂ density[286]	4340 Kg/m ³
VO ₂ thermal conductivity[286]	6 W/m · K
Heat transfer coefficient of Air[287]	5 W/m ² · K

It is worth noting that the total thermal conductivity of a material is given by $K_{\text{total}} = K_{\text{phonon}} + K_{\text{electron}}$. In insulators and semiconductors, phonon thermal conductivity plays a dominant role because these materials contain very few free electrons, meaning heat is primarily transported via lattice vibrations (phonons). In contrast, for metallic materials, according to the Wiedemann–Franz law, thermal conductivity is proportional to electrical conductivity. There has been significant controversy regarding the thermal conductivity of VO₂ in previous studies, as illustrated in Fig. 4.6. Some studies have reported that the total thermal conductivity of VO₂ remains almost unchanged across the metal-insulator transition (MIT), with a value of approximately 6 W/m.K ($\Delta K_{\text{tot}} \sim 0.2$ W/m.K) [288, 289]. However, other studies claim that the electronic thermal conductivity increases by 60 % in the metallic phase, which aligns well with the expected contribution of free electrons to thermal transport [66]. In this work, the thermal conductivity of VO₂ is assumed to be 6 W/(m.K) in both states to be consistent with our previous work and to reduce the nonlinearity of the system [286].

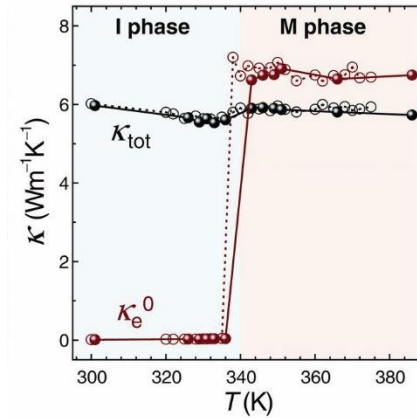


Figure 4.6. Temperature dependence of the measured total thermal conductivity (K_{tot}) and expected electronic thermal conductivity (K_e^0) of VO_2 .

4.2.6 Time-Harmonic EM Heating and two-way coupling

There are four study types for time-harmonic electromagnetic (EM) heating problems in COMSOL:

1. Frequency-Stationary, One-Way Coupled, Electromagnetic Heating
2. Frequency-Transient, One-Way Coupled, Electromagnetic Heating
3. Frequency-Stationary, two-way coupled
4. Frequency-Transient, two-way coupled

The first two study types utilised in the simulations are designed to address linear problems. However, this project involves four different materials: Silicon (Si), Silicon dioxide (SiO_2), Air, and VO_2 . The properties of Si, SiO_2 , and Air are constant, whereas VO_2 exhibits temperature-dependent properties, introducing nonlinearity into the model. To manage this complexity, the two-way coupled Frequency-Stationary and Frequency-Transient study types are employed. These study types are adept at handling scenarios with temperature-dependent material properties.

Depending on the degree of model nonlinearity, these studies can adopt either a low memory consumption segregated approach or a high memory consumption fully coupled approach. In the segregated approach, the simulation iteratively alternates between the electromagnetic

module and the heat transfer module until the convergence criteria are met. On the other hand, the fully coupled approach deals with all couplings within a single, large system in one iteration, requiring more memory but increasing efficiency for solving highly nonlinear problem [290, 291].

Given the large size of the model, which consists of 10 million Degrees of Freedom (DOF), the default solver setting employed is the 'Suggested Iterative Solver'. This solver is advantageous due to its lower memory consumption, typically below 200 GB. However, it is not able to handle large models with nonlinear problems effectively. For time-dependent problems, particularly those involving nonlinearity, the direct solver becomes the only option. The direct solver, while demanding a significant amount of memory (around 520 GB), offers better convergence and the capability to manage nonlinear problems.

Within the direct solver category, there are four options: PARDISO, MUMPS, SPOOLES, and Dense matrix. The latter two are barely used in practice. MUMPS solver has the benefits of providing a multithreaded cluster and slightly more stability, whereas the advantage of PARDISO is known for its faster computation speed. Due to compatibility issues, COMSOL MPI cannot be utilised on the Iridis supercomputer. In this work, the main concern is 'time'. Therefore, considering these factors, the PARDISO solver emerges as the most suitable choice for this particular model.

In COMSOL, there are three main reasons to make the model converge slowly or not converge at all:

1. The load changes too fast.
2. Mesh is not fine enough to analysis the physics field.
3. Model is too large.

After lots of attempts, the most significantly nonlinear component in this model is the step function of the heat capacity. This is evident in part of the log file, as shown in Fig. 4.7. The log indicates that due to the rapid change in heat capacity, the time step in the simulation had to be reduced to an extremely small value of $2.2\text{E-}14$ s. This time step is five orders of magnitude smaller than the required time step.

An important observation is the computation time required for these small time steps. Completing just 197 steps took a duration of 5 days. Given this rate of progress, it becomes apparent that completing the entire computation could potentially require months. This highlights the significant computational demands and challenges posed by the nonlinear aspects of the model, particularly the step function of heat capacity.

```

Step      Time      Stepsize      Res  Jac  Sol Order Tfail NLfail  LinErr  LinRes
197  2.6026e-09  2.2888e-14   7332 592 7332    1    0    101      5.5e-13 3.1e-12
      Group #1:   3666 296 3666
      Group #2:   3666 296 3666
----- Current Progress: 67 % - Assembling sparsity pattern
Memory: 305174/313177 350388/358391

```

Figure 4.7. Part of the log file generated from the Iridis, the step size is 0.00002 ns at 2.6 ns.

By keeping the same amount of area of the origin heat capacity in Fig. 4.8 (a), the heat capacity is therefore Gauss fitted in Fig. 4.8 (b) to decrease the model nonlinearity and computation time.

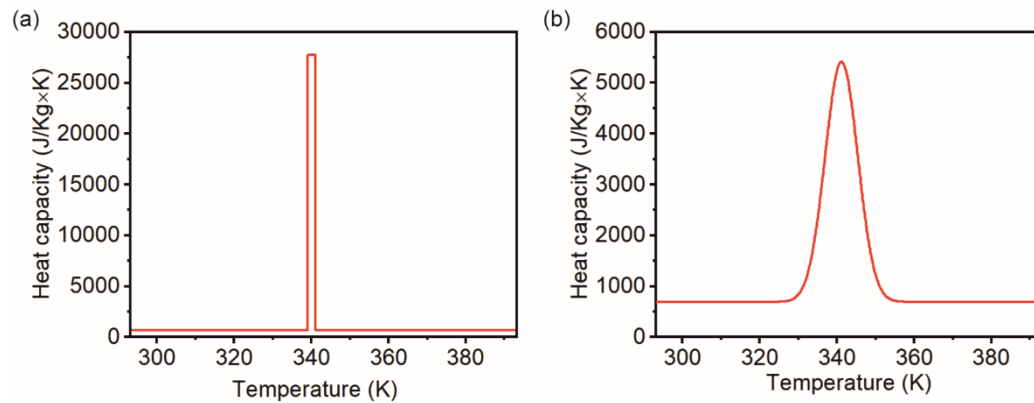


Figure 4.8. The original heat capacity data in Table 4.2, Ref [286], the heat capacity changes dramatically in the very short temperature range. (b) The Gauss-fitted heat capacity to overcome the difficulty in the simulation, where the transition range is between 60°C and 80°C. Both (a) and (b) have the same amount of area.

4.2.7 Study of comparison between Lumerical and COMSOL

Due to the relatively long computation times associated with COMSOL, Lumerical is utilised for the optimisation of optical simulations in this study. Lumerical offers significantly faster

computation speeds, allowing for more efficient exploration of various simulation parameters and optimisation strategies. This efficiency is particularly beneficial when conducting extensive parametric studies is necessary.

(a) Mesh generation in Lumerical

In Lumerical FDTD, the default rectangular mesh is generated based on the Mesh Accuracy slider in the software's meshing interface. Mesh Accuracy is an indicator used by the FDTD adaptive meshing algorithm to determine the mesh size, with 8 levels of precision: 1 represents low accuracy, and 8 represents high accuracy (smaller mesh size). Mesh Accuracy level 1 corresponds to 6 mesh points per wavelength (ppw). Level 2 corresponds to 10 ppw, and so on, with each increment on the slider adding 4 ppw. The wavelength here refers to the shortest wavelength within the material.

For example, with an input light wavelength of 1550 nm entering silicon waveguide at Mesh Accuracy level 8, the mesh is divided into 34 points per wavelength. This results in a mesh size of $1550 / 3.47 / 34 \approx 13$ nm. Thus, the minimum mesh size at Mesh Accuracy 8 is 13 nm, consistent with the actual measurements in the model (Appendix A4). The actual mesh sizes for a 1550 nm input light in a silicon waveguide at Mesh Accuracy levels 1 to 8 are shown in Table 4.3.

In numerical simulations, a larger mesh size leads to faster simulation run times but less accurate results, whereas a smaller mesh size results in slower run times, and greater computational resource consumption, but more accurate results. Therefore, finding a balance between speed and accuracy can not only improve the accuracy of subsequent work but also help future researchers quickly perform simulations. In this study, Mesh Accuracy level 3 was chosen as a reasonable starting point for subsequent mesh refinement studies [292-294].

Table 4.3. Conversion between mesh accuracy levels and actual mesh sizes in Lumerical FDTD for a 1550 nm input light in a silicon waveguide.

Mesh accuracy	Mesh size (nm)
1	74
2	45
3	32

4	24
5	20
6	17
7	15
8	13

(b) Mesh convergence study in Lumerical

The main factors influencing the simulation output results include the following: 1. Mesh, 2. Material properties, and 3. Boundary conditions. Optical waveguides, being simple in geometry and small in volume, are commonly used optical components and were initially chosen for mesh convergence studies in Lumerical. Figure 4.9 (a) shows a top view of the straight waveguide used for the mesh convergence study in Lumerical. The rib waveguide has a length of 8 μm , a width of 500 nm, a standard SOI height of 220 nm, and an etch depth of 120 nm. The input light source mode is the fundamental TE mode. Figure 4.9 (b) shows the transmission values for the straight waveguide at a 1550 nm input wavelength as the mesh accuracy increases from 3 to 8. It can be seen that different mesh accuracies have almost no impact on the results, indicating that lower mesh accuracy can be used for simulating straight waveguides in Lumerical to obtain accurate results more quickly.

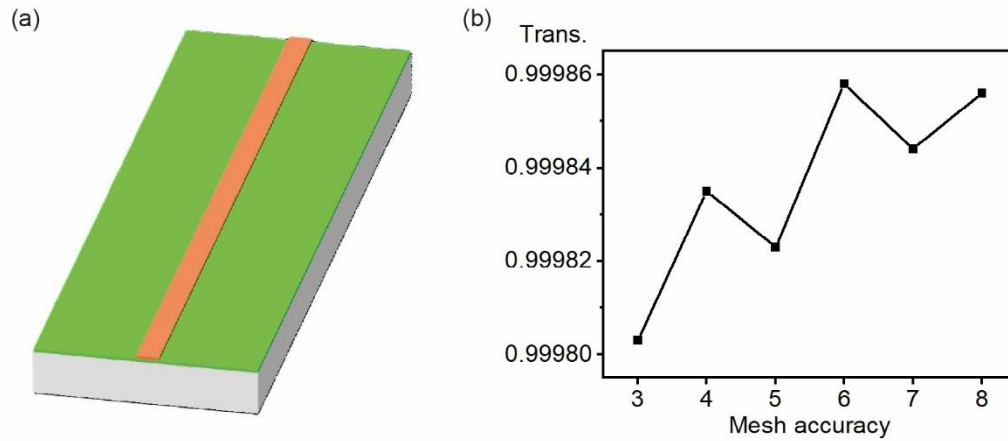


Figure 4.9. (a) Top view of the straight waveguide geometry used for the mesh convergence study in Lumerical FDTD. (b) Transmission values for the straight waveguide at a 1550 nm input wavelength as the mesh accuracy increases from 3 to 8.

Since the main simulation part in this work is based on a VO₂-patched silicon microring resonator, and silicon microring is a crucial component in many optical memory works, detailed mesh convergence research is essential. However, to my best knowledge, little study has thoroughly investigated mesh convergence in silicon microring. Therefore, conducting a mesh convergence study on silicon microring resonators not only supports this work but also provides valuable simulation guidelines for future research.

Figure 4.10 (a) shows the silicon microring used for the mesh convergence study. The microring has a radius of 5 μm , the straight waveguide has a length of 16 μm , and the coupling gap between the straight waveguide and the microring is 50 nm. The remaining geometric dimensions and light source settings are consistent with the previous straight waveguide simulation. Figure 4.10 (b) shows the drop port transmission spectra of the microring at input wavelengths from 1535 to 1555 nm for different mesh accuracies. The blue dashed line represents the simulation results in COMSOL with the same geometric dimensions. As seen in Fig. 4.10 (b), unlike the previous straight waveguide, the resonance peaks of the microring transmission spectrum are highly sensitive to mesh accuracy. The resonance wavelength does not monotonically blue or red shift with increasing mesh density. Even with the mesh accuracy set to the maximum value of 8, no significant convergence of the results is observed.

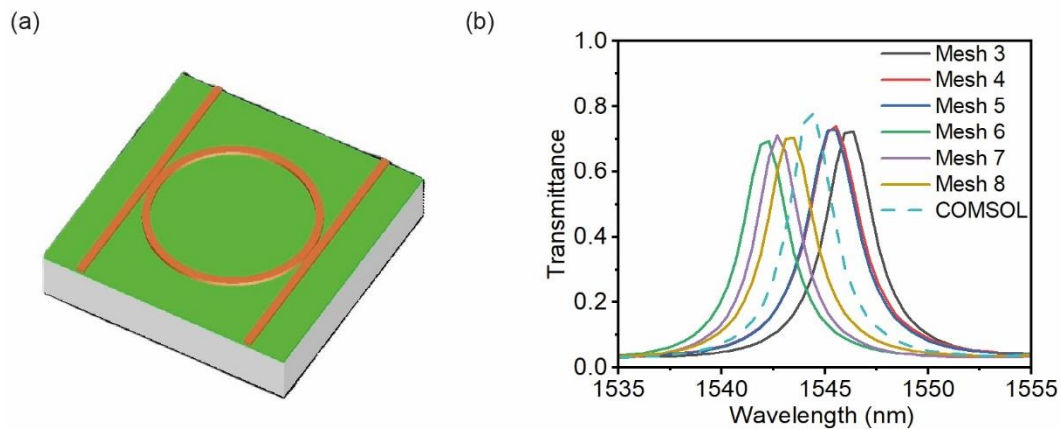


Figure 4.10. (a) Geometry of the silicon microring resonator used for the Lumerical mesh convergence study. (b) Drop port transmission spectra of the microring at input wavelengths from 1535 nm to 1555 nm for different mesh accuracies.

The boundary conditions used in Lumerical microring optical simulations are Perfectly Matched Layers (PML). As an open boundary condition, PML can simulate an infinite space by absorbing incident electromagnetic waves and preventing them from reflecting into the main simulation area. A thinner PML might not perfectly absorb the incident electromagnetic waves, so increasing the PML thickness was attempted to improve mesh convergence.

Figure 4.11 shows the comparison of results after adjusting the PML thickness for mesh accuracies of 4 and 8 in the silicon ring simulation. According to the official information, higher mesh densities often require more PML layers [295]. Therefore, I increased the default PML layers from 8 to 22 for mesh accuracy 4, and to a maximum of 64 layers for mesh accuracy 8, ensuring effective absorption. However, the results showed that the transmission spectra before and after adjusting the PML thickness were almost identical (Fig. 4.11 (a)), and the resonance wavelengths were almost unchanged (Fig. 4.11 (b)).

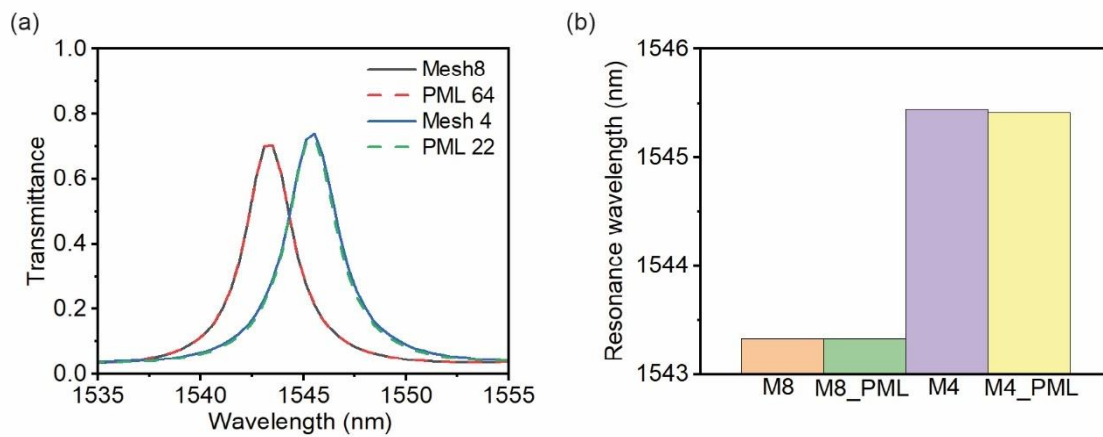


Figure 4.11. (a) Transmission spectra of the silicon microring resonator for mesh accuracies of 4 and 8, comparing the effects of different PML thicknesses. (b) Resonance wavelengths corresponding to the transmission spectra in (a) illustrate that adjusting the PML thickness has minimal impact on the resonance wavelength, as the spectra and resonance positions remain nearly unchanged.

Lumerical provides various meshing options, such as conformal variant 0/1, staircase, dielectric volume average, and Yu-Mittra method. Different meshing methods were tested in this section for convergence. The default conformal variant 0 setting is suitable for most FDTD simulations, while conformal variant 1 is claimed to achieve better convergence when multiple materials are

present in the simulation region. Other meshing methods are recommended only for specific cases or when boundary conditions are not PML [296].

Figure 4.12 shows the transmission spectra and resonance wavelengths for a pure silicon ring (a, b) and a silicon ring covered with a VO₂ patch (c, d) at mesh accuracies of 4, 5, and 6, comparing the default conformal variant 0 with the adjusted conformal variant 1. In (c) and (d), the VO₂ patch is in its insulating phase. It can be observed that at different mesh densities, the resonance wavelengths and corresponding transmission values remain almost unchanged when altering the meshing refinement options. This demonstrates that the default conformal variant 0 is adequate for microring simulation.

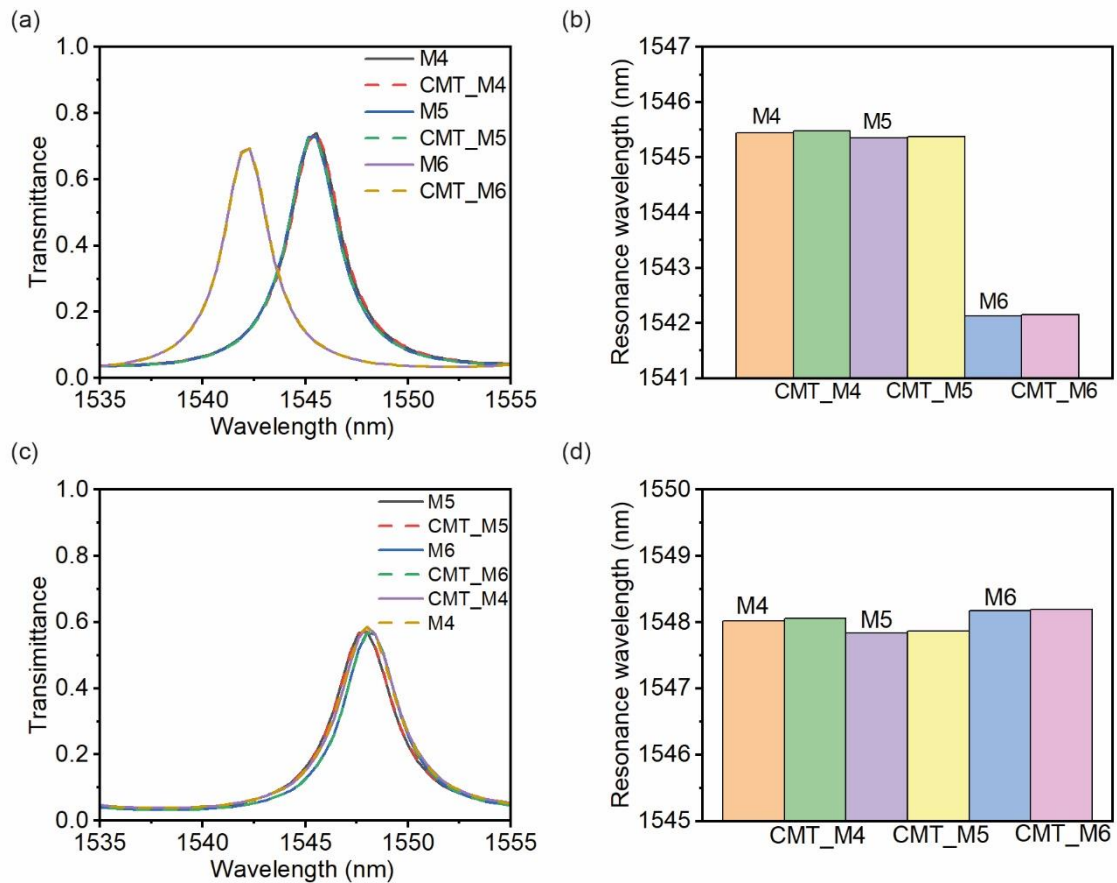


Figure 4.12. (a) Transmission spectra of a silicon ring at mesh accuracies 4, 5, and 6, comparing the default conformal variant 0 (M4, M5, M6) with the adjusted conformal variant 1 (CMT_M4, CMT_M5, CMT_M6). (b) Resonance wavelengths corresponding to the transmission spectra in (a). (c) Transmission spectra of a silicon ring with a VO₂

patch in its insulating state at mesh accuracies 4, 5, and 6, comparing the default conformal variant 0 (M4, M5, M6) with the adjusted conformal variant 1 (CMT_M4, CMT_M5, CMT_M6). (d) Resonance wavelengths corresponding to the transmission spectra in (c).

Increasing simulation time and decreasing the auto shut-off min parameter are other factors that can affect the simulation results. Extending the simulation time allows the simulation to run longer, ensuring that the observed results are stable. The auto shut-off min parameter is another time control setting, typically used to terminate the simulation process and prevent over-simulation. Reducing the auto shut-off min can achieve higher accuracy or lower error by allowing the simulation to run longer.

Figure 4.13 compares the transmission spectra and resonance wavelengths of a silicon ring for mesh accuracies of 5 and 6 using the default settings (5000 fs simulation time and $1e-5$ auto shut-off min) and the adjusted settings (500000 fs simulation time and $1e-8$ auto shut-off min). As seen in Fig. 4.13 (a), there is no change in the transmission spectra before and after adjusting the parameters. Similarly, Fig. 4.13 (b) confirms that the resonance wavelengths remain unchanged, verifying the stability of the results with the adjusted settings.

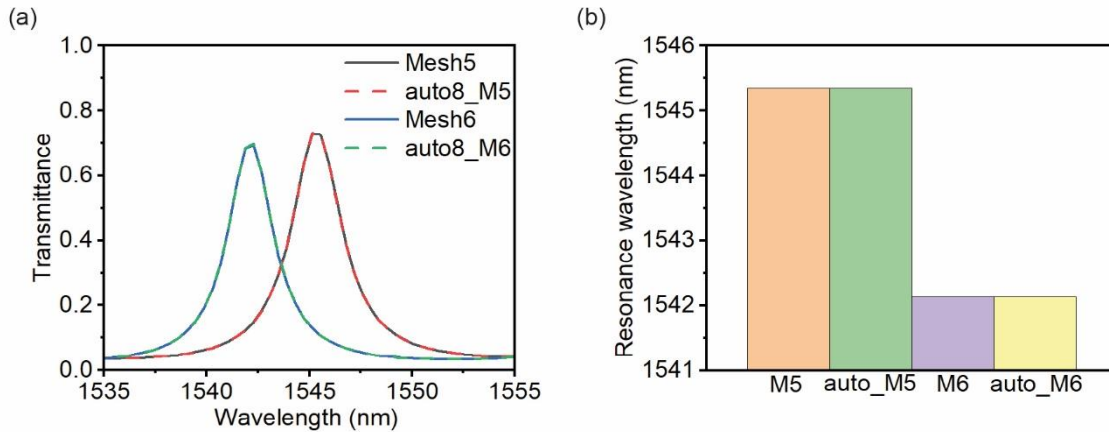


Figure 4.13. (a) Transmission spectra of the pure silicon ring at mesh accuracies 5 and 6, comparing the default settings (Mesh5 and Mesh6) with the adjusted settings (auto8_M5 and auto8_M6). (b) Resonance wavelengths corresponding to the transmission spectra in (a).

Unlike COMSOL, the mesh shape in Lumerical is rectangular and not adaptive to the geometry itself. Consequently, when changing the mesh, the curved parts of the structure may appear with different ‘shapes’, leading the system to take an intermediate value between the two different media when calculating the effective refractive index in the ring structure. Figure 4.14 shows the different effective refractive indices on the outer side of the ring for mesh accuracy of 5 (Fig. 4.14 (a)) and 6 (Fig. 4.14 (b)). Therefore, a possible approach is to refine the mesh until the error becomes negligible.

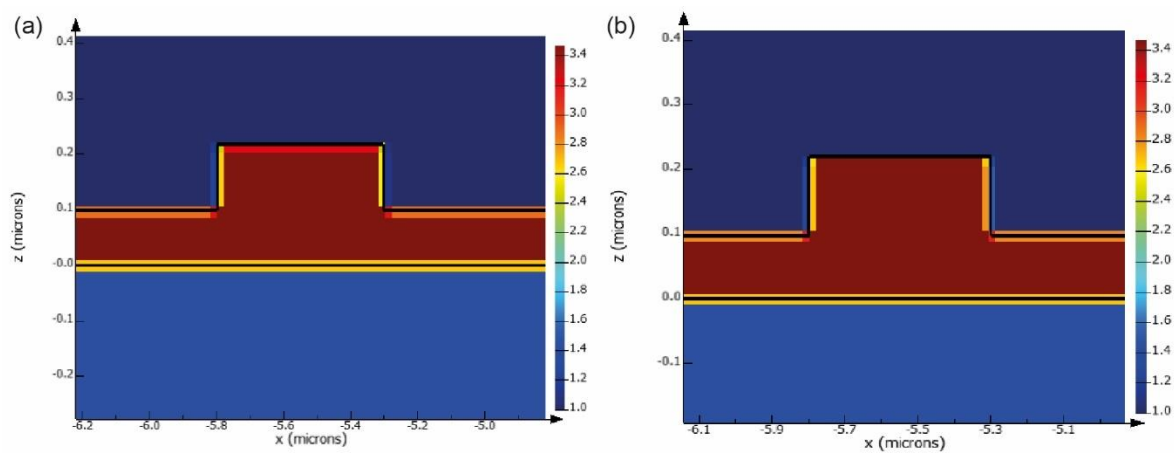


Figure 4.14. Effective refractive index distribution on the outer side of the ring structure at different mesh accuracies. (a) Mesh accuracy is 5. (b) Mesh accuracy is 6.

As shown in Table 4.3, in Lumerical FDTD, the mesh density is generated by the Mesh Accuracy slider. At the maximum slider value of 8, the actual mesh size is 13 nm. Further mesh refinement requires adding custom meshes to the model. However, excessively small meshes can drastically increase computational resources and time. As shown in Fig. 4.15 (a), when reducing the mesh size of the pure silicon ring model from 13 nm to 5 nm, the computation time increases from 1.2 hours to 20.4 hours.

Thanks to multithreading optimisation in Lumerical, large models can be parallelised across multiple nodes during computation. Figure 4.15 (b) shows the computation time for the pure silicon ring model using different numbers of Iridis nodes. Using 10 nodes speeds up the

computation by approximately 6 times compared to using a single node. However, using too many nodes can significantly increase queue time. Using 7 batch nodes is considered a compromise between computation speed and queue time and is used in subsequent simulations.

Figure 4.13 (c) presents a detailed mesh convergence study for silicon microring, showing how different mesh sizes affect the resonance wavelength of the ring resonator. When reducing the mesh size from the initial 32 nm to 13 nm (corresponding to Mesh Accuracy 3-8), the resonance wavelength fluctuates irregularly around the COMSOL simulation resonance wavelength of 1544.4 nm (red dashed line). However, as the mesh size continues to decrease, the resonance wavelength at a Lumerical mesh size of 12 nm (1544.9 nm) is closest to the COMSOL value. The resonance wavelength stabilises around 1545.3 nm for mesh sizes smaller than 10 nm, differing by approximately 0.9 nm from the COMSOL result.

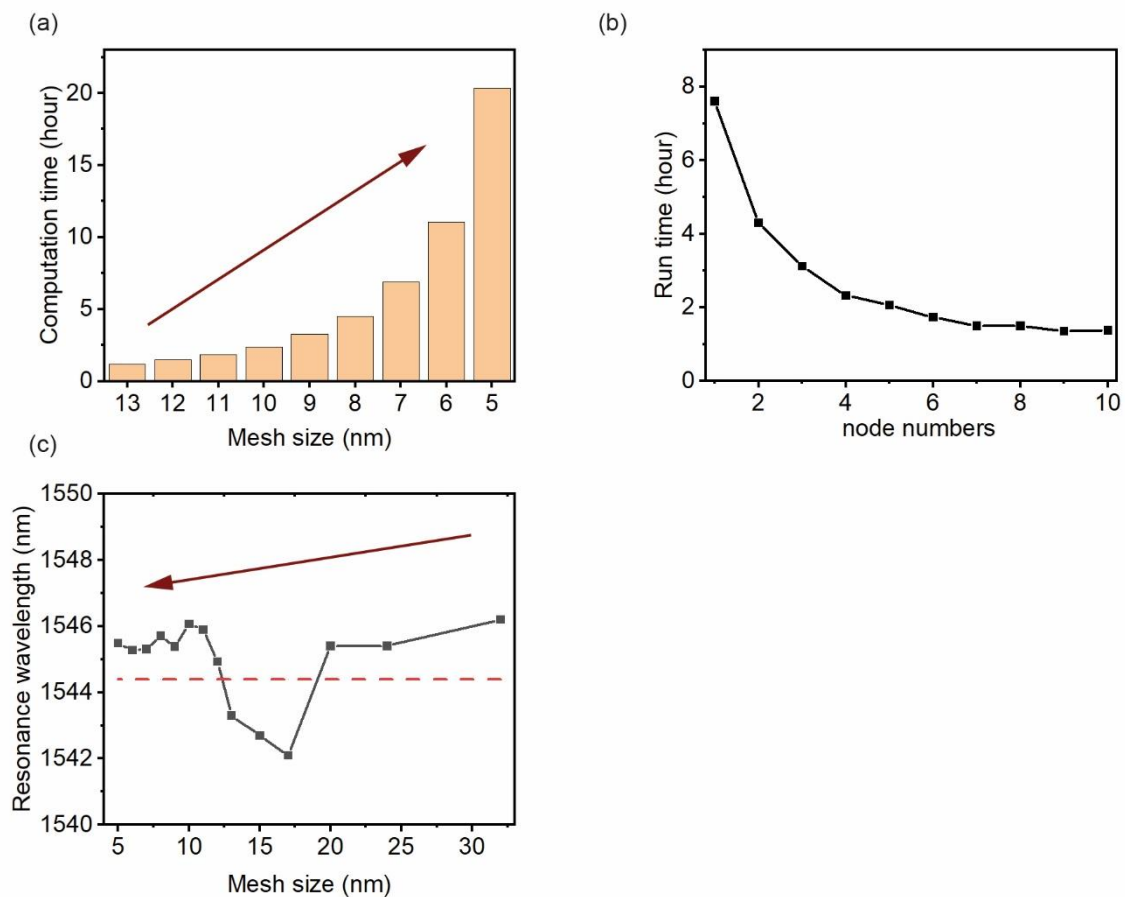


Figure 4.15. (a) Computation time for the silicon ring as the mesh size decreases from 13 nm to 5 nm, indicated by the red arrow, showing a significant increase in computation time, from 1.2 hours to 20.4 hours. (b) Run time for the silicon ring model using different numbers of Iridis nodes. (c) Detailed mesh convergence study

for silicon microring. The red dashed line represents the resonance wavelength obtained from the COMSOL simulation (1544.4 nm).

In the ring with a VO₂ patch, similar results were observed. As shown in Fig. 4.16 (a), when the Lumerical mesh size decreases from 32 nm to 13 nm, the resonance wavelength fluctuates between 1548.4 nm and 1546.3 nm. However, as the mesh size continues to decrease, the resonance wavelength at a Lumerical mesh size of 12 nm (1547.2 nm) closely matches the COMSOL result of 1547.1 nm. The resonance wavelength stabilises around 1547.4 nm for mesh sizes smaller than 10 nm, differing by approximately 0.3 nm from the COMSOL result. Figure 4.16 (b) shows the transmission spectra comparison between the Lumerical simulation and COMSOL at a mesh size of 12 nm, demonstrating a high degree of similarity. These results confirm the effectiveness and necessity of further refining the mesh beyond mesh accuracy 8 in the ring model, providing insights for future simulation work.

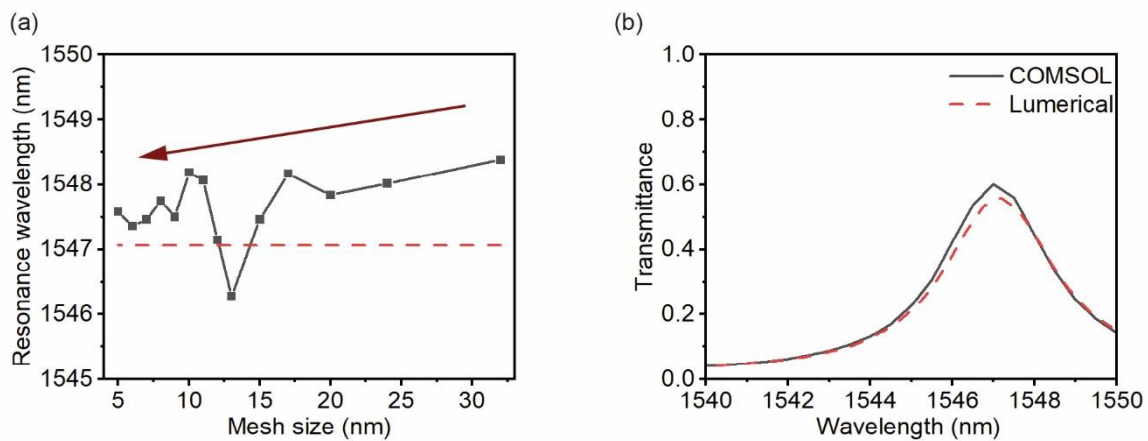


Figure 4.16. (a) Resonance wavelength fluctuations for the ring with a VO₂ patch as the Lumerical mesh size decreases from 32 nm to 13 nm. The red arrow indicates the trend of decreasing mesh size, and the red dashed line represents the COMSOL result. (b) Transmission spectra comparison between Lumerical and COMSOL simulations at a mesh size of 12 nm, showing high similarity.

(c) Discussion

The adaptive meshing mechanism in Lumerical offers different levels of mesh refinement, ranging from coarse to fine. Simulation results indicate that even using the system's default highest precision mesh (Mesh accuracy = 8) may not converge to a relatively stable result, especially for the resonance peak positions, which are highly sensitive to simulation conditions.

In this study, I explored various optimisation strategies to improve the accuracy of microring resonator simulations by comparing the results from Lumerical and COMSOL (Table 4.4).

When using PML as boundary conditions for optical simulations, it is commonly believed that increasing the PML thickness is an effective method to enhance absorption and reduce boundary reflections. However, our simulation results show that even significantly increasing the number of PML layers does not necessarily result in noticeable changes in the transmission spectrum or resonance wavelength. Additionally, while extending the simulation time and reducing the auto shut-off time are common strategies to improve simulation stability, this study indicates that these methods do not significantly improve the results for microring structures.

This section emphasises that although theoretically, mesh density, mesh configuration, and simulation time collectively determine the accuracy of simulations in Lumerical, our comprehensive evaluation of these factors reveals that mesh size plays a dominant role. In some cases, even using the default smallest mesh size is insufficient to achieve complete convergence of the results. This is because, even with maximised mesh density, the fixed rectangular mesh shape can lead to inaccurate effective refractive index calculations for certain geometries (e.g., the edges of the microring) due to the non-adaptive nature of the mesh. This work provides valuable experiences for future simulation works.

Table 4.4. Evaluation of Lumerical optimisation methods in optical ring resonator simulation.

Optimisation method in ring resonator simulation	Effectiveness
Thicker PML	No
Mesh construction method	No
Increasing simulation time	No
Decreasing auto shut-off time	No
Mesh size refinement	Yes

4.3 Device-level bistability in a straight waveguide

To illustrate the concept of device-level bistability, we numerically simulated the optical and thermal properties of a Si rib waveguide with a segment covered by a VO₂ thin film (Fig. 4.15). Figures 4.15 (a) and 4.15 (b) are schematics of the device, where the VO₂ patch is in its entirely insulating and metallic phases, respectively. The VO₂ patch is 90 nm thick, 1300 nm long along the waveguide, and 2000 nm wide. The rest of the waveguide structure is described in the previous section 4.2.1.

The optical and thermal properties of the device shown in Fig. 4.15 were obtained using a finite element method-based numerical simulation tool (COMSOL Multiphysics). The simulations presented in this section correspond to the steady-state behaviour of the device, without considering time-dependent evolution. As the analysis progresses, more advanced simulation will be introduced, which are detailed in later sections.

Figure 4.15 (c) shows the transmission of the device in its two pure phases over a 20 nm wavelength range centred around 1550 nm. Both spectra are flat, indicating that the device exhibits no resonances within this spectral range. While the transmission reaches approximately 0.87 in the insulating phase, it drops significantly to around 0.11 in the metallic phase. This stark contrast highlights the substantial difference in the VO₂ patch's light absorption capabilities between the two phases.

Based on these spectra, we selected the wavelength of 1550 nm, a standard telecommunications wavelength, and analysed the dependence of the VO₂ patch's temperature on the input laser power. Figure 4.15 (d) shows the average temperature of the portion of the VO₂ patch in direct contact with the Si waveguide, as this region interacts with the evanescent field and is optical significant. Here, we define the phase transition temperature window as spanning from 67°C to 75°C (10 %-90 % range, from our previous work), and highlight it as a horizontal blue band in Figure 1(d). Below this range, the VO₂ patch is entirely insulating, while above it, the patch is entirely metallic. Both temperature lines exhibit a linear dependence on input power and extrapolate to the ambient temperature of 20°C.

Device-level bistability is clearly visible in the power range of 4 to 27 mW, where the red and the black lines intersect the blue band. Within this range, any given input power can sustain two stable states of the device, with the VO₂ patch at either the fully insulating or fully metallic phase. The optical manifestation of this bistability is shown in Fig. 4.15 (e), where two transmission levels (0.11 and 0.87) co-exist for the same input laser power. It is worth noting that different definitions can introduce slight variations in the bistable input power range because the temperature distribution within the VO₂ patch depends on its phase. Similar phenomenon was reported in a recent publication [130, 297], where the Appendix A7 illustrates the bistable performance based on the definition of the average temperature across both ends of the patch .

To gain deeper insight into the mechanism of device-level bistability, we selected an input power of 5 mW and analysed the corresponding electric field and temperature distributions, as shown in Figs. 4.15 (f)-(i). Figs. 4.15 (f) and 4.15 (g) show the electric field strength at the middle height of the rib waveguide. This stark difference in attenuation results in a substantial difference in the VO₂ temperature shown in Figs. 4.15 (f) and 4.15 (g). It is evident that the insulating phase (Fig. 4.15 (h)) causes significantly smaller optical attenuation compared to the metallic phase (Fig. 4.15(i)).

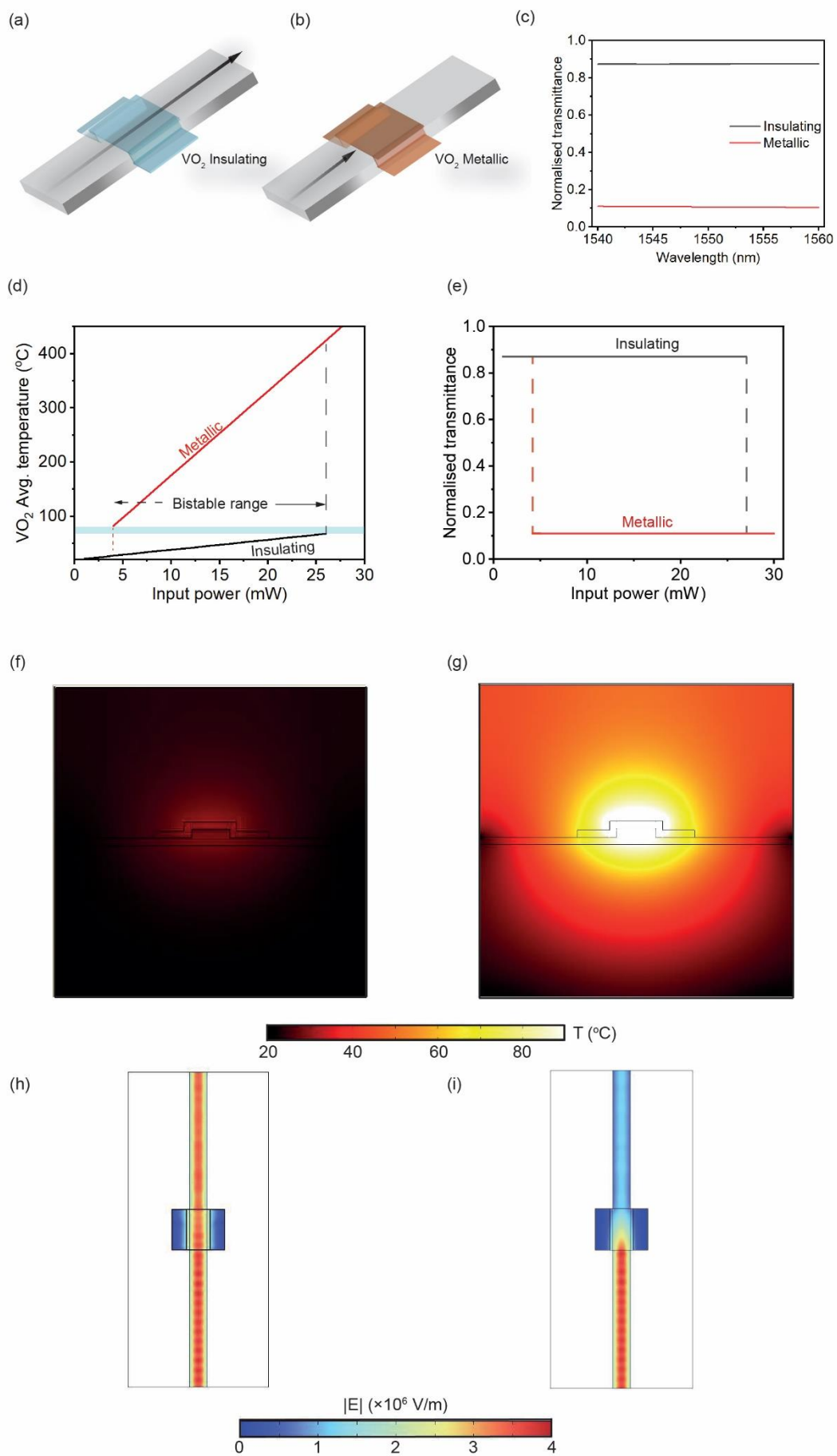


Figure 4.15. Schematic diagram and analysis of bistable behaviour in a VO₂-integrated waveguide. (a) Schematic diagram of insulating VO₂ placed at the top of waveguide. (b) Schematic diagram of metallic VO₂ placed at the top of waveguide. (c) Waveguide transmission level when VO₂ patch at different phases. (d) Thermal bistability without introducing VO₂ material hysteresis. The input wavelength is at 1550 nm. The blue band represents the VO₂ material transition range. (e) Corresponding optical bistability from panel (c), with input power ranging from 4 mW to 27 mW. The black line represents the high-transmittance state when VO₂ is in the insulating phase, while the red line indicates the low-transmittance state when VO₂ is in the metallic phase. (f) and (g) Cross-sectional temperature field distribution of the straight waveguide with VO₂ in (f) the insulating phase and (g) the metallic phase, under the same 1550 nm wavelength and 5 mW power. The cross-sections are taken at the midpoint of the waveguide. (h) and (i) Top view of the electric field distribution in the straight waveguide with VO₂ in (h) the insulating phase and (i) the metallic phase, under a 1550 nm input wavelength and 5 mW input power. The slice is taken at the middle of the rib waveguide.

The relationship between the optical attenuation and the temperature of the VO₂ patch is described by Equation 4.3, which links the heat power density $Q(r)$ to the permittivity ε and the electric field strength $|E(r)|$ for any location r within the patch [298, 299]:

$$Q(r) = \frac{\omega}{2} \text{Im}(\varepsilon) \varepsilon_0 |E(r)|^2 \quad (4.3)$$

It shows that the heat power density is directly related to the local electric field intensity and the imaginary part of the dielectric constant. Where ε_0 is the permittivity of free space, ω is the angular frequency of the input light and $|E(r)|^2$ is the intensity of the electric field. The imaginary part of the permittivity, $\text{Im}(\varepsilon)$, is calculated as:

$$\text{Im}(\varepsilon) = 2nk \quad (4.4)$$

Although the electric field strength $|E(r)|$ is relatively low across the entire patch in the metallic phase, the imaginary part of the permittivity $\text{Im}(\varepsilon)$ is 8.8, much higher than its value of 0.3 in the insulating phase. As a result, the conversion of optical power into thermal dissipation is much more pronounced in the metallic phase, leading to a higher VO₂ temperature.

Figure 4.16 illustrates the optical bistability of straight waveguides that have VO₂ patches of varying lengths on top. First, when the VO₂ patch is 500 nm long (Fig. 4.16 (a)), the input power range for bistable operation is approximately 5–40 mW. In the insulating phase, the device’s normalised transmission at the output is about 0.93, whereas it drops to about 0.45 in the metallic phase.

When the VO₂ patch length is increased to 1000 nm (Fig. 4.16 (b)), the upper limit of the bistable power range drops to 31 mW. This is because a longer patch expands the light–VO₂ interaction region, making the phase transition easier to initiate and sustain. Meanwhile, the longer metallised VO₂ region increases the overall propagation loss, further reducing the transmission to 0.18. Extending the patch length to 1500 nm (Fig. 4.16 (c)) narrows the bistable window to around 20 mW, but raises the device’s extinction ratio to 10.31 dB.

In Fig. 4.16 (d), the black curve shows how the bistable power range decreases with increasing patch length, from 124 mW at 100 nm down to 20 mW at 1500 nm, following a roughly logarithmic trend. This indicates that a longer VO₂ patch more readily initiates and completes the phase transition, thereby shrinking the power window in which bistability can be maintained. Meanwhile, the red curve reveals that the extinction ratio is positively correlated with patch length, rising monotonically from about 0.62 dB at 100 nm to 10.31 dB at 1500 nm. In other words, the longer the patch, the greater the transmission contrast between the insulating and metallic states, producing a more pronounced “ON/OFF” effect. As shown in Fig. 4.16, achieving a higher extinction ratio requires sacrificing some portion of the bistable power range, whereas retaining a wider operational window entails accepting a lower extinction ratio. Meanwhile, the short patch length requires larger input power to trigger the IMT, from a practical standpoint, overly large input power should be avoided to prevent excessive heating that could harm the device.

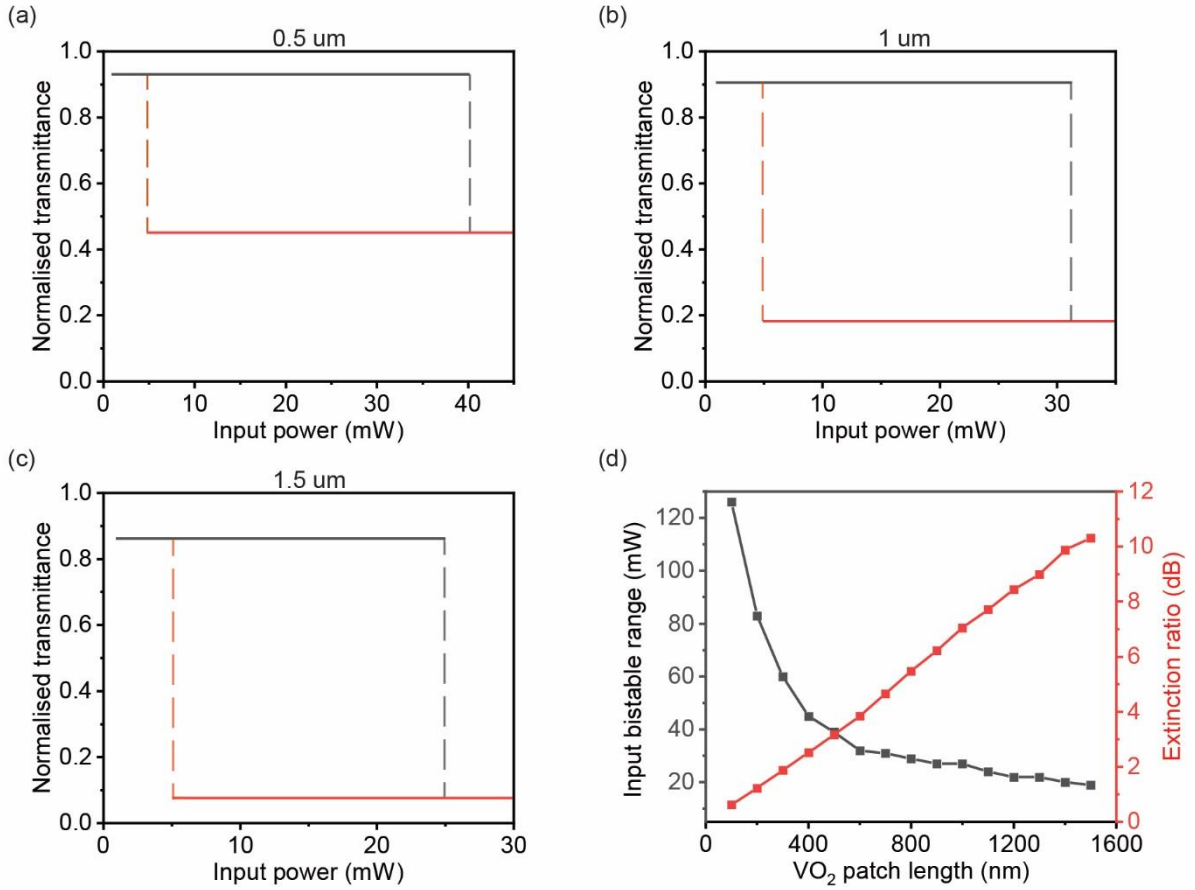


Figure 4.16. Device level optical bistability in straight waveguides integrated with VO₂ patches of different lengths, (a) 500 nm, (b) 1000 nm, and (c) 1500 nm. Black and red solid lines represent the transmission level when the VO₂ patch fully switches to insulating and metallic states, respectively. (d) Relationship between VO₂ patch length with bistable input power range and the corresponding extinction ratio.

4.4 Device-level bistability on VO₂-Integrated microring resonator

Since achieving bistability in straight waveguide devices requires a high-power threshold, and the significant temperature jump after the phase transition could potentially cause irreversible damage to the device, it is crucial to explore alternative structures that enable bistability at lower input power thresholds. Previous studies have identified resonant optical cavities as promising candidates for low-power operation [300]. Additionally, the compact structure of microring resonators makes them particularly advantageous for applications requiring precise optical

signal control, such as optical memory and neuromorphic computing. In this section, we explore the device-level bistable behaviour of VO₂-integrated microring resonators.

Figure 4.17 (a,b) schematically depicts the layout of the VO₂ integrated dual-waveguide MRR. The VO₂ patch, which could be conformally coated onto the microring using atomic layer deposition (ALD), has a uniform thickness of 90 nm. It has a planar size of 1.5 μm (along the x axis) by 1.3 μm (along the y axis) viewing from the top. It is positioned at equal distance from the two bus waveguides, and the whole device possesses mirror symmetry with respect to the vertical xz plane. The dimension of the waveguide and Si microring are described in the previous section 4.2.1.

The device-level optical bistability is depicted in Figs. 4.17 (a) and 4.17 (b), via their contrast in both the light propagation and the phase of the VO₂ patch. Laser light is launched into the device at port B , and is collected at port S . In Fig. 4.17 (a), most of the B input couples into the microring rather than reaching the output port S . The VO₂ patch stabilises at the insulating phase. Conversely, the same B input (i.e., identical in wavelength and power) produces a much larger S output in Fig. 4.17 (b), where the VO₂ patch stabilises at the metallic phase. Figs. 4.17 (a,b) depict two stable states under identical input, and the device consequently possesses optical bistability and optical memory.

Figures 4.17 (c) and 4.17 (d) show the S/B and S/F transmission, respectively, for identifying the working wavelengths of the device. Figure 4.17 (c) shows the S/B transmission at the two pure VO₂ phases, and a whispering gallery mode (WGM) resonance is observed in both curves. The central wavelength and the minimal transmission of the WGM resonance are 1547.0 nm and 0.05, respectively. Its quality factor (Q factor) is 487, extracted from Lorentz fitting of the resonance peak. The value is limited by both the bending loss of the microring (due to its relatively small radius) and the optical absorption of the VO₂ patch. As the VO₂ patch changes from the insulating phase to the metallic phase, the resonance wavelength changes from 1547.0 to 1543.0 nm. This wavelength shift reveals a change in the effective refractive index of the microring, which originates from a change in the refractive index of the VO₂. The Q factor decreases from 487 to 228, as the metallic phase is more absorptive than the insulating phase. Across the whole 10-nm wavelength range simulated here, the largest optical modulation induced by the phase transition

occurs at the WGM peak wavelength of 1547.0 nm. This wavelength is consequently chosen as the working wavelength for port *B*.

Similarly, Fig. 4.17 (d) shows the S / F transmission, which is used to identify the working wavelength of port *F*. The two WGM resonances also appear in the two spectra here, but as peaks instead, as *S* is a drop port for *F*. Because configuration #1 in afterwards Table 4.1 requires $S / F > T_{th}$, a large S / F value should be chosen to provide a good margin for T_{th} . We consequently set the working wavelength of port *F* at 1547.2 nm, which has a large S / F value of 0.60 and a slight difference of 0.2 nm from the working wavelength of port *B*. Introducing this small wavelength difference is mainly to highlight that the inputs of *B* and *F* do not need to be temporally coherent for the device to function. It also allows for these two input signals (i.e., the unconditioned and the conditioned stimuli, respectively, after the conditioning) to be separated based on wavelength in subsequent signal processing, which could benefit certain applications in the future.

Under the above-mentioned working wavelength, by feeding power to *B*, as shown in Fig. 4.17 (e), the average temperature of the VO₂ patch embedded in the microring resonator exhibits a clear hysteresis loop as the input power increases and decreases, confirming thermal bistability. The transition window marked in blue represents the temperature range over which VO₂ undergoes its phase change. In Fig.4.17 (f), the corresponding optical bistability is demonstrated by the normalised transmittance as a function of input power. When the input power increases, the VO₂ patch transitions from the insulating to the metallic phase, resulting in a sharp increase in transmission due to increased optical absorption. Conversely, when the input power decreases, the transmission gradually returns to its low-transmission state as the VO₂ reverts to its insulating phase. The distinct paths followed during the power-up and power-down cycles provide clear evidence of optical bistable behaviour.

Moreover, the bistability phenomenon shown in Figure 4.17 can also be qualitatively explained in Equation 4.3. When the input optical power in the waveguide gradually increases, the thermal power density slightly increases as the material properties remain unchanged. When VO₂ is continuously driven by photothermal energy to reach the phase transition threshold temperature (the bottom line of the blue band), a positive feedback phenomenon begins to occur. At this point,

the material starts to transition from the insulating state to the metallic state, which leads to an increase in the absorption coefficient. VO_2 then absorbs more optical energy and converts it into thermal energy, forming a self-accelerating process that sharply increases the temperature, causing VO_2 to rapidly transition from the insulating to the metallic state [301].

When the input optical power in the waveguide gradually decreases, VO_2 remains in the metallic state, and the imaginary part of the permittivity stays constant, resulting in a slight decrease in thermal power density. As it passes through the transition range, the imaginary part of the permittivity initially does not change much, and the thermal power density continues to decrease slightly. Once the VO_2 temperature approaches to the bottom line of the blue band, the imaginary part of the permittivity sharply decreases, leading to a rapid drop in temperature below the phase transition point.

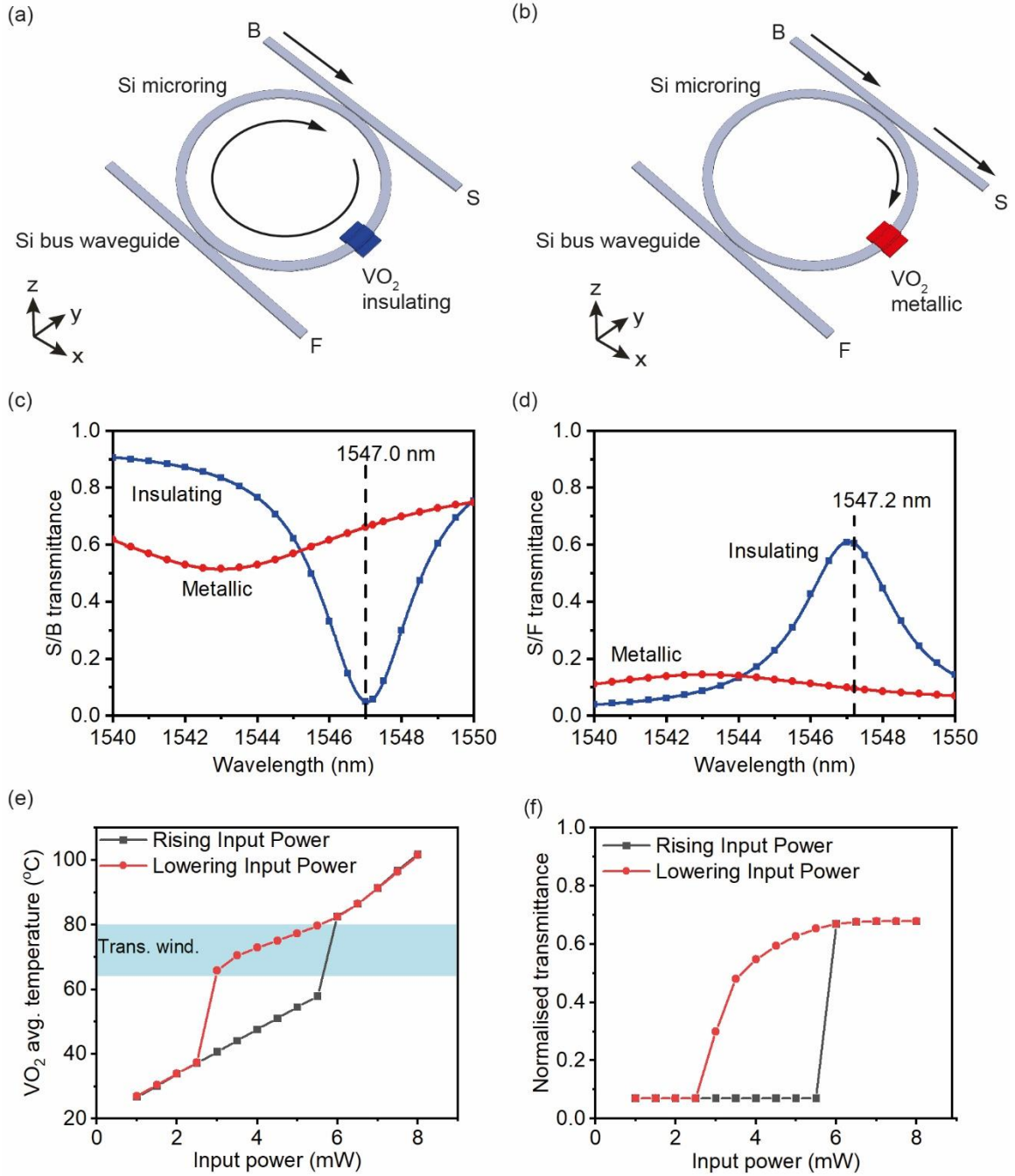


Figure 4.17. VO₂-Si hybrid microring resonator that possesses optical bistability. The Si microring, partly covered by a thin film patch of VO₂, is evanescently coupled to straight bus waveguides on either side. The whole device resides on the SiO₂ BOX layer (buried oxide layer, not depicted) of a SOI (silicon-on-oxide) wafer. The device possesses two stable states, where the VO₂ patch is in either (a) the low-temperature, insulating phase, or (b) the high-temperature, metallic phase. The black arrows indicate the light propagation directions. Notably, only port B has input and the input remains identical across these two stable states. (c) Spectra of S / B transmission.

The VO₂ temperature is assumed to be homogeneous, with the material at either the insulating or the metallic phase. The simulated transmission (dots) is fitted using the Lorentz function (lines). The wavelength used in the optical conditioning is specified using the vertical dashed line. (d) Corresponding S / F transmission spectra. (e) Thermal bistability is shown by the average temperature of the VO₂ patch as a function of input power, displaying a hysteresis loop. The transition window (Trans. wind.) highlights the temperature range over which the phase transition occurs. (f) Corresponded optical bistability is shown by the normalised transmittance versus input power, showing distinct paths for raising and lowering input power.

4.4.1 Analysis of VO₂ side part effect on the device performance

Considering the future device fabrication, the VO₂ patch in this work is designed like a “bridge”, coated on the top of the silicon micro ring. The surface temperature distribution of the cross-section of the VO₂ patch is plotted in Fig. 4.18. It can be seen that the temperature field of either insulating or metallic VO₂ is mostly distributed on the patch surrounding the Si microring.

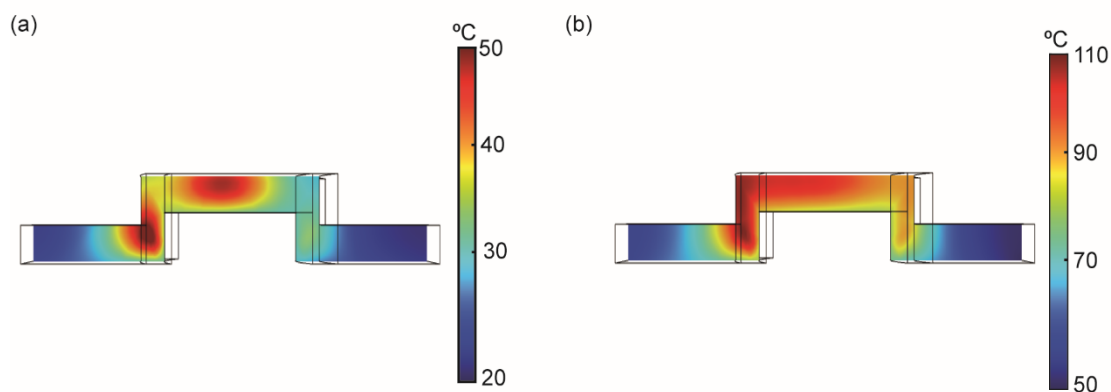


Figure 4.18. Surface temperature distribution of cross-section of VO₂ patch. The VO₂ is at either (a) the insulating phase or (b) the metallic phase.

Figure 4.19 shows the transmission spectra for all four configurations after the removal of two side parts from the VO₂ patches. A noticeable leftward shift in the resonant frequency is observed following this modification. Despite this shift, by selecting two new modulation wavelengths, the device performance, especially the optical contrast, is effectively maintained at 0.55. This observation indicates that the VO₂ patch surrounding the Silicon microring is the primary contributor to the optical and thermal performance of the device.

Consequently, only the VO₂ patch surrounding the Si microring will be taken into account in the simulation used in this work that involves temperature volume averaging. This approach ensures that the analysis is concentrated on the most impactful component of the device, leading to more accurate outcomes.

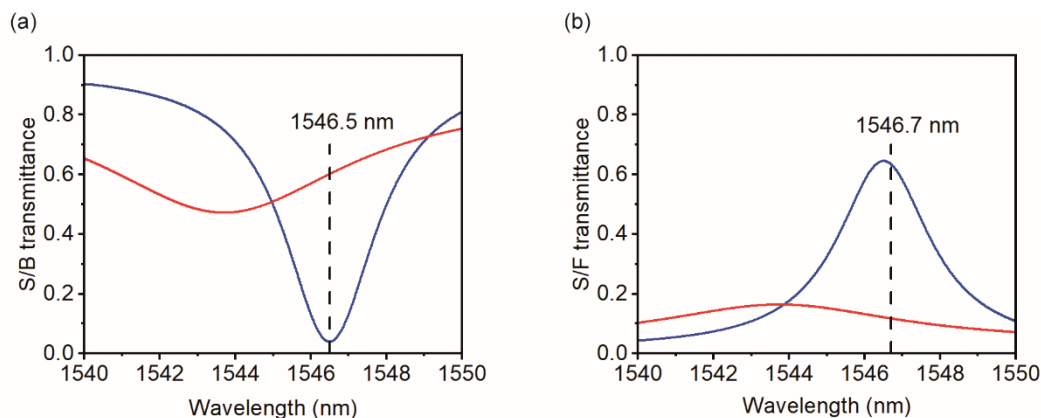


Figure 4.19. Transmission spectra obtained at output port S when there is no side part of VO₂ patch, the input launched from (a) port B and (b) port F. The VO₂ is at either the insulating or the metallic phase. Two vertical dashed lines specify the wavelengths used for optical modulation.

4.4.2 Implementation of photonic associative learning in microring resonator

After demonstrating device-level bistability in the VO₂-integrated microring resonator, we now explore how to utilise this bistable behaviour for associative learning. The Pavlov experiment demonstrated the existence of associative learning, involving two types of stimuli: in most cases, one stimulus is biologically relevant (unconditioned stimulus – US, food), while the other is biologically neutral (conditioned stimulus – CS, bell). Before training, the dog salivates only in response to the US and not to the CS. During training, the CS and US are presented simultaneously to train the dog to salivate, thereby establishing an association between the CS and US. After training, the CS alone can trigger the dog's salivation, a process known as conditioning, with the behaviour of salivating in response to the CS referred to as a conditioned response (CR). When the CR is repeatedly triggered without the US, this associative learning may fade, and the disappearance of the association between CS and US is called extinction. In fields

such as neuromorphic computing, associative learning can be further divided into short-term and long-term. Inspired by the classical conditioning demonstrated in Pavlov's experiment, the dual-waveguide microring device provides a platform for implementing short-term VO₂ photonic associative memory (VPAM). By leveraging the phase transition of VO₂ to modulate light transmission between two stable states, the microring resonator coupled with two waveguides can effectively mimic short-term associative learning. Based on this device layout in Fig. 4.17, Table 4.5 lists all four configurations of the VPAM required to demonstrate photonic associative learning. In the original biological experiment, presenting food and ringing a bell constitute two types of stimuli. Their optical analogues in the VPAM are input at port *F* (for food) and port *B* (for bell), respectively. Simultaneously, the VPAM counterpart of the dog's salivation is the output at port *S* (for salivation). Consequently, the response of the device to an optical stimulus can be conveniently described as transmission *S* / *F* and *S* / *B*, which denotes the output *S* induced by the input *F* and *B*, respectively. A specific transmission level T_{th} is used to identify the state of the output.

Table 4.5. The optical transmission and the VO₂ phase required to implement photonic associative learning in the VPAM. The threshold value T_{th} distinguishes false and true (or equivalently digital zero and digital one) in the output. A difference in the VO₂ phase between configurations #2 and #4 is required to implement optical memory in the device. The VO₂ phase of the other two configurations are determined in subsequent numerical simulation.

Input configuration	Learning procedure	Output requirement	VO ₂ phase
#1, only from <i>F</i>	US	$S / F > T_{th}$	
#2, only from <i>B</i>	CS	$S / B < T_{th}$	Insulating
#3, from both <i>F</i> and <i>B</i>	US+CS	$S / F + S / B > T_{th}$	
#4, only from <i>B</i>	CR	$S / B > T_{th}$	Metallic

More specifically, the optical transmission of the VPAM needs to show this contrast: it is below T_{th} before the conditioning (input configuration #2), whilst it is above T_{th} after the conditioning (configuration #4). These two requirements are expressed as $S / B < T_{th}$ and $S / B > T_{th}$, for before and after the conditioning, respectively. Based on the original biological experiment, the other

two requirements are $S / F > T_{th}$ (configuration #1) and $S / F + S / B > T_{th}$ (configuration #3). The full set of these requirements is listed in the third column of Table 4.5.

The final column of Table 4.5 highlights our strategy to optically replicate Pavlov's experiment in our VPAM. It is to map the classical conditioning observed in the dog onto the phase transition of VO_2 . This strategy enables us to identify the optical equivalent of the biological associative memory within our device. It is revealed in configurations #2 and #4 of the table, where the VO_2 patch exhibits different phases. As the VPAM operates in the linear optics regime, this phase contrast is necessary for the device to possess optical bistability. The analysis of the following two sections further associates configurations #2 with the insulating phase and configurations #4 with the metallic phase.

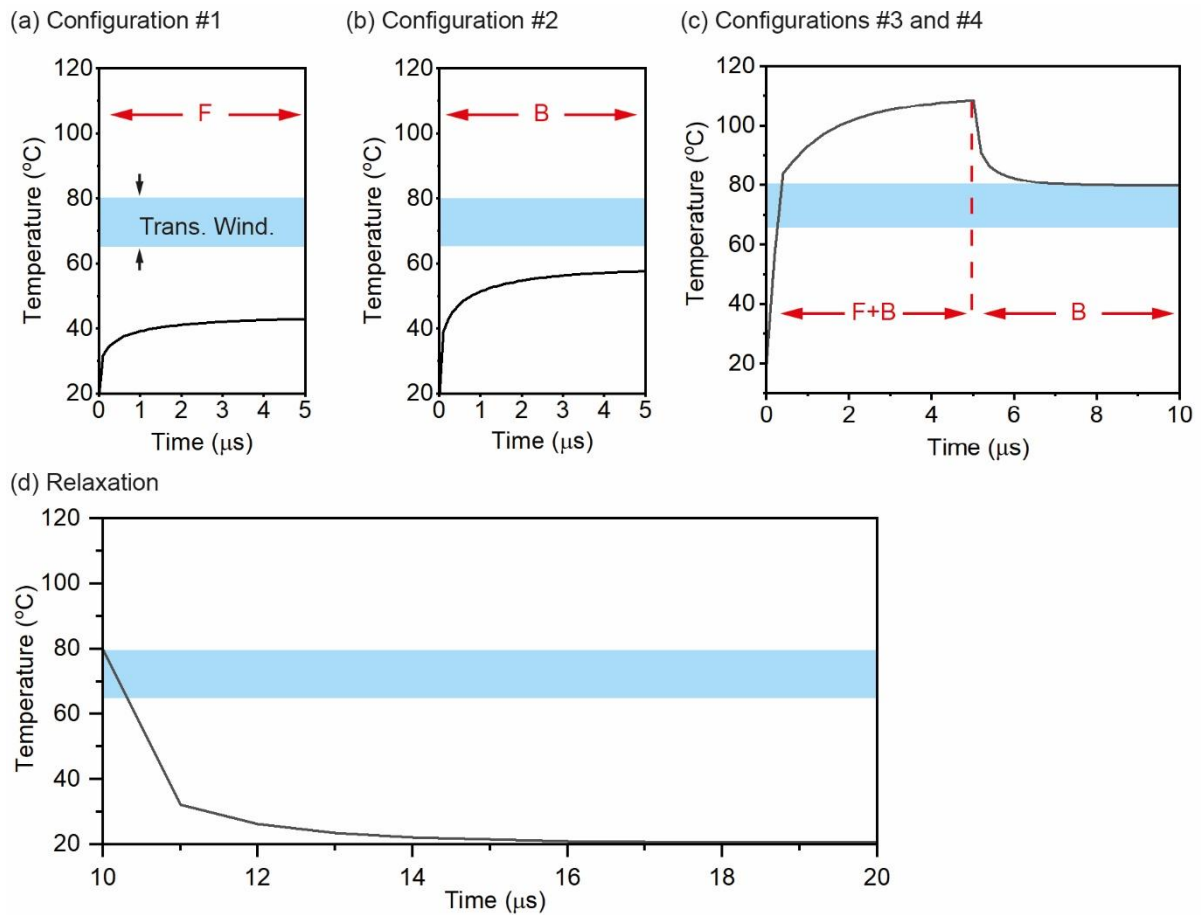


Figure 4.20. Optical conditioning at the microsecond scale. The time dependence of the average temperature of the VO_2 patch is numerically simulated under different input configurations. The input is (a) only from port F , (b) only from port B , (c) from both ports F and B for 5 μs, after which only from port B . The input power of a single port is 5.5 mW. (d) Relaxation, where no input stimulus applies to the system. The

horizontal blue band highlights the largest temperature window for the VO₂ phase transition that the optical conditioning can tolerate.

Figure 4.20 illustrates the temporal behaviour of short-term associative learning using a resonance wavelength around 1550 nm (same wavelength in Fig. 4.17 c,d), with an input power set at 5.5 mW, which lies within the bistable input range depicted in Fig. 4.17. Although this is not the only power level within the bistable range, a lower input power would result in a slower response time, while a higher input power would exceed the bistable range. Figure 4.20 (a) shows the average temperature of the optically significant part of the VO₂ film under input *F*. The input is initiated at time zero and remains at 5.5 mW for 5 μ s. The VO₂ temperature experiences an immediate rise from the ambient temperature of 20°C. At the end of the 5 μ s period, it reaches 45.0°C. A similar time dependence is seen in Figure 4.20 (b), where the input changes from *F* to *B*. The VO₂ temperature steadily ascends from the ambient temperature to 57.6°C at the end of the 5 μ s period, this temperature below the phase transition temperature window (depicted as the blue band in Figure 4.20).

Figure 4.20 (c) shows that the VO₂ can reach temperatures above the blue band and transit to the metallic phase, once *F* and *B* are launched simultaneously into the device. Similar to Fig.4.17, the temperature ascends steadily from time zero and reaches 108.5°C at 5 μ s. Input *F* is then withdrawn, and the VO₂ temperature immediately decreases. It gradually stabilises at 79.7°C at 10 μ s.

Figure 4.20 (d) shows the average temperature of the VO₂ patch over time in the absence of input excitation (i.e., the "relaxation" process). Starting from 10 μ s, the input is completely removed, causing the VO₂ temperature to drop rapidly. During the entire relaxation process, the VO₂ temperature drops rapidly from 80°C to 32°C in 1 μ s, and then gradually decreases, and approaches the ambient temperature of 20°C in the following 5 μ s.

It is worth noting that, in order to reach the steady-state temperatures the input is sustained for a relatively extended duration (here 5 μ s) in all the simulation. As seen in Fig. 4.20 (c), this time period exceeds what is actually essential for the VPAM to function. The VO₂ temperature reaches the top of the blue band within 0.4 μ s, and this is the time required for the VPAM to acquire photonic associative memory at the input power level of 5.5 mW. The corresponding energy consumption for the optical conditioning is consequently 4.4 nJ (calculated at 5.5 mW \times 0.4 μ s \times

2 input channels). Additionally, based on Figs. 4.17 (e,f), once the VO₂ temperature exceeds the upper limit of the blue band, the association can be maintained even if the input power is reduced, as long as it remains within the bistable range.

Besides, although the fastest reported speed for device-level VO₂ photothermal switching is on the order of hundreds of nanoseconds [302], the switching time of the insulator-to-metal transition (IMT) in VO₂ could potentially be reduced to pico- and femtosecond time scales. This could be achieved by precisely tuning the excitation source to selectively trigger the electronic Mott transition, minimising parasitic heat generation and the structural phase transition (SPT).

4.4.3 Optimisation strategy for optical contrast

Evaluating the performance of VPAM typically relies on three key factors: 1. Optical contrast; 2. Power consumption; and 3. Computational speed. Since the VO₂ patch used in this work is driven by photothermal excitation, optimising power consumption and computational speed requires the use of COMSOL multiphysics simulations. However, multiphysics simulations are computationally intensive and time-consuming, making global optimisation impractical for this work. Therefore, the optimisation of the photonic memory device in this work focuses primarily on optical contrast, using Lumerical FDTD for optical optimisation.

In this work, optical contrast is defined as the difference in optical transmission at the resonant wavelength between the metallic and insulating phases of the VO₂ material. Specifically, we calculate the transmission difference for both the saliva/bell (S/B) and saliva/food (S/F) configurations, and the optical contrast is determined by taking the smaller of the two values. For example, if the difference in S/B is 0.5 but S/F is 0.46, the optical contrast is defined as 0.46.

$$\text{Optical contrast} = \min\left(\Delta T_{\frac{S}{B}}, T_{\frac{S}{F}}\right) \quad (4.5)$$

Improving optical contrast enhances the distinction between the two states, which is crucial for achieving stable optical bistability. To achieve this, the following key parameters need to be optimised:

(a) Coupling gap optimisation

The coupling gap directly affects the coupling coefficient k . Reducing the coupling gap increases the coupling strength, allowing more light to couple into the ring resonator, resulting in a more pronounced difference in transmitted light intensity and thus improving optical contrast. However, in this work, since there are two input ports (located at the Input and Add ports) and one output port (located at the Drop port), simply decreasing or increasing the coupling gap will not straightforwardly improve overall performance. Increasing the transmittance on one side could reduce the performance on the other side (Figure 4.21). Therefore, optimising the coupling gap requires balancing the performance between the two ports. Based on discussions with our cleanroom engineers, 50 nm was selected as the starting point for the minimum coupling gap scan, as this is a practical value that can be achieved using electron beam lithography and subsequent etching processes. The transmission value is extracted based on the same strategy in the previous section, where the raw simulation results are provided in Appendix A6.

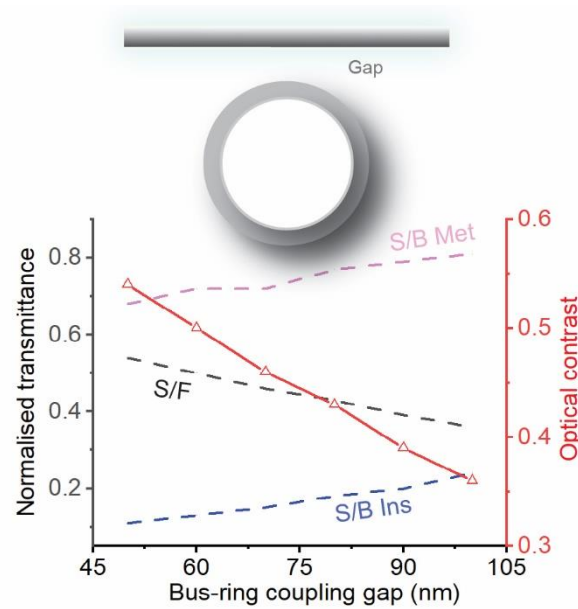


Figure 4.21. Relationship between the waveguide-ring coupling gap, port transmission, and device contrast. The VO_2 patch length is fixed at 1300 nm, and its thickness is fixed at 90 nm.

(b) VO_2 patch coverage fraction

The coverage of the VO_2 patch significantly affects the effective refractive index of the ring resonator. As the coverage increases, the phase transition of VO_2 can induce different resonance frequency shifts in the two states, leading to two distinct optical outputs at the same input wavelength, thereby enhancing optical contrast. Higher coverage increases absorption contrast because more light interacts with the VO_2 . However, excessive VO_2 coverage can introduce

significant insertion losses and lowering overall contrast (Fig. 4.22). Additionally, previous studies have shown that overly long VO₂ patches not only increase the switching energy but also add optical losses, further impacting device performance [303]. Since the different fractions of VO₂ patch will affect the N_{eff} and hence affect the resonance wavelength, the operation wavelength is picked differently with different lengths of VO₂ to make sure the best contrast value is obtained, the raw simulation results are provided in Appendix A6.

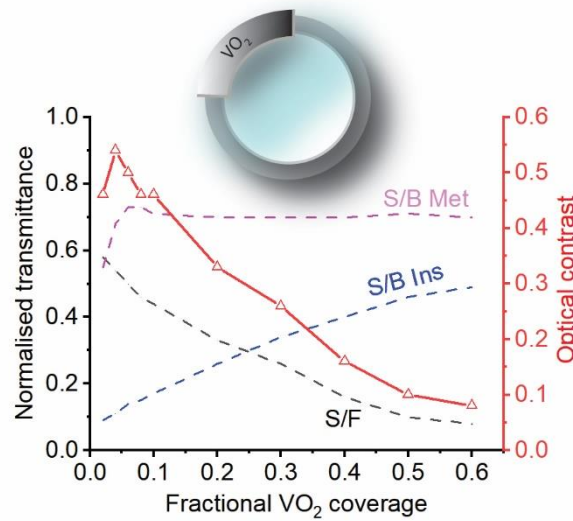


Figure 4.22. Relationship between the VO₂ patch length, port transmission, and device contrast. The coupling gap is fixed at 50 nm, and the VO₂ thickness is fixed at 90 nm.

(c) VO₂ Thickness

As shown in Fig. 4.23, the thickness of the VO₂ layer also has a significant impact on optical contrast. A thicker VO₂ layer can increase light absorption in both phases, thereby amplifying the absorption difference between the insulating and metallic states, which enhances optical contrast. However, excessive absorption, especially in the metallic phase, can lead to a reduction in overall transmission, increasing optical losses and degrading device performance. Since the VO₂ patch in this work is deposited using atomic layer deposition (ALD), a thicker VO₂ layer will significantly increase deposition time and cost. Therefore, a thickness range of 20-100 nm was chosen for the scanning range in this study, as it avoids the poor optical response caused by directly depositing a too-thin VO₂ layer on Si, while also preventing excessive time and cost consumption. Similar operation wavelength strategy is applied to obtain the best contrast performance, the raw simulation results are provided in Appendix A6.

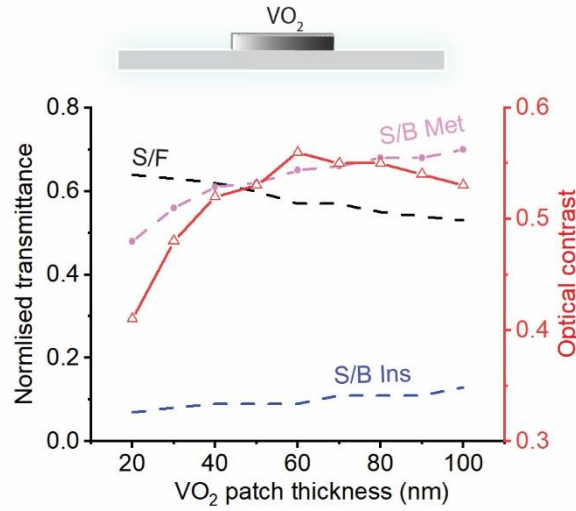


Figure 4.23. Relationship between the VO₂ patch thickness, port transmission, and device contrast. The patch length is fixed at 1300 nm, and the coupling gap is fixed at 50 nm.

Figure 4.24 shows the optimisation results for the optical contrast of the VO₂ integrated microring resonator as a function of VO₂ coverage fraction (%) and VO₂ thickness (nm) for different coupling gaps between the ring and the bus waveguide (50 nm, 70 nm, and 90 nm). The optimisation results show several important trends. For the smallest coupling gap (50 nm), higher optical contrast is observed for VO₂ thicknesses in the range of 40-80 nm, particularly at coverage fractions between 6% and 10%.

As the coupling gap increases to 70 nm and 90 nm, the maximum achievable contrast generally decreases. The plot for the 70 nm gap indicates that optical contrast is still relatively high for coverage fractions between 4 % and 8 %, but the overall contrast values are lower compared to the 50 nm gap configuration. This is likely due to reduced coupling efficiency as the gap widens, resulting in less coupling coefficient. For the largest gap of 90 nm, most of the contrast values are lower, regardless of the VO₂ coverage fraction and thickness. This result highlights that the coupling strength diminishes significantly as the gap increases, reducing the optical contrast.

The results indicate that the highest optical contrast is achieved at a coupling gap of 70 nm, with a VO₂ thickness of 20 nm and a coverage fraction of 6 %, resulting in a contrast of 0.59. However,

it is noteworthy that the point corresponding to a gap of 50 nm, a thickness of 40 nm, and a coverage fraction of 8 % yields a very similar contrast of 0.58, just 1 % lower. Importantly, the point at 50 nm gap exhibits a higher degree of tolerance to variations in VO_2 thickness and coverage fraction compared to the 70 nm configuration. The surrounding points in the parameter space for the 50 nm gap configuration maintain relatively high contrast values, indicating that slight deviations in VO_2 thickness or coverage fraction during fabrication would not significantly degrade the optical contrast. This feature makes the 50 nm gap configuration more advantageous for practical device fabrication, as it offers greater robustness against fabrication imperfections.

In contrast, the configuration with a gap of 70 nm, although achieving the highest contrast value, has less favourable surrounding points, implying that small deviations from the optimal thickness or coverage fraction could lead to a more significant drop in contrast. Therefore, while the 70 nm configuration may offer a slightly higher contrast, the 50 nm gap configuration is more reliable and practical for achieving consistent performance in real-world applications. Overall, the optimisation suggests that the best trade-off between high optical contrast and fabrication tolerance is achieved with a 50 nm coupling gap, a VO_2 thickness of 40 nm, and a coverage fraction of 8 %.

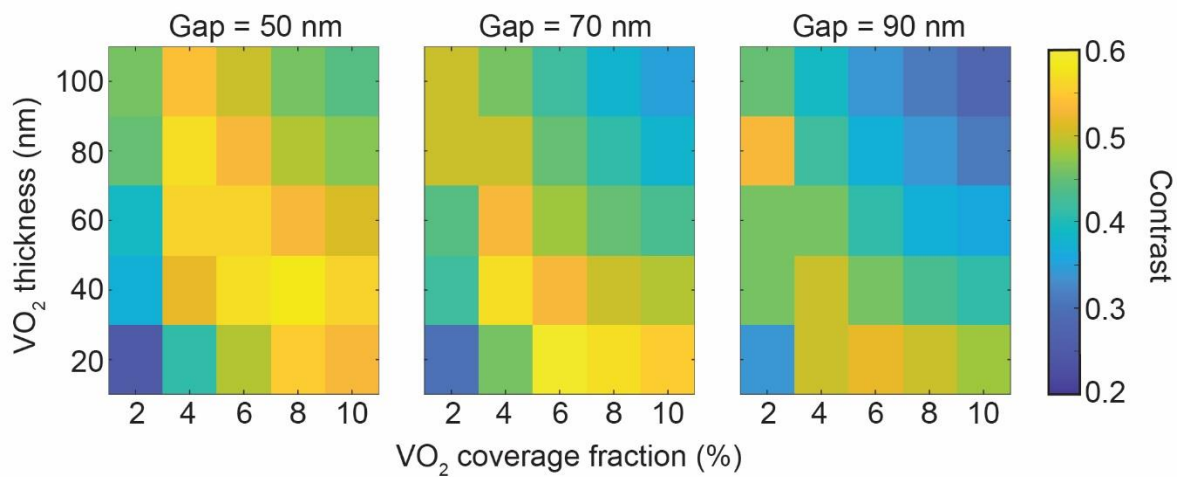


Figure 4.24. Optimisation of optical contrast for a VO_2 -integrated microring resonator as a function of VO_2 coverage fraction and VO_2 thickness at different coupling gaps (50 nm, 70 nm, and 90 nm). The colour bar represents the contrast with yellow indicating higher contrast values and blue indicating lower values.

4.5 Conclusion to Chapter 4

This chapter constructs an all-optically controllable device with bistability based on VO_2 , focusing on how to achieve optical switching and short-term memory responses at the device level through structural design and localised photothermal manipulation. Compared to traditional methods that rely on external temperature control or electrical heating, this study utilises localised laser heating to control the VO_2 phase transition, achieving both state switching and state retention driven by optical input on a silicon-based integrated platform.

In a straight waveguide structure, simulation results demonstrate that the photothermal effect induced by controlling the laser input power effectively drives the VO_2 phase transition, resulting in a pronounced transmittance bistability. While achieving this bistability does not bypass the intrinsic phase transition hysteresis of the VO_2 material, localized, controllable photothermal input keeps the VO_2 phase transition temperature within the hysteresis window, enabling state selection and retention. Furthermore, the bistability input window can be tuned by varying the VO_2 geometry.

Furthermore, this chapter extends this mechanism to microring resonator structures. By systematically optimising parameters such as VO_2 cover length, thickness, and coupling gap, a normalised transmittance variation of up to 0.59 (ER = 8.04 dB) was achieved. Furthermore, the structural design enables the device to respond to input light stimuli within a bistable region, mimicking the ‘stimulus-memory-forget’ process in biological synapses and exhibiting optical short-term associative learning. This mechanism demonstrates the potential of VO_2 materials in neuro-inspired optical systems, particularly by enabling short-term state retention and optical logic responses without electrical actuation, relying solely on optical input.

In summary, this chapter demonstrates the device-level bistable behavior and preliminary neuromorphic functionality of VO_2 films under photothermal control. The next chapter summarises the main research findings and future prospects of this thesis.

Chapter 5. Conclusions and future work

5.1 Conclusions

This thesis develops a low-temperature annealing process at 300°C for VO₂ thin films fabricated via atomic layer deposition (ALD), enabling post-metal processing temperatures compatible with CMOS technology. By increasing the oxygen partial pressure to 2.5 Torr, high-quality VO₂ films were successfully formed on both silicon substrates and flexible polyimide, achieving notable infrared emissivity contrast values of 0.47 and 0.30, respectively. The film quality and crystallinity were verified through SEM, Raman spectroscopy, ellipsometer and XPS. It was observed that high-temperature annealing at 400°C led to the formation of V₂O₅, whereas low-temperature annealing at 250°C was insufficient for crystallisation, indicating that the minimum thermal budget required for VO₂ formation is constrained by crystallisation.

Through a combination of multiple characterisation techniques, this study identifies lattice strain effects as the core mechanism of the annealing process, analysing the impact of different annealing conditions on VO₂ phase transition temperature, refractive index, and material quality. These insights provide guidance for the fabrication of high-quality VO₂ films tailored for different applications. Additionally, by correlating XPS analysis with Raman spectroscopy, a quantitative method was developed to extract VO₂ composition variations of less than 10 % from XPS data through fitting parameters. Moreover, SEM imaging revealed distinct morphologies of VO₂ under different annealing conditions (both lower and higher temperatures), highlighting the variations in VO₂ quality assessment approaches. Finally, investigations into W-doped VO₂ demonstrated that tungsten doping influences the annealing conditions, requiring additional oxidation compared to undoped VO₂.

This thesis also proposes a device-level bistable control method, which leverages the refractive index contrast between the insulating and metallic states of VO₂. The approach exhibits different bistable ranges across various device structures, offering a novel implementation for VO₂-based optical memory. Unlike conventional VO₂ optical storage devices that rely on hysteresis by globally tuning the device temperature, our approach making the device more feasible for optimised design and large-scale manufacturing. For microring structures, we further explored their bistable characteristics and numerically demonstrated a VO₂-based photonic device, which

we term VPAM (VO_2 -based Photonic Associative Memory). This device, designed on a silicon photonic platform, enables device-level bistability and mimics associative learning. The VPAM structure consists of a silicon microring resonator partially covered with VO_2 thin-film patches, generating two distinct normalised transmission states (0.11 vs. 0.70) under the same input conditions. The transition between low- and high-transmission states is induced by simultaneous input at two ports, mimicking classical conditioning as demonstrated in Pavlov's dog experiment. Through systematic finite element simulations, we optimised the structure parameters and achieved a high optical contrast of 0.59 (8.04 dB). This configuration offers an optimal balance between high optical contrast and fabrication tolerance, making it suitable for practical implementation.

The proposed VPAM exhibits optical modulation on the microsecond scale with an energy consumption of 4.4 nJ, underscoring its efficiency for neuromorphic applications. The natural forgetting time of associative memory is within 1 μs , enabling fast and bio-inspired memory emulation. Although the fastest reported VO_2 photothermal switching at the device level occurs on a sub 100 ns timescale, the insulator-to-metal transition (IMT) in VO_2 can be reduced to the picosecond to femtosecond regime. This can be achieved by precisely tuning the excitation source to selectively trigger an electronic Mott transition, thereby minimising parasitic heat generation and structural phase transition (SPT) effects. By demonstrating the integration of VO_2 with silicon platform to achieve bistability and associative learning, this work establishes a practical and energy-efficient pathway for photonic neuromorphic computing. The potential bistable mechanisms enabled by the VO_2 phase transition open new opportunities for the design of phase change material based photonic devices, bridging the gap between optical processing and bio-inspired computing.

5.2 Future work

- **VO_2 material toxicity: optimisation of fabrication processes and strategies for enhancing biocompatibility**

In this thesis, the formation temperature of VO_2 has been successfully reduced to 300°C, enabling its deposition onto heat-sensitive flexible substrates. This achievement marks a significant step toward the realisation of VO_2 -based wearable devices and related applications. However, further research is required to address the toxicity concerns of VO_2 , particularly regarding its potential risks in biomedical and environmental

applications. While VO_2 itself is generally considered a biocompatible material, prolonged exposure to environmental conditions may lead to its oxidation into V_2O_5 , a compound known for its toxicity. Previous studies have demonstrated that V_2O_5 exposure in rodent models can induce various toxic effects, including neurological impairments, functional disorders in the liver and bones, and, notably, pulmonary issues and leukocyte DNA damage due to inhalation of vanadium oxides [304-306]. Therefore, developing passivation layer technologies will be an essential strategy for mitigating the toxicity of VO_2 . Although previous research has demonstrated the potential of coating technologies in enhancing the biocompatibility of VO_2 thin films, systematic studies evaluating the impact of different coating thicknesses and materials are still lacking [307, 308]. Additionally, future research should focus on optimising the fabrication process of VO_2 thin films to improve the purity of the $\text{VO}_2(\text{M1})$ phase. Leveraging the advantages of ALD could further enhance film adhesion, improving its stability when applied to medical device surfaces.

- **Low-Cost oxygen vacancy engineering for non-volatile VO_2 in neuromorphic computing**

In this thesis, our VPAM (VO_2 -based Photonic Associative Memory) design based on a microring structure has been numerically demonstrated to exhibit device-level bistability, with the potential for short-term associative learning. To further explore the feasibility of long-term associative learning in VO_2 , thereby advancing its application in neuromorphic computing, it is crucial to investigate mechanisms that stabilise its phase transition behaviour. As discussed in Section 1.4.3, previous studies have typically achieved non-volatile behaviour by modifying the electronic structure of VO_2 or controlling oxygen vacancies under external stimuli. However, these approaches often require high costs or complex experimental conditions.

Beyond lattice strain modification, annealing has also been identified as an effective means of altering oxygen vacancies in VO_2 [254, 309]. Therefore, further investigation into annealing-controlled oxygen vacancy engineering is essential to unlocking the non-volatile potential of VO_2 at a lower cost, making it more practical for large-scale applications in neuromorphic computing.

- **Exploration of annealing effects on Tungsten-doped VO₂**

In this work, tungsten-doped VO₂ (W:VO₂) has been found as a material with significant potential for low-power applications, owing to its reduced phase transition temperature. Various annealing conditions for three different tungsten doping ratios within W:VO₂ to understand the annealing effects were applied in this work. However, due to practical limitations, experimental verification for this piece of work was planned but not completed. Consequently, our analysis was confined to Fourier Transform Infrared Spectroscopy (FTIR) and room-temperature Raman spectroscopy measurements. These methods, while informative, do not suffice to comprehensively understand the effects of annealing on W:VO₂. Therefore, in future research, a more comprehensive and systemic investigation of the annealing effect on W:VO₂ samples is necessary.

Appendix A. Simulations and Optimisation for VPAM

A1. Run code in Iridis supercomputer

```
#!/bin/bash
#SBATCH --time=120:00:00
#SBATCH --mail-type=ALL
#SBATCH --mail-user=yd5u19@soton.ac.uk
#SBATCH --partition=highmem
#SBATCH --nodes=1
#SBATCH --ntasks=64
FILENAME='Sample_test'
cd $SLURM_SUBMIT_DIR
module load comsol/6.0
comsol batch -autosave off -nn 1 -np $SLURM_NTASKS -tmpdir /scratch/$USER/ -batchlog
$FILENAME.log -inputfile $FILENAME.mph -outputfile $FILENAME.solved.mph
```

A2. COMSOL mesh density comparison of all four condition steps

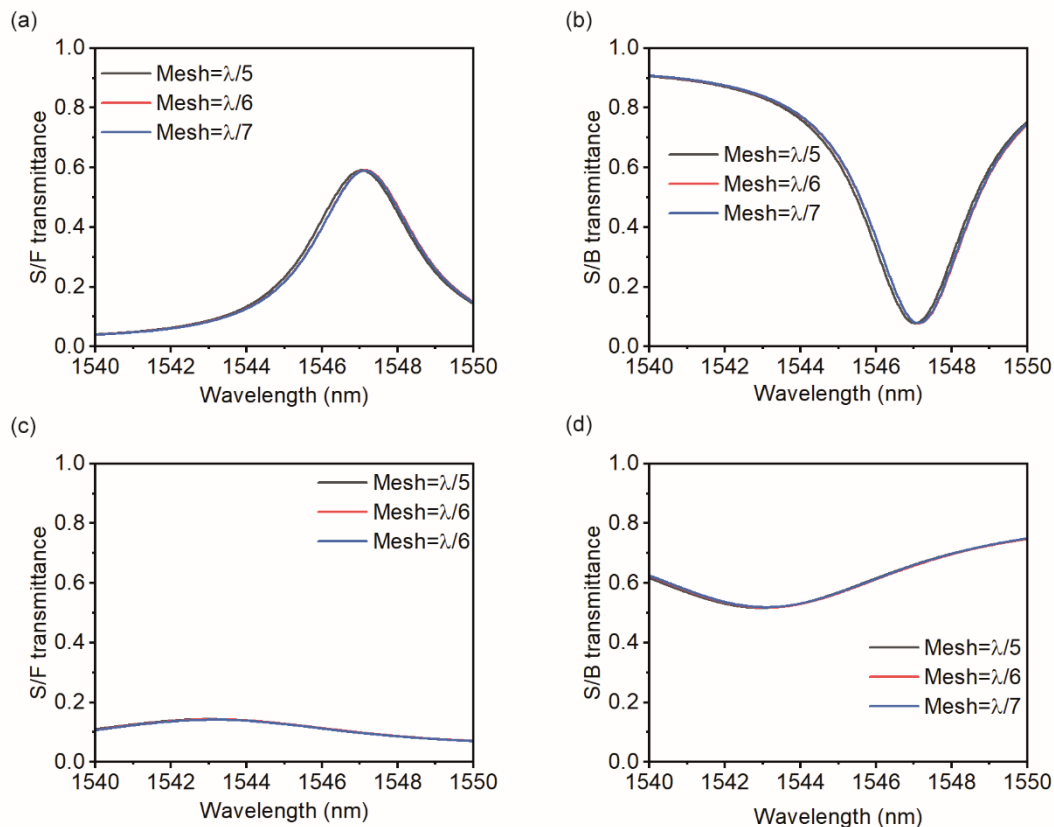


Figure. A1. COMSOL mesh density comparison of all four condition steps transmission spectrum, the maximum mesh size is selected as $\lambda/5$, $\lambda/6$, $\lambda/7$. (a) Condition step 1 (food only). (b) Condition step 2 (bell only, before conditioning). (c) Condition step 3 (food and bell). (d) Condition step 4 (bell only, after conditioning).

A3. Discovery of VO₂ patch relative position effect on the Si microring.

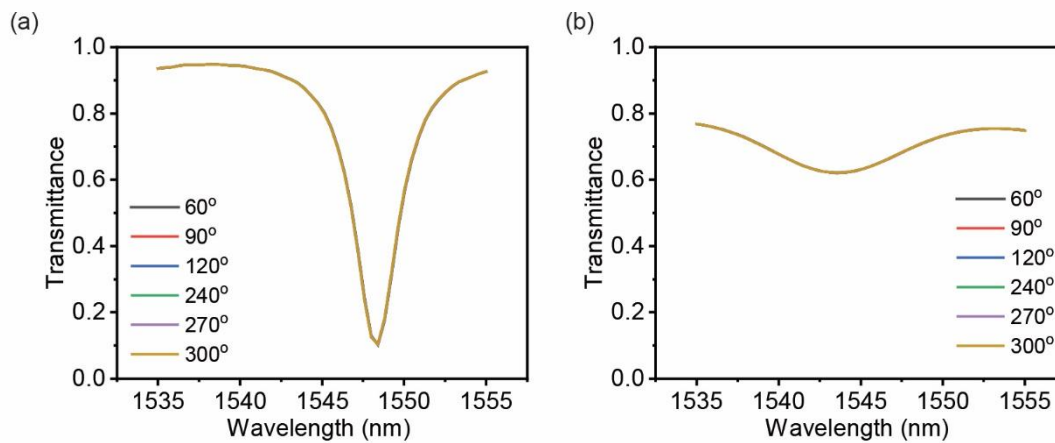


Figure A2. Transmittance comparison of VO₂ patch at a) insulating phase and b) metallic phase placed at the different position on the Si MRR, the 0° is defined as the position closet to the left waveguide.

A4. Actual measured values of mesh size in Lumerical software

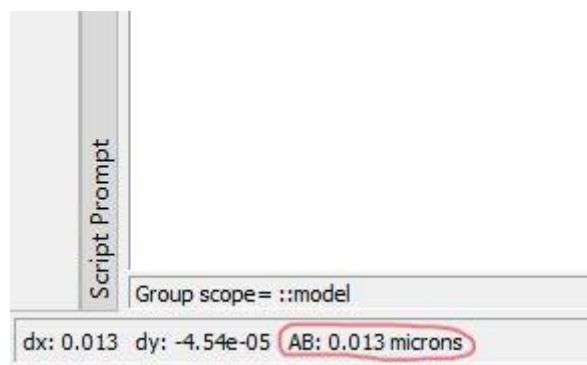


Figure A3. Actual mesh size of Si MRR measured in Lumerical software at 1550 nm wavelength (Mesh size = 8).

A5. Comparison between device level bistability with and without applying the Looyenga mixing rule

All other geometries and the simulation settings are identical to Fig. 4.17 in the main text.

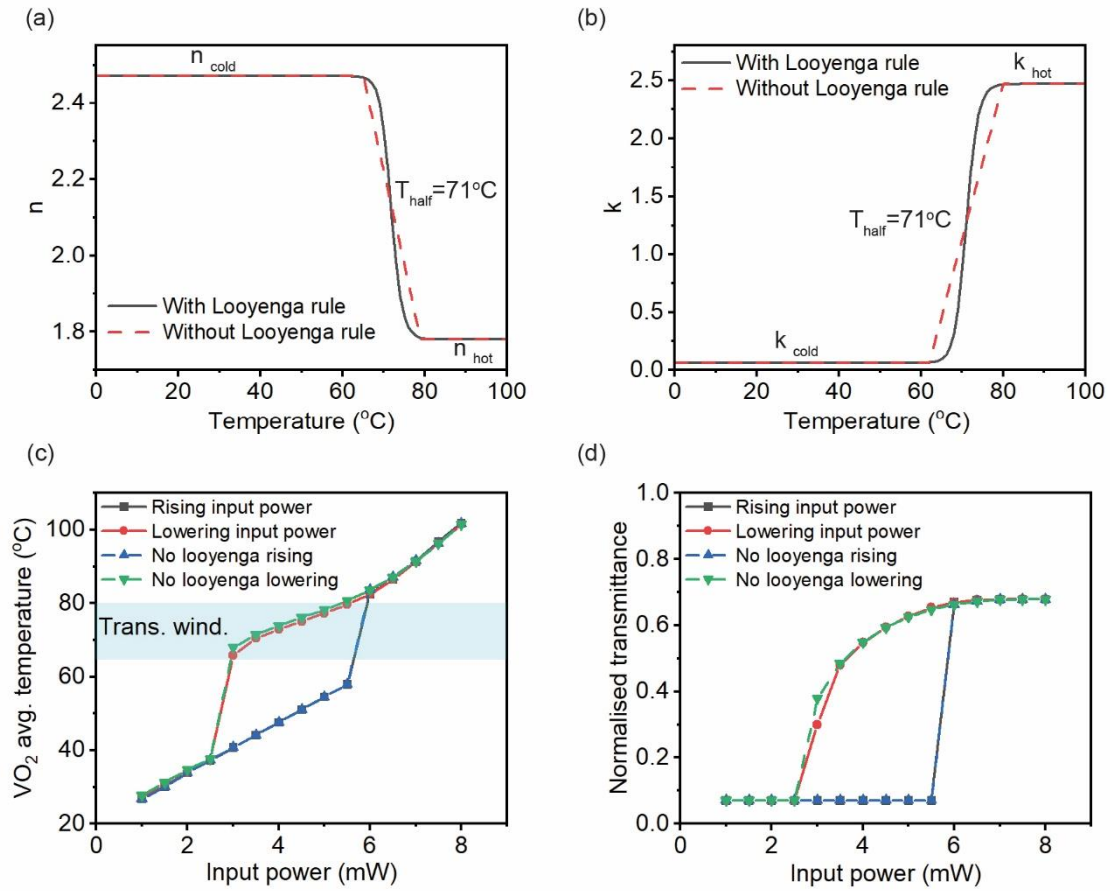


Figure A4. Comparison between applying and not Looyenga mixing rule. (a) real and (b) imaginary part of the refractive index. (c) Thermal bistability and (d) optical bistability.

A6. Raw simulation results in the main text, Fig. 4.21-Fig. 4.23.

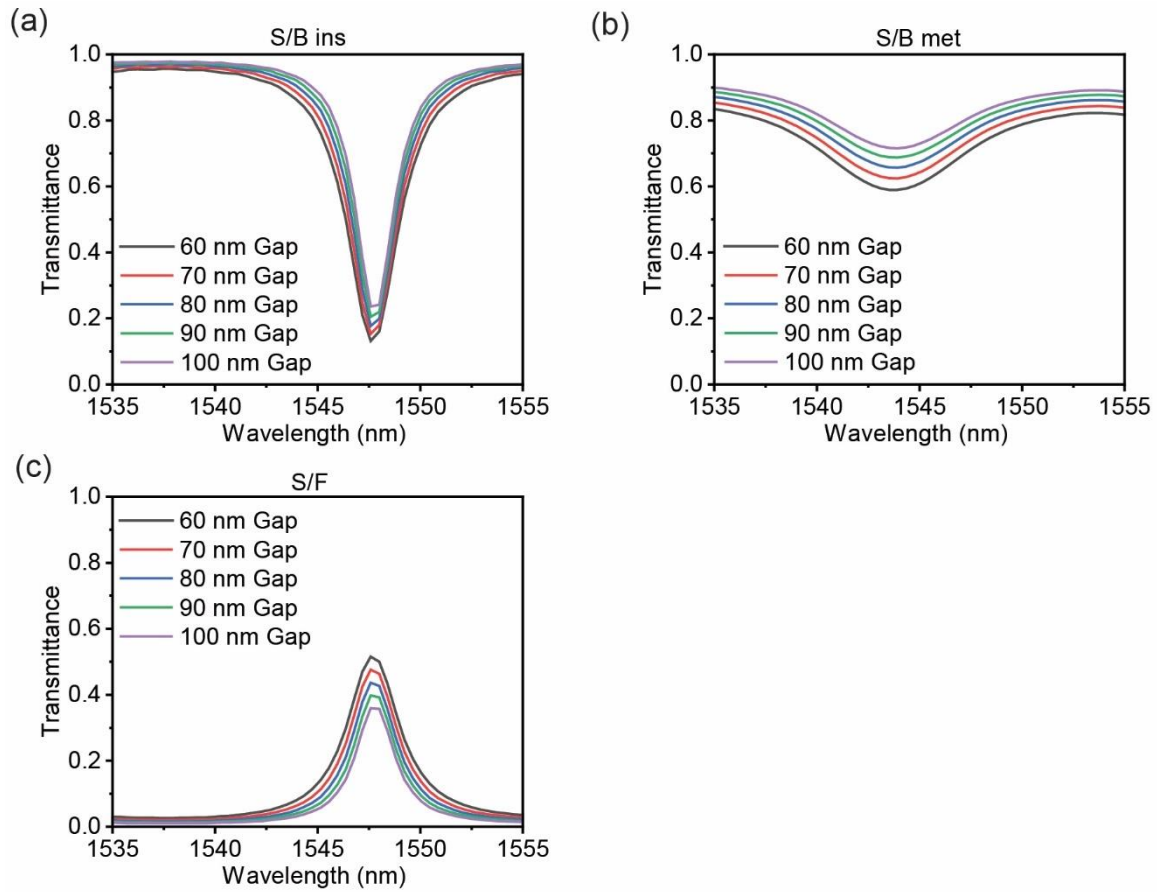


Figure A6. Raw simulation data support for Fig. 4.21 in the main text.

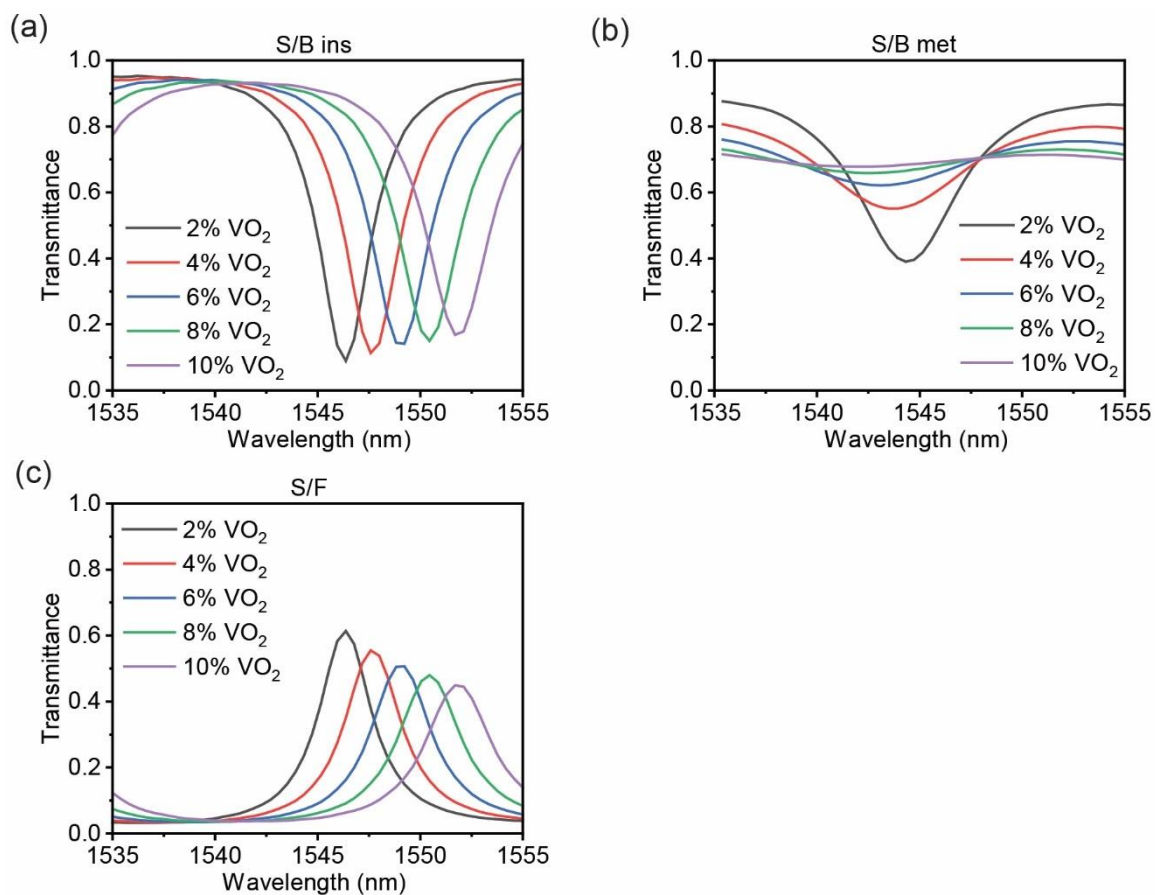


Figure A7. Raw simulation support for Fig. 4.22 in the main text.

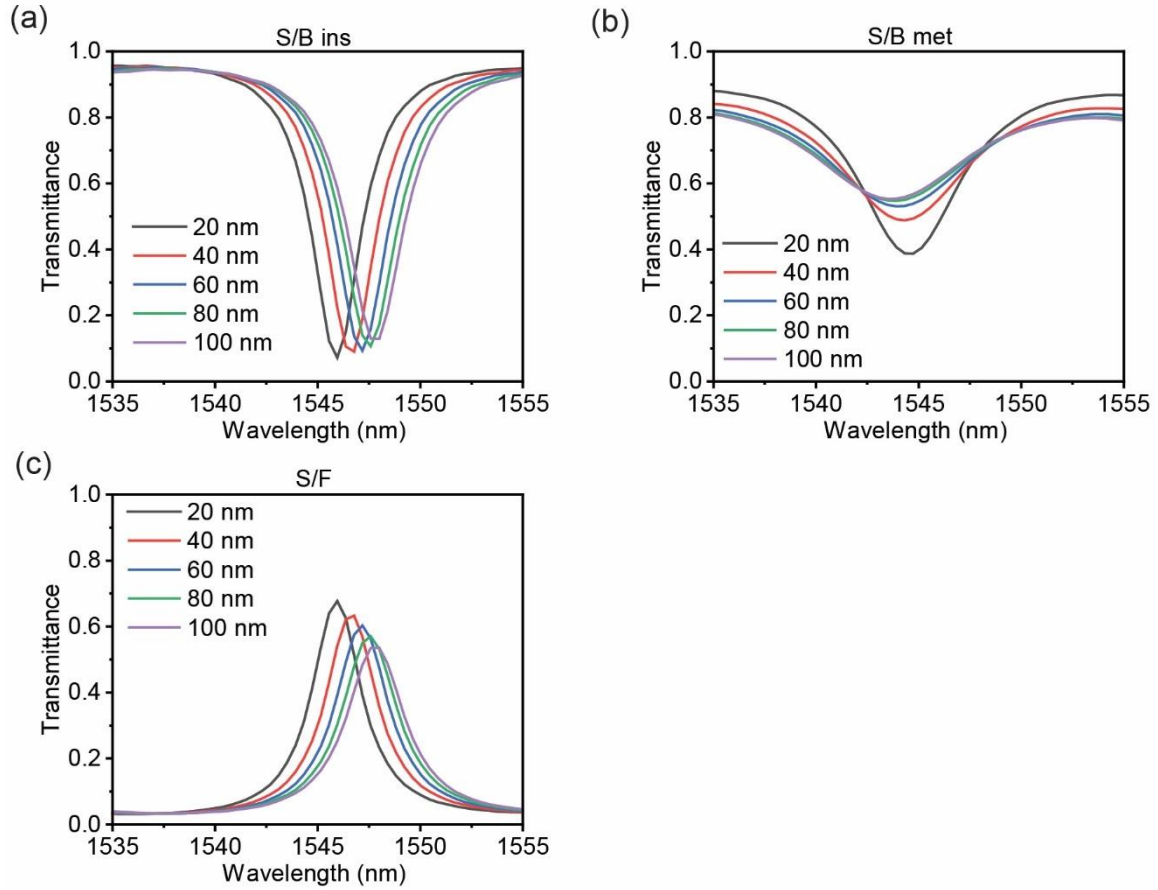


Figure A8. Raw simulation data support for Fig. 4.23 in the main text.

A7. Optical bistability of straight waveguides that have VO₂ patches of varying lengths on top.

The bistable power range is defined based on the average temperature across both ends of the patch. Specifically, once the input power in the insulating state increases to a specific value, the temperature at one end of the patch reaches the transition temperature, triggering the phase transition and vice versa.

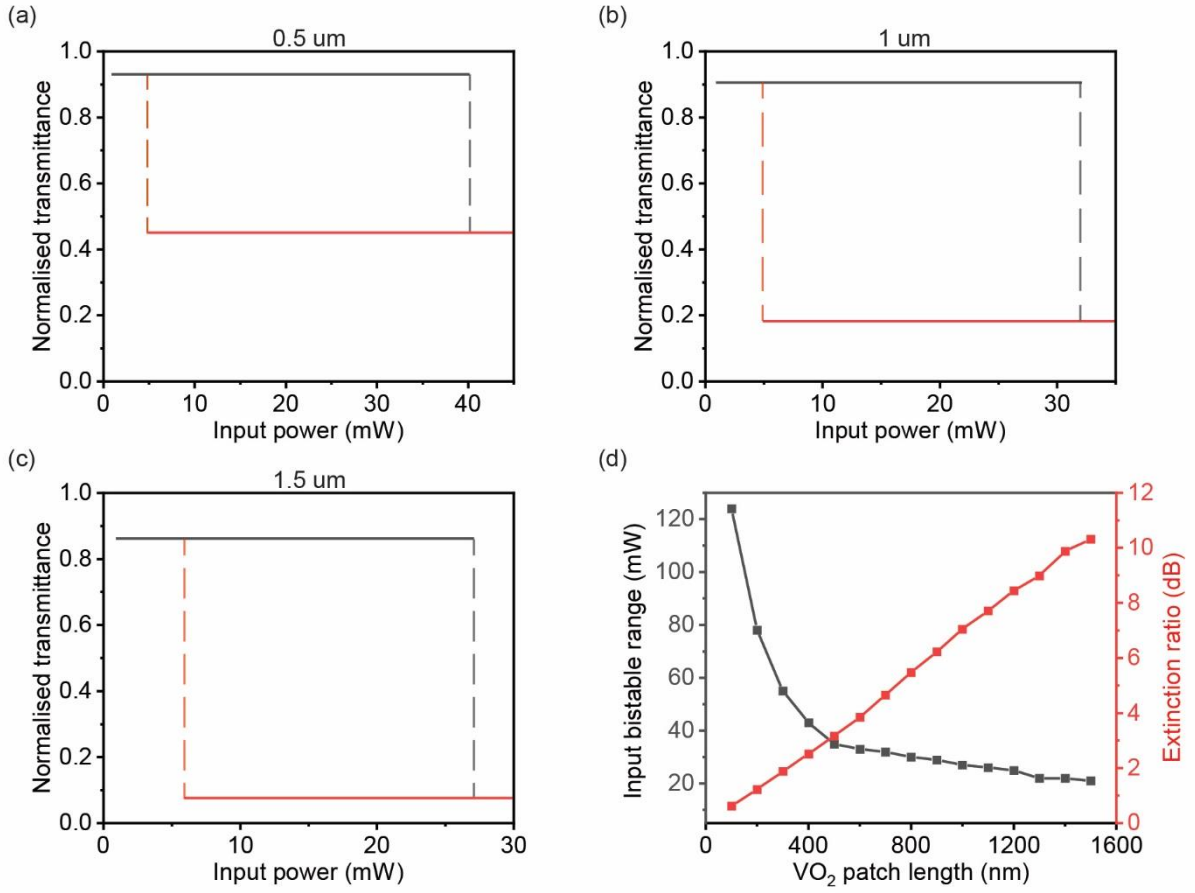


Figure A9. Device level optical bistability in straight waveguides integrated with VO₂ patches of different lengths, (a) 500 nm, (b) 1000 nm, and (c) 1500 nm. Black and red solid lines represent the transmission level when the VO₂ patch switches to insulating and metallic states, respectively. (d) Relationship between VO₂ patch length with bistable input power range and the corresponding extinction ratio.

Appendix B. Annealing optimisation for flexible polyamide

Figure B1 shows the FTIR reflectance spectra for vanadium dioxide (VO_2) coatings on different substrates measured at 20°C low temperature and 100°C high temperature under various annealing conditions. It is worth noting that the annealing conditions applied for (b) and (c) are identical and it is for comparison only.

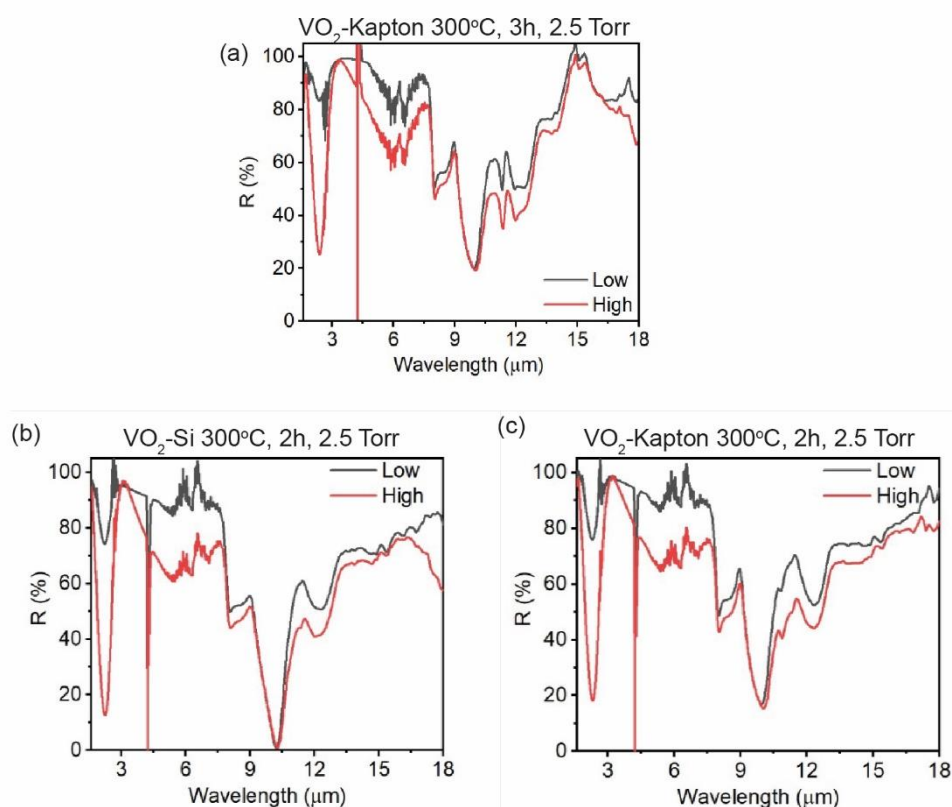



Figure B1. FTIR Reflectance spectra for vanadium dioxide (VO_2) coatings on different substrates and annealing conditions. (a) VO_2 coated on Kapton measured at high and low temperatures under 3 hours at 300°C and 2.5 Torr pressure annealing. (b) Reflectance of VO_2 on silicon substrate under 2 hours at 300°C and 2.5 Torr annealing. (c) The same conditions as (b) applied to a Kapton substrate.

Appendix C. Datasheet contains information on the decomposition temperature of DuPont Kapton FPC 350.^[310]

Article Information Sheet



DuPont™ Kapton® FPC, HN, HPP-ST, PST, VN (1.75 - 3 mil)

Version 2.0

Revision Date 10.07.2012

Ref. 150000003829

Possibility of hazardous reactions	: No dangerous reaction known under conditions of normal use. The product is chemically stable under recommended conditions of storage, use and temperature.
Conditions to avoid	: Decomposition temperature : > 350 °C
Incompatible materials	: Strong acids strong oxidizers
Hazardous decomposition products	: Hazardous thermal decomposition products may include: Carbon oxides nitrogen oxides (NOx)

Toxicological information

Information on toxicological effects

Acute oral toxicity

- N,N-Dimethylacetamide
LD50 / rat : 5,830 mg/kg

Acute inhalation toxicity

- N,N-Dimethylacetamide
LC50 / 4 h rat : 2.2 mg/l
Value applicable only if respirable particles are formed.

Acute dermal toxicity

- N,N-Dimethylacetamide
LD50 / rabbit : 2,100 mg/kg

Skin irritation

- N,N-Dimethylacetamide
rabbit
Classification: Not classified as irritant
Result: No skin irritation

Eye irritation

- N,N-Dimethylacetamide
rabbit
Classification: Irritating to eyes.
Result: Moderate eye irritation

Sensitisation

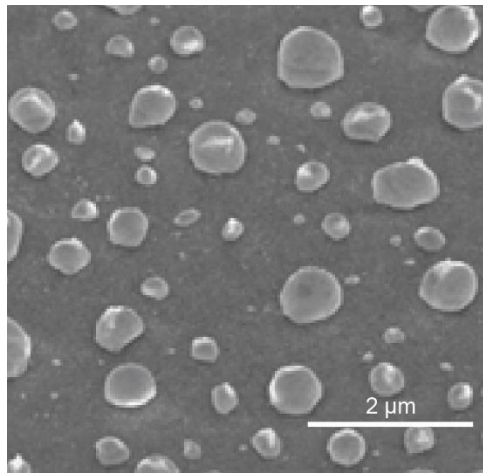
- N,N-Dimethylacetamide
guinea pig
Classification: Not a skin sensitizer.
Result: Did not cause sensitization on laboratory animals.

6/9

Print Date: 2013 - 4 - 23

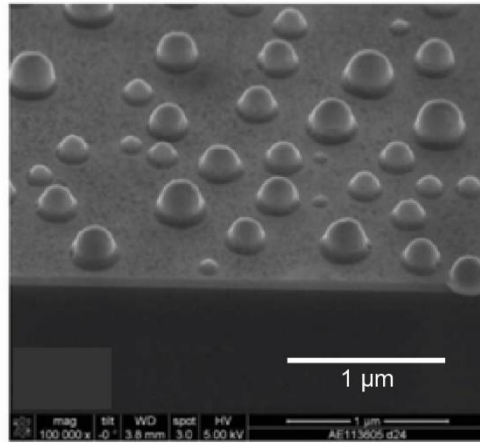
Appendix D. ‘Particle-like’ surface morphology introduced by dewetting and substrates

D1. Dewetting behaviour of Au thin film under annealing temperature of 550°C [311]



D2. 460°C annealed VO₂ film on 90 nm SiO₂ synthesised by ALD using TEMAV and O₃ precursors [147]

On thick SiO₂, the morphology is of well-separated nanoparticles, while on Al₂O₃ it tends to form an island-like morphology.



Appendix E. Raman peak position of known vanadium oxides.^[201]

Phase	Space group	Raman-active modes	Main peak positions, cm ⁻¹
α (V)	$Im\bar{3}m$	—	—
α' (V ₈ O)	$P4_2/mnm$	$4A_{1g} + 4B_{1g} + 4B_{2g} + 4E_g$?
β (V ₄ O)	$I4/mmm$	—	—
β' (V ₁₆ O ₃)	$I4/mmm$	$7A_{1g} + 8B_{1g} + 7B_{2g} + 11E_g$?
γ (V ₁₄ O ₆)	$C2/m$	$8A_g + 4B_g$?
δ (VO)	$Fm\bar{3}m$	—	—
δ' (V ₅₂ O ₆₄)	$I4_1/amd$	$11A_{1g} + 12B_{1g} + 10B_{2g} + 22E_g$?
V ₃ O ₄	$Fd\bar{3}m$	$A_{1g} + E_g + 3T_{2g}$?
V ₂ O ₃ HT	$R\bar{3}c$	$2A_{1g} + 5E_g$	218, 240, 300, 340, 510, 600
V ₂ O ₃ LT	$C2/c$	$7A_g + 8B_g$	191, 232 , 281, 332 , 342, 446 , 525, 588, 603, 680
V ₂ O ₃ HP	$C2/c$	$7A_g + 8B_g$?
V ₂ O ₃ bix.	$Ia\bar{3}$	$4A_g + 4^1E_g + 4^2E_g + 14T_g$?
V ₃ O ₅ LT	$P2/c$	$20A_g + 22B_g$	155 , 183, 223, 304 , 487, 563 , 593, 641, 738
V ₃ O ₅ HT	$C2/c$	$10A_g + 11B_g$	152, 161 , 213 , 320, 500, 570, 800
V ₃ O ₅ an.	$Cmcm$	$8A_g + 5B_{1g} + 3B_{2g} + 8B_{3g}$?
V _{2k} O _{4k+1}	$P\bar{1}$	$(18k-3)A_g$?
V _{2k+1} O _{4k+1}	$P\bar{1}$	$(18k+3)A_g$?
VO _x	?	?	177, 204 , 242, 304 , 360, 420, 492, 555, 743, 805
VO ₂ (M1)	$P2_1/c$	$9A_g + 9B_g$	137, 194, 224 , 262, 310, 393, 442, 499, 612 , 820
VO ₂ (T)	$P2_1/c$	$18A_g$	126, 198, 224 , 306, 376, 407, 444, 575, 631 , 828
VO ₂ (M2)	$C2/m$	$10A_g + 8B_g$	202, 228 , 275, 295, 435, 454, 651 , 833
VO ₂ (M3)	$P2/m$	$4A_g + 2B_g$?
VO ₂ (O)	?	?	?
VO ₂ (R)	$P4_2/mnm$	$A_{1g} + B_{1g} + B_{2g} + E_g$	240, 390, 510 , 625
VO ₂ (A) LT	$P4/ncc$	$9A_{1g} + 9B_{1g} + 9B_{2g} + 18E_g$	159 , 180, 212, 291, 413, 518, 666, 887 , 910, 938
VO ₂ (A) HT	$P4_2/ncm$	$10A_{1g} + 8B_{1g} + 10B_{2g} + 18E_g$	123 , 184, 197, 275, 305, 415, 510, 575, 725, 868
VO ₂ (B)	$C2/m$	$12A_g + 6B_g$	191 , 270, 399 , 470, 670, 880
VO ₂ (C)	?	?	?
VO ₂ (D)	$P2/c$	$8A_g + 10B_g$?
VO ₂ (P)	$Pnma$	$6A_g + 3B_{1g} + 6B_{2g} + 3B_{3g}$?
VO ₂ (BCC)	?	?	?
VO ₂ (N)	?	?	?

V ₆ O ₁₃ HT	<i>C2/m</i>	18A _g + 9B _g	94, 137 , 188, 275 , 300, 403, 475, 520, 684, 990
V ₆ O ₁₃ LT	<i>Pc</i>	55A' + 56A''	?
β-V ₆ O ₁₃	<i>Fmmm</i>	9A _g + 5B _{1g} + 4B _{2g} + 9B _{3g}	?
V ₄ O ₉	<i>Pnma</i>	26A _g + 13B _{1g} + 26B _{2g} + 13B _{3g}	?
V ₄ O ₉	<i>Cmcm</i>	21A _g + 19B _{1g} + 17B _{2g} + 21B _{3g}	122, 258, 407, 465, 602, 645, 762, 886, 906 , 1010
V ₇ O ₁₆	<i>P1̄</i>	69A _g	162, 250, 910
V ₃ O ₇	<i>C2/c</i>	44A _g + 46B _g	157 , 292, 694, 840 , 880 , 930 , 990, 1030
V _{3.047} O ₇	<i>P3</i>	17A + 17 ¹ E + 17 ² E	197, 277, 367, 429, 760, 835
α-V ₂ O ₅	<i>Pmmn</i>	7A _g + 3B _{1g} + 7B _{2g} + 4B _{3g}	104, 146 , 198, 285 , 306, 406, 483, 528, 701, 996
β-V ₂ O ₅	<i>P2₁/m</i>	14A _g + 7B _g	96 , 176, 230, 301, 340, 357, 476, 686, 942 , 1021
δ-V ₂ O ₅	<i>C2/c</i>	10A _g + 11B _g	?
ζ-V ₂ O ₅	<i>C2/m</i>	20A _g + 10B _g	?
γ'-V ₂ O ₅	<i>Pnma</i>	14A _g + 7B _{1g} + 14B _{2g} + 7B _{3g}	91, 138 , 152, 170, 266 , 282, 349, 602, 694, 1001
ε'-V ₂ O ₅	<i>C2/m</i>	14A _g + 7B _g	109, 157 , 242, 269 , 378, 436, 481, 531, 703, 1044

Bibliography

1. H. Amodai, "AI and compute" (OpenAI, 2018), retrieved <https://openai.com/blog/ai-and-compute/>.
2. Thompson, Neil C., et al. "The computational limits of deep learning." arXiv preprint arXiv:2007.05558 10 (2020): 2.
3. A. Mehonic and A. J. Kenyon, "Brain-inspired computing needs a master plan," *Nature* **604**, 255-260 (2022).
4. S. J., "The future of computing beyond Moore's Law," *Philos Trans A Math Phys Eng Sci.* **378**, 2166 (2020).
5. T. Alexoudi, et al., "Optical RAM row with 20 Gb/s optical word read/write," *Journal of Lightwave Technology* **39**, 7061-7069 (2021).
6. C. Pappas, et al., "Caching with light: a 16-bit capacity optical cache memory prototype," *IEEE Journal of Selected Topics in Quantum Electronics* **29**, 1-11 (2023).
7. H. Schulte and A. Rack, "Optical delay line memory," *IEEE Journal of Quantum Electronics* **3**, 246-246 (1967).
8. J. Liu and Y. Chen, "Optical flip-flop," *Electronics letters* **21**, 236-238 (1985).
9. Z. Fang, et al., "Fast and Energy-Efficient Non-Volatile III-V-on-Silicon Photonic Phase Shifter Based on Memristors," *Advanced Optical Materials* **11**, 2301178 (2023).
10. D. Mandal, "Design of optically controlled read and write memory unit with reversible logic gates using GaAs–AlGaAs-based micro-ring resonators," *Journal of Optics* **53**, 4671-4689 (2024).
11. L. Yin, et al., "Emerging 2D memory devices for in-memory computing," *Advanced Materials* **33**, 2007081 (2021).
12. M. Wei, et al., "Electrically programmable phase-change photonic memory for optical neural networks with nanoseconds in situ training capability," *Advanced Photonics* **5**, 046004 (2023).
13. P. P. Ravichandiran and P. D. Franzon, "A review of 3D-dynamic random-access memory based near-memory computation," in *2021 IEEE International 3D Systems Integration Conference (3DIC)*, (IEEE, 2021), 1-6.
14. G. O. Puglia, et al., "Non-volatile memory file systems: A survey," *IEEE Access* **7**, 25836-25871 (2019).
15. Y. Zhang, et al., "Nonvolatile multilevel adjustable optical switch based on plasmonic slot waveguide and GST segmented structure," *Optics Express* **32**, 16548-16562 (2024).
16. C. Ríos, et al., "Integrated all-photonic non-volatile multi-level memory," *Nature photonics* **9**, 725-732 (2015).
17. Y. Yuan, et al., "All-silicon non-volatile optical memory based on photon avalanche-induced trapping," *Communications Physics* **8**, 39 (2025).
18. A. Zylbersztein and N. F. Mott, "Metal-insulator transition in vanadium dioxide," *Physical Review B* **11**, 4383 (1975).
19. K. Liu, et al., "Recent progresses on physics and applications of vanadium dioxide," *Materials Today* **21**, 875-896 (2018).
20. J. J. Seoane, et al., "Ultra-high endurance silicon photonic memory using vanadium dioxide," *npj Nanophotonics* **1**, 37 (2024).
21. T. Ratier, et al., "Vanadium dioxide by atomic layer deposition: A promising material for next-generation memory devices," *The Journal of Physical Chemistry Letters* **15**, 9811-9819 (2024).
22. Y. Jung, et al., "Integrated hybrid VO₂–silicon optical memory," *ACS Photonics* **9**, 217-223 (2022).

23. O. Maher, et al., "A CMOS-compatible oscillation-based VO₂ Ising machine solver," *Nature Communications* **15**, 3334 (2024).
24. J. Peng, et al., "ALD-Assisted VO₂ for Memristor Application," *Advanced Engineering Materials* **27**, 2402614 (2025).
25. D. Kang, et al., "High-quality VO₂ thin films sputter-deposited on borosilicate glass substrates for modulating solar transmission and thermal emission," *Journal of Alloys and Compounds* **1008**, 176793 (2024).
26. S. Singh, et al., "Controlling the Mott–Peierls transition in epitaxial VO₂ (M1) film grown by PLD for near-IR photodetection," *Journal of Applied Physics* **137**, 054501 (2025).
27. T. Chao, *Introduction to semiconductor manufacturing technology* (Prentice Hall New Jersey, 2000).
28. S. A. Howard, et al., "Digital tuning of the transition temperature of epitaxial VO₂ thin films on MgF₂ substrates by strain engineering," *Advanced Materials Interfaces* **8**, 2001790 (2021).
29. J. P. Ganesan, et al., "Semiconductor-to-metal transition in atomic layer deposition (ALD) of VO₂ films using VCl₄ and water," *Applied Physics Letters* **118**, 261901 (2021).
30. Z. Baji, et al., "VO₂ layers with high resistive switching ratio by atomic layer deposition," *Materials Science in Semiconductor Processing* **162**, 107483 (2023).
31. Z. Che, et al., "Implantable triboelectric nanogenerators for self-powered cardiovascular healthcare," *Small* **19**, 2207600 (2023).
32. I. Rezaei, et al., "Wearable Kapton graphene biosensor for detection of toxic gases," *Journal of Hazardous Materials Advances* **15**, 100452 (2024).
33. QIOPTIQ, "Optical Solar Reflectors", retrieved <https://www.excelitas.com/product/optical-solar-reflectors>.
34. P. Kepic, et al., "Coexisting Phases of Individual VO₂ Nanoparticles for Multilevel Nanoscale Memory," *ACS nano* **19**, 1167-1176 (2025).
35. S. Kunwar, et al., "Reconfigurable resistive switching in VO₂/La_{0.7}Sr_{0.3}MnO₃/Al₂O₃ (0001) memristive devices for neuromorphic computing," *ACS Applied Materials & Interfaces* **16**, 19103-19111 (2024).
36. P. Schofield, et al., "Harnessing the metal–insulator transition of VO₂ in neuromorphic computing," *Advanced Materials* **35**, 2205294 (2023).
37. R. Yuan, et al., "A neuromorphic physiological signal processing system based on VO₂ memristor for next-generation human-machine interface," *Nature Communications* **14**, 3695 (2023).
38. Y. Jung, et al., "Observation of optically addressable nonvolatile memory in VO₂ at room temperature," *Advanced electronic materials* **7**, 2001142 (2021).
39. L. Wang, et al., "Nanoscale insights on phase transition dynamics of doped VO₂ for memristor devices," *Applied Physics Reviews* **12**, 011406 (2025).
40. R. Naik B, et al., "Effect of chemical doping on memristive behavior of VO₂ microcrystals," *Applied Physics Letters* **120**(2022).
41. R. Basu, et al., "Role of vanadyl oxygen in understanding metallic behavior of V₂O₅ (001) nanorods," *The Journal of Physical Chemistry C* **120**, 26539-26543 (2016).
42. J. Qi, et al., "Independent regulation of electrical properties of VO₂ for low threshold voltage electro-optic switch applications," *Sensors and Actuators A: Physical* **335**, 113394 (2022).
43. E. Haddad, et al., "Review of the VO₂ smart material applications with emphasis on its use for spacecraft thermal control," *Frontiers in Materials* **9**, 1013848 (2022).
44. K. Okimura, et al., "High luminous transmittance and solar modulation of VO₂-based smart windows with SiO₂ anti-reflection coatings," *Solar Energy Materials and Solar Cells* **251**, 112162 (2023).

45. T. Massalski, "Phase diagrams," Encyclopedia of Materials: Science and Technology, 6842-6851 (2001).
46. M. Darwish, et al., "Recent Advances of VO₂ in Sensors and Actuators," Nanomaterials **14**, 582 (2024).
47. J. Jeong, "Vanadium Dioxide for Memory, Oscillators, and Optical Beam Manipulation," (University of Toronto (Canada), 2021).
48. J. B. Goodenough, "The two components of the crystallographic transition in VO₂," Journal of Solid State Chemistry **3**, 490-500 (1971).
49. N. B. Aetukuri, et al., "Control of the metal–insulator transition in vanadium dioxide by modifying orbital occupancy," Nature Physics **9**, 661-666 (2013).
50. R. E. Peierls, *Quantum theory of solids* (Clarendon Press, 1996).
51. S. R. Popuri, et al., "Presence of Peierls pairing and absence of insulator-to-metal transition in VO₂(A): a structure–property relationship study," Physical Chemistry Chemical Physics **19**, 6601-6609 (2017).
52. N. F. Mott, "The basis of the electron theory of metals, with special reference to the transition metals," Proceedings of the Physical Society. Section A **62**, 416 (1949).
53. C. Ling, et al., "Hole dopants disentangling peierls–mott relevance states of VO₂ by first-principles calculation," The Journal of Physical Chemistry C **125**, 5816-5823 (2021).
54. D. Lee, et al., "Understanding the phase transition evolution mechanism of partially M2 phased VO₂ film by hydrogen incorporation," The Journal of Physical Chemistry Letters **11**, 9680-9688 (2020).
55. V. Eyert, "The metal-insulator transitions of VO₂: A band theoretical approach," Annalen der Physik **514**, 650-704 (2002).
56. A. S. Johnson, et al., "Ultrafast X-ray imaging of the light-induced phase transition in VO₂," Nature Physics **19**, 215-220 (2023).
57. J. Xu, et al., "Decoupled ultrafast electronic and structural phase transitions in photoexcited monoclinic VO₂," Science Advances **8**, eadd2392 (2022).
58. Y. Gutiérrez, et al., "Subpicosecond Spectroscopic Ellipsometry of the Photoinduced Phase Transition in VO₂ Thin Films," ACS Photonics **11**, 4883-4893 (2024).
59. P. Hu, et al., "Vanadium oxide: phase diagrams, structures, synthesis, and applications," Chemical Reviews **123**, 4353-4415 (2023).
60. A. Cavalleri, et al., "Evidence for a structurally-driven insulator-to-metal transition in VO₂: A view from the ultrafast timescale," Physical Review B—Condensed Matter and Materials Physics **70**, 161102 (2004).
61. S. Biermann, et al., "Dynamical singlets and correlation-assisted Peierls transition in VO₂," Physical review letters **94**, 026404 (2005).
62. S. R. Popuri, et al., "Presence of Peierls pairing and absence of insulator-to-metal transition in VO₂(A): a structure–property relationship study," Physical Chemistry Chemical Physics **19**, 6601-6609 (2017).
63. Z. Hiroi, "Structural instability of the rutile compounds and its relevance to the metal–insulator transition of VO₂," Progress in Solid State Chemistry **43**, 47-69 (2015).
64. R. M. Wentzcovitch, et al., "VO₂: Peierls or Mott-Hubbard? A view from band theory," Physical review letters **72**, 3389 (1994).
65. H. Kim, et al., "Direct observation of the M2 phase with its Mott transition in a VO₂ film," Applied Physics Letters **109**, 23 (2016).
66. D.W. Oh, et al., "Thermal conductivity and dynamic heat capacity across the metal-insulator transition in thin film VO₂," Applied Physics Letters **96**, 15 (2010).
67. H. Lu, et al., "Modelling the enthalpy change and transition temperature dependence of the metal–insulator transition in pure and doped vanadium dioxide," Physical Chemistry Chemical Physics **22**, 13474-13478 (2020).

68. A. Cavalleri, et al., "Femtosecond structural dynamics in VO₂ during an ultrafast solid-solid phase transition," *Physical review letters* **87**, 237401 (2001).
69. X. He, et al., "Orbital change manipulation metal–insulator transition temperature in W-doped VO₂," *Physical Chemistry Chemical Physics* **17**, 11638-11646 (2015).
70. J. Zhang, et al., "Boron-tuning transition temperature of vanadium dioxide from rutile to monoclinic phase," *The Journal of chemical physics* **141**, 19 (2014).
71. L. Mai, et al., "Electrical property of Mo-doped VO₂ nanowire array film by melting-quenching sol–gel method," *The Journal of Physical Chemistry B* **110**, 19083-19086 (2006).
72. L. Song, et al., "Preparation and thermochromic properties of Ce-doped VO₂ films," *Materials Research Bulletin* **48**, 2268-2271 (2013).
73. B. Chen, et al., "Al³⁺-doped vanadium dioxide thin films deposited by PLD," *Solar Energy Materials and Solar Cells* **93**, 1550-1554 (2009).
74. J.-L. Victor, et al., "Doubling of the phase transition temperature of VO₂ by Fe doping," *The Journal of Physical Chemistry Letters* **12**, 7792-7796 (2021).
75. Y. Cui, et al., "Hydrogen-doping induced reduction in the phase transition temperature of VO₂: a first-principles study," *Physical Chemistry Chemical Physics* **17**, 20998-21004 (2015).
76. Y. Cui, et al., "First-principles study on the phase transition temperature of X-doped (X= Li, Na or K) VO₂," *RSC advances* **6**, 64394-64399 (2016).
77. J. Zhang, et al., "Giant reduction of the phase transition temperature for beryllium doped VO₂," *Physical Chemistry Chemical Physics* **15**, 4687-4690 (2013).
78. N. Wang, et al., "Mg/W-codoped vanadium dioxide thin films with enhanced visible transmittance and low phase transition temperature," *Journal of Materials Chemistry C* **3**, 6771-6777 (2015).
79. K. Miyazaki, et al., "Correlation between thermal hysteresis width and broadening of metal–insulator transition in Cr-and Nb-doped VO₂ films," *Japanese Journal of Applied Physics* **53**, 071102 (2014).
80. J. Du, et al., "Significant changes in phase-transition hysteresis for Ti-doped VO₂ films prepared by polymer-assisted deposition," *Solar Energy Materials and Solar Cells* **95**, 469-475 (2011).
81. F. Pintchovski, et al., "Experimental study of the electronic and lattice contributions to the VO₂ transition," *Journal of Physics and Chemistry of Solids* **39**, 941-949 (1978).
82. C. Batista, et al., "Synthesis and characterization of VO₂-based thermochromic thin films for energy-efficient windows," *Nanoscale research letters* **6**, 1-7 (2011).
83. L. Hu, et al., "Porous W-doped VO₂ films with simultaneously enhanced visible transparency and thermochromic properties," *Journal of Sol-Gel Science and Technology* **77**, 85-93 (2016).
84. L. A. Ladd and W. Paul, "Optical and transport properties of high quality crystals of V₂O₄ near the metallic transition temperature," *Solid State Communications* **7**, 425-428 (1969).
85. J. Wei, et al., "New aspects of the metal–insulator transition in single-domain vanadium dioxide nanobeams," *Nature nanotechnology* **4**, 420-424 (2009).
86. Y. Muraoka, et al., "Large modification of the metal–insulator transition temperature in strained VO₂ films grown on TiO₂ substrates," *Journal of Physics and Chemistry of Solids* **63**, 965-967 (2002).
87. G. Xu, et al., "Thickness dependence of optical properties of VO₂ thin films epitaxially grown on sapphire (0001)," *Applied Surface Science* **244**, 449-452 (2005).
88. E. Radue, et al., "Effect of a substrate-induced microstructure on the optical properties of the insulator-metal transition temperature in VO₂ thin films," *Journal of Applied Physics* **113**, 23 (2013).

89. Y. Cui and S. Ramanathan, "Substrate effects on metal-insulator transition characteristics of RF-sputtered epitaxial VO₂ thin films," *Journal of Vacuum Science & Technology A* **29**, 4 (2011).
90. S. Yu, et al., "A metal-insulator transition study of VO₂ thin films grown on sapphire substrates," *Journal of Applied Physics* **122**, 23 (2017).
91. Y. Guo, et al., "Study of the phase transition properties and electronic band structures of VO₂ thin films grown on different substrates," *Materials Research Express* **6**, 026409 (2018).
92. C. Zhang, et al., "Synthesis, structure and optical properties of high-quality VO₂ thin films grown on silicon, quartz and sapphire substrates by high temperature magnetron sputtering: Properties through the transition temperature," *Journal of Alloys and Compounds* **848**, 156323 (2020).
93. Y. Choi, et al., "Correlation between symmetry and phase transition temperature of VO₂ films deposited on Al₂O₃ substrates with various orientations," *Advanced Electronic Materials* **7**, 2000874 (2021).
94. W. Brückner, et al., "The range of homogeneity of VO₂ and the influence of the composition on the physical properties. II. The change of the physical properties in the range of homogeneity," *physica status solidi (a)* **29**, 63-70 (1975).
95. N. Kimizuka, et al., "Behavior of vanadium dioxide single crystals synthesized under the various oxygen partial pressures at 1500 K," *Journal of Solid State Chemistry* **9**, 69-77 (1974).
96. Y. Yang, et al., "Transmittance change with thickness for polycrystalline VO₂ films deposited at room temperature," *Journal of Alloys and Compounds* **791**, 648-654 (2019).
97. C. Geng, et al., "Tracking the optical constants of self-patterned VO₂-based on smart windows during metal-insulator transition," *Solar Energy Materials and Solar Cells* **272**, 112892 (2024).
98. A. Driouach, et al., "Film thickness dependent electron transport and optical properties of thermochromic VO₂," *Thin Solid Films* **779**, 139921 (2023).
99. K. Han, et al., "Enhanced metal-insulator transition in freestanding VO₂ down to 5 nm thickness," *ACS Applied Materials & Interfaces* **13**, 16688-16693 (2021).
100. Z. Shao, et al., "Controllable phase-transition temperature upon strain release in VO₂/MgF₂ epitaxial films," *Journal of Applied Physics* **128**, 4 (2020).
101. J. Jian, et al., "Continuous tuning of phase transition temperature in VO₂ thin films on c-cut sapphire substrates via strain variation," *ACS applied materials & interfaces* **9**, 5319-5327 (2017).
102. B. Zhi, et al., "Thickness-dependent metal-to-insulator transition in epitaxial VO₂ films," *Materials Research Express* **1**, 046402 (2014).
103. G. Xu, et al., "Thickness dependence of optical properties of VO₂ thin films epitaxially grown on sapphire (0001)," *Applied Surface Science* **244**, 449-452 (2005).
104. F. Egorov, "Controllable fiber-optic light modulator based on vanadium dioxide," *Sov. Tech. Phys. Lett* **17**, 817-819 (1991).
105. F. Chudnovskii, et al., "Electrical transport properties and switching in vanadium anodic oxides: effect of laser irradiation," *physica status solidi (a)* **172**, 391-395 (1999).
106. C. Kübler, et al., "Coherent Structural Dynamics and Electronic Correlations during an Ultrafast Insulator-to-Metal Phase Transition in VO₂," *Physical Review Letters* **99**, 116401 (2007).
107. C. Kittel and P. McEuen, *Introduction to solid state physics* (John Wiley & Sons, 2018).
108. J. D. Ryckman, et al., "Photothermal optical modulation of ultra-compact hybrid Si-VO₂ ring resonators," *Optics express* **20**, 13215-13225 (2012).

109. J. D. Ryckman, et al., "Ultra-compact silicon photonic devices reconfigured by an optically induced semiconductor-to-metal transition," *Optics express* **21**, 10753-10763 (2013).
110. J. Parra, et al., "All-Optical Hybrid VO₂/Si Waveguide Absorption Switch at Telecommunication Wavelengths," *Journal of Lightwave Technology* **39**, 2888-2894 (2021).
111. Z. Wang, et al., "Femtosecond laser-induced phase transition in VO₂ films," *Optics Express* **30**, 47421-47429 (2022).
112. K. A. Hallman, et al., "Sub-picosecond response time of a hybrid VO₂: silicon waveguide at 1550 nm," *Advanced Optical Materials* **9**, 2001721 (2021).
113. T. Alexoudi, et al., "Optical RAM and integrated optical memories: a survey," *Light: Science & Applications* **9**, 91 (2020).
114. Z. Fang, et al., "Non-volatile materials for programmable photonics," *APL Materials* **11**, 10 (2023).
115. J. Feldmann, et al., "Calculating with light using a chip-scale all-optical abacus," *Nature communications* **8**, 1256 (2017).
116. L. Pellegrino, et al., "Multistate memory devices based on free-standing VO₂/TiO₂ microstructures driven by Joule self-heating," *Advanced Materials (Deerfield Beach, Fla.)* **24**, 2929-2934 (2012).
117. J.-J. Seoane, et al., "2-μm-long VO₂/Si device with multilevel-memory response," in *2024 IEEE Silicon Photonics Conference (SiPhotonics)*, (IEEE, 2024), 1-2.
118. J. J. Seoane, et al., "Enhanced BaTiO₃/Si₃N₄ integrated photonic platform with VO₂ technology for large-scale neuromorphic computing," *Optical Materials Express* **13**, 3266-3276 (2023).
119. X. Yu, et al., "Graphene-Assisting Nonvolatile Vanadium Dioxide Phase Transition for Neuromorphic Machine Vision," *Advanced Functional Materials* **34**, 2312481 (2024).
120. X. Xu, et al., "Nanoelectrical monitoring the nonvolatile behavior of VO₂ under multi-field stimulate by conductive atomic force microscopy," *Materials Letters* **363**, 136236 (2024).
121. S. Basak, et al., "Spatially Distributed Ramp Reversal Memory in VO₂," *Advanced Electronic Materials* **9**, 2300085 (2023).
122. G. Li, et al., "Photo-induced non-volatile VO₂ phase transition for neuromorphic ultraviolet sensors," *Nature communications* **13**, 1729 (2022).
123. Y. J. Lee, et al., "Nonvolatile control of metal-insulator transition in VO₂ by ferroelectric gating," *Advanced Materials* **34**, 2203097 (2022).
124. X. Guo, et al., "Integrated neuromorphic photonics: synapses, neurons, and neural networks," *Advanced Photonics Research* **2**, 2000212 (2021).
125. M. Suri, et al., "Physical aspects of low power synapses based on phase change memory devices," *Journal of Applied Physics* **112**, 5 (2012).
126. I. Chakraborty, et al., "Toward fast neural computing using all-photonic phase change spiking neurons," *Scientific reports* **8**, 12980 (2018).
127. G. Lee, et al., "Artificial neuron and synapse devices based on 2D materials," *Small* **17**, 2100640 (2021).
128. X. Gao, et al., "Multi-level operation in VO₂-based resistive switching devices," *AIP advances* **12**, 015218 (2022).
129. J. Parra, et al., "Sub-milliwatt threshold power and tunable-bias all-optical nonlinear activation function using vanadium dioxide for wavelength-division multiplexing photonic neural networks," *arXiv preprint arXiv:2407.16472* (2024).
130. J.-F. Morcillo, et al., "On-chip electro-optical spiking VO₂/Si device with an inhibitory leaky integrate-and-fire response," *Optical Materials Express* **14**, 2681-2693 (2024).
131. W. Yi, et al., "Biological plausibility and stochasticity in scalable VO₂ active memristor neurons," *Nature communications* **9**, 4661 (2018).

132. L. Wang, et al., "Thermally modulated photoelectronic synaptic behavior in HfS_2/VO_2 heterostructure," *Rare Metals*, 1-12 (2024).
133. R. Wang, et al., "SD-PCM: Constructing reliable super dense phase change memory under write disturbance," *ACM SIGARCH Computer Architecture News* **43**, 19-31 (2015).
134. W. Zhou, et al., "Fabrication and integration of photonic devices for phase-change memory and neuromorphic computing," *International Journal of Extreme Manufacturing* **6**, 022001 (2024).
135. Z. Yang and S. Ramanathan, "Breakthroughs in photonics 2014: phase change materials for photonics," *IEEE Photonics Journal* **7**, 1-5 (2015).
136. F. C. Case, "Modifications in the phase transition properties of predeposited VO_2 films," *Journal of Vacuum Science & Technology A: Vacuum, Surfaces, and Films* **2**, 1509-1512 (1984).
137. M. Wuttig, et al., "Phase-change materials for non-volatile photonic applications," *Nature photonics* **11**, 465-476 (2017).
138. F. Morin, "Oxides which show a metal-to-insulator transition at the Neel temperature," *Physical review letters* **3**, 34 (1959).
139. H. Coy, et al., "Optoelectronic and all-optical multiple memory states in vanadium dioxide," *Journal of Applied Physics* **108**, 113115 (2010).
140. Y. Cui, et al., "Thermochromic VO_2 for energy-efficient smart windows," *Joule* **2**, 1707-1746 (2018).
141. R. Shi, et al., "Single-crystalline vanadium dioxide actuators," *Advanced Functional Materials* **29**, 1900527 (2019).
142. J. Qi, et al., "Synthesis, characterization, and thermodynamic parameters of vanadium dioxide," *Materials Research Bulletin* **43**, 2300-2307 (2008).
143. J. Ye, et al., "Preparation, characterization and properties of thermochromic tungsten-doped vanadium dioxide by thermal reduction and annealing," *Journal of Alloys and Compounds* **504**, 503-507 (2010).
144. V.-H. Pham, et al., "Microstructure and luminescence of VO_2 (B) nanoparticle synthesis by hydrothermal method," *Green Processing and Synthesis* **8**, 802-807 (2019).
145. C. Cao, et al., "Pure single-crystal rutile vanadium dioxide powders: synthesis, mechanism and phase-transformation property," *The Journal of Physical Chemistry C* **112**, 18810-18814 (2008).
146. V. Prasad, et al., "Study of VO_2 thin film synthesis by atomic layer deposition," *Materials Today Chemistry* **12**, 332-342 (2019).
147. P. A. Premkumar, et al., "Process study and characterization of VO_2 thin films synthesized by ALD using TEMAV and O_3 precursors," *ECS Journal of Solid State Science and Technology* **1**, P169 (2012).
148. K. Sun, et al., " VO_2 metasurface smart thermal emitter with high visual transparency for passive radiative cooling regulation in space and terrestrial applications," *Nanophotonics* **11**, 4101-4114 (2022).
149. H. Park, et al., "Study of a vanadium precursor for VO_2 thin-film growth in the atomic layer deposition process by multiscale simulations," *The Journal of Physical Chemistry C* **120**, 28193-28203 (2016).
150. M. O. Mavukkandy, et al., "Thin film deposition techniques for polymeric membranes—A review," *Journal of Membrane Science* **610**, 118258 (2020).
151. M. Fang and J. C. Ho, "Area-selective atomic layer deposition: conformal coating, subnanometer thickness control, and smart positioning," *ACS nano* **9**, 8651-8654 (2015).
152. E. Shkondin, et al., "Fabrication of high aspect ratio TiO_2 and Al_2O_3 nanogratings by atomic layer deposition," *Journal of Vacuum Science & Technology A* **34**, 3 (2016).
153. Y. Xue and S. Yin, "Element doping: a marvelous strategy for pioneering the smart applications of VO_2 ," *Nanoscale* **14**, 11054-11097 (2022).

154. K. Sun, et al., "Room Temperature Phase Transition of W-Doped VO₂ by Atomic Layer Deposition on 200 mm Si Wafers and Flexible Substrates," *Advanced Optical Materials* **10**, 2201326 (2022).
155. C. Ji, et al., "Al-doped VO₂ films as smart window coatings: reduced phase transition temperature and improved thermochromic performance," *Solar Energy Materials and Solar Cells* **176**, 174-180 (2018).
156. A. A. Muller, et al., "Radio Frequency Temperature Transducers Based on Insulator-Metal Phase Transition in VO₂ and Ge-Doped VO₂ ALD Thin Films," in *2021 21st International Conference on Solid-State Sensors, Actuators and Microsystems (Transducers)*, (IEEE, 2021), 1355-1358.
157. S. Wang, et al., "Al-Doping-Induced VO₂ (B) Phase in VO₂ (M) Toward Smart Optical Thin Films with Modulated ΔT_{vis} and ΔT_c ," *Advanced Engineering Materials* **21**, 1900947 (2019).
158. B. Rajeswaran and A. M. Umarji, "Defect engineering of VO₂ thin films synthesized by Chemical Vapor Deposition," *Materials Chemistry and Physics* **245**, 122230 (2020).
159. D. Vernardou, et al., "Thermochromic amorphous VO₂ coatings grown by APCVD using a single-precursor," *Solar energy materials and solar cells* **128**, 36-40 (2014).
160. H. Nishinaka, et al., "Rapid homoepitaxial growth of (010) β -Ga₂O₃ thin films via mist chemical vapor deposition," *Materials Science in Semiconductor Processing* **128**, 105732 (2021).
161. D. Malarde, et al., "Optimized atmospheric-pressure chemical vapor deposition thermochromic VO₂ thin films for intelligent window applications," *ACS omega* **2**, 1040-1046 (2017).
162. K. Choy, "Chemical vapour deposition of coatings," *Progress in materials science* **48**, 57-170 (2003).
163. A. H. Simon, "Sputter processing," in *Handbook of thin film deposition* (Elsevier, 2018), pp. 195-230.
164. X.-B. Wei, et al., "Growth mode and texture study in vanadium dioxide thin films deposited by magnetron sputtering," *Journal of Physics D: Applied Physics* **41**, 055303 (2008).
165. H.-C. Ho, et al., "High quality thermochromic VO₂ films prepared by magnetron sputtering using V₂O₅ target with in situ annealing," *Applied Surface Science* **495**, 143436 (2019).
166. S. Mobtakeri, et al., "Gallium oxide films deposition by RF magnetron sputtering; a detailed analysis on the effects of deposition pressure and sputtering power and annealing," *Ceramics International* **47**, 1721-1727 (2021).
167. C. M. Furqan, et al., "GaN thin film: growth and characterizations by magnetron sputtering," *Surfaces and Interfaces* **26**, 101364 (2021).
168. K. Pinggen, et al., "High growth rate magnetron sputter epitaxy of GaN using a solid Ga target," *Vacuum*, 112852 (2023).
169. M. Zhu, et al., "The novel preparation method of thermochromic VO₂ films with a low phase transition temperature by thermal oxidation of V-Mo cosputtered alloy films," *Ceramics International* **49**, 11803-11812 (2023).
170. C. Wen, et al., "A review of the preparation, properties and applications of VO₂ thin films with the reversible phase transition," *Frontiers in Materials* **11**, 1341518 (2024).
171. G. Li, et al., "Computational elements based on coupled VO₂ oscillators via tunable thermal triggering," *Nature Communications* **15**, 5820 (2024).
172. J. M. C. Garrido and J. M. Silveyra, "A review of typical PLD arrangements: Challenges, awareness, and solutions," *Optics and Lasers in Engineering* **168**, 107677 (2023).
173. A. Spitzig, et al., "Ultrathin VO₂ grown with oxygen plasma molecular beam epitaxy on TiO₂ (001) and Al₂O₃ (0001)," *Journal of Vacuum Science & Technology A* **41**(2023).
174. C. Liu, et al., "Low-temperature growth of high-quality VO₂ epitaxial film on c-plane sapphire by reactive magnetron sputtering," *Applied Physics Letters* **125**(2024).

175. A. Kumar, et al., "A Comprehensive Review on Synthesis, Phase Transition, and Applications of VO₂," *Journal of Superconductivity and Novel Magnetism* **37**, 475-498 (2024).
176. Y. Dachuan, et al., "Vanadium dioxide films with good electrical switching property," *Journal of Physics D: Applied Physics* **29**, 1051 (1996).
177. V. Devthade and S. Lee, "Synthesis of vanadium dioxide thin films and nanostructures," *Journal of Applied Physics* **128**, 23 (2020).
178. Z. Li, et al., "Phase Change Kinetics of Vanadium Dioxide Thin Film Prepared by Sol–Gel Deposition," *The Journal of Physical Chemistry C* **128**, 7773-7783 (2024).
179. X. Ding, et al., "Sol-gel derived tungsten doped VO₂ thin films on Si substrate with tunable phase transition properties," *Molecules* **28**, 3778 (2023).
180. M. Basso, et al., "Rapid laser-induced low temperature crystallization of thermochromic VO₂ sol-gel thin films," *Applied Surface Science* **631**, 157507 (2023).
181. C. O. Ba, et al., "Formation of VO₂ by rapid thermal annealing and cooling of sputtered vanadium thin films," *Journal of Vacuum Science & Technology A* **34**, 031505 (2016).
182. D. H. Jung, et al., "Low temperature growth of amorphous VO₂ films on flexible polyimide substrates with a TiO₂ buffer layer," *Journal of Vacuum Science & Technology A* **36**, 03E102 (2018).
183. G. Sun, et al., "Low-temperature deposition of VO₂ films with high crystalline degree by embedding multilayered structure," *Solar Energy Materials and Solar Cells* **161**, 70-76 (2017).
184. K. Zhang, et al., "Synthesis of VO₂ thin films by atomic layer deposition with TEMAV as precursor," *ECS Transactions* **50**, 175 (2013).
185. M. Tangirala, et al., "VO₂ films prepared by atomic layer deposition and RF magnetron sputtering," *ECS Transactions* **58**, 49 (2013).
186. M. Tangirala, et al., "Physical analysis of VO₂ films grown by atomic layer deposition and RF magnetron sputtering," *ECS Journal of Solid State Science and Technology* **3**, N89 (2014).
187. M. Currie, et al., "Atomic layer deposition of vanadium dioxide and a temperature-dependent optical model," *JoVE (Journal of Visualized Experiments)*, e57103 (2018).
188. V. P. Prasad, et al., "Atomic layer deposition of vanadium oxides: Process and application review," *Materials Today Chemistry* **12**, 396-423 (2019).
189. G. Rampelberg, et al., "Crystallization and semiconductor-metal switching behavior of thin VO₂ layers grown by atomic layer deposition," *Thin Solid Films* **550**, 59-64 (2014).
190. A. C. Kozen, et al., "Structural characterization of atomic layer deposited vanadium dioxide," *The Journal of Physical Chemistry C* **121**, 19341-19347 (2017).
191. H. H. Park, et al., "Tunable electrical properties of vanadium oxide by hydrogen-plasma-treated atomic layer deposition," *ACS omega* **2**, 1259-1264 (2017).
192. X. Lv, et al., "Atomic layer deposition of VO₂ films with Tetrakis-dimethyl-amino vanadium (IV) as vanadium precursor," *Applied Surface Science* **396**, 214-220 (2017).
193. M. J. Tadjer, et al., "Temperature and electric field induced metal-insulator transition in atomic layer deposited VO₂ thin films," *Solid-State Electronics* **136**, 30-35 (2017).
194. G. Bai, et al., "Preparation of atomic layer deposited vanadium dioxide thin films using tetrakis (ethylmethylamino) vanadium as precursor," *Journal of Vacuum Science & Technology A* **38**(2020).
195. J. Li, et al., "Thermochromatic vanadium dioxide (VO₂) thin films synthesized by atomic layer deposition and post-treatments," *Applied Surface Science* **529**, 147108 (2020).
196. A. M. Boyce, et al., "Actively tunable metasurfaces via plasmonic nanogap cavities with sub-10 nm VO₂ films," *Nano Letters* **22**, 3525-3531 (2022).
197. J. Kang, et al., "Modular and reconfigurable stretchable electronic systems," *Advanced Materials Technologies* **4**, 1800417 (2019).

198. J. H. Chow, et al., "Twist testing for flexible electronics," in *2019 IEEE 69th Electronic Components and Technology Conference (ECTC)*, (IEEE, 2019), 785-791.
199. B. Schrader, *Infrared and Raman spectroscopy: methods and applications* (John Wiley & Sons, 2008).
200. D. Tuschel, "Practical group theory and Raman spectroscopy, part i: Normal vibrational modes," *Spectroscopy* **29**, 14 (2014).
201. P. Shvets, et al., "A review of Raman spectroscopy of vanadium oxides," *Journal of Raman spectroscopy* **50**, 1226-1244 (2019).
202. K. Shibuya and A. Sawa, "Polarized Raman scattering of epitaxial vanadium dioxide films with low-temperature monoclinic phase," *Journal of Applied Physics* **122**, 1 (2017).
203. D. N. G. Krishna and J. Philip, "Review on surface-characterization applications of X-ray photoelectron spectroscopy (XPS): Recent developments and challenges," *Applied Surface Science Advances* **12**, 100332 (2022).
204. H. Katzke, et al., "Theory of morphotropic transformations in vanadium oxides," *Physical Review B* **68**, 024109 (2003).
205. Z. Zhang, et al., "Thermochromic VO₂ thin films: solution-based processing, improved optical properties, and lowered phase transformation temperature," *Langmuir* **26**, 10738-10744 (2010).
206. E. K. Barimah, et al., "Infrared optical properties modulation of VO₂ thin film fabricated by ultrafast pulsed laser deposition for thermochromic smart window applications," *Scientific Reports* **12**, 11421 (2022).
207. D. B. Nash, "Mid-infrared reflectance spectra (2.3–22 μm) of sulfur, gold, KBr, MgO, and halon," *Applied optics* **25**, 2427-2433 (1986).
208. THORLABS, "Calcium Fluoride Positive Meniscus Lenses, Uncoated", retrieved https://www.thorlabschina.cn/newgroupage9.cfm?objectgroup_id=5435.
209. H. G. Tompkins, *A user's guide to ellipsometry* (Courier Corporation, 2006).
210. J. Ramirez-Rincon, et al., "Thermal hysteresis measurement of the VO₂ dielectric function for its metal-insulator transition by visible-IR ellipsometry," *Journal of Applied Physics* **124**, 195102 (2018).
211. I. Voloshenko, et al., "Microscopic nature of the asymmetric hysteresis in the insulator-metal transition of VO₂ revealed by spectroscopic ellipsometry," *Applied Physics Letters* **113**, 201906 (2018).
212. E. D. Palik, *Handbook of optical constants of solids* (Academic press, 1998), Vol. 3.
213. Y. Su, et al., "Silicon photonic platform for passive waveguide devices: materials, fabrication, and applications," *Advanced Materials Technologies* **5**, 1901153 (2020).
214. A. Rickman, et al., "Silicon-on-insulator optical rib waveguide loss and mode characteristics," *Journal of Lightwave Technology* **12**, 1771-1776 (1994).
215. X. Xu, et al., "An investigation of the mode characteristics of SOI submicron rib waveguides using the film mode matching method," *Journal of Optics A: Pure and Applied Optics* **11**, 015508 (2008).
216. W. Bogaerts, et al., "Silicon microring resonators," *Laser & Photonics Reviews* **6**, 47-73 (2012).
217. I. Demirtzioglou, et al., "Frequency comb generation in a silicon ring resonator modulator," *Optics express* **26**, 790-796 (2018).
218. L. Hu, et al., "Theoretical investigation of VO₂ smart window with large-scale dynamic infrared emittance adjustment for adaptive thermal management," *Solar Energy* **277**, 112734 (2024).
219. K. Sun, et al., "VO₂ thermochromic metamaterial-based smart optical solar reflector," *Acs Photonics* **5**, 2280-2286 (2018).
220. K. Tang, et al., "Temperature-adaptive radiative coating for all-season household thermal regulation," *Science* **374**, 1504-1509 (2021).

221. S. Wang, et al., "Scalable thermochromic smart windows with passive radiative cooling regulation," *Science* **374**, 1501-1504 (2021).
222. H. Jiang, et al., "Active optical switch and polarization-selective absorption in a VO₂ based metasurface in THz region," *Optics Communications* **536**, 129380 (2023).
223. O. Maher, et al., "Highly reproducible and CMOS-compatible VO₂-based oscillators for brain-inspired computing," *Scientific Reports* **14**, 11600 (2024).
224. B. Gui, et al., "Design of scene-adaptive infrared camouflage emitter based on Au-VO₂-Al₂O₃-Au metamaterials," *Optics Communications* **512**, 128016 (2022).
225. M. M. Qazilbash, et al., "Mott transition in VO₂ revealed by infrared spectroscopy and nano-imaging," *Science* **318**, 1750-1753 (2007).
226. Y. Bleu, et al., "Towards room temperature phase transition of W-doped VO₂ thin films deposited by pulsed laser deposition: thermochromic, surface, and structural analysis," *Materials* **16**, 461 (2023).
227. Z. Mao, et al., "In-situ stirring assisted hydrothermal synthesis of W-doped VO₂ (M) nanorods with improved doping efficiency and mid-infrared switching property," *Journal of Alloys and Compounds* **821**, 153556 (2020).
228. S. Chen and H. Zhang, "High visible transmittance of VO₂ film prepared by DC magnetron sputtering with situ annealing," *Journal of Optics* **50**, 508-511 (2021).
229. A. Sarangan, et al., "Optical switching performance of thermally oxidized vanadium dioxide with an integrated thin film heater," *Optical Materials Express* **11**, 2348-2358 (2021).
230. S. A. Bukhari, et al., "The effect of oxygen flow rate on metal-insulator transition (MIT) characteristics of vanadium dioxide (VO₂) thin films by pulsed laser deposition (PLD)," *Applied Surface Science* **529**, 146995 (2020).
231. P. Panburana, et al., "Effect of annealing conditions on VO₂ thin films prepared by sol-gel method," in *Journal of Physics: Conference Series*, (IOP Publishing, 2023), 012055.
232. C. Wu, et al., "Microfabrication of VO₂ thin films via a photosensitive sol-gel method," *Coatings* **11**, 1264 (2021).
233. T. Ratier, et al., "Vanadium Dioxide by Atomic Layer Deposition: A Promising Material for Next-Generation Memory Devices," *The Journal of Physical Chemistry Letters* **15**, 9811-9819 (2024).
234. E. Hryha, et al., "Stoichiometric vanadium oxides studied by XPS," *Surface and interface analysis* **44**, 1022-1025 (2012).
235. H. G. Tompkins and J. N. Hilfiker, *Spectroscopic ellipsometry: practical application to thin film characterization* (Momentum Press, 2015).
236. M. H. Mahdiah and M. Sohrabi, "Precise Design of VO₂ Thin Films for Smart Windows by Employing Thickness-Dependent Refractive Index," *physica status solidi (a)* **220**, 2200553 (2023).
237. M. Currie, et al., "Characterizing the tunable refractive index of vanadium dioxide," *Optical Materials Express* **7**, 1697-1707 (2017).
238. K. Marshall and R. Breuch, "Optical solar reflector-A highly stable, low alpha sub S/epsilon spacecraft thermal control surface," *Journal of Spacecraft and Rockets* **5**, 1051-1056 (1968).
239. X. Guo, et al., "High quality VO₂ thin films synthesized from V₂O₅ powder for sensitive near-infrared detection," *Scientific Reports* **11**, 21749 (2021).
240. Q. Su, et al., "Formation of vanadium oxides with various morphologies by chemical vapor deposition," *Journal of alloys and compounds* **475**, 518-523 (2009).
241. A. V. Ivanov, et al., "Fabrication of epitaxial W-doped VO₂ nanostructured films for terahertz modulation using the solvothermal process," *ACS Applied Nano Materials* **4**, 10592-10600 (2021).

242. G. Pan, et al., "Synthesis and thermochromic property studies on W doped VO₂ films fabricated by sol-gel method," *Scientific reports* **7**, 6132 (2017).
243. K. Kotsis and V. Staemmler, "Ab initio calculations of the O1s XPS spectra of ZnO and Zn oxo compounds," *Physical Chemistry Chemical Physics* **8**, 1490-1498 (2006).
244. H. Kakiuchida, et al., "Optical properties of vanadium dioxide film during semiconductive–metallic phase transition," *Japanese Journal of Applied Physics* **46**, L113 (2007).
245. M. Tazawa, et al., "Optical constants of V_{1-x}W_xO₂ films," *Applied optics* **37**, 1858-1861 (1998).
246. T. N. Tran, et al., "Synthesis of amorphous silica and sulfonic acid functionalized silica used as reinforced phase for polymer electrolyte membrane," *Advances in Natural Sciences: Nanoscience and Nanotechnology* **4**, 045007 (2013).
247. M. A. Kats, et al., "Ultra-thin perfect absorber employing a tunable phase change material," *Applied Physics Letters* **101**, 22 (2012).
248. S. B. Khemis, et al., "Comparative structural study of Al₂O₃–SiO₂ glasses and amorphous thin films," *International Journal of Applied Glass Science* **15**, 212-226 (2024).
249. T. Huang, et al., "Study of the phase evolution, metal-insulator transition, and optical properties of vanadium oxide thin films," *Optical Materials Express* **6**, 3609-3621 (2016).
250. G. Silversmit, et al., "Determination of the V2p XPS binding energies for different vanadium oxidation states (V5+ to V0+)," *Journal of Electron Spectroscopy and Related Phenomena* **135**, 167-175 (2004).
251. Z. Cao, et al., "A simple and low-cost combustion method to prepare monoclinic VO₂ with superior thermochromic properties," *Scientific reports* **6**, 39154 (2016).
252. K. Nishikawa, et al., "Phase transition behavior in nanostructured VO₂ with M1, M2, and R phases observed via temperature-dependent XRD measurements," *Journal of Vacuum Science & Technology A* **40**, 3 (2022).
253. F. Arteaga-Cardona, et al., "Simple thermal decomposition synthesis of monoclinic VO₂," *Applied Physics A* **127**, 1-7 (2021).
254. K. L. Gurunatha, et al., "Combined effect of temperature induced strain and oxygen vacancy on metal-insulator transition of VO₂ colloidal particles," *Advanced Functional Materials* **30**, 2005311 (2020).
255. B. Hu, et al., "External-strain induced insulating phase transition in VO₂ nanobeam and its application as flexible strain sensor," *Adv. Mater* **22**, 5134-5139 (2010).
256. K. Okimura, et al., "Stress-induced VO₂ films with M2 monoclinic phase stable at room temperature grown by inductively coupled plasma-assisted reactive sputtering," *Journal of Applied Physics* **111**, 7 (2012).
257. H. W. Verleur, et al., "Optical properties of VO₂ between 0.25 and 5 eV," *Physical Review* **172**, 788 (1968).
258. S. Oukassi, et al., "A spectroscopic ellipsometry investigation of RF-sputtered crystalline vanadium pentoxide thin films," *physica status solidi c* **5**, 1109-1112 (2008).
259. F. Mattelaer, et al., "Atomic layer deposition of vanadium oxides for thin-film lithium-ion battery applications," *RSC advances* **6**, 114658-114665 (2016).
260. W.-E. Hong and J.-S. Ro, "Kinetics of solid phase crystallization of amorphous silicon analyzed by Raman spectroscopy," *Journal of Applied Physics* **114**, 073511 (2013).
261. Y. Huang, et al., "Phase transition analysis of thermochromic VO₂ thin films by temperature-dependent Raman scattering and ellipsometry," *Applied Surface Science* **456**, 545-551 (2018).
262. K. Sun, "Low cost Si nanowire biosensors by recrystallisation technologies," (University of Southampton, 2011).
263. Y. Sun, et al., "Facile synthesis of vanadium oxide thin films by atomic layer deposition and post-annealing," *Applied Physics Letters* **126**, 5 (2025).

264. M. Zaghrioui, et al., "Polarized Raman scattering of large crystalline domains in VO₂ films on sapphire," *Vibrational Spectroscopy* **80**, 79-85 (2015).
265. S. H. Alrefaee, et al., "Effect of titanium oxide (TiO₂) nanoparticles on the opto-mechanical properties of polyethylene terephthalate (PET) fibers," *Optical Materials* **157**, 116242 (2024).
266. J. D. Kendall and S. Kumar, "The building blocks of a brain-inspired computer," *Applied Physics Reviews* **7**, 1 (2020).
267. A. Sebastian, et al., "Memory devices and applications for in-memory computing," *Nature nanotechnology* **15**, 529-544 (2020).
268. S. Wang, et al., "The road for 2D semiconductors in the silicon age," *Advanced Materials* **34**, 2106886 (2022).
269. T. F. De Lima, et al., "Machine learning with neuromorphic photonics," *Journal of Lightwave Technology* **37**, 1515-1534 (2019).
270. X. Zhuge, et al., "Photonic synapses for ultrahigh-speed neuromorphic computing," *physica status solidi (RRL)–Rapid Research Letters* **13**, 1900082 (2019).
271. C. M. Yang, et al., "Bidirectional all-optical synapses based on a 2D Bi₂O₂Se/graphene hybrid structure for multifunctional optoelectronics," *Advanced Functional Materials* **30**, 2001598 (2020).
272. M. Xu, et al., "Recent advances on neuromorphic devices based on chalcogenide phase-change materials," *Advanced Functional Materials* **30**, 2003419 (2020).
273. W. Lu, et al., "All optical artificial synapses based on long-afterglow material for optical neural network," *Nano Research* **16**, 10004-10010 (2023).
274. J. Gosciniaik, et al., "Bistable all-optical devices based on nonlinear epsilon-near-zero (ENZ) materials," *Laser & Photonics Reviews* **17**, 2200723 (2023).
275. Y. Ke, et al., "Emerging thermal-responsive materials and integrated techniques targeting the energy-efficient smart window application," *Advanced Functional Materials* **28**, 1800113 (2018).
276. T. D. Vu, et al., "Durable vanadium dioxide with 33-year service life for smart windows applications," *Materials Today Energy* **26**, 100978 (2022).
277. H. Takeya, et al., "Bolometric photodetection using plasmon-assisted resistivity change in vanadium dioxide," *Scientific reports* **8**, 12764 (2018).
278. J. K. Clark, et al., "Photoinduced metal-like phase of VO₂ with subns recovery," *ACS photonics* **7**, 2395-2404 (2020).
279. G. Wei, et al., "Optically induced phase change for magnetoresistance modulation," *Advanced Quantum Technologies* **3**, 1900104 (2020).
280. D. Y. Lei, et al., "Optically-triggered nanoscale memory effect in a hybrid plasmonic-phase changing nanostructure," *ACS photonics* **2**, 1306-1313 (2015).
281. Y. Hu, et al., "Spatiotemporal terahertz metasurfaces for ultrafast all-optical switching with electric-triggered bistability," *Laser & Photonics Reviews* **15**, 2000456 (2021).
282. C. Wan, et al., "On the optical properties of thin-film vanadium dioxide from the visible to the far infrared," *Annalen der Physik* **531**, 1900188 (2019).
283. J. D. Ryckman, et al., "Photothermal optical modulation of ultra-compact hybrid Si-VO₂ ring resonators," *Optics express* **20**, 13215-13225 (2012).
284. Y. Arosa and R. de la Fuente, "Refractive index spectroscopy and material dispersion in fused silica glass," *Optics Letters* **45**, 4268-4271 (2020).
285. I. a. J. H. L. John H. Lienhard, *A heat transfer textbook* (2019).
286. O. L. Muskens, et al., "Antenna-assisted picosecond control of nanoscale phase transition in vanadium dioxide," *Light: Science & Applications* **5**, e16173-e16173 (2016).
287. X. Wen, et al., "Experimental study on heat transfer coefficient between air and liquid in the cross-flow heat-source tower," *Building and Environment* **57**, 205-213 (2012).

288. S. Lee, et al., "Anomalously low electronic thermal conductivity in metallic vanadium dioxide," *Science* **355**, 371-374 (2017).
289. C. Berglund and H. Guggenheim, "Electronic Properties of VO₂ near the Semiconductor-Metal Transition," *Physical Review* **185**, 1022 (1969).
290. COSMOL, retrieved 2022, <https://www.comsol.com/support/knowledgebase/1258>.
291. A. Tomasian, "Which Study Type Should I Use for My Electrothermal Analysis?" (2020), retrieved 2022, <https://www.comsol.com/blogs/which-study-type-should-i-use-for-my-electrothermal-analysis?setlang=1>.
292. L. Agarwal, et al., "Highly reflective Er-doped ZnO thin-film coating for application in a UV optical ring resonator," *Nanotechnology* **28**, 465707 (2017).
293. D. Yang, et al., "Nanoslotted microring resonator for high figure of merit refractive index sensing," *Optica Applicata* **50**, 37--47 (2020).
294. M. Angelini, et al., "Convergence and Performance Analysis of a Particle Swarm Optimization Algorithm for Optical Tuning of Gold Nanohole Arrays," *Materials* **17**, 807 (2024).
295. Lumerical, "Convergence testing process for FDTD simulations", retrieved <https://optics.ansys.com/hc/en-us/articles/360034915833-Convergence-testing-process-for-FDTD-simulations>.
296. Lumerical, "Selecting the best mesh refinement option in the FDTD simulation object", retrieved <https://optics.ansys.com/hc/en-us/articles/360034382614-Selecting-the-best-mesh-refinement-option-in-the-FDTD-simulation-object>.
297. J. Parra, et al., "Low-threshold power and tunable integrated optical limiter based on an ultracompact VO₂/Si waveguide," *APL Photonics* **6**, 121301 (2021).
298. K. Miwa, et al., "Photo-thermoelectric conversion of plasmonic nanohole array," *Applied Sciences* **10**, 2681 (2020).
299. G. Baffou and R. Quidant, "Thermo-plasmonics: using metallic nanostructures as nano-sources of heat," *Laser & Photonics Reviews* **7**, 171-187 (2013).
300. L. Del Bino, et al., "Optical memories and switching dynamics of counterpropagating light states in microresonators," *Optics Express* **29**, 2193-2203 (2021).
301. M. Lust, et al., "Thermo-optic VO₂-based silicon waveguide mid-infrared router with asymmetric activation thresholds and large bi-stability," *Optics Express* **31**, 23260-23273 (2023).
302. J. Parra, et al., "All-optical hybrid VO₂/Si waveguide absorption switch at telecommunication wavelengths," *Journal of Lightwave Technology* **39**, 2888-2894 (2021).
303. H. M. Wong, et al., "Broadband, integrated, micron-scale, all-optical Si₃N₄/VO₂ modulators with pJ switching energy," *ACS Photonics* **6**, 2734-2740 (2019).
304. F. L. Assem and L. S. Levy, "A review of current toxicological concerns on vanadium pentoxide and other vanadium compounds: gaps in knowledge and directions for future research," *Journal of Toxicology and Environmental Health, Part B* **12**, 289-306 (2009).
305. S. K. Ghosh, et al., "Toxicity of inorganic vanadium compounds," *Research on Chemical Intermediates* **41**, 4873-4897 (2015).
306. L. S. Rhoads, et al., "Cytotoxicity of nanostructured vanadium oxide on human cells in vitro," *Toxicology in Vitro* **24**, 292-296 (2010).
307. J. Guo, et al., "Nano vanadium dioxide films deposited on biomedical titanium: a novel approach for simultaneously enhanced osteogenic and antibacterial effects," *Artificial Cells, Nanomedicine, and Biotechnology* **46**, 58-74 (2018).
308. J. Li, et al., "Vanadium dioxide nanocoating induces tumor cell death through mitochondrial electron transport chain interruption," *Global Challenges* **3**, 1800058 (2019).
309. H. Xu, et al., "Effects of annealing ambient on oxygen vacancies and phase transition temperature of VO₂ thin films," *RSC advances* **6**, 79383-79388 (2016).

310. "Communication on Article Information Sheets " (DUPONT, 2014), retrieved chrome-extension://efaidnbmnnnibpcajpcglclefindmkaj/https://polymerfilms.com/wp-content/uploads/2023/06/Polymerfilms-DuPont-Kapton-Datasheet.pdf.
311. X. Zhao, et al., "Dewetting behavior of Au films on porous substrates," *Thin Solid Films* **519**, 706-713 (2010).